Ministry of Education and Science of the Russian Federation
Saint Petersburg National Research University of Information Technologies, Mechanics, and Optics

NANOSYSTEMS:

PHYSICS, CHEMISTRY, MATHEMATICS

2014, volume 5(2)

Наносистемы: физика, химия, математика
2014, том 5, № 2

NANO
Ф&Х&М

NANOSYSTEMS:

PHYSICS, CHEMISTRY, MATHEMATICS

Address: University ITMO, Kronverkskiy pr., 49, St. Petersburg 197101, Russia.
Phone: +7(812)232-67-65, **Journal site:** http://nanojournal.ifmo.ru/,
E-mail: popov1955@gmail.com

AIM AND SCOPE

The scope of the journal includes all areas of nano-sciences. Papers devoted to basic problems of physics, chemistry, material science and mathematics inspired by nanosystems investigations are welcomed. Both theoretical and experimental works concerning the properties and behavior of nanosystems, problems of its creation and application, mathematical methods of nanosystem studies are considered.

The journal publishes scientific reviews (up to 30 journal pages), research papers (up to 15 pages) and letters (up to 5 pages). All manuscripts are peer-reviewed. Authors are informed about the referee opinion and the Editorial decision.

Content

FROM THE EDITORIAL BOARD

Obituary
Ivanovskii Aleksandr Leonidovich

Born February 16, 1953

Aleksandr Leonidovich Ivanovskii, a member of the Editorial Board of "Nanosystems: Physics, Chemistry, Mathematics", Doctor of Chemistry, Professor, the leader of the Laboratory of quantum chemistry and spectroscopy at the Institute of Solid State Chemistry, which was created and guided by him until his last days, suddenly passed away on the 28th of February 2014 at the age of 61.

A.L. Ivanovskii began working at the ISSCh UB RAS in 1976 after graduation from the famous physicotechnical faculty of the Ural Polytechnical Institute with the speciality of engineer-physicist. In 1980, under the guidance of Prof. V.A. Gubanov and Prof. G.P. Shveikin, A.L. Ivanovskii defended his PhD thesis "Examination of the electronic structure and chemical bonding in some vanadites and vanadates" and soon became one of the leading specialists in a new field of science – solid state quantum chemistry. Prof. V.A. Gubanov exerted a large influence on his making as a scientist. In the 1980's, A.L. Ivanovskii took part in the simulation of physicochemical properties and the nature of chemical bonding in refractory interstitial phases based on transition metals. After the defence of his doctoral thesis (1989), A.L. Ivanovskii actively developed a new scientific area – application of modern computational methods of quantum chemistry for the modeling of physicochemical properties of novel compounds and materials.

A.L. Ivanovskii is the author and co-author of more than 860 scientific works in domestic and international journals, 16 monographs and more than 20 reviews devoted to the problems of computer materials science of inorganic systems. He has carried out large fundamental works on the analysis of the electronic structure and functional properties of a vast class of practically important materials – carbides, nitrides, oxides, borides, silicides and hydrides of metals, their solid solutions, as well as alloys and intermetallic compounds. These results found a broad reception among the scientific community, as demonstrated by the more than six thousand citations of his works. The works of A.L. Ivanovskii had a profound effect on the development of physicochemical foundations of technologies for the production of cermets, refractory coatings, condensing materials and new-generation complex polyfunctional ceramics with the use of technogeneous materials. Priority information on the microscopic properties of nonstoichiometric compounds and surface properties has been obtained and an important contribution to the theory of reactivity of solid-phase substances has been made under the Ivanovskii's leadership.

A series of works, *Quantum Chemistry and Spectroscopy of Solid State,* carried out by A.L. Ivanovskii and a team of Ural and Siberian scientists, was awarded the State Prize of the Russian Federation in the field of science and engineering (1995).

In recent years, A.L. Ivanovskii actively developed a new research field in quantum materials science of inorganic nanostructures (nanotubes and fullerene-like clusters) and nanomaterials based thereon. He has published the first domestic monographs on novel structured nanomaterials (*Nanotubular Forms of Substance*, 1999, *Metal Oxide Nanotubes*, 2005). In 2005, the academic Company *Nauka/Interperiodika* awarded to A.L. Ivanovskii the prize *For the Best Publication* for a series of works on the quantum chemistry of nanostructures. Along with the examination of tubulenes, the works of A.L. Ivanovskii which were devoted to the chemical nature of high-temperature superconductivity in borides and arsenides have been highly recognized by the international scientific community.

A.L. Ivanovskii was a talented science organizer who paid much attention to research and organizational activities, as well as to training of top-tier scientists. He has trained 12 researchers holding PhD degrees and 2 Doctors. In 1998, A.L. Ivanovskii was awarded an academic title of professor of analytical chemistry and in 2000 – professor of mathematical and quantum chemistry. As a Professor of the Ural State University since 1992, A.L. Ivanovskii delivered lectures on quantum and general chemistry. He was a member of the Joint Council of the UB RAS for chemical sciences, the Scientific Council of the ISSC UB RAS, two dissertation councils (at the ISSC UB RAS and USU), editorial boards of the journals *Strukturnaya khimiya* and *Alternativnaya energetika*. From 1989 to 2000, he was an academic secretary and from 2000 to 2003 – a deputy director for science at the ISSC UB RAS. A.L. Ivanovskii was an academic secretary and deputy chairman of organizing committees of many all-Russian and international conferences. In 2007, A.L. Ivanovskii was awarded an honorary title of Honored Scientist of the Russian Federation.

A.L. Ivanovskii was and remains for us an example of the Russian scientist committed to the ideals of science, education and culture. As with all truly talented people, his creative life was not limited to vocational interests; he was fond of and deeply felt music, painting, literature and received a university education with a degree in art appreciation (USU, 1982). We know and will always remember our colleague, a remarkable scientist and friend Aleksandr Leonidovich Ivanovskii as a well-bred intellectual, a man of principle and a highly cultured person having solid scholarship, who readily showed initiative, creative enthusiasm and vitality.

Editorial Board of "Nanosystems: Physics, Chemistry, Mathematics",

ISSC UB RAS administration and colleagues

NANOSYSTEMS: PHYSICS, CHEMISTRY, MATHEMATICS, 2014, 5 (2), P. 210–216

OPTICAL INDUCTION OF 3D REFRACTIVE LATTICES IN DOUBLY DOPED $LiNbO_3$ PHOTOREFRACTIVE CRYSTAL

A. Badalyan[1], P. Mantashyan[1], V. Mekhitaryan[1], V. Nersesyan[1*] and R. Drampyan[1,2]

[1]Institute for Physical Research, National Academy of Sciences of Armenia, 0203, Ashtarak-2, Armenia

[2]Armenian – Russian (Slavonic) University, H. Emin str. 123, 0051, Yerevan, Armenia

*vars.nersesyan@gmail.com

PACS 42.70.Qs, 78.67.Pt

The optical induction of 3D rotational symmetry refractive lattices in doubly doped photorefractive and photochromic $LiNbO_3$:Fe:Cu crystal by combined interferometric-mask method was performed. The method is based on the spatial light modulation by amplitude mask in the transverse plane and the use of counter-propagating beam geometry building up a Gaussian standing wave, which defines the light intensity modulation in the axial direction with half-wavelength periodicity. Masks with rotationally symmetrical structures are used in the experiment. The created intensity pattern was imparted into the $LiNbO_3$:Fe:Cu crystal thus creating refractive lattice with the periods of 20 – 60 μm in the radial and azimuthal directions and 266 nm in the axial direction. The refractive and dispersive properties of the recorded lattices were studied.

Keywords: Photonic lattice, photorefractive and photochromic effects, lithium niobate, micro- and nano-structures.

1. Introduction

Light controlling systems, such as two- and three-dimensional (2D, 3D) photonic crystals and optically induced refractive lattices are of great interest for various applications, including guiding and trapping systems, photonic bandgap materials, all-optical devices, information storage and processing, telecommunication systems, optical computers, etc.

There are well known methods for creating the refractive structures by electronic beam, UV lithography or etching techniques which permit the formation of micro- and nano-scale permanently fixed refractive structures in the materials with high refractive index, providing pronounced photonic bandgaps. The holographic technique is based on the illumination of a photorefractive medium by spatially modulated light beam which leads to the corresponding refractive index modulation and creates refractive lattices in the medium (photonic lattices). The optical induction methods provide relatively low refractive index contrast. Nevertheless such an approach becomes particularly attractive for applications which require the ability to tune and adapt photonic lattices in real time. Photonic lattices are very promising for high capacity information storage and readout [1], for controlling and manipulating the light flow [2], and higher order rotational symmetry 3D lattices provide the appearance of isotropic and complete photonic bandgaps [3, 4]. Photorefractive crystals are one of the promising photosensitive materials for the formation of photonic lattices.

Recently, we suggested the combined interferometric–mask method (CIM) [5, 6] for formation of 3D photonic lattices. The main concept was the combination of a well known computer generated mask technique, providing the formation of 2D gratings with two-beam interference method, providing the formation of 1D gratings. Our approach is based on the spatial light modulation by amplitude mask in the transverse plane and the use of counter-propagating

beam geometry building up Gaussian standing wave, which defines the light intensity modulation in the axial direction with half-wavelength periodicity. The created intensity patterns can be imparted into the photorefractive medium and create micro- and nano-scale 3D refractive index volume lattices. In fact, the formed 3D intensity pattern is an assembly of numerous mask-generated 2D periodic or quasi-periodic structures located in each anti-node of the standing wave. Thus, the CIM method allows the optical induction of 3D photonic lattices with the nanoscale 200 – 300 nm lattice periodicities along the axial direction. The method was realized in $LiNbO_3$:Fe crystal with the use of 7-fold rotational symmetry mask in [5] and 2-fold rotational symmetry mask in [6].

In this paper, we present the experimental results for the study of 3D refractive lattice formation in doubly doped lithium niobate (LN) crystals with the use of a 2-fold rotational symmetry amplitude mask. In the experiment, the LN:Fe:Cu crystal was used since doubly doped photorefractive crystals reveal also the photochromic effect, i.e. the dependence of the absorption coefficient on light intensity [7]. Photochromic properties provide the decreasing of the erasure of the lattices during readout by weaker probe beam at the recording wavelength. The photochromic properties of LN:Fe:Cu crystal allowed us to study the dispersive properties of refractive lattices by diffraction of white light from the lattices.

2. Optical induction of 3D refractive lattices

The 3D refractive lattices were optically induced by combined interferometric-mask method in a $LiNbO_3$ crystal doped by 0.05 wt% Fe and Cu (LN:Fe:Cu). The photorefractive LN:Fe:Cu crystal was illuminated through the 2-fold rotational symmetry micrometric scale mask by cw 532 nm, 100 mW laser beam in combination with back reflecting mirror (Fig. 1) over 30 – 60 min. The counter-propagating beam geometry builds up a Gaussian standing wave, which determines the half-wavelength periodic light modulation in the axial direction.

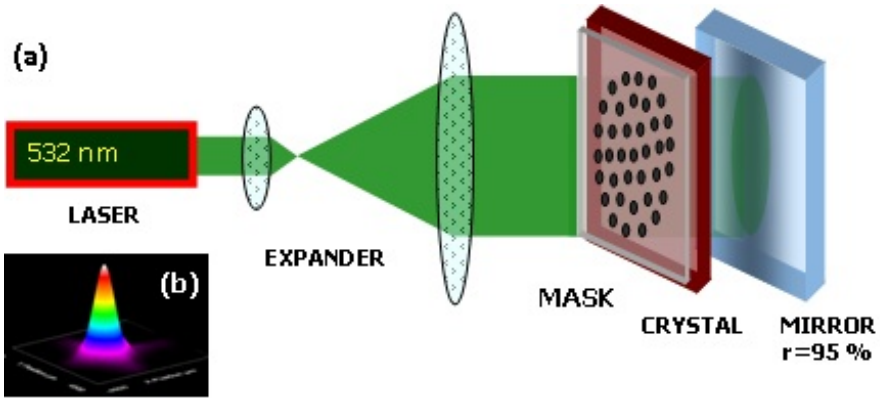

FIG. 1. (a) Experimental setup for induction of 3D lattices by CIM method. Removing the back reflecting mirror leads to the formation of 2D lattices with refractive index modulation in the transverse plane, (b) the Gaussian intensity distribution of the laser beam with the wavelength of 532 nm

Figure 2a shows the fragment of the used 2-fold rotational symmetry mask. The prepared negative mask had a distance of 20 – 60 μm between 10 μm transparent holes on the opaque disk. The mask consists of $\sim$ 10,000 holes disposed along the 100 hypothetical concentric circles. The technique of mask preparation is described in detail elsewhere [5,6]. The diffraction patterns from the mask were obtained in the far field by a red 633 nm He-Ne single mode laser beam, as well as by a light emitted diode (LED) source emitting white light as a mix of the

emissions in blue (480 nm), green (570 nm) and red (640 nm) spectral ranges. The diffraction patterns are shown in Fig. 2b and c, respectively. In the case of the LED source, the emitted light after passing through the 1mm diaphragm illuminates the mask placed 150 cm from the diaphragm. The high contrast diffraction patterns from the mask confirm the high quality of the prepared masks.

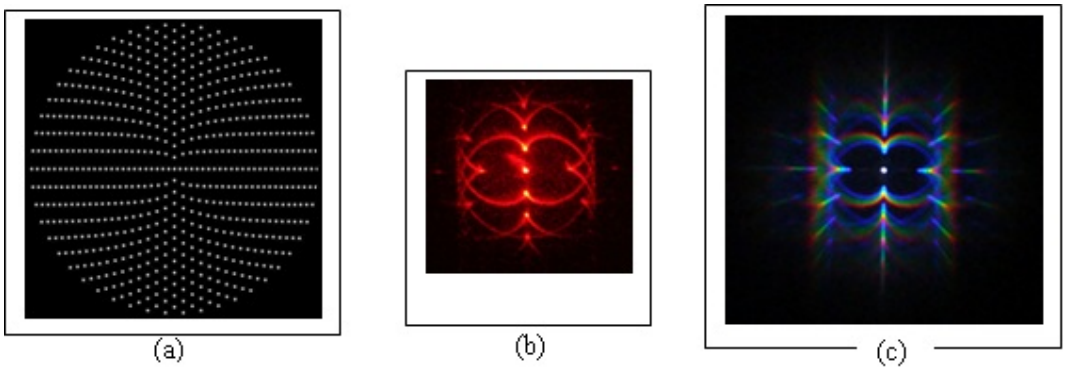

FIG. 2. (a) Fragment of 2-fold rotational symmetry mask. (b) and (c) are far field diffraction patterns from the mask obtained by red 633 nm laser beam and tricolor LED source, respectively

The formed 3D rotational symmetry photonic lattice inside the crystal represents itself a set of numerous mask-generated 2D quasi-periodic structures located in each anti-node of the standing wave and has 20 – 60 μm periods in the radial and azimuthal directions and half-wavelength 266 nm period in the axial direction (Fig. 3). The 2D lattice, modulated only in the transverse plane, can be recorded by simply removing the back reflecting mirror shown in Fig. 1.

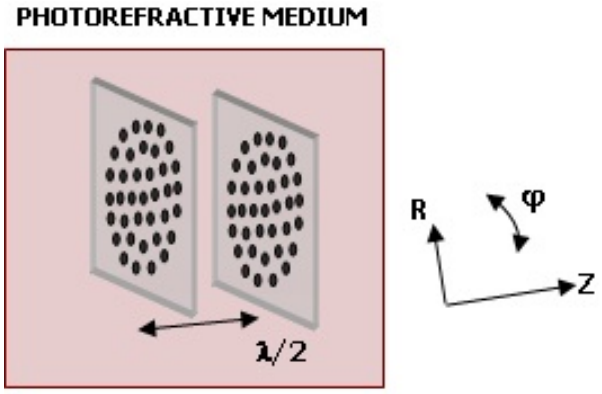

FIG. 3. Schematic of two neighboring anti-nodes of standing wave, where the mask created quasi-periodic structures are located. The scale along the direction of standing wave (Z-axis) is enlarged relative to R and φ directions

3. Optical testing of the recorded refractive lattices

The optical testing of the recorded lattices was performed by observation of the diffraction patterns from the 3D lattices in the far field using a monochromatic 633 nm probe laser

beam. The results are shown in Fig. 4a. The testing beam wavelength of 633 nm was used to decrease the erasure of the recorded lattices during the readout.

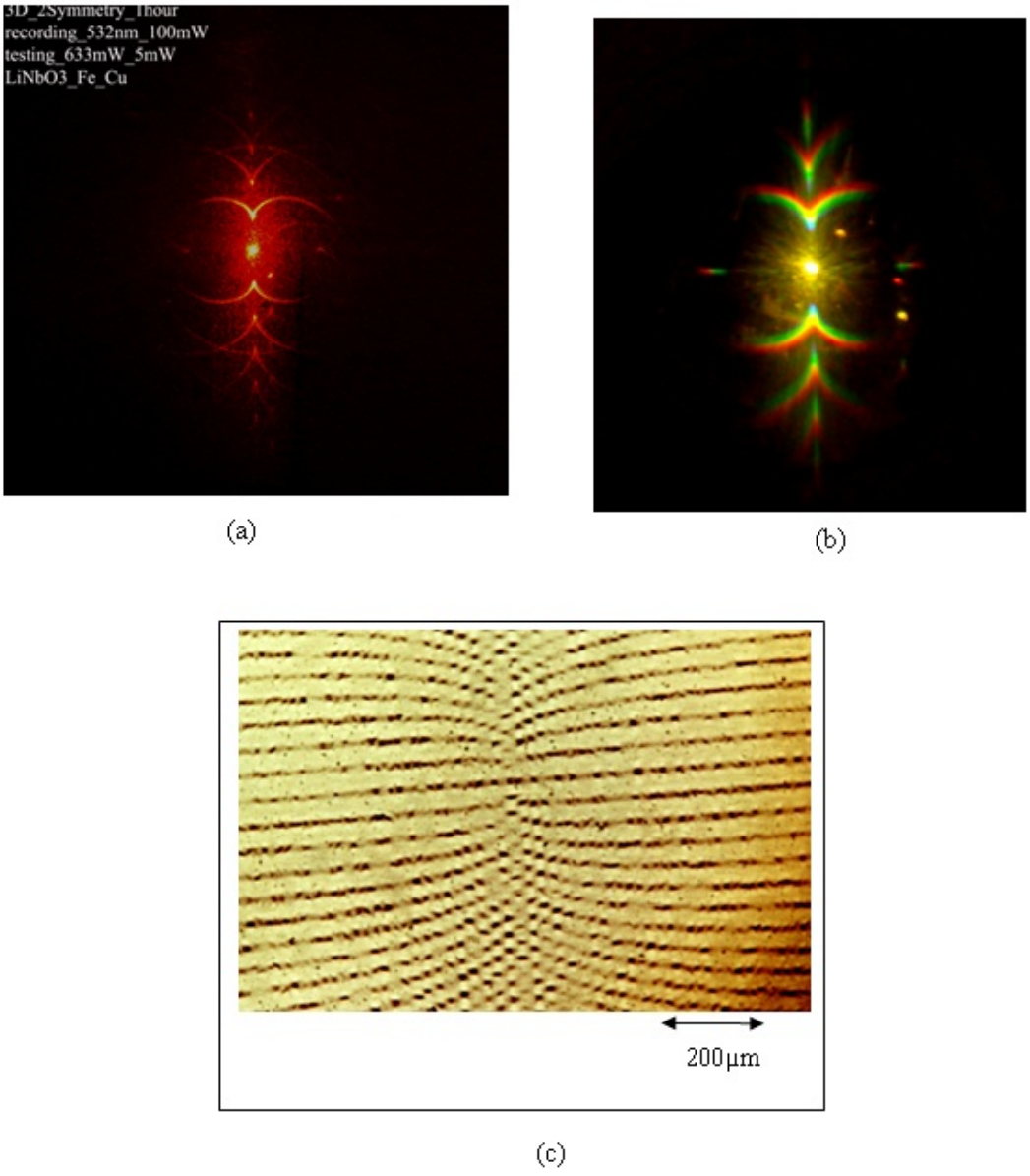

FIG. 4. (a, b) Far field diffraction patterns from recorded 3D lattice obtained by red 633 nm beam (a) and tricolor LED source (b), respectively. (c) Fragment of phase microscope images of transverse X-Y plane of 3D photonic lattices recorded inside of 2 mm thick LN:Fe:Cu crystal by 2-fold symmetry mask and 100 mW green laser beam during 1 hour

The dispersive properties of the recorded 3D volume refractive lattices have been studied by diffraction testing with the use of a tricolor LED source. The far field diffraction pattern is shown in Fig. 4b. The absence of the blue color contour in diffraction pattern is due to the strong absorption of blue light in the crystal. Fig. 4b shows that the diffraction efficiency of recorded pattern is approximately equal for visible spectral range.

The diffraction efficiency of recorded 3D lattice was measured from testing experiment with the use of an e-polarized 633 nm probe laser beam with an input power $P_{input} = 16.5$ mW.

Diffraction efficiency η was calculated as $\eta = P_{dif}/P_{input} = \{(P_{sc} - P_{bg})/P_{input}\} \times 100\%$, where the diffracted power P_{dif} is determined as a total forward scattered power P_{sc} minus background power P_{bg} transmitted through the clean part of crystal without recorded lattice, and equaled 2.3 %.

The direct observation of recorded lattices by phase microscope was also performed. Fig. 4c shows the phase microscope image of the transverse X-Y plane of 3D lattice recorded in LN:Fe:Cu crystal. The interference contrast observation was performed. The microscope allowed to strictly reveal the refractive index lattice with estimated refractive index modulation of $\delta n \sim 10^{-4} - 10^{-5}$, however, it did not allow one to perform quantitative measurements.

4. Discussion

The interest of holographic recording in doubly doped LN:Fe:Cu crystal is connected with photochromic properties of this crystal, namely the increase of absorption coefficient with the intensity of illuminating light [7, 8]. This allows the decreasing of erasure of stored lattices during readout by weaker probe beam at the recording wavelength [7].

The physical mechanism of holographic recording is connected with electro-optic effect. The illumination of photorefractive crystals by inhomogeneous light redistributes photo-charges, excited by photo-ionization, builds up internal electric field E, and so, changes the refractive index via electro-optic effect, $\delta n = 0.5 r_{33} E$, where r_{33} is electro-optic coefficient, thus allowing the induction of photonic refractive lattice structures. The electric field, induced due to spatial charge separation, is caused by the photovoltaic effect and diffusion of the photo-induced charge carriers. The photocurrent density J, along the crystalline C-axis due to the photovoltaic effect, equals $J = k_1 \alpha I$, where k_1 is Glass constant depending on the nature of absorbing centers and light wavelength, α is absorption coefficient and I is light intensity [9, 10]. The diffusion of charge carriers takes place in all directions and can be neglected for lattice spatial frequencies $K = 1/d$ having the values less than $\sim 10^5$ lines/cm, where d is the lattice period [9].

In comparison to the singly doped LN:Cu crystal, where electrons excited from Cu^{1+} are captured by Cu^{2+} centers, the doubly doped LN:Fe:Cu crystal also has Fe^{2+} center photo-excited electrons , move to the conductivity band and then are captured by both Fe^{3+} and Cu^{2+}. The capturing by Cu^{2+} forms additional Cu^{1+} centers. The increase of the ratio of Cu^{1+}/ Cu^{2+} leads to an increase in the absorption coefficient of the crystal [7, 8, 11]. The band diagram for two-center recording is shown in Fig. 5.

It is worth noting that the diffraction efficiency of 3D lattice recorded in LN:Fe:Cu crystal is lower than for the lattices recorded in LN:Fe crystal [5,6]. This is connected with lower value of the Glass constant and larger value of photoconductivity in LN:Fe:Cu crystal, while the absorption coefficients of LN:Fe and LN:Fe:Cu at 532 nm wavelength are approximately the same. The diffraction efficiency of the lattice in LN:Fe:Cu crystal can be increased by optimization of Fe and Cu concentration in the LN crystal, since conductivity depends on the dopant ions' concentrations.

The life-time of recorded lattices in the doped lithium niobate crystals in the absence of external affects, such as light and heating is up to one year [12, 13]. At room temperature, the dark storage time of recorded lattices in LN:Fe:Cu crystal, which are used in the present experiment is more than a period of one year. The recorded structures can be erased by homogeneous light, more effectively by intense UV light, thus allowing the multiple recording and readout of photonic structures in the crystal.

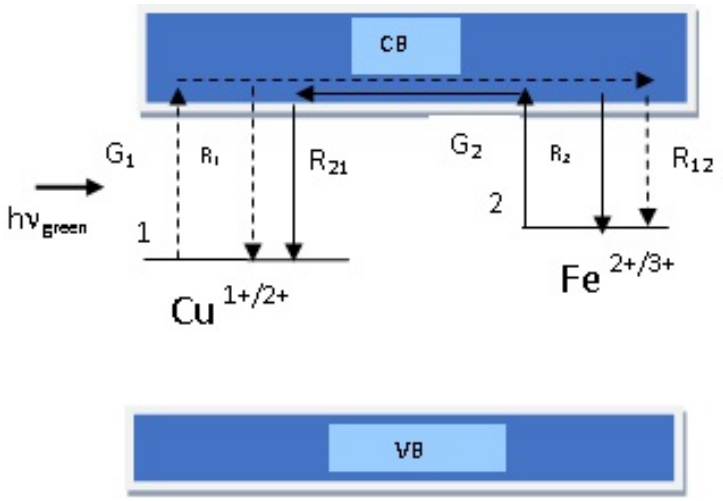

FIG. 5. Band diagram of the two-center charge transport model. CB is the conduction band, VB is the valence band. Arrows indicate excitation and recombination of electrons at Cu^{1+}/Cu^{2+} and Fe^{2+}/Fe^{3+}. G_1, G_2 are absorption cross sections, R_1, R_2 are recombination rates of Fe and Cu centers. R_{12}, R_{21} are recombination rates between Cu–Fe and Fe–Cu centers, respectively (see [8, 11])

5. Conclusion

The recording of 3D photonic lattices in photorefractive LN:Fe:Cu crystals, also revealing a photochromic effect, was realized by an interferometric-mask method. The formed 3D lattices had 20 – 60 μm periods in the radial and azimuthal directions and 266 nm period in the axial direction. The recorded lattices were tested by diffraction of 633 nm probe laser beam, as well as by white light which revealed the dispersive properties of the lattice. Direct observation of recorded lattices by phase microscope was also performed. The diffraction efficiency of recorded lattice was measured at 2.3 %.

2D and 3D periodic and quasi-periodic photonic structures in photorefractive materials are promising for many applications, including guiding and trapping systems, photonic bandgap materials, all-optical devices, high capacity information storage and processing, spatial soliton formation, telecommunication systems, optical computers etc.

Acknowledgments

This work was supported by International Science and Technology Center Grant, Project A-1517 and National Grant of State Committee of Science of Armenia, Project 1-6/HK.

References

[1] A. Adibi, K. Buse, D. Psaltis. Two-center holographic recording. *JOSA B*, **18**, P. 584–601 (2001).

[2] K. Buse, C. Denz, W. Krolikowski. Photorefractive materials, effects, and devices: control of light and matter. *Appl. Phys. B*, **95** (3), P. 389–390 (2009).

[3] M.E. Zorob, M.D.B. Charlton, et al. Complete photonic bandgaps in 12-fold symmetric quasicrystals. *Nature*, **404**, P. 740 (2002).

[4] W. Man, M. Megens, P.G. Steinhardt, P.M. Chaikin. Experimental measurement of the photonic properties of icosahedral quasicrystals. *Nature*, **436**, P. 993 (2005).

[5] A. Badalyan, R. Hovsepyan, et al. Combined interferometric-mask method for creation of micro- and submicrometric scale 3D structures in photorefractive materials. Proceedings of SPIE, International Conference on Laser Physics 2010, **7998**, P. 7998OH-1–10 (2011).

[6] A. Badalyan, T. Gevorgyan, et al. Engineering of 2D and 3D holographic gratings in photorefractive media. Proceedings of SPIE, Photonics and Micro- and Nano-structured Materials 2011, **8414**, P. 8414 05-1–11 (2012).
[7] P. Mantashyan. Photochromic effect and holographic recording in doubly doped $LiNbO_3$ crystals. Proceedings of SPIE, International Conference on Laser Physics 2010, **7998**, P. 7998OJ-1–9 (2011).
[8] G.T. Avanesyan, E.S. Vartanyan, et al. Mechanisms of photochromic and photorefractive effects in doubly doped lithium niobate crystals. *Physica Status Solidi A*, **126** (1), P. 245–252 (1991).
[9] A.M. Glass, D. von der Linde, T.J. Negran. High-voltage bulk photovoltaic effect and the photorefractive process in $LiNbO_3$. *Appl. Phys. Lett.*, **25**, P. 233–235 (1974).
[10] F.S. Chen. Optically induced change of refractive indices in lithium niobate and lithium tantalate. *J. Appl. Phys.*, **40**, P. 3389 (1969).
[11] K. Buse. Light-induced charge transport processes in photorefractive crystals. *Appl. Phys. B*, **64** (3), P. 273–291 (1997).
[12] Y. Yang, I. Nee, K. Buse, D. Psaltis. Ionic and electronic dark decay of holograms in $LiNbO_3$:Fe crystals. *Appl. Phys. Lett.*, **78**, P. 4076 (2011).
[13] I. Nee, M. Muller, K. Buse, E. Kratzig. Role of iron in lithium-niobate crystals for the dark-storage time of holograms. *J. Appl. Phys.*, **88**, P. 4282 (2000).

NANOSYSTEMS: PHYSICS, CHEMISTRY, MATHEMATICS, 2014, 5 (2), P. 217–233

SPECTRAL PROPERTIES OF SHUNGITE QUANTUM DOTS

B. S. Razbirin[1], N. N Rozhkova[2], E. F. Sheka[3],
D. K. Nelson[1], A. N. Starukhin[1], A. S. Goryunov[4]

[1]Ioffe Physical-Technical Institute, RAS, Saint Petersburg, Russia
[2]Institute of Geology Karelian Research Centre RAS, Petrozavodsk, Russia
[3]Peoples' Friendship University of Russia, Moscow, Russia
[4]Institute of Biology Karelian Research Centre RAS, Petrozavodsk, Russia
[3]sheka@icp.ac.ru

PACS 73.63.Kv, 73.23.Hk, 73.43.Lp, 78.67.Wj

A low-temperature study has been performed for aqueous shungite, carbon tetrachloride, and toluene dispersions. Spectral characteristics for graphene quantum dots (GQDs) of shungite, attributed to individual fragments of reduced graphene oxide (rGO), reveal a dual character of the dispersions emitting centers: individual GQDs are responsible for the spectra position while fractal structure of GQD colloids provides large broadening of the spectra due to structural inhomogeneity of the colloidal dispersions and a peculiar dependence of photoluminescence of dispersions on excitation wavelength. For the first time, photoluminescence spectra of individual GQDs were observed in frozen toluene dispersions, which pave the way for a theoretical treatment of GQDs photonics.

Keywords: graphene quantum dots, fractals, photoluminescence, colloidal dispersions, shungite.

1. Introduction

The fractal structure of shungite promotes the formation of its water dispersions, for which homogeneity can be achieved by sonication and filtration. The dispersions present colloidal aggregates of nanosize fragments of reduced graphene oxide (rGO) of ~ 1 nm in size dissolved in water. These pristine fragments are attributed to graphene quantum dots (GQDs) of shungite [1]. The spectral study presented in the current paper was aimed at revealing a similarity in spectral behavior for GQDs of shungite and synthetic GQDs, thus confirming the grounds for the fractal structure of shungite.

Originally, the term 'graphene quantum dot' (GQD) appeared in theoretical research and was attributed to fragments limited in size, or domains, of a single-layer two-dimensional graphene crystal. The subject of these investigations concerned quantum size effects, manifested in the spin [2, 3], electronic [4] and optical [5–10] properties of the fragments. The latter study significantly stimulated the interest in GQDs, so that the question arose of their preparation. This proved to be a difficult task, and the progress achieved to this point has been presented in exhaustive reviews [11, 12]. Spectral studies have found that in almost all cases, GQDs are not single-layer graphene domains, but multi-layer formations containing up to 10 layers of reduced graphene oxide (rGO) from 10 to 60 nm in size. However, to obtain single-layer GQDs is also not uncommon (see, for example [13–17]).

Optical spectroscopy, specifically photoluminescence (PL), is the primary method for studying the properties of the GQDs. The review [12] presents an exhaustive complete picture of the results. As was shown, optical spectroscopy of GQDs gives a complicated picture with many features. However, in spite of this diversity, common patterns can be identified that can serve as a basis for spectral analysis of the GQDs. These general characteristics include:

1) structural inhomogeneity of GQDs solutions, better called dispersions; 2) low concentration limit that provides surveillance of the PL spectra; 3) dependence of the GQD PL spectrum on the solvent, and 4) dependence of the GQD PL spectrum on the excitation light wavelength. These four circumstances determine the usual conditions under which the spectral analysis of complex polyatomic molecules is performed. Optimization of conditions, including, primarily, the choice of solvent and the experiment performance at low temperature, in many cases, led to good results, based on structural PL spectra (see, for example, the relevant research of fullerenes solutions [18–21]). In this paper, we will show that implementation of this optimization for spectral analysis of the GQDs turns out to be quite successful.

2. Fractal Nature of the Object under Study

A concept on GQD evidently implies a dispersed state of a number of nanosize rGO fragments. Empirically, the state is provided by the fragments' dissolution in a solvent. Once dissolved, the fragments unavoidably aggregate, forming colloidal dispersions. As mentioned earlier, so far only aqueous dispersions of synthetic GQDs have been studied [11, 12]. In the case of shungite GQDs, two above-mentioned organic solvents were used when replacing water in the pristine dispersions. In each of these cases, the colloidal aggregates are the main object of the study. In spite of that, so far, there has not been any direct confirmation of their fractal structure, there are serious reasons to suppose that this is an obvious reality. Actually, first, the rGO fragments formation occurred under conditions that unavoidably involve elements of randomness during both laboratory chemical reactions and natural graphitization [1]; the latter concerns the fragments' size and shape. Second, the fragments' structure certainly bears the stamp of polymers, for which fractal structure of aggregates in dilute dispersions has been convincingly proven (see [22] and references therein).

As shown in [22], the fractal structure of colloidal aggregates is highly sensitive to the solvent around, the temperature of the aggregate formation, as well as other external factors such as mechanical stress and so forth. This fact makes the definition of quantum dots of colloidal dispersions at the structural level quite undefined. In the case of the GQDs of different origin, the situation is additionally complicated, since the aggregation of synthetic (Sy) and natural shungite (Sh) rGO fragments occurred under different external conditions. In view of this, it must be assumed that not only rGO-Sy and rGO-Sh aggregates, but the same solvent dispersions are quite different.

Looking for the answer to the question if the same term GQD can be attributed to colloidal dispersion in the above two cases, one should recall that a feature of fractal structures is that fractals are typically self-similar patterns, where 'self-similar' means that they are 'the same from near as from far' [23]. This means that the peculiarities of, say, optical behavior for both rGO-Sy and rGO-Sh colloidal dispersions obey the same law. From this viewpoint, there is apparently no difference for which the structural element of a multilevel fractal structure of their colloidal aggregates should be attributed to a quantum dot. However, the identity of both final and intermediate fractal structures of aggregates in different solvents is highly questionable and only the basic rGO structural units cast no doubts. Because of this, GQDs of both rGO-Sy and rGO-Sh dispersions should to be associated with rGO individual fragments. Therefore, different fractal nets of GQDs provided by different colloidal dispersions present the object under the current study. Addressing the spectral behavior of the dispersions, we should expect an obvious generality provided by the common nature of GQDs, but simultaneously complicated by the difference in fractal packing of the dots in the different-solvent dispersions. The current study provides confirmation for this vision of spectral behavior on an example of rGO-Sh dispersions.

3. Experimental Techniques

Morphological investigation of rGO-Sh dispersions concerned defining the size distribution of the dispersions' colloidal aggregates and obtaining overview pictures of the structure of films obtained therein by evaporation of the solvent. The relevant size-distribution profiles were obtained using dynamic light scattering incorporated in nanoparticle size analyzer Zetasizer Nano ZS (Malvern Instruments). Processing of the results was carried out using a spherical shape approximation for the aggregates. Spectral studies were carried out at 293 K and 80 K. Emission spectra of liquid and frozen dispersions were excited by laser lines λ_{exc} of 337.1, 405, 457, 476.5, 496.5, 514.5 and 532 nm. The resulting spectra were normalized to the power of the laser radiation at different excitations. The spectra were recorded under identical conditions on a DFS-12 spectrometer with a spectral resolution $\approx$ 0.2 nm. The obtained data are related to shungite of 98 wt.% carbon.

4. Aqueous Dispersions

In full agreement with commonly used methods [24, 25], rGO-Sh aqueous dispersions were obtained by sonication of the pristine shungite powder for 15 min with an ultrasonic disperser US-2M (at a frequency of 22 kHz and the operating power 300 W) at 300 °C followed by filtration and ultracentrifugation [26]. The maximum achievable concentration of carbon is less than 0.1 mg/ml, which is consistent with poor water solubility of graphene and its derivatives [24]. The resulting dispersions are quite stable, and their properties vary little over time. The size-distribution characteristic profile of rGO-Sh aggregates is shown in Fig. 1a. The average size of the aggregates is 54 nm, its full width at half maximum constitutes 26 nm so that the resulting colloids are significantly inhomogeneous. The inhomogeneity obviously concerns both the size and shape (and, consequently, chemical composition) of basic rGO fragments, and thus GQDs. The structure of the carbon condensate formed after water evaporation from the dispersion droplets on a glass substrate is shown in Fig. 1b and 1c. As seen from the figure, the condensate is of a fractal structure formed by ball-like aggregates. It should be mentioned that the condensate's fractal structure should not be identical to that one of the pristine dispersion [22], although, no doubt, some continuity of the structure should take place.

Figure 2a shows an overview of the characteristic patterns for the emission spectrum of rGO-Sh aqueous dispersions at different excitation lines. Increasing the temperature to 293 K did not cause a significant change in the spectra, resulting in only a slight broadening of their structural component related to the Raman spectrum of water at the O–H stretching vibrations of $\sim$ 3400 cm^{-1}. When excited at λ_{exc} 405 and 457 nm, Raman spectrum superimposes the broad luminescence band in the 17000 – 22000 cm^{-1} region. The emission of the dispersion at λ_{exc} 532 nm is weak. Fig. 2b shows the PL spectra of the aqueous dispersion at λ_{exc} 405 and 457 nm after subtraction of the Raman spectra of water. Both spectra present broad bands characteristic of the PL spectra for rGO-Sy aqueous dispersions (see [12]). In spite of the large width of PL spectra, their position in the same spectral region for both rGO-Sy and rGO-Sh aqueous dispersions gives evidence for a common nature of emitting GQDs.

The similarity of the spectral behavior for the two dispersions also involves a considerable overlapping of their absorption and PL spectra, so that a set of new PL spectra can be excited with an increase λ_{exc}. Of course, a shift of these new PL spectra maxima towards longer wavelengths with increasing λ_{exc} is observed. Such behavior usually indicates the presence of an inhomogeneously broadened absorption spectrum of the emitter, which widely overlap with PL one and whose excitation at different λ_{exc} within the overlapping region results in selective

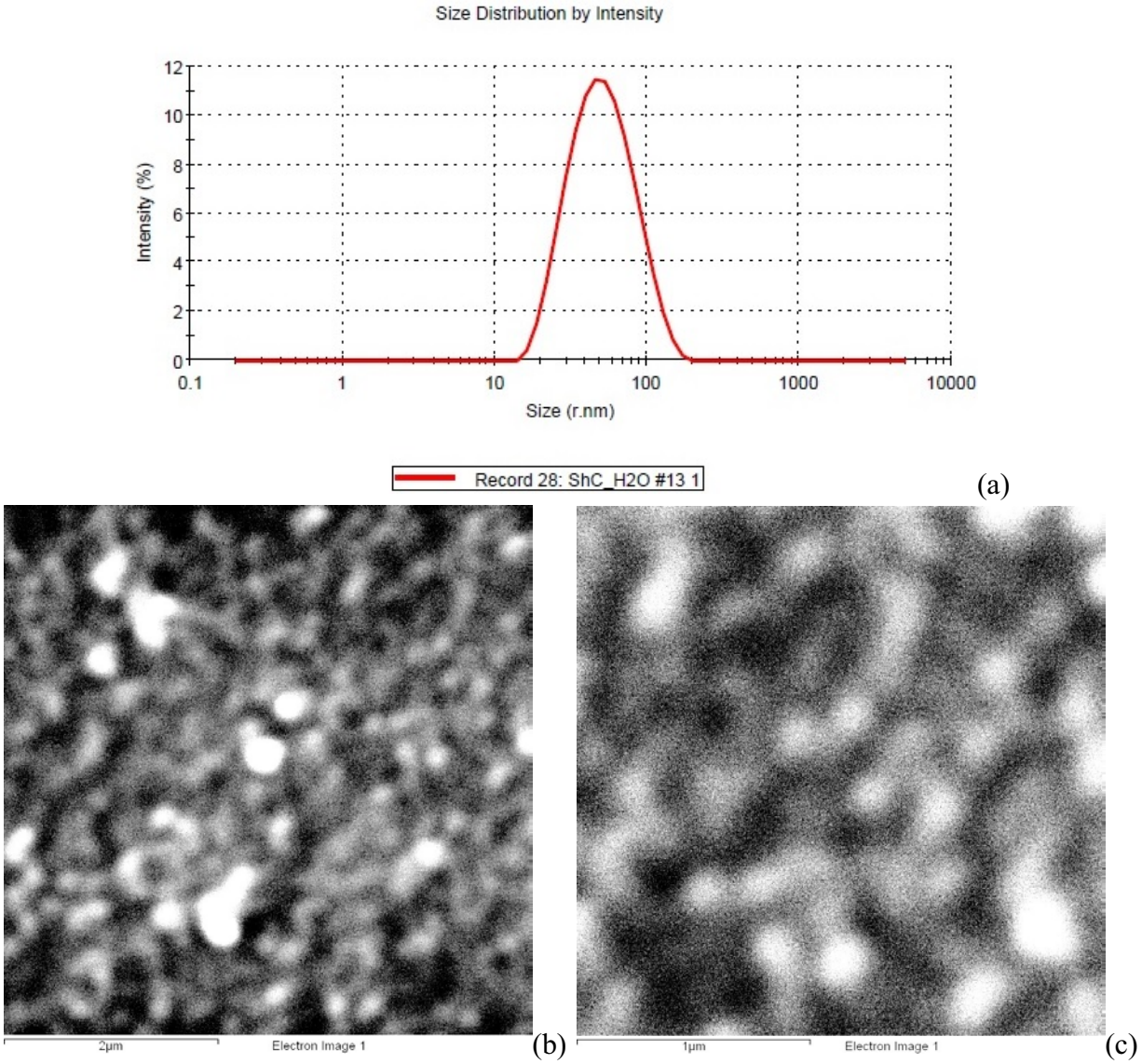

FIG. 1. Size-distribution profile of colloidal aggregates in shungite water dispersion (a) and SEM images of the dispersion condensate on glass substrate (b) and (c): Scale bar 2 μm and 1 μm, respectively. Carbon concentrations constitute 0.1 mg/ml

excitation of different sets of emitting centers. In the case of rGO-Sy dispersions, the inhomogeneous broadening of the spectra is usually explained by scatter in the GQDs (rGO fragments) linear dimensions [12]. However, not only GQDs linear dimensions, but their shape as well as the composition of colloidal aggregates may largely vary, which should be expected for the rGO-Sh dispersions, in particular. This is clearly seen on the example of various aggregates structure of the condensates shown in Fig. 1b and 1c. Unfortunately, the large width of the PL spectra does not allow one to exhibit those spectral details that might speak about aggregated structure of GQDs.

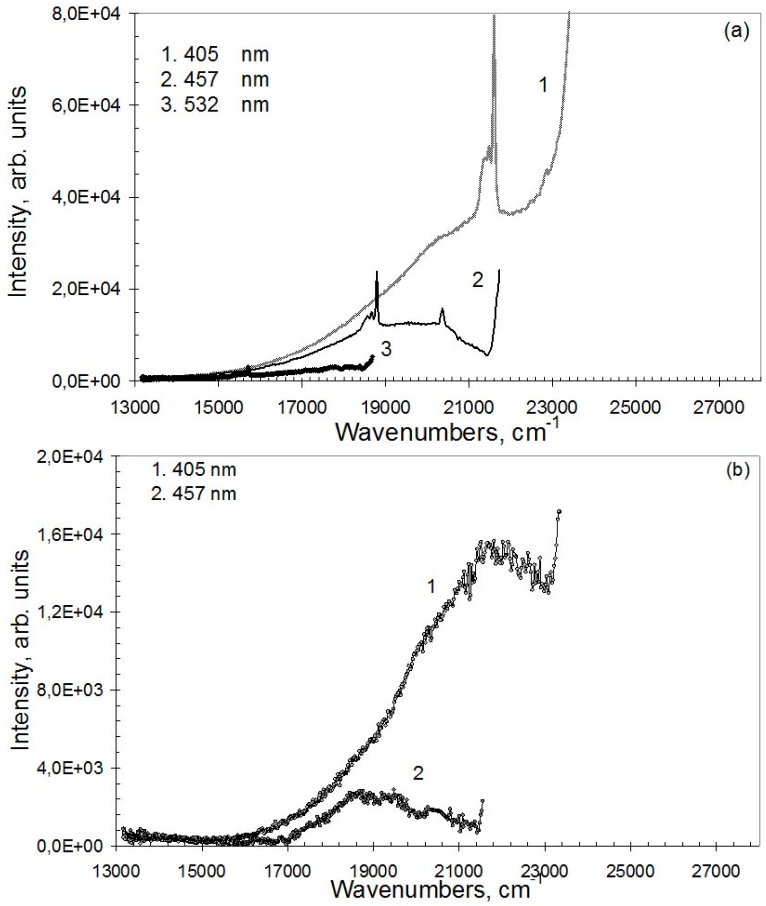

FIG. 2. Photoluminescence spectra of shungite water dispersions at 80 K as observed (a) and after subtraction of Raman scattering of water (b). Figures mark excitation wavelengths

5. Dispersions in Organic Solvents

Traditionally, the best way to overcome difficulties caused by inhomogeneous broadening of optical spectra of complex molecules is the use of their solutions in specially selected crystalline matrices. Carbon tetrachloride and toluene are known to provide a reliable monitoring of fine-structured spectra for individual molecules (Shpolskii's effect [27]) as it was, say, in the case of fullerenes [18–21]. Detection of PL structural spectra or structural components of broad PL spectra not only simplify spectral analysis, but indicate the dispersing of emitting centers of complex structure into individual molecules. It is this fact that was the basis for the solvent choice when studying spectral properties of shungite GQDs.

Organic rGO-Sh dispersions were prepared from the pristine aqueous dispersions during sequential replacement of water by isopropyl alcohol first and then by carbon tetrachloride or toluene [26]. The morphology and spectral properties of these dispersions turned out to be quite different.

5.1. Dispersions in Carbon Tetrachloride

When analyzing CTC-dispersion morphology, the first important discovery was that a drastic change in the size-distribution profiles occurs for the dispersion aggregates in comparison with those of the aqueous dispersions (see Fig. 3) . This finding gives direct evidence for the

fractal nature of the GQDs aggregates in water, since only under these conditions can such a strong effect, caused by solvent substitution, be observed [22]. he second result concerns the high incertitude in this fractal structure. Thus, Figs. 3a and 3b present size-distribution profiles related to CTC-dispersions, which were most different from this viewpoint. Figs. 3c and 3d show images of film agglomerates obtained when drying the CTC-dispersion droplets on glass. As can be seen by comparing Fig. 1 and Fig. 3, the average colloidal aggregate size drastically increases when water is substituted with carbon tetrachloride. Simultaneously, the scatter of sizes increases that is comparable with the size itself in the limiting case. The nearly spherical shape of aggregates in Figs. 1b and 1c is replaced by lamellar faceting, mostly characteristic of microcrystals. The absence of small aggregates is noteworthy, which indicates a complete absence of individual GQDs in the dispersions. Therefore, the change in size-distribution profiles as well as in shape of the aggregates of the condensate points to a strong influence of solvent on the aggregates' structure, thus decisively confirming their fractal character.

The conducted spectral studies are very consistent with these findings. Fig. 4 shows PL spectra of CTC-dispersion DC1, morphological properties of which are near to those shown in Fig. 3a. The dispersions have a faint yellow-brown color, which indicates the presence of significant absorption of the solutions in the visible region (see Fig. 4a). PL spectra were studied for a wide range of dispersions obtained at different times. As found both these spectra behavior at different exciting lasers λ_{exc} and the PL spectra shape of different dispersions are largely similar, while the spectral intensity can differ substantially. Arrows in Fig. 4a show wave number values λ_{exc}^{-1} corresponding to laser lines at 405, 457, 476.5, 496.5, 514.5 and 532 nm. As can be seen in Fig. 4a, the dispersion absorption increases when advancing to the UV region. It can be assumed that the absorption of each component of the aggregates' conglomerate increases with decreasing λ_{exc}, so that the excitation with UV light at $\lambda_{exc} = 337.1$ nm affects almost all luminescence centers in the crystal matrix. Actually, the UV excited PL spectrum in Fig. 4a is very broad and covers the region from 27000 to 15000 cm^{-1}. In this case, the PL spectrum overlaps with the absorption spectrum over the entire spectral range. Such a large overlapping gives evidence for the inhomogeneously broadened character of both spectra that is, the formation of an ensemble of emitting centers, which differ in the probability of emission (absorption) at given wavelength. Actually, successive PL excitation by laser lines 1, 3, 4 and 5 (see Fig. 4a) causes a significant modification of the PL spectra (Fig. 4b). The width of the spectra decreases as λ_{exc} increases, the PL band maximum is shifted to longer wavelengths, and the spectrum intensity decreases. This is due to selective excitation of a certain group of centers. In general, the observed pattern is typical for structurally disordered systems discussed in the previous section. To simplify further comparative analysis of the spectra obtained at different λ_{exc}, we shall denote them according to the excitation wavelength, namely: 405-, 476-, 496-spectrum, etc.

Comparing the PL spectra of dispersion DC1 at different excitations, we note that 1) PL spectra, obtained when excited in the region of overlapping absorption and emission spectra in Fig. 4a, have a more distinct structure than the 337-one but still display a superpositioning character of the spectra; 2) the intensity of the 405-spectrum is almost an order of magnitude higher than the intensity of the rest of the spectra. Before discussing the observed spectral features, let us look at the PL spectra of dispersion DC2 that is close in morphology to the dispersion shown in Fig. 3b. Fig. 5a compares the 337- and 405- spectra of DC2 with those of DC1 described earlier. The 337-spectrum of DC2 exhibits a new UV band, intensity of its 405-spectrum decreases by several times. The spectrum of DC2 still retains a three-peak shape, but their intensities are significantly redistributed. This evidently refers to the superpositioning

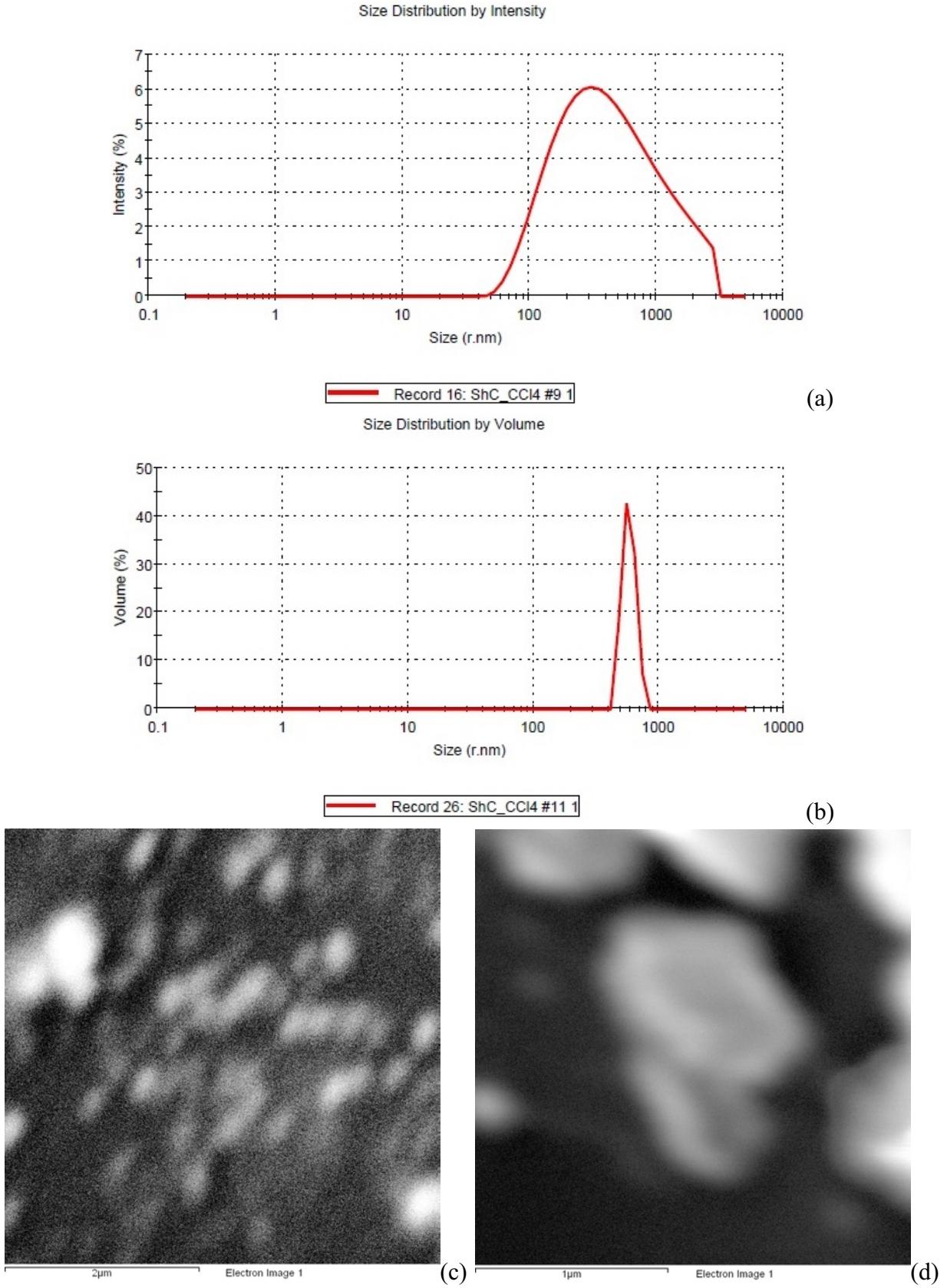

FIG. 3. Size-distribution profiles of colloidal aggregates in shungite dispersion in carbon tetrachloride (a and b) (see text) and SEM images of the dispersion condensates on glass substrate (c) and (d): Scale bar 2 μm and 1 μm, respectively

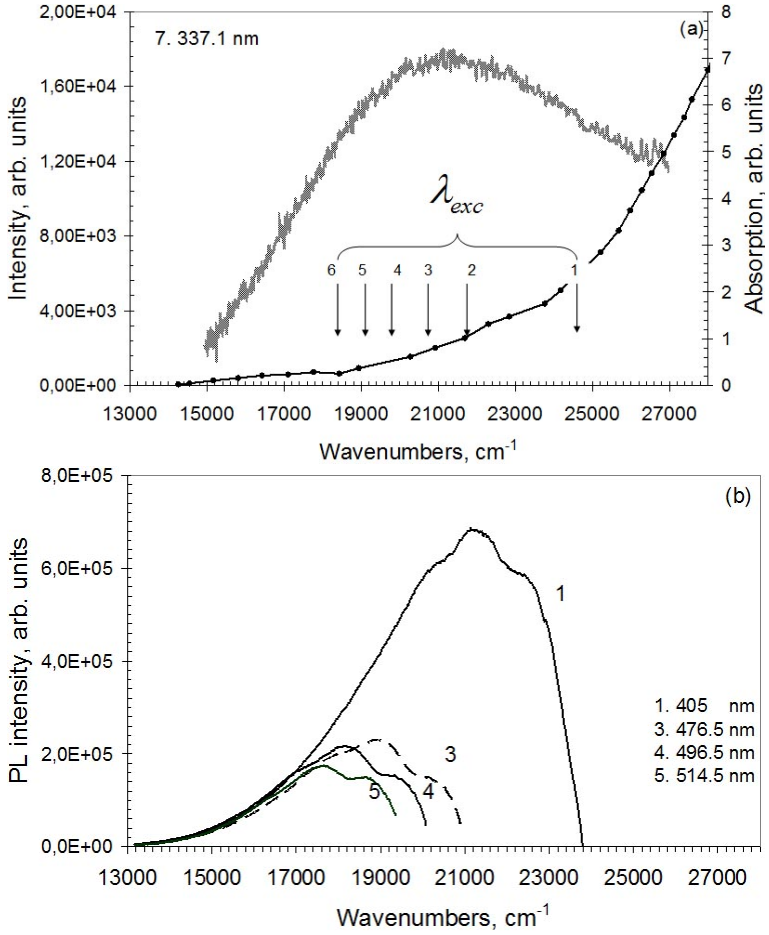

FIG. 4. Photoluminescence (a and b) and absorption (a) spectra of shungite dispersion in carbon tetrachloride DC1 at 80 K after background emission subtraction. Figures mark excitation wavelengths

character of the spectrum as said before. It is important to note that the 405-spectrum of DC2 is still the most intense among other DCQ spectra (see Fig. 5b).

Comparative analysis of the PL spectra of dispersions DC1 and DC2 shows that the above-mentioned spectral regularities are sensitive to the CTC-dispersion's structure and are directly related to the degree of structural inhomogeneity. Thus, the narrowing of the size-distribution profile related to dispersion DC2, undoubtedly causes narrowing of inhomogeneously broadened absorption and emission spectra, so that the intensity of the long-wavelength emission spectra of DC2 dispersion decreases. Because of the cutoff of the long-wavelength absorption spectrum of DC2 dispersion the structure of its 405-spectrum becomes more noticeable, apparently due to an additional feature of the distribution of emitting centers in DC2 over energy. The predominant intensity of the 405-peak is unchanged in both sets of spectra.

The difference in the structural inhomogeneity of dispersions raises the question of their temporal stability. Spectral analysis of their PL allows one to answer this question. Fig. 6 shows data related to dispersion DC1, but after 1.5 years (dispersion DC1*). As can be seen from Fig. 6a, in the PL spectrum DC1* there are new emitting centers, responsible for the PL in the UV region. Otherwise, 337-spectrum changes little, keeping its intensity and large width. Changes in PL spectra in the visible range are less pronounced (see Fig. 6b). Attention is drawn to high intensity of the 457-spectrum of DC1*.

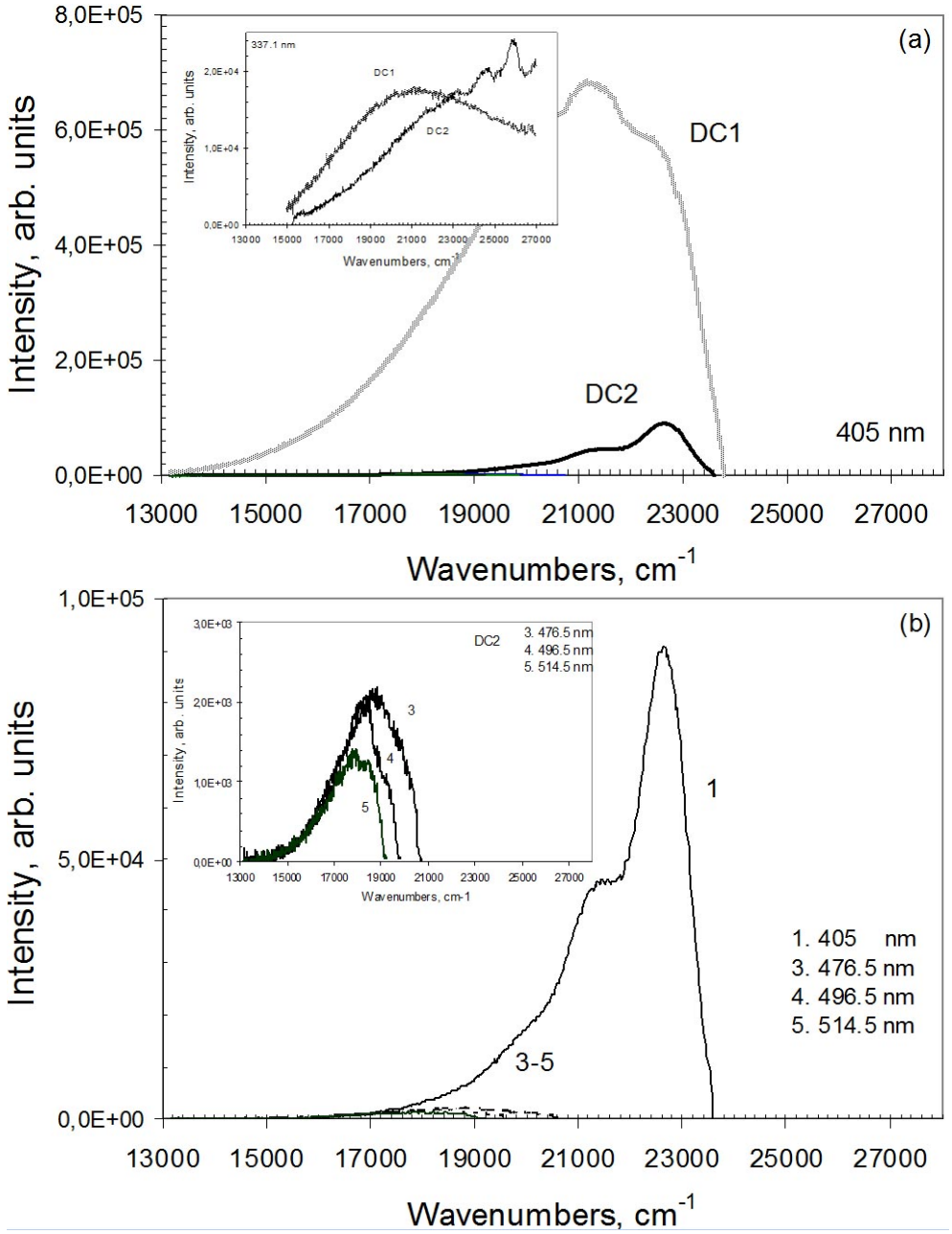

FIG. 5. Photoluminescence spectra of shungite dispersions in carbon tetrachloride at 80 K after background emission subtraction. A comparative view of 405- and 337-spectra (insert) of DC1 and DC2 dispersions (a); the same for spectra of DC2 dispersions at different excitations (b). Figures mark excitation wavelengths

Thus, in the low-temperature PL spectra of crystalline CTC-dispersions none of fine-structured spectra similar to Shpolskii's spectra of organic molecules was observed. This is consistent with the absence of small particles in the size-distribution profiles of the relevant colloidal aggregates. The PL spectra are broad and overlapping with the absorption spectrum over a wide spectral range. This fact testifies to the inhomogeneous broadening of the spectra, which is the result of non-uniform distribution of the dispersions colloidal aggregates, confirmed by morphological measurements. The observed high sensitivity of PL spectra to the structural

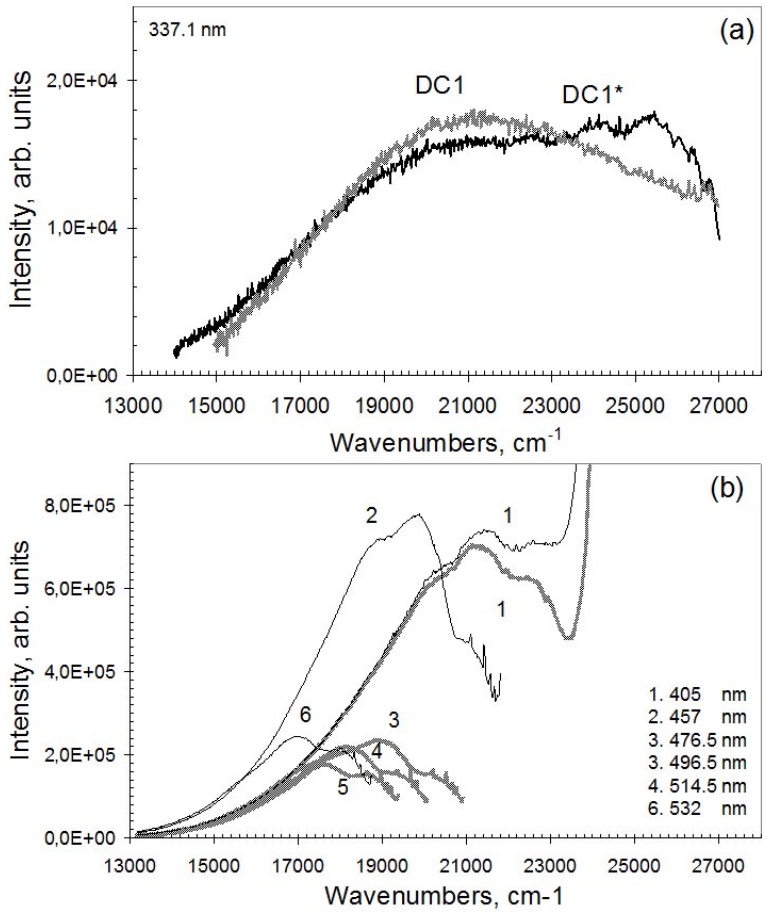

FIG. 6. Photoluminescence spectra of shungite dispersions in carbon tetrachloride at 80 K after background emission subtraction. A comparative view of 337-spectra (insert) of DC1 and DC1* dispersions (see text) (a); the same for spectra of DC1 (thickened curves) and DC* (thin curves) dispersions at different excitations (b). Figures mark excitation wavelengths

inhomogeneity of dispersions allows the use fluorescent spectral analysis as a method of tracking the process of the formation of primary dispersions and their aging over time. Selective excitation of emission spectra by different laser lines allows decomposition of the total spectrum into components corresponding to the excitation of different groups of emitting centers. In this case, common to all the studied dispersions is the high intensity of the emission spectra excited at λ_{exc} 405 and 457 nm.

5.2. Dispersion in Toluene

The behavior of rGO-Sh toluene dispersions is more intricate from both morphological and spectral viewpoints. Basic GQDs of aqueous dispersions are sparingly soluble in toluene, thereby resulting in toluene dispersions that are essentially colorless due to low solute concentration. In addition, the low concentration makes the dispersion very sensitive to any change in both the content and structure of dispersions. This causes structural instability of dispersions which is manifested, in particular, in the time dependence of the relevant size-distribution profiles. Thus, the three-peak distribution of the initial toluene dispersion shown in Fig. 7a, is gradually replaced by a single-peaked distribution in Fig. 7b for one to two hours. The

last distribution does not change with time and represents the distribution of the solute in the supernatant.

By analogy with carbon tetrachloride, toluene causes a drastic change in the colloidal aggregates structure thus proving once again the fractal structure of the pristine GQD colloids in the aqueous dispersions. However, if the carbon tetrachloride action can be attributed to the consolidation of the pristine colloids, the toluene results in quite an opposite effect, leading to their dispersing. Three-peak structure in Fig. 7a shows that, at the initial stage of water replacement by toluene, in resulting liquid medium there are three kinds of particles with average linear dimensions of about 2.5, 70 and 1100 nm. All three sets are characterized by a wide dispersion. Large particles are seen in the electron microscope (Fig. 7c and 7d) as freaky sprawled fragments. Over time, these three entities are replaced by one with an average size of $\sim$ 0.25 nm. Thus, freshly produced dispersions, containing GQD aggregates of varying complexity, turns into a dispersion of individual GQDs. It should be noted that the obtained average size seems to be too small. This might be a result of the program processing the particle distribution in Zetasizer Nano ZS that is based on a spherical 3D particle approximation, whereby the output data can be assigned to the two-dimensional structural anisotropic particles with a large stretch. This makes one accept the value of 0.25 nm as very approximate and only consistent on the order of magnitude with the empirical value of $\sim$ 1 nm for the average size of GQDs in shungite [1].

The conversion of the aqueous dispersion of aggregated GQDs into the colloidal dispersion of individual GQDs in toluene is a peculiar manifestation of the interaction of solvents with fractals described in [22]. Apparently, GQD fractals are differently 'opaque' or 'transparent' with respect to CTC and toluene, which causes a large effect. Certainly, the finding may stimulate the consideration of nanosize graphene dispersions in the framework of the fractal science similarly to the polymer study [22]. As for the graphene photonics, the obtained toluene dispersion has allowed the investigation of individual GQDs for the first time.

Figure 8 shows the PL spectra of colloidal dispersions for individual GQDs in toluene. The *brutto* experimental spectra, each of which is a superposition of the Raman spectrum of toluene and PL spectrum of the dispersion, are presented in Fig. 8a. Note the clearly visible enhancement of Raman scattering of toluene from 20000 – 17000 cm^{-1}. Fig. 8b shows the PL spectra after subtracting Raman spectra. The spectra presented in the figure can be divided into three groups. The first group includes the 337-spectrum (7) that in the UV region is the PL spectrum, similar in shape to the UV PL spectrum of toluene, but shifted to longer wavelengths. This part of the spectrum should apparently be attributed to the PL of some impurities in toluene. The main contribution into the PL 337-spectrum from 24000 – 17000 cm^{-1} is associated with the emission of all GQDs available in the dispersion. This spectrum is broad and structureless, which apparently indicates the structural inhomogeneity of the GQD colloids.

PL 405- and 476-spectra (1 and 3 from 23000 – 17000 cm^{-1} should be attributed to the second group. Both spectra have clearly defined structure that is most clearly expressed in the 405-spectrum. The spectrum is characteristic of a complex molecule with allowed electronic transitions. Assuming that the maximum frequency at 22910 cm^{-1} determines the position of pure electronic transition, the longer wavelength doublet at $\sim$ 21560 – 21330 cm^{-1} can be interpreted as vibronic transitions. The distance between the doublet peaks and the pure electronic band constitutes 1350 – 1580 cm^{-1} that is consistent with the frequencies of totally symmetric vibrations of C–C graphene skeleton, commonly observed in the Raman spectra. Similarly, two peaks of the much lower intensity 476-spectrum, which are wider than in the previous case, are divided by the average frequency of 1490 cm^{-1}. PL 457-spectrum, shown in Fig. 8c (curve 2) is similar to spectra 1 and 3, in intensity closer to the 405-spectrum. All

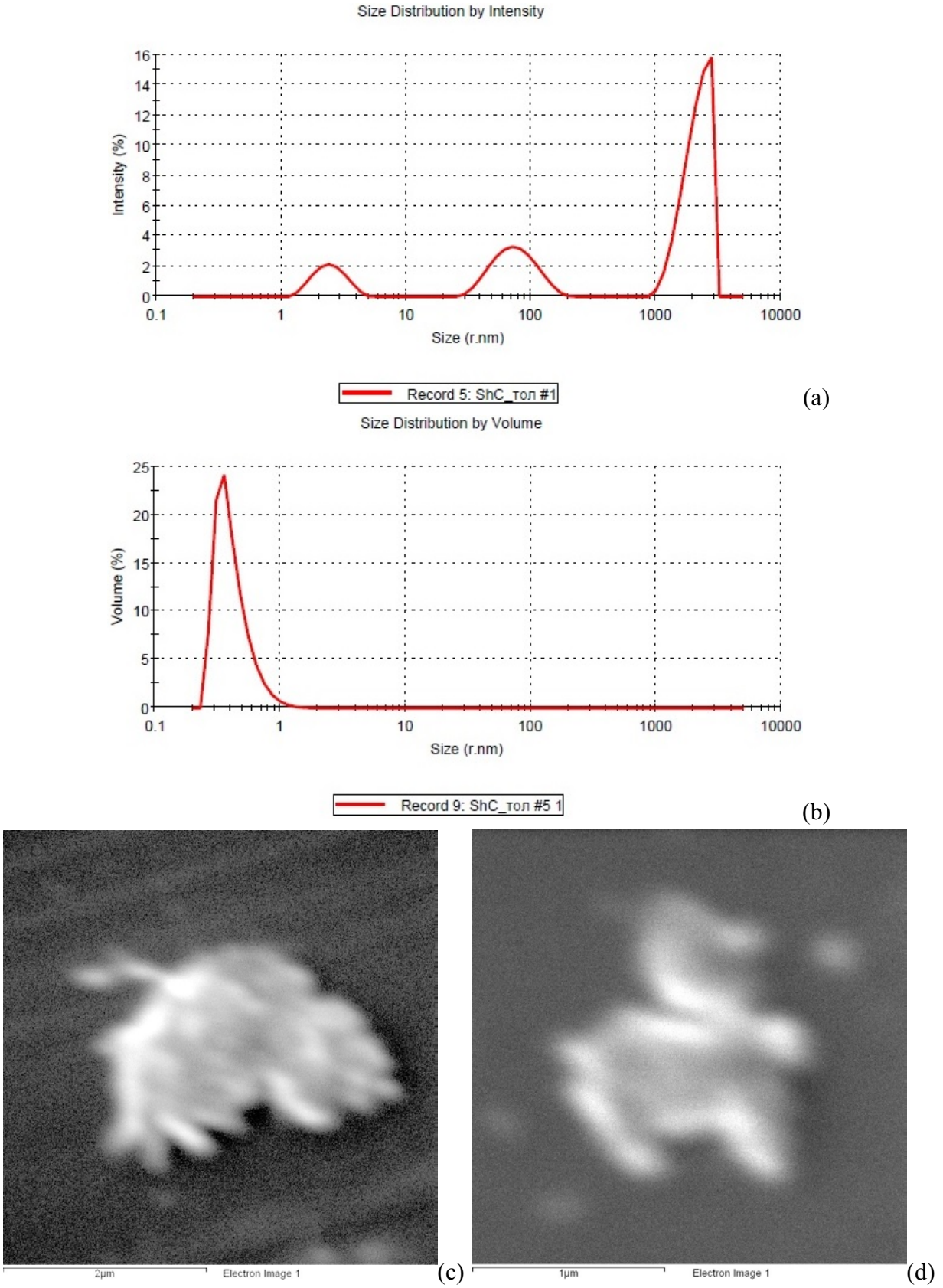

FIG. 7. Size-distribution profiles of colloidal aggregates in shungite toluene dispersion (a and b) (see text) and SEM images of the dispersion condensates on glass substrate (c) and (d): Scale bar 2 μm and 1 μm, respectively. Carbon concentrations constitute 0.08 (a) and 0.04 (b) mg/ml

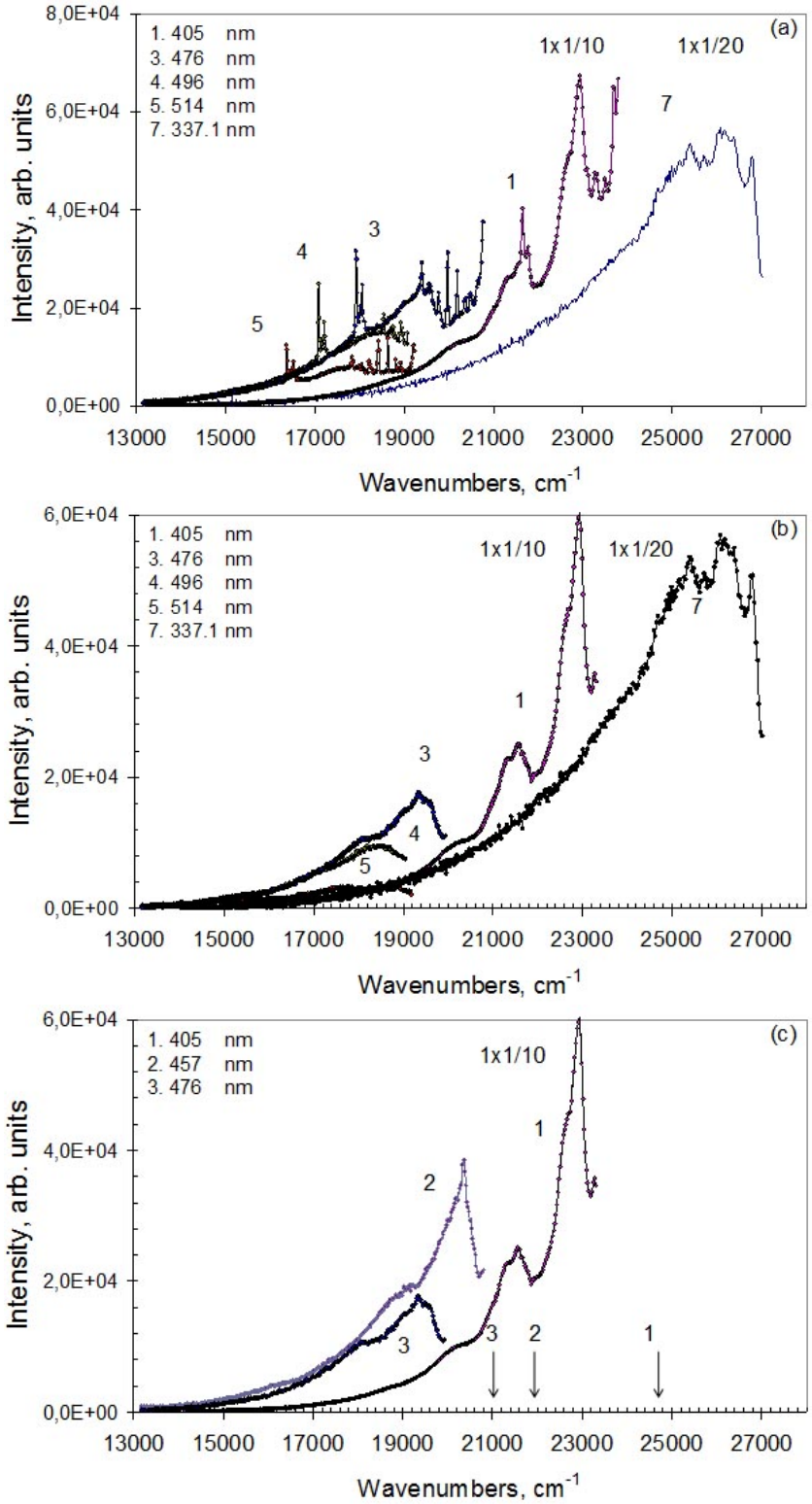

FIG. 8. Photoluminescence spectra of shungite toluene dispersion at 80 K as observed (a), after subtraction of Raman scattering of toluene (b), and attributed to individual GQDs only (c). Figures and arrows mark excitation wavelengths

three spectra are related to individual rGO fragments, albeit of different size that increases when going from 405-spectrum to 457- and 476-spectrum.

The shape of 496- and 514-spectrum substantially differs from that of the second group spectra. Instead of the two peaks, a broad band is observed in both cases. This feature makes these spectra attributable to the third group and associate them with the appearance of not individual frozen GQDs but with their possible clusters (such as, say, dimeric homo- (GQD+GQD) and hetero- (GQD+toluene) structured charge transfer complexes and so forth). The evidence of such a possibility will be discussed in the next section.

The conducted spectral studies of the rGO-Sh toluene dispersions confirmed once again the status of toluene as a good solvent and a good crystalline matrix, which allows for obtaining structured spectra of individual complex molecules under conditions when in other solvents the molecules form fractals. This ability of toluene allowed for the first time to get the spectra of both individual GQDs and their small clusters. The finding represents the first reliable empirical basis for further theoretical treatment of the spectra observed. Simultaneously with this, use of toluene and carbon tetrachloride as solvents convincingly showed a strong tendency of nanoscale graphenes to form fractals, which should be taken into account in practical applications.

6. Discussion

As follows from the results presented in the previous sections, rGO-Sh dispersions are colloidal dispersions regardless of the solvent, whether water, carbon tetrachloride or toluene. The dispersion colloid's structure depends on the solvent and thereafter is substantially different. This issue deserves a special investigation. Thus, the replacement of water with carbon tetrachloride leads to multiple enlargement of the pristine colloids which promotes the formation of a quasi-crystalline image of the condensate structure. At present, the colloid's detailed structure remains unclear. In contrast to carbon tetrachloride, toluene causes the decomposition of pristine colloids into individual rGO fragments. The last facts cast doubt on a direct link between the structure of the dispersions fractals and the elements of fractal structure of solid shungite or its post-treated condensate. The observed solvent-stimulated structural transformation is a consequence of the geometric peculiarities of fractals behavior in liquids [22]. The resulting spectral data can be the basis for further study of this effect.

The spectral behavior of the aqueous and CTC-dispersions with large colloids is quite similar, despite the significant difference in size and structure of the latter. Moreover, the features of the PL spectra of these dispersions practically replicate patterns that are typical for the aqueous rGO-Sy dispersions discussed in detail in Section 1. This allows one to conclude that one and the same structural element of the colloidal aggregates of both rGO-Sh and rGO-Sy dispersions is responsible for the emission in spite of pronounced morphological difference of its packing in all these cases. According to the modern view of the shungite structure [1] and a common opinion on the origin of synthetic GQDs [11, 12], nanosize rGO fragments should play a role thus representing GQDs of the rGO colloidal dispersions in all these cases.

Specific effects of toluene, which caused the decomposition of pristine particles into individual rGO fragments with succeeding embedding of them into a crystalline matrix of toluene, allowed us for the first time to obtain the PL spectrum of individual rGO fragments. Obviously, resulting fragments are of different size and shape, which determines the structural inhomogeneity of toluene dispersions. This feature of toluene dispersions is common with the other dispersions and explains the dependence of PL spectra on λ_{exc} that is the main spectral feature of GQDs, both synthetic [11, 12] and of shungite origin.

The structural inhomogeneity of GQDs colloidal dispersions is mainly a result of two causes, namely, internal and external. The internal cause concerns the uncertainty in the structure

(size and shape) of the basic rGO fragments. It is the most significant for shungite while, under laboratory conditions, the rGO fragments' structure might be more standardized [11, 12]. Nanosize rGO basic structural elements of solid shungite are formed under the conditions of a serious competition of different processes [1], among which the most valuable are: 1) natural graphitization of carbon sediments, accompanied by a simultaneous oxidation of the graphene fragments and their reduction in water vapor; 2) the retention of water molecules in space between fragments and removal of the water molecules from the space into the environment, and 3) the multilevel aggregation of rGO fragments providing the formation of a monolithic fractal structure. Naturally, that achieved balance between the kinetically-different-factors is significantly influenced by random effects, so that the rGO fragments of natural shungite, which were created via natural processes, are statistically averaged over a wide range of fragments that differ in size, shape, and chemical composition. Obviously, the reverse procedure of the shungite dispersion in water is statistically also nonuniform with respect to colloidal aggregates, so that there is a strong dependence of the dispersions on the technological protocol, which results in a change in the dispersion composition caused by slight protocol variations.

The external cause is due to the fractal structure of colloidal aggregates. The fractals themselves are highly inhomogeneous, moreover, they strongly depend upon the solvent. These two reasons determine the feature of the GQD spectra in aqueous and CTC-dispersions, while the first one dominates in the case of toluene dispersions. The same two reasons lay the foundation for the main feature of GQDs spectra, explaining their positions by the energy, on the one hand, and large broadening, on the other.

The structural PL spectra allow one to pose the question about identifying the interaction effect of dissolved rGO fragments with each other and with the solvent. Nanosize rGO fragments have high donor-and-acceptor properties (low ionization potential and high electron affinity) and can exhibit both donor and acceptor properties, so that clusters of fragments (dimers, trimers, and so forth) are typical charge transfer complexes. Besides this, toluene is a good electron donor, due to which it can form a charge-transfer complex with any rGO fragment, which acts as an electron acceptor. The energy spectrum of the complex electron-hole states , which depends on the distance between the molecules, on the initial parameters, is similar to the electron-hole spectrum of fullerenes C_{60} clusters themselves and with toluene [19], positioned in the 17000 – 20000 cm^{-1} region. By analogy, with fullerene C_{60} solutions [19], the enhancement of the Raman spectrum of toluene is due to superposition of the spectrum over that one of electron-hole states, in accordance with the theory of light amplification caused by nonlinear optical phenomena [28]. Additionally, the formation of rGO-toluene charge transfer complexes may promote the formation of stable chemical composites during photochemical reactions [29] that might be responsible for the PL spectra of the third group that were observed in toluene dispersions. Certainly, this assumption requires further theoretical and experimental investigation.

7. Conclusion

The photonics of shungite colloidal dispersions faces the problem that the large statistical inhomogeneity inherent in the quantum dot as an object of the study makes it difficult to interpret the results in detail. Consequently, common patterns that are observed on the background of this inhomogeneity become most important. In the case of the considered dispersions, the common patterns include, primarily, the dispersion PL in the visible region, which is characteristic for large molecules consisting of fused benzenoid rings. This made it possible to confirm the earlier findings that graphene-like structures of limited size, namely, rGO fragments are the basic structural elements for all the dispersions. The second feature concerns the dependence

of the position and intensity of selective PL spectra on the exciting light wavelength λ_{exc}. This feature lies in the fact that regardless of the composition and solvent of dispersions, the PL excitation at λ_{exc} 405 and 457 nm provides the highest PL intensity while excitation at either longer or shorter wavelengths produces a much lesser intensity of the emission. The answer to this question must be sought in the calculated absorption and photoluminescence spectra of graphene quantum dots, which we attributed to nanosize fragments of reduced graphene.

Acknowledgments

A financial support provided by the Ministry of Science and High Education of the Russian Federation grant 2.8223.2013, Basic Research Program, RAS, Earth Sciences Section-5, and grant RFBI 13-03-00422 is highly acknowledged.

References

[1] Rozhkova N.N., Sheka E.F. Shungite as loosely packed fractal nets of graphene-based quantum dots. `arXiv:1308.0794 [cond-mat.mtrl-sci]` (2013).
[2] Trauzettel B., Bulaev D.V., Loss D., Burkard G. Spin qubits in graphene quantum dots. *Nat. Phys.*, **3**, P. 192–196 (2007).
[3] Guclu A., Potasz P., Hawrylak P. Electric-field controlled pin in bilayer triangular graphene quantum dots. *Phys. Rev. B*, **84**, P. 035425 (2011).
[4] Ritter K.A., Lyding J.W. The influence of edge structure on the electronic properties of graphene quantum dots and nanoribbons. *Nat. Mater.*, *8*, P. 235–242 (2009).
[5] Pan D., Zhang J., Li Z., Wu M. Hydrothermal route for cutting graphene sheets into blue-luminescent graphene quantum dots. *Adv. Mater.*, **22**, P. 734–738 (2010).
[6] Shen J., Zhu Y., et al. Facile preparation and upconversion luminescence of graphene quantum dots. *Chem. Commun.*, **47**, P. 2580–2582 (2011).
[7] Zhang Z.Z., Chang K. Tuning of energy levels and optical properties of graphene quantum dots. *Phys. Rev. B*, **77**, P. 235411 (2008).
[8] Gupta V., Chaudhary N., et al. Luminscent graphene quantum dots for organic photovoltaic devices. *J. Am. Chem. Soc.*, **133**, P. 9960–9963 (2011).
[9] Liu R., Wu D., Feng X., Mullen K. Bottom-up fabrication of photoluminescent graphene quantum dots with uniform morphology. *J. Am. Chem. Soc.*, **133**, P. 15221–15223 (2011).
[10] Yan X., Li B., Li L-S. Colloidal graphene quantum dots with well-defined structures. *Acc. Chem. Res.*, DOI: 10.1021/ar300137p.
[11] Tang L., Ji R., et al. Deep ultraviolet photoluminescence of water-soluble self-passivated graphene quantum dots. *ACS Nano*, **6**, P. 5102–5110 (2012).
[12] Li L., Wu G., et al. Focusing on luminescent graphene quantum dots: current status and future perspectives. *Nanoscale*, **5**, P. 4015–4039 (2013).
[13] Zhou X., Zhang Y., et al. Photo-Fenton reaction of graphene oxide: A new strategy to prepare graphene quantum dots for DNA cleavage. *ACS Nano*, **6**, P. 6592–6599 (2012).
[14] Dong Y., Chen C., et al. One-step and high yield simultaneous preparation of single- and multi-layer graphene quantum dots from CX-72 carbon black. J. *Mater. Chem.*, **22**, P. 8764–8766 (2012).
[15] M. Zhang, L. Bai, et al. Facile synthesis of water-soluble, highly fluorescent graphene quantum dots as a robust biological label for stem cells. *J. Mater. Chem.*, **22**, P. 7461–7467 (2012).
[16] Lin L., Zhang S. Creating high yield water soluble luminescent graphene quantum dots via exfoliating and disintegrating carbon nanotubes and graphite flakes. *Chem. Commun.*, **48**, P. 10177–10179 (2012).
[17] Chen S., Liu J.-W., et al. Unusual emission transformation of graphene quantum dots induced by self-assembled aggregation. *Chem. Commun.*, **48**, P. 7637–7639 (2012).
[18] Razbirin B.S., Sheka E.F., et al. Enhanced Raman scattering provided by fullerene nanoclusters. *JETP Lett.*, **87**, P. 133–139 (2008).
[19] Razbirin B.S., Sheka E.F., et al. The nature of enhanced linear and nonlinear optical effects in fullerenes in solution. *JETP*, **108**, P. 738–750 (2009).
[20] Razbirin B.S., Sheka E.F., et al. Shpolski effect in optical spectra of frozen solutions. *Phys. Sol. State*, **51**, P. 1315–1319 (2009).

[21] Sheka E.F., Razbirin B.S., et al. Fullerene-cluster amplifiers and nanophotonics of fullerene solutions. *J. Nanophoton.*, **3**, P. 033501 (2009).
[22] Witten T.A. Polymer solutions: A geometric introduction. In Soft Matter Physics. Eds. M. Daoud and C.E. Williams. Springer-Verlag, Berlin Heidelberg, 1999, P. 261–288.
[23] Gouyet J.-F. *Physics and Fractal Structures*. Masson Springer: Paris/New York, 1996.
[24] Park S., An J., et al. Colloidal suspensions of highly reduced graphene oxide in a wide variety of organic solvents. *Nano Lett.*, **9**, P. 1593–1597 (2009).
[25] Hamilton C.E., Lomeda J.R., et al. High-yield organic dispersions of unfunctionalized graphene. *Nano Lett.*, **9**, P. 3460–3462 (2009).
[26] Rozhkova N.N., Yemel'yanova G.I., et al. From stable aqueous dispersion of carbon nanoparticles to the clusters of metastable shungite carbon. *Glass Phys. Chem.*, **37**, P. 613–618 (2011).
[27] Shpol'skii E.V. New data on the nature of the quasilinear spectra of organic compounds. *Phys.-Uspekhi*, **6**, P. 411–427 (1963).
[28] Heritage J.P., Glass A.M. Nonlinear optical effects. In Surface Enhanced Raman Scattering. Eds. R.K.Chang and F.E.Furtak. NY and London: Plenum Press. 1982, P. 391–412.
[29] Sheka E.F. Nanophotonics of fullerene. 1. Chemistry and medicine. *Nanosci. Nanothechn. Lett.*, **3**, P. 28–33 (2011).

NANOSYSTEMS: PHYSICS, CHEMISTRY, MATHEMATICS, 2014, 5 (2), P. 234–248

LOCALIZED STATES AND STORAGE OF OPTICAL INFORMATION UNDER THE QUBIT-LIGHT INTERACTION IN MICRO-SIZE CAVITY ARRAYS

[1]E. S. Sedov, [1]S. M. Arakelian, [1,2]A. P. Alodjants

[1] Department of Physics and Applied Mathematics, Vladimir State University named after A. G. and N. G. Stoletovs, Gorky Street 87, RU-600000, Vladimir, Russia
[2] Russian Quantum Center, 100 Novaya str., Skolkovo, Moscow region, 143025, Russia
alodjants@vlsu.ru

PACS 42.50.Pq, 05.45.Yv, 42.50.Ex, 71.36.+c

We suggest the model of lattice low branch (LB) polaritons based on the array of weakly coupled micro-size cavities, each containing a small but macroscopic number of two-level systems (qubits). We reveal various dynamical regimes, such as diffusive, self-trapped, breathing and solitonic for polariton wave packet propagation under tight-binding approximation. We focus our attention on the bright polariton soliton formation in a high quality cavity array emerging due to two-body polariton-polariton scattering processes that take place at each cavity under the qubit-light interaction. A physical algorithm for the spatially distributed storage of optical information where various dynamical LB polariton soliton states are used is proposed. This algorithm can be realized with the help of manipulating group velocity of a polariton soliton in the cavity array and obtained by smooth variation of qubit-light detuning.

Keywords: polariton, quantum information, qubit, soliton, spatially-periodic structure.

1. Introduction

The current remarkable achievements with trapped atomic gases, semiconductor technologies and photonic crystal devices represent important progress towards solving problems for the design of novel devices operating at the quantum level of matter-light field interaction [1]. In particular, memory devices recently proposed in quantum physics for the above purposes explore different methods for the entanglement of atoms (or two- or multi-level oscillators) with quantized electromagnetic fields and mapping of the quantum state of light onto matter by using slow light phenomenon [2]. Physically, various quantum optical memory protocols, widely discussed now for different types of interaction of quantized light field with two or multi-level atoms are linear (see, e.g. [1, 3]) as rule, and based on linear coupling between matter excitations and quantized field. Actually, they can be realized in very dilute atomic gases [4]. In this sense, the processes occurring in the systems as well as relevant quantum optical memory protocols can be explained in a very elegant way by using polaritons representing a linear superposition of a quantized field and collective excitations in matter, [5]. In this case, the essential reduction of the group velocity of an optical pulse emerging in the atomic medium, under EIT effect as an example, may be controlled by a pump field and can be explained by polariton transformation in the medium. More precisely, the group velocity of light in this limit is determined by the velocity of atom-like polaritons that could be low enough due to large polariton mass that is $m_{\rm pol} \simeq m_{\rm at}$, cf. [6].

However, this simple physical picture, as well as quantum memory protocols, requires essential clarification if we deal with optical pulse propagation in lattice structures.

It is worth noting that at present, various lattice models of qubit-light interaction of different dimensionality represent an important tool to provide quantum information storage and processing within the framework of modern scalable quantum technologies, cf. [7, 8]. In this sense, it seems promising to exploit cavity arrays (or 2D lattices) containing two-level systems (atoms, quantum dots, Cooper pair boxes) strongly interacting with the cavity field at each site [9, 10]. Addressability and controlling of qubits at each cavity make such systems good candidates for quantum computing [11]. Thus, if we speak about the properties of the group velocity of polaritons in a lattice system, we should take into account the fact that the group velocity in the lattices is strongly modified within the Brillouin zone [12].

Nonlinear effects become important under the strong matter-field interaction in semiconductor microstructures. Recently, macroscopic coherent effects such as polariton lasing and superfluidity have been observed for low-branch (LB) exciton-polaritons in semiconductor quantum well structures embedded in Bragg microcavities [13–15]. In such systems, strong Kerr-like nonlinearity caused by two-body polariton-polariton interaction leads to the formation of bright polariton solitons, even for a small number of particles; this open new perspectives for storing and processing quantum information, cf. [16].

Thus, in solid state systems the behavior of a coupled matter-field state is connected with the interplay between dispersion characteristics and strong nonlinearity. In this sense, it seems to be important and useful to refer to the problem of dynamical phases of atomic Bose-Einstein condensates (BEC) confined in a deep optical lattice potential [17, 18]. In particular, it is shown that intrinsically localized excitations, such as breathers and/or solitons, as well as self-trapping and diffusive regimes can exist in the presence of a repulsive atom-atom interaction.

In the present paper, we continue our theoretical investigation of mean field collective properties of coupled atom-light states – LB polaritons emerging due to the interaction of two-level systems (qubits) with a single-mode optical field in a cavity array, [19]. In previous work, we reveal the existence of bright polariton soliton solutions by using the complex Ginzburg-Landau equation that was derived in the continuum limit, taking into account the effects of cavity field dissipation and qubit dephasing [20]. Although we suggested rubidium atoms for numerical simulations, our model could be applied to different qubit systems, such as quantum dots, Cooper pair boxes, etc. One of the main features of our approach is strong nonlinearity which occurs due to small cavity volumes occupied by optical field, that is $V \simeq (\lambda/2n)^3$, where λ is light wavelength, n is refractive index. Current nanotechnologies enable the design of such cavities by using, for example, defects in semiconductor membranes, representing 2D photonic crystals [21], or cavities with whispering gallery modes [22]. In this paper, we consider a tight-binding model that includes neighbor hopping effects for photonic fields. This model leads to strong photonic correlations and nonlinear properties for coupled matter-field states in the lattice. In practice, small period 1D lattices could be created by using silicon heterostructures [23] or by a waveguide array [24].

The paper is arranged as follows: in Sec. 2, we explain in detail our model where qubit-light interaction in a cavity array is realized at microscales. In this case, a tight-binding model will be established. In Sec. 3, we introduce a coupled qubit-light excitation basis for our system. Apart from the results obtained previously (see e.g. [20]), LB polaritons emerging at each site of the cavity array are the subject of our study in the rest of the paper. In order, to obtain polariton wave packet behavior in the QED cavity array, we use a time dependent variational approach. Basic equations for the wave packet parameters

and their general properties are established in Sec. 4. The main results of the paper are given in Sec. 5 and relay to investigation of 1D lattice polariton wave packet dynamical regimes. In Sec. 6 we propose a novel algorithm of storing of optical information by using lattice polariton solitons. In the conclusion, we summarize the results obtained. In the Appendix we discuss realistic properties of cavity-QED array parameters for two-level rubidium atoms chosen as a qubit system and interacting with an optical field.

2. Qubit-light interaction model

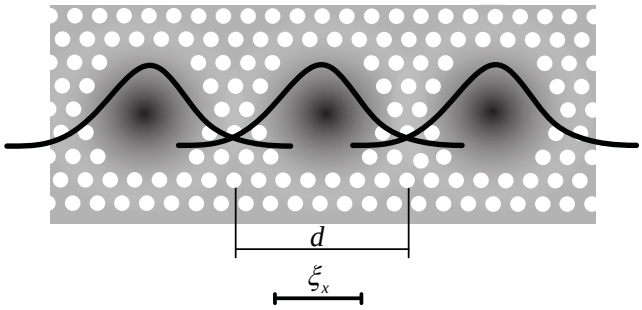

Fig. 1. Schematic for the proposed 1D cavity QED arrays, where each cavity contains an ensemble of two-level systems (TLS) – qubits. Parameter d represents the size of the cavity, ξ_x is characteristic spatial scale of the optical field localization. The shaded region in the center of each cavity depicts the TLS wave function of scale σ_x. In the paper we assume that $\sigma_x < \xi_x \leqslant d$

We consider a one-dimensional (1D) array of small (microscale) cavities, each containing an ensemble of small but macroscopic number N_n of interacting two-level systems (TLS) – qubits, see Fig. 1. The total Hamiltonian $\hat{H}$ for the qubit–light coupled system in Fig. 1 can be represented as:

$$\hat{H} = \hat{H}_{\rm TLS} + \hat{H}_{\rm PH} + \hat{H}_{\rm I}, \tag{1}$$

where $\hat{H}_{\rm TLS}$ is a quantum field theory Hamiltonian for *noninteracting* qubits, $\hat{H}_{\rm PH}$ is responsible for the photonic field distribution, and term $\hat{H}_{\rm I}$ characterizes the qubit-light interaction in each cavity. The parts of the total Hamiltonian can be written in the second quantized form as:

$$\hat{H}_{\rm TLS} = \sum_{\substack{i,j=1,2 \\ i\neq j}} \int \hat{\Phi}_j^{\dagger} \left(-\frac{\hbar^2 \Delta}{2M_{\rm at}} + V_{\rm ext}^{(j)} \right) \hat{\Phi}_j d\vec{r}, \tag{2}$$

$$\hat{H}_{\rm PH} = \int \hat{\Phi}_{\rm ph}^{\dagger} \left(-\frac{\hbar^2 \Delta}{2M_{\rm ph}} + V_{\rm ph} \right) \hat{\Phi}_{\rm ph} d\vec{r}, \tag{3}$$

$$\hat{H}_{\rm I} = \hbar\kappa \int \left(\hat{\Phi}_{\rm ph}^{\dagger} \hat{\Phi}_1^{\dagger} \hat{\Phi}_2 + \hat{\Phi}_2^{\dagger} \hat{\Phi}_1 \hat{\Phi}_{\rm ph} \right) d\vec{r}, \tag{4}$$

where $M_{\rm at}$ is a mass of free two-level particles, $M_{\rm ph}$ is a mass of trapped photons. In (2) – (4), quantum field operators $\hat{\Phi}_{1,2}(\vec{r})$, $\hat{\Phi}_{1,2}^{\dagger}(\vec{r})$ ($\hat{\Phi}_{\rm ph}(\vec{r})$, $\hat{\Phi}_{\rm ph}^{\dagger}(\vec{r})$) annihilate and create particles (photons) at position $\vec{r}$; $V_{\rm ext}^{(j)}$ $(j = 1, 2)$, and $V_{\rm ph}$ are trapping potentials for TLS and photons, respectively.

In general, one can expand atomic ($\hat{\Phi}_j$) and photonic ($\hat{\Phi}_{\rm ph}$) field operators as follows:

$$\hat{\Phi}_j(\vec{r}) = \sum_n \hat{a}_{j,n}\varphi_{j,n}(\vec{r}), \qquad \hat{\Phi}_{\rm ph}(\vec{r}) = \sum_n \hat{\psi}_n \xi_n(\vec{r}), \quad j = 1, 2, \tag{5}$$

where wave functions $\varphi_{j,n}(\vec{r})$, $\xi_n(\vec{r})$ are real (Wannier) functions responsible for the spatial distribution of qubits and photons at n–site. They fulfill a normalization condition $\int_{-\infty}^{+\infty}(\varphi_{j,n}(\vec{r}))^2 d\vec{r} = \int_{-\infty}^{+\infty}(\xi_n(\vec{r}))^2 d\vec{r} = 1$. In the Appendix, we use a variational Gaussian ansatz approach for estimating $\varphi_{j,n}(\vec{r})$, $\xi_n(\vec{r})$ functions.

Annihilation operators $\hat{a}_{1,n}$ and $\hat{a}_{2,n}$ in (5) characterize the dynamical properties of qubit ensembles (quantum modes) at internal lower ($|1\rangle$) and upper ($|2\rangle$) levels, respectively. Annihilation operator $\hat{\psi}_n$ in (5) describes the temporal behavior of a photonic mode located at the nth lattice cavity. Substituting (5) for (2)–(4) one can obtain:

$$\hat{H}_{\rm TLS} = \hbar \sum_{j=1}^{2}\sum_{n}^{M}\left[\omega_n^{(j)}\hat{a}_{j,n}^{\dagger}\hat{a}_{j,n} - \beta_{j,n}\left(\hat{a}_{j,n}^{\dagger}\hat{a}_{j,n+1} + \hat{a}_{j,n}^{\dagger}\hat{a}_{j,n-1}\right)\right], \tag{6}$$

$$\hat{H}_{\rm PH} = \hbar \sum_{n}^{M}\left[\omega_{n,\,\rm ph}\hat{\psi}_n^{\dagger}\hat{\psi}_n - \alpha_n\left(\hat{\psi}_n^{\dagger}\hat{\psi}_{n+1} + \hat{\psi}_n^{\dagger}\hat{\psi}_{n-1}\right)\right], \tag{7}$$

$$\hat{H}_{\rm I} = \hbar \sum_{n}^{M}\frac{g}{\sqrt{N_n}}\left[\hat{\psi}_n^{\dagger}\hat{a}_{1,n}^{\dagger}\hat{a}_{2,n} + \hat{a}_{2,n}^{\dagger}\hat{a}_{1,n}\hat{\psi}_n\right], \tag{8}$$

where $N_n = \hat{a}_{1,n}^{\dagger}\hat{a}_{1,n} + \hat{a}_{2,n}^{\dagger}\hat{a}_{2,n}$ is an operator of a total number of TLS at nth lattice cell. Frequencies $\omega_n^{(j)}$, $\omega_{n,\,\rm ph}$ and hopping constants $\beta_{j,n}$, α_n look like:

$$\omega_n^{(j)} = \frac{1}{\hbar}\int\left(\frac{\hbar^2}{2M_{\rm at}}(\vec{\nabla}\varphi_{j,n})^2 + \varphi_{j,n}V_{\rm ext}^{(j)}\varphi_{j,n}\right)d\vec{r}, \tag{9}$$

$$\omega_{n,\rm ph} = \frac{1}{\hbar}\int\left(\frac{\hbar^2}{2M_{\rm at}}(\vec{\nabla}\xi_n)^2 + \xi_n V_{\rm ph}\xi_n\right)d\vec{r}, \tag{10}$$

$$\beta_{j,n} = -\frac{1}{\hbar}\int\left(\frac{\hbar^2}{2M_{\rm at}}\vec{\nabla}\varphi_{j,n}\cdot\vec{\nabla}\varphi_{j,n+1} + \varphi_{j,n}V_{\rm ext}^{(j)}\varphi_{j,n+1}\right)d\vec{r}, \tag{11}$$

$$\alpha_n = -\frac{1}{\hbar}\int\left[\frac{\hbar^2}{2M_{\rm ph}}\vec{\nabla}\xi_n\cdot\vec{\nabla}\xi_{n+1} + \xi_n V_{\rm ph}\xi_{n+1}\right]d\vec{r}, \tag{12}$$

$$g = \kappa\int\xi_n\varphi_{1,n}\varphi_{2,n}d\vec{r}. \tag{13}$$

Thereafter, we assume for simplicity that all cavities are identical to each other and contain the same average number $N = \langle N_n\rangle$ of qubits. In this case, it is convenient to suppose that functions $\varphi_{j,n}(\vec{r})$ are identical for all n, that is $\varphi_{j,n}(\vec{r}) \simeq \varphi_{j,n\pm1}(\vec{r})$.

Parameter $\alpha_n \equiv \alpha$ in (12) describes overlapping of the optical field for nearest-neighbor cavities. Coupling coefficients $\beta_{j,n} \equiv \beta_j$ in (11) are hopping constants for qubits in the 1D lattice structure.

3. Polaritons in the cavity array

Now, we use the Schwinger representation to describe a matter-field interaction and introduce TLS excitation operators $\hat{S}_{+,\,n} = \hat{a}_{2,n}^{\dagger}\hat{a}_{1,n}$, $\hat{S}_{-,\,n} = \hat{a}_{1,n}^{\dagger}\hat{a}_{2,n}$ and population imbalance operator $\hat{S}_{z,\,n} = \frac{1}{2}\left(\hat{a}_{2,n}^{\dagger}\hat{a}_{2,n} - \hat{a}_{1,n}^{\dagger}\hat{a}_{1,n}\right)$. Then, we map the operators onto the atomic

excitation operators $\hat{\phi}_n$, $\hat{\phi}_n^\dagger$, applying the so-called Holstein–Primakoff transformation:

$$\hat{S}_{+,n} = \hat{\phi}_n^\dagger \sqrt{N - \hat{\phi}_n^\dagger \hat{\phi}_n}, \quad \hat{S}_{-,n} = \sqrt{N - \hat{\phi}_n^\dagger \hat{\phi}_n}\,\hat{\phi}_n, \quad \hat{S}_{z,n} = \hat{\phi}_n^\dagger \hat{\phi}_n - N/2. \tag{14}$$

It is worth noting that atomic excitation operators $\hat{\phi}_n$, $\hat{\phi}_n^\dagger$ obey usual bosonic commutation relations $\left[\hat{\phi}_n, \hat{\phi}_m^\dagger\right] = \delta_{mn}$. Strictly speaking, it is possible to treat the operators $\hat{a}_{1,n}$ and $\hat{a}_{2,n}$ describing particles at lower and upper levels respectively, as $\hat{a}_{1,n} \approx \sqrt{N} - \frac{\hat{\phi}_n^\dagger \hat{\phi}_n}{2N^{1/2}}$, cf. [19].

Thus, if number N at each cavity is macroscopic, but not so large, one can keep all the terms in expansion of $\hat{a}_{1,n}$. In this limit, for Hamiltonian $\hat{H} = \hat{H}_{\rm L} + \hat{H}_{\rm C} + \hat{H}_{\rm NL}$, we obtain the following:

$$\hat{H}_{\rm L} = \hbar \sum_n \left[\tilde{\omega}_{12} \hat{\phi}_n^\dagger \hat{\phi}_n + \omega_{n,\,\rm ph} \hat{\psi}_n^\dagger \hat{\psi}_n + g \left(\hat{\psi}_n^\dagger \hat{\phi}_n + H.C. \right) \right], \tag{15}$$

$$\hat{H}_{\rm C} = -\hbar \sum_n \left[\beta \hat{\phi}_n^\dagger \hat{\phi}_{n+1} + \alpha \hat{\psi}_n^\dagger \hat{\psi}_{n+1} + H.C. \right], \tag{16}$$

$$\hat{H}_{\rm NL} = -\hbar \sum_n \left[\frac{g}{2N} \left(\hat{\psi}_n^\dagger \hat{\phi}_n^\dagger \hat{\phi}_n^2 + H.C. \right) \right], \tag{17}$$

where we have introduced new parameters $\tilde{\omega}_{12} = \omega_n^{(2)} - \omega_n^{(1)} + 2\beta_{1,n}$, $\beta = \beta_2$.

Let us introduce lattice polariton operators as follows:

$$\hat{\Xi}_{1,n} = X_n \hat{\psi}_n + C_n \hat{\phi}_n, \qquad \hat{\Xi}_{2,n} = X_n \hat{\phi}_n - C_n \hat{\psi}_n, \tag{18}$$

where X_n and C_n are Hopfield coefficients defined as:

$$\begin{pmatrix} X_n \\ C_n \end{pmatrix} = \frac{1}{\sqrt{2}} \left(1 \pm \frac{\delta_n}{\sqrt{4g^2 + \delta_n^2}} \right)^{1/2}. \tag{19}$$

In Eq. (19), $\delta_n = \omega_{n,\,\rm ph} - \tilde{\omega}_{12}$ is a qubit-light field detuning chosen at each cavity. Note that parameters X_n and C_n are considered equivalent for all cavities (sites n), assuming that $X \equiv X_n$ and $C \equiv C_n$. This approach implies equal qubit-light detuning $\delta = \delta_n$ for all cavities as well.

Operators $\hat{\Xi}_{1,n}$ and $\hat{\Xi}_{2,n}$ in (18) characterize two types of Bose-quasiparticles, i.e. upper and lower branch polaritons occurring at each site of the lattice due to the matter–field interaction. At the low density limit, Eqs. (18) and (19) represent the exact solution that diagonalizes a linear part $\hat{H}_{\rm L}$ of the total Hamiltonian $\hat{H}$.

At equilibrium, the lowest polariton branch is much more heavily populated. Here, we use a mean-field approach to replace the corresponding polariton field operator $\hat{\Xi}_n$ with its average value $\left\langle \hat{\Xi}_n \right\rangle$, which simply characterizes the LB polariton wave function at the nth cavity. For further processing, we introduce the nth normalized polariton amplitude as $\Psi_n = \left\langle \hat{\Xi}_n \right\rangle / \sqrt{N_{\rm pol}}$, where $N_{\rm pol} = \sum_n \left\langle \hat{\Xi}_n^\dagger \hat{\Xi}_n \right\rangle$ is the total number of LB polaritons at the array. Under this approach, substituting (18) for (15)–(17) and keeping LB polariton terms only, we arrive at:

$$H = \hbar \sum_n^M \left[\Omega_{\rm LB} \left| \Psi_n \right|^2 - \Omega_{\rm T} \left(\Psi_n^* \Psi_{n+1} + C.C. \right) + \frac{1}{2} \Omega_{\rm I} \left| \Psi_n \right|^4 \right], \tag{20}$$

where we have introduced characteristic frequency $\Omega_{\rm LB}$, polariton tunneling rate $\Omega_{\rm T}$ and interaction strength $\Omega_{\rm I}$ as follows:

$$\Omega_{\rm LB}=\frac{1}{2}\left(\tilde{\omega}_{12}+\omega_{n,\,\rm ph}-\sqrt{\delta^2+4g^2}\right),\quad \Omega_{\rm T}=\beta X^2+\alpha C^2,\quad \Omega_{\rm I}=2gCX^3\frac{N_{\rm pol}}{N}. \tag{21}$$

Actually, in the limit of negative and large qubit-light field detuning chosen as $|\delta|\gg g$, $\delta<0$ ($X\simeq g/|\delta|, C\simeq 1$), the LB polaritons behave as photons, i.e. $\Xi_{2,n}\simeq\psi_n$. Thus, we can represent the frequency parameters as $\Omega_{\rm LB}\simeq\omega_{\rm ph}$, $\Omega_{\rm T}=\alpha$, $\Omega_{\rm I}=2N_{\rm pol}g^4/N|\delta|^3$.

In another limit, we can take $|\delta|\gg g$, $\delta>0$ ($X\simeq 1$, $C\simeq g/\delta$) and then LB polaritons behave as excited atoms, i.e. $\Xi_{2,n}\simeq\phi_n$. We readily find for the coefficients $\Omega_{\rm LB}\simeq\tilde{\omega}_{12}$, $\Omega_{\rm T}=\beta+\alpha\frac{g^2}{\delta^2}$, $\Omega_{\rm I}=\frac{2g^2}{\delta}\frac{N_{\rm pol}}{N}$.

4. Time-dependent variational approach

To analyze different regimes of polaritons in the lattice, we study the dynamical evolution of in-site Gaussian shape wave packet, which we represent as:

$$\Psi_n=\quad \mathbb{N}\exp\left[-\frac{(x-\mathrm{X}(t))^2}{\Gamma(t)^2}+ik(t)(x-\mathrm{X}(t))+i\frac{\theta(t)}{2}(x-\mathrm{X}(t))^2\right], \tag{22}$$

where $X(t)$ and $\Gamma(t)$ are a time dependent center and a width of the wave packet, respectively, $k(t)$ is momentum and $\theta(t)$ is curvature, $\mathbb{N}=\left(\sqrt{2}/\sqrt{\pi}\Gamma(t)\right)^{1/2}$ is a normalization constant (the wave packet amplitude). Lattice coordinate x relays to the number of sites (cavities) n as $x=nd$. The wave packet dynamical evolution can be obtained in accordance with a variational principle from the Lagrangian density:

$$L=\hbar\sum_n^M\left[\frac{i}{2}\left(\Psi_n^*\frac{\partial\Psi_n}{\partial t}-\Psi_n\frac{\partial\Psi_n^*}{\partial t}\right)-\Omega_{\rm LB}\,|\Psi_n|^2+\Omega_{\rm T}\left(\Psi_n^*\Psi_{n+1}+C.C.\right)-\frac{1}{2}\Omega_{\rm I}|\Psi_n|^4\right]. \tag{23}$$

Plugging Eq. (22) into Eq. (23), it is possible to calculate the effective Lagrangian $\bar{L}$ by averaging the Lagrangian density (23), as

$$\bar{L}=\quad \hbar\left[k\dot{X}-\frac{\dot{\theta}\Gamma^2}{8}+2\Omega_{\rm T}\cos(kd)\,e^{-\sigma}-\frac{\Omega_{\rm I}d}{2\Gamma\sqrt{\pi}}\right], \tag{24}$$

where we gave the following denotation $\sigma=\frac{\Gamma^2\theta^2d^2}{8}+\frac{d^2}{2\Gamma^2}$. Noting that Eq. (24) is valid when parameter Γd is not too small, that is $\Gamma d\geqslant 1$, cf. [17,18].

Using Lagrangian (24), one can obtain the following variational equations for the canonically conjugate polariton wave packet parameters:

$$\dot{k}=0,\quad \dot{X}=2d\Omega_{\rm T}\sin(kd)\,e^{-\sigma},\quad \dot{\Gamma}=\frac{\hbar\Gamma\theta}{M^*},\quad \dot{\theta}=\frac{\hbar}{M^*}\left(\frac{4}{\Gamma^4}-\theta^2\right)+\frac{2\Omega_{\rm I}d}{\sqrt{\pi}\Gamma^3}. \tag{25}$$

In Eq. (25), we also introduced an effective polariton mass in the lattice

$$M^*=\frac{1}{\hbar^2}\frac{\partial^2H}{\partial k^2}=\frac{m_{\rm ex}m_{\rm ph}}{m_{\rm ex}C^2+m_{\rm ph}X^2}, \tag{26}$$

for which we use the definition of photon $m_{\rm ph}=\hbar e^{\sigma}\sec(kd)/2d^2\alpha$ and qubit exciton $m_{\rm ex}=\hbar e^{\sigma}\sec(kd)/2d^2\beta$ masses in the lattice respectively. In Eq. (26) H is the Hamiltonian for

the system (25) that looks like:

$$H = -\frac{\hbar^2}{d^2 M^*} + \frac{\hbar \Omega_{\mathrm{I}} d}{2\sqrt{\pi}\Gamma}. \tag{27}$$

Using Eq. (26) for the group velocity of a polariton wave packet one can obtain

$$v_g \equiv \frac{1}{\hbar}\frac{\partial H}{\partial k} = \dot{\mathrm{X}} = \frac{\hbar}{d}\frac{\tan(kd)}{M^*}. \tag{28}$$

The first equation in (25) implies that the momentum of a polariton wave packet is preserved in time, i.e. $k(t)|_{t=0} \equiv k_0$. Hence, we are able to consider the properties of a polariton wave packet by fixing initial value of momentum k. For a small momentum such as $kd \ll 1$, which is typically associated with the middle area of the Brillouin zone from Eqs. (26) and (28), one can obtain a convenient result for the polariton group velocity, that is $v_g \approx \frac{\hbar k}{M^*}$, where $M^* \simeq \hbar e^{\sigma}/2d^2\Omega_{\mathrm{T}}$.

In this paper, we are interested mainly in the polaritons with large and negative effective mass M^*. Practically, in this case we anticipate slow soliton regimes for a polariton wave packet spreading in the lattice.

The maximal negative polariton mass $M_0^* = -\hbar e^{\sigma}/2d^2\Omega_{\mathrm{T}}$ can be obtained at $\cos(kd) = -1$ that corresponds to the edge of the Brillouin zone, cf. [19]. Obviously, the group velocity of a polariton wave packet vanishes, i.e. $v_g = 0$.

For further analysis, it is also fruitful to rewrite Eq. (25) introducing dimensionless variables $p = kd$, $\xi = X/d$, $\gamma = \Gamma/d$ and $\eta = \theta d^2$. In this case, the set of Eq. (25) takes the form of:

$$\dot{\xi} = \omega_{\mathrm{T}} \sin(p)\, e^{-\sigma}, \quad \dot{\gamma} = \frac{\gamma\eta}{m^*}, \quad \dot{\eta} = \frac{1}{m^*}\left(\frac{4}{\gamma^4} - \eta^2\right) + \frac{4\omega_{\mathrm{I}}}{\gamma^3}, \tag{29}$$

where $t \to t/2|\Omega_{\mathrm{T}}|$ and $m^* = 2|\Omega_{\mathrm{T}}| d^2 M^*/\hbar$ are dimensionless time coordinate and polariton mass, respectively, $\omega_{\mathrm{T}} = \mathrm{sgn}(\Omega_{\mathrm{T}})$, $\omega_{\mathrm{I}} = \Omega_{\mathrm{I}}/(4\sqrt{\pi}|\Omega_{\mathrm{I}}|)$.

Phase diagrams for various dynamical regimes are determined by the property of polariton mass m^* and by the sign of Hamiltonian H that is supposed to be a conserved quantity. In particular, at $m^* > 0$ a polariton wave packet exhibits diffusive and self-trapping regimes for which $\gamma \to \infty$, $\eta \to 0$ and $\gamma \to const$, $\eta \to \infty$ at large, and in the limit case – at infinite, time scales ($t \to \infty$), respectively.

A phase diagram of a polariton wave packet is richer in the case of a negative polariton mass, i.e. at $m^* < 0$. In this case, the sign of the Hamiltonian function H becomes important, and in dimensionless coordinates, it looks like:

$$H = -\omega_{\mathrm{T}} \cos(p)\, e^{-\sigma} + \frac{\omega_{\mathrm{I}}}{\gamma}. \tag{30}$$

The transition between different regimes occurs at $H = H_0 = 0$, which implies $\cos(p) \simeq 0$; we denote H_0 as the initial value of Hamiltonian H which is, obviously, a conserved quantity in the absence of dissipation.

A physically important bound state for our problem occurs in the domain of negative polariton mass ($m^* < 0$) and this can be associated with the soliton formation for a polariton wave packet. The polariton (bright) soliton wave packet propagates with the initial width $\gamma_0 \equiv \gamma(t=0)$, mass $m^* = m_0^* < 0$ and velocity $v_g = -\tan(p_0)/|m_0^*|$ being unchanged in time. The mass of a soliton wave packet can be found from:

$$\frac{1}{m_0^*} = \omega_{\mathrm{T}} \cos(p_0)\, e^{-\sigma_0}. \tag{31}$$

Strictly speaking, Eq. (31) defines a characteristic domain of the allowed wave packet momentum where solitonic regime can be achieved. In particular, this domain is determined by characteristic values of the polariton momentum which obeys the inequality $\cos(p) < 0$ that corresponds to the physical situation described in [17] for atomic BEC lattice solitons.

5. Polariton wave packet dynamics

For further analysis, it is much better to regard special cases which reflect physical features of polaritons in the lattice. In Fig. 2, we build a phase diagram for various dynamical regimes of the polariton wave packet formation in the lattice. In particular, according to our analysis of Eqs. (29)–(31), we deal with only two domains defined for $\cos(p_0) > 0$ and $\cos(p_0) < 0$ respectively. To be more specific, we suppose that $\Omega_{\mathrm{T}} > 0$, i.e. $\omega_{\mathrm{T}} = 1$.

In Fig. 2a, we plotted trajectories in the $\gamma - \eta$ plane which are relevant to the area where $\cos(p_0) > 0$. Such trajectories can be found by using the equation for energy conservation, i. e. $H = H_0$ which implies that:

$$\eta = \frac{2}{\gamma}\left(2\ln\left[\frac{\gamma^2\cos(p_0)}{\gamma\omega_{\mathrm{I}} - H_0\gamma^2}\right] - \frac{1}{\gamma^2}\right)^{1/2}. \tag{32}$$

From (32), when $H_0 > 0$, we can obtain the maximal the value of the wave packet width $\gamma_{\max} = \frac{\omega_{\mathrm{I}}}{H_0}$ for which a self-trapping regime is realized. Actually, in this case, polariton group velocity v_g and effective mass m^* are limited by the value $v_g \simeq \frac{\tan(p_0)}{m^*}$ with mass $m^* = \sec(p_0)\exp\left\{\frac{\gamma_{\max}^2\eta^2}{8} + \frac{1}{2\gamma_{\max}^2}\right\}$, respectively.

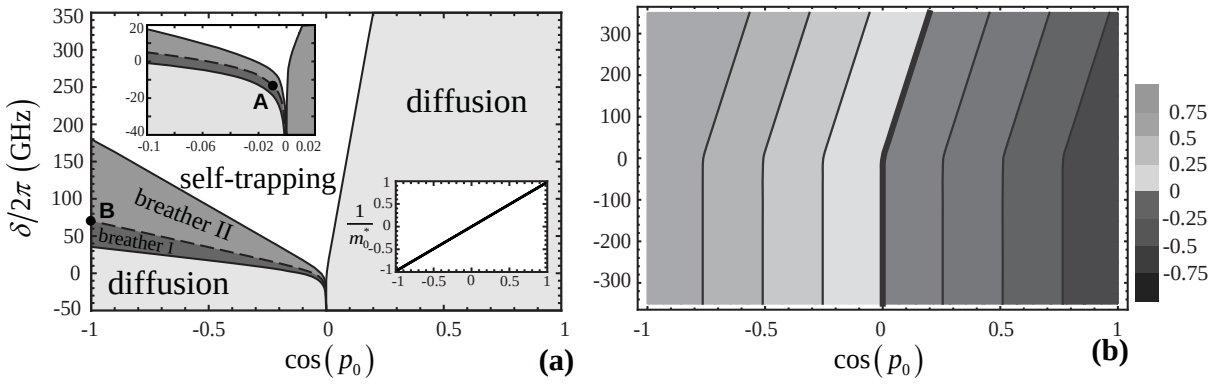

Fig. 2. (a) – Dynamical phase diagram in $\delta - \cos(p_0)$ plane, and, (b) – relevant Hamiltonian contour for $d = 4\mu\mathrm{m}$. Initial conditions are: $\gamma_0 = 5$, $\eta_0 = 0$. The right inset shows the behavior of inverse polariton mass $1\,/\,m_0^*$ versus $\cos(p_0)$. The dashed curve corresponds to the soliton regime and separates two breathing domains, respectively

Asymptotic properties of the wave packet at infinite time ($t \to \infty$) for which $\eta \gg 1$ implies that LB polaritons in the cavity array can be fully stopped, i.e. $v_g \to 0$ when the effective mass goes to infinity, i. e. $m^* \to \infty$, see Fig. 3a.

Now, let us consider the limit of the negative Hamiltonian, that is $H_0 < 0$. At long times, i. e. for $t \gg 1$ the width is $\gamma \gg 1$; the LB polariton wave packet spreads with

mass $m^* \approx 1/|H_0|$ and parameter $\eta \approx \frac{2}{\gamma}\sqrt{2\ln[m^*\cos(p_0)]} \equiv \eta_{\rm D}$, that corresponds to the *diffusive regime* of polariton wave packet propagation.

In practice, it is more convenient to change atom-light detuning δ for tuning polariton-polariton scattering parameters. In this case, the equation $H_0 = 0$ defines some critical value $\delta_{\rm C}$ of atom-field detuning for which transition between different regimes occurs – see Fig. 3a. Analytically, it is easy to elucidate a polariton behavior for small values of the momentum parameter $\cos(p_0)$. In this case, the critical value of $\delta_{\rm C}$ can be inferred from the equation $\frac{\omega_{\rm I}}{\gamma_0} = |\cos(p_0)|\, e^{-\sigma_0}$. Since the atom-field coupling parameter g is essentially smaller than the photon tunneling rate α for the appropriate experimental situation, the equation under discussion permits only negatively defined solutions for δ. In other words, in this limit, we deal with photon-like polaritons for which modulus of critical detuning $\delta_{\rm C}$ approaches

$$|\delta_{\rm C}| \simeq \left(\frac{g^4 N_{\rm pol} e^{\sigma_0}}{2\sqrt{\pi}\gamma_0 |\cos(p_0)|\,\alpha N}\right)^{1/3}, \tag{33}$$

where we suppose that condition $g \ll |\delta|$ is satisfied.

Now we suppose that the initial wave packet momentum obeys to a condition $\cos(p_0) < 0$, which implies initially negative polariton mass, Fig. 3a. Analysis of different regimes can be performed by using the initial value of Hamiltonian $H_0 = \frac{1}{|m_0^*|} + \frac{\omega_{\rm I}}{\gamma_0}$ which is certainly positive – see Fig. 3b. By using the energy conservation law $H_0 = H$, it is easy to determine if $H_0 > |\cos(p_0)|$, a wave packet width remains finite and we deal with localized polariton states, i.e. with self-trapping or breathing regimes. Conversely, the diffusive regime with $\gamma \to \infty$ and $\eta = \eta_{\rm D}$ occurs if $H_0 < |\cos(p_0)|$.

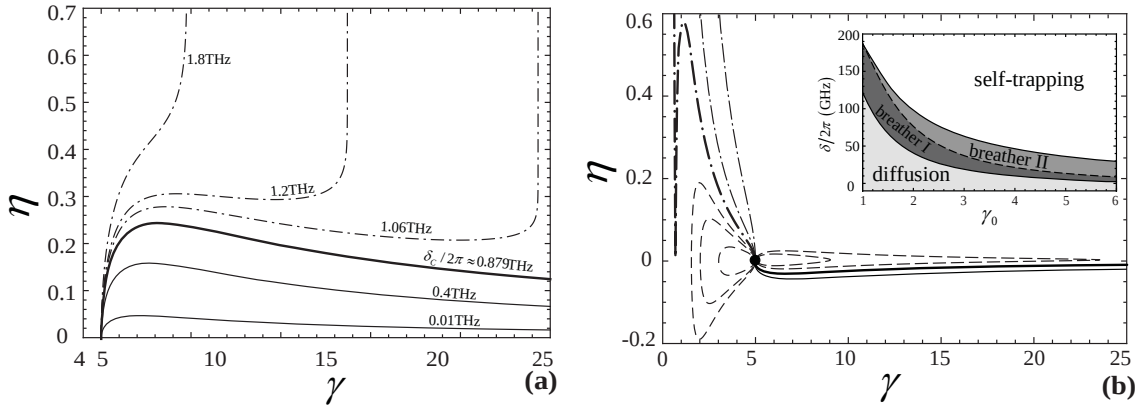

Fig. 3. Trajectories in the $\eta - \gamma$ plane for various atom-field detuning δ in the case where (a) – $\cos(p_0) > 0$ and, (b) – $\cos(p_0) < 0$. The initial values of the wave packet width and curvature are $\gamma_0 = 5$, $\eta_0 = 0$, respectively. Other parameters are: $d = 4\mu$m, $\cos(p_0) = 0.5$ for (a), and, $\cos(p_0) = -0.2$ for (b). In the inset the dependence of δ on γ_0 for $\cos(p_0) = -0.2$ is plotted. The magnitudes of $\delta/2\pi$ beginning with the bottom line in (b) are: -10GHz, $\delta_{\rm C}/2\pi \approx 5.112$GHz (bold curve) for solid curves, respectively; 7.1GHz, 10GHz and 18GHz, 23GHz, 27GHz for dashed curves, respectively; $\delta_{\rm BR}/2\pi \approx 36.138$GHz (bold dashed-dotted curve); 60GHz and 200GHz for dashed-dotted curves, respectively. The black dot in (b) corresponds to the solitonic regime of wave packet parameters obtained at $\delta_{\rm S}/2\pi \approx 13.422$GHz

The transition between the discussed physical situations is characterized by the condition $H_0 = |\cos(p_0)|$. Thus, polaritons with detuning $\delta < \delta_{\rm C}$ undergo a diffusive regime for which we asymptotically have $\gamma \to \infty$ and $\eta \to 0$.

If atom-field detuning belongs to $\delta_{\rm C} < \delta < \delta_{\rm S}$ domain, the first breathing regime can be obtained. The trajectories in $\eta - \gamma$ space are closed; the effective mass $m^*(t)$ and $\gamma(t)$ oscillating in time. The latest one oscillates between the initial value γ_0 and the value $\gamma_{\max}^{\rm osc}$, that is $\gamma_{\max}^{\rm osc} > \gamma_0$. For atom-field detuning chosen from the second breathing region $\delta_{\rm S} < \delta < \delta_{\rm BR}$, parameters $\gamma(t)$ and $\eta(t)$ also undergo temporal oscillations. However, in this case, the width $\gamma_{\min}^{\rm osc}$ of a polariton wave packet is limited by the initial value γ_0, that is $\gamma_{\min}^{\rm osc} < \gamma_0$.

Frequencies $\omega_{\rm BR\,1,2}$ of small amplitude oscillations of the wave packet width γ for the above discussed breathing regimes could be easily found by linearizing Eqs. (29) around some average values $\gamma_{1,2}$, and have the form:

$$\omega_{\rm BR\ 1,2} = \left[\frac{8\omega_{\rm I}}{\gamma_{1,2}^3}\left(\frac{1}{\gamma_{1,2}^2} - 1\right)|\cos(p)| - \frac{4}{\gamma_{1,2}^4}\left(\frac{5}{\gamma_{1,2}^2} - 3\right)|\cos(p)|^2\right]^{1/2}, \qquad (34)$$

where indexes "1" and "2" are relevant to two types of breathing regimes, respectively.

The dashed curve in Fig. 2a (see also inset to Fig. 3b), which corresponds to detuning $\delta_{\rm S}$ and separates two breathing regimes, characterizes bright soliton solution of Eqs. (29) taken for $\dot{\gamma} = 0$, $\eta = 0$.

On the other hand, a half-matter–half-photon polariton soliton with $\delta_{\rm S} = 0$ propagates in the cavity array with momentum $p_0 \simeq \left|\arccos\left(\frac{gN_{\rm pol}\gamma_0 e^{\sigma_0}}{4\sqrt{\pi}\alpha N}\right)\right|$.

Finally, if $\delta > \delta_{\rm BR}$, a polariton self-trapping regime is established. However, apart from the case of $\cos(p_0) > 0$ in this limit one can obtain $\gamma \to \gamma_{\min} < \gamma_0$ with $\eta \to \infty$.

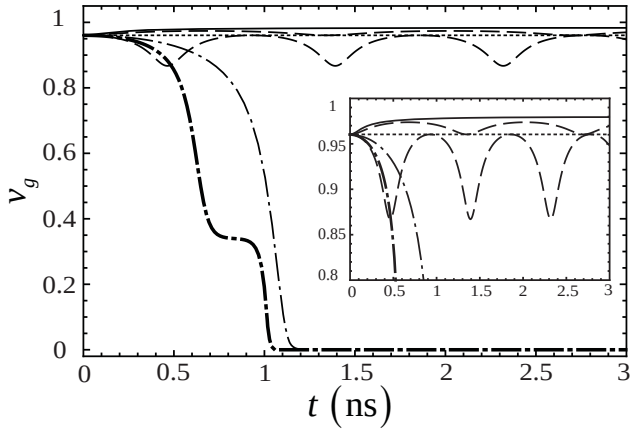

Fig. 4. Polariton wave packet group velocity v_g versus time t for $\gamma_0 = 5$, $\cos(p_0) = -0.2$. Beginning from the top of the figure, $\delta/2\pi = \delta_{\rm C}/2\pi \approx 5.112$GHz and $v_0 \equiv v_g(t=0) = 2888030$m/s (solid curve); 10GHz and $v_0 = 2150090$m/s (upper dashed curve); $\delta/2\pi = \delta_{\rm S}/2\pi \approx 13.421$GHz and $v_0 = 1630070$m/s (dotted line); 23GHz and $v_0 = 812925$m/s (lower dashed curve); $\delta/2\pi = \delta_{\rm BR}/2\pi \approx 36.138$GHz and $v_0 = 387474$m/s (dashed-dotted bold curve); 60GHz and $v_0 = 152560$m/s (dashed-dotted curve)

Figure 4 demonstrates typical temporal dynamics of the wave packet group velocity v_g in the discussed case. For detuning $\delta < \delta_{\rm C}$, we deal with the diffusive regime for which a group velocity tends to the constant value $v_g \approx \sin(p_0)$ asymptotically. On the other

hand, a group velocity oscillates in time within the window $\delta_{\rm C} < \delta < \delta_{\rm BR}$ (small-amplitude oscillations of the group velocity are shown in the inset in Fig. 4). For $\delta > \delta_{\rm BR}$, i.e. for a self-trapping regime, v_g rapidly vanishes and goes to zero. The soliton regime is established for atom-field detuning $\delta = \delta_{\rm S}$ and is obviously characterized by a constant value of the group velocity – dotted line in Fig. 4.

6. Physical algorithm of storing of photonic information

Different regimes obtained in the paper enable us to use them for the quantum optical information storage with the help of LB polariton solitons. As an example, here we establish a physical protocol of optical information storage by using specific points **A** and **B** in the phase diagram represented in Fig. 2, these points corresponding to polariton soliton formation. Physical principles of our protocol are established in Fig. 5. The protocol is based on the manipulation with a group velocity of photonic field (polariton mass) in the cavity array which has been discussed in detail in Sec. 4. In particular, at the first (writing) stage a photonic wave packet should enter a cavity array completely. In this case, LB polaritons are photon-like ($\Xi_{2,n} \propto \psi_n$) with mass $M^* \approx m_{\rm ph}$. Initially, soliton parameters that correspond to point **A** in Fig. 2a were given by the values $\cos\left(p_0^{\rm ph}\right) = -0.01$, $\delta \equiv \delta_{\rm ph} \approx -2\pi \times 12.763{\rm GHz}$, respectively. Then, we should switch atom-filed detuning to magnitude $\delta \equiv \delta_{\rm at} \approx 2\pi \times 70.328{\rm GHz}$ and choose LB polariton momentum as $\cos(p_0^{\rm at}) = -1$ for mapping optical information into coherent matter excitations. This situation is displayed in Fig. 2 by moving across the solitonic phase boundary toward point **B** that corresponds to matter-like LB polaritons ($\Xi_{2,n} \propto \phi_n$) with the mass $M^* \approx m_{\rm ex}$ posing low enough group velocity – see Fig. 4.

At the last stage the original wave packet can be reconstructed at the entrance of the cavity array. The time interval $\tau_{\rm R}$ corresponds to the restoration of optical information by using the process which is reversed with respect to detuning δ and momentum p_0. In the ideal case, we should obtain the same, photon-like polariton soliton wave packet as a result – see Fig. 5.

However, in the real world all time intervals characterizing writing, storing and retrieving stages for quantum memory purposes strictly depend on dissipation and decoherence effects with a coupled qubit-light system in the cavity array. The specifics of these effects that leads to diminishing quantum optical information storage fidelity depends on the peculiarities of a concrete realization of the system represented in Fig. 1. This important question requires separate analysis and this will be discussed elsewhere.

7. Conclusion

In this work, we consider the problem of lattice polariton soliton formation in the array of weakly coupled qubit ensembles interacting with the quantized photonic field in a tunnel-coupled cavity array – 1D lattice structure. Such cavities can be designed by using photonic crystal structures with the defects posing small (micro-scale) spatial sizes. We have demonstrated that this feature plays an essential role in the consideration of fundamental tunneling processes between cavities at different spatial scales. In particular, we focus on LB polariton wave packet properties obtained in the limit of strong qubit-light coupling condition and under the low temperatures when the upper polariton branch population can be neglected. We have shown that polariton wave packet exhibits four different dynamical regimes. First, there is a *diffusive regime* for which a polariton wave packet extends representing approximately a half matter–half photon quasi-particle state.

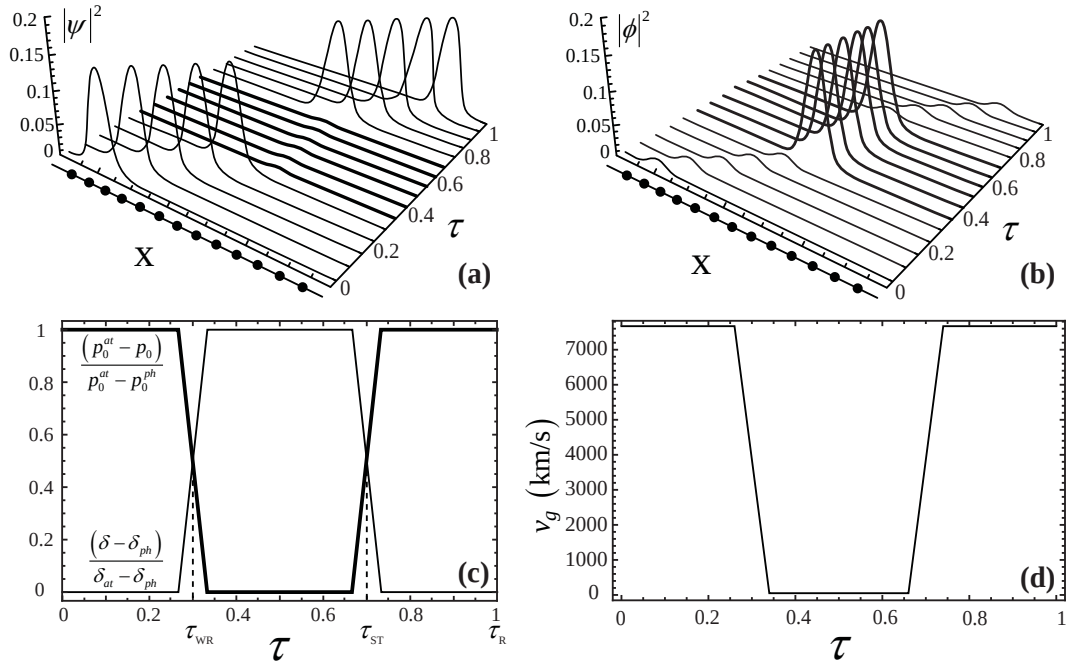

Fig. 5. Coherent spatio-temporal evolution of (a) – photonic ($|\psi|^2$) and, (b) – atomic excitation ($|\phi|^2$) components of the LB bright polariton soliton wave packet propagating in 1D cavity array (cavities are shown as bold points in x direction). The manipulation in time is realized by using scaled detuning δ and momentum p_0, respectively, shown in (c) and, by group velocity – (d). Axes are taken in arbitrary units

The second regime corresponds to intrinsically localized polaritonic modes; this is the so-called *breathing regime* when a wave packet moves with an oscillating width. Third, we deduce a *self-trapping regime* when a matter-like polariton wave packet can be stopped and localized within a few cavities only. Finally, we elucidate the regime of bright *polariton soliton* formation that corresponds to the propagation of the polariton wave packet in the lattice with constant velocity and its shape unchanged. One of the important features of the solitonic regime being under discussion is connected with the fact that it may be formed for both photon-like and matter-like domains of a coupled qubit-light system in the cavity array. Such a property of polariton solitons in our problem seems to be very attractive for the storage of quantum optical information.

In this paper we suggest a new physical algorithm for quantum optical memory which is based on the transformation and manipulation by polariton solitons in the cavity array. Although we do not examine any dissipation and quantum decoherence effects for a coupled qubit-light system considered in the paper, we hope that our approach opens new perspectives for quantum information processing with the help of polariton solitons containing a small particle number. Here, we would like to represent some arguments in favor of our point of view.

Obviously, the quantum optical information can be stored within the time interval that in practice depends on the qubit decoherence time and quality factor of a cavity array. One can expect that for the qubits based on the semiconductor QDs cavity QED array it is possible to achieve the storage time within tens of picoseconds domain with high enough

fidelity, [25]. Conversely, if we use two-level ultracold atoms, or NV-centers in diamonds as qubits we can operate with a memory device within tens of nanoseconds or more [26].

Second, our protocol of the optical information storage with the help of soliton states posses some important advantages with respect to other methods, which are based on the quantum information storage of operating other Gaussian-type optical pulses. In particular, solitons seem to be much more robust to small perturbations. Even in the presence of small dissipation and decoherence effects, it is possible to operate with a soliton-like shape, preserving wave packets in accordance with perturbation approach for polariton solitons, cf. [20].

Third, if dissipation and decoherence effects become significant, we hope that it will be possible to find some solitonic regimes for pulse propagation that corresponds to dissipation solitons. In this limit, solitons are formed due to some additional optical pumping. Quantum properties of such solitons and the fragility of their quantum states against decoherence and dissipation effects, which seem very important, especially for quantum optical information memory devices, can be optimized by using non-classical states for a pumping field, cf. [27].

Appendix: Estimation of tunneling coefficients for atomic system

Here, we discuss properties of parameters (11), (12) for the cavity-QED array containing two-level atoms as a qubit system. To be more specific, we consider ultracold two-level rubidium atoms with resonance frequency $\omega_{12} / 2\pi = 382\mathrm{THz}$ that corresponds to mean weighted rubidium *D*-lines. To get a variational estimate for the tunneling coefficients mentioned above, we assume that the Wannier wave functions for atomic and photonic parts localized at the *j*th cavity may be approached by (cf. [28]):

$$\varphi_{j,n}\left(\vec{r}\right) = C_j e^{\frac{-(x-x_n)^2}{2\sigma_{x,j}^2}} e^{\frac{-\left(y^2+z^2\right)}{2\sigma_j^2}}, \qquad \xi_n\left(\vec{r}\right) = C_\xi e^{\frac{-(x-x_n)^2}{2\xi_x^2}} e^{\frac{-\left(y^2+z^2\right)}{2\xi^2}}, \tag{A.1}$$

where $C_j = \left(\pi^{3/2}\sigma_{x,j}\sigma_j^2\right)^{-1/2}$ $(j = 1, 2)$, $C_\xi = \left(\pi^{3/2}\xi_x\xi^2\right)^{-1/2}$ are relevant normalization constants. Taking into account the realistic values of variational parameters $\sigma_{x,j}$, σ_j and ξ_x, ξ, which are widths of atomic and photonic wave functions, respectively, we assume that:

$$\sigma_{x,j} \ll \sigma_j, \quad \xi_x \ll \xi. \tag{A.2}$$

Here, we also propose some trapping of the atoms in the cavity. In the simplest case, we can choose harmonic trapping potentials $V_{\mathrm{exp}} = V_{\mathrm{opt}} + V_{\mathrm{m}}$ with components:

$$V_{\mathrm{m}} = \frac{M_{\mathrm{at}}}{2}\left(\omega_{\mathrm{mag},x}^2 x^2 + \omega_{\mathrm{mag},\perp}^2\left(y^2+z^2\right)\right), \quad V_{\mathrm{opt}} = sE_{\mathrm{R}}\sin^2\left(kx\right) \approx \frac{M_{\mathrm{at}}}{2}\omega_x^2\left(x-x_n\right)^2, \tag{A.3}$$

where $E_{\mathrm{R}} = \hbar^2k^2/2M_{\mathrm{at}}$ is recoil energy, $s = V_0/E_{\mathrm{R}}$ is a dimensionless parameter which denotes the lattice depth. We take a cylindrically symmetric trap potential with characteristic axial and radial frequencies $\omega_{\mathrm{mag},x}$ and $\omega_{\mathrm{mag},\perp}$ respectively. We suppose that the minima of the 1D periodic potential (A.3) are located at the centers $x_n = nd$ of nth cavity, i. e. $\omega_x = \left(2sE_{\mathrm{R}}k^2/M_{\mathrm{at}}\right)^{1/2}$. For the typical values of trapping frequencies $\omega_{\mathrm{mag},x}$ and ω_x, it is possible to obtain $\omega_x \gg \omega_{\mathrm{mag},x}$, cf, [28]. After substituting (A.1), for (11), (12) and taking into account (A.2), for the atomic tunneling rate β we obtain:

$$\beta = -\frac{\hbar}{4M_{\mathrm{at}}\sigma_x^2}e^{\frac{-d^2}{4\sigma_x^2}}\left(1-\frac{d^2}{2\sigma_x^2}\right) - \frac{M_{\mathrm{at}}\omega_x^2}{4\hbar}e^{\frac{-d^2}{4\sigma_x^2}}\left(\sigma_x^2+\frac{d^2}{2}\right). \tag{A.4}$$

In the experimental situation the second term in (A.4) is essentially smaller than the first one. Thus, we can assume that $\beta \approx -\frac{\hbar}{4M_{\rm at}\sigma_x^2} e^{\frac{-d^2}{4\sigma_x^2}} \left(1 - \frac{d^2}{2\sigma_x^2}\right)$. The atomic tunneling rate β is positive if the cavity effective size is $d > \sqrt{2}\sigma_x \approx 1.414\sigma_x$. The latest one ($\sigma_x$) is typically few hundred nanometers in real experiments [18].

A calculation of the photon tunneling rate α between the cavities can be given in the same way. In particular, we obtain:

$$\alpha = -\frac{\hbar}{4M_{\rm ph}\xi_x^2} e^{-\frac{d^2}{4\xi_x^2}} \left(1 - \frac{d^2}{2\xi_x^2}\right). \tag{A.5}$$

Since $M_{\rm at} \gg M_{\rm ph}$ the relation $|\alpha| \gg |\beta|$ is fulfilled for the relevant tunneling rates and we can assume that $\Omega_{\rm T} \simeq \alpha C^2$ in Eq. (21).

Acknowledgements

This work was supported by RFBR Grants No. 14-02-31443, and No. 14-02-97503 and by the Russian Ministry of Education and Science state task 2014/13. A. P. Alodjants acknowledges support from “Dynasty” Foundation.

References

[1] C. Simon, M. Afzelius, J. Appel, et al. Quantum memories. *Eur. Phys. J. D*, **58**, P. 1–22 (2010).
[2] N. S. Ginsberg, S. R. Garner and L. V. Hau. Coherent control of optical information with matter wave dynamics. *Nature*, **445**, P. 623–626 (2007).
[3] A. I. Lvovsky, B. C. Sanders and W. Tittel. Optical quantum memory. *Nature Phot.*, **3**, P. 706–714 (2009).
[4] K. Hammerer, A. S. Sorensen, E. S. Polzik. Quantum interface between light and atomic ensembles. *Rev. Mod. Phys.*, **82**, P. 1041–1093 (2010).
[5] M. Fleischhauer and M. D. Lukin. Quantum memory for photons: Dark-state polaritons. *Phys. Rev. A*, **65**, P. 022314 (2002).
[6] A. P. Alodjants, S. M. Arakelian, and A. Yu. Leksin. Storage of quantum optical information based on the intracavity polaritons under the BoseEinstein Condensation conditions. *Laser Physics*, **17**, P. 1432–1440 (2007).
[7] A. Kitaev. Fault-tolerant quantum computation by anyons. *Ann. Phys.*, **303**, P. 2–30 (2003); ibid D. Jaksch, P. Zoller. The cold atom Hubbard toolbox. **315**, P. 52–79 (2005).
[8] L. Jiang, G. K. Brennen, A. V. Gorshkov, et al. Anyonic interferometry and protected memories in atomic spin lattices. *Nature Phys.*, **4**, P. 482–488 (2008); A. J. Daley, J. Ye, and P. Zoller. State-dependent lattices for quantum computing with alkaline-earth-metal atoms. *Eur. Phys. J. D*, **65**, P. 207–217 (2011).
[9] A. Tomadin and R. Fazio. Many-body phenomena in QED-cavity arrays. *J. Opt. Soc. Am. B*, **27**, P. A130–A136 (2010); M. J. Hartmann, F. G. S. L. Brandao, and M. B. Plenio. Effective Spin Systems in Coupled Microcavities. *Phys. Rev. Lett.*, **99**, P. 160501 (2007).
[10] S.-C. Lei and R.-K. Lee. Quantum phase transitions of light in the Dicke-Bose-Hubbard model. *Phys. Rev. A*, **77**, P. 033827 (2008).
[11] D. G. Angelakis, M. F. Santos, and S. Bose. Photon-blockade-induced Mott transitions and XY spin models in coupled cavity arrays. *Phys. Rev. A*, **76**, P. 031805(R) (2007).
[12] C. Kittel, *Introduction to Solid State Physics*, 7th ed., Wiley, New York, 673 p. (1996).
[13] H. Deng, G. Weihs, D. Snoke, et al. Polariton lasing vs. photon lasing in a semiconductor microcavity. *PNAS*, **100**, P. 15318–15323 (2003).
[14] A. Amo, S. Pigeon, D. Sanvitto, et al. Polariton Superfluids Reveal Quantum Hydrodynamic Solitons. *Science*, **332**, P. 1167–1170 (2011).
[15] B. Nelsen, R. Balili, D. W. Snoke, et al. Lasing and Polariton Condensation: Two Distinct Transitions in GaAs Microcavities with Stress Traps. *J. Appl. Phys.*, **105**, P. 122414 (2009).
[16] M. Sich, D. N. Krizhanovskii, M. S. Skolnick, et al. Observation of bright polariton solitons in a semiconductor microcavity. *Nat. Photon.*, **6**, P. 50–55 (2012).

[17] A. Trombettoni and A. Smerzi. Discrete Solitons and Breathers with Dilute Bose-Einstein Condensates. *Phys. Rev. Lett.*, **86**, P. 2353–2356 (2001).

[18] J.-J. Wang, A.-X. Zhang, K.-Zh. Zhang, J. Ma, and J.-K. Xue. Two-component Bose-Einstein condensates in D-dimensional optical lattices. *Phys. Rev. A*, **81**, P. 033607 (2010); A.-X. Zhang and J.-K. Xue. Coherent matter waves of a dipolar condensate in two-dimensional optical lattices. *Phys. Rev. A*, **82**, P. 013606 (2010).

[19] A. P. Alodjants, I. O. Barinov, and S. M. Arakelian. Strongly localized polaritons in an array of trapped two-level atoms interacting with a light field. *J. Phys. B*, **43**, P. 095502 (2010); E. S. Sedov, A. P. Alodjants, S. M. Arakelian, Y. Y. Lin, and R.-K. Lee. Nonlinear properties and stabilities of polaritonic crystals beyond the low-excitation-density limit. *Phys. Rev. A*, **84**, P. 013813 (2011).

[20] I-H. Chen, Y. Y. Lin, Y.-C. Lai, et al. Solitons in cavity-QED arrays containing interacting qubits. *Phys. Rev. A*, **86**, P. 023829 (2012).

[21] M. Notomi, E. Kuramochi, and T. Tanabe. Large-scale arrays of ultrahigh-Q coupled nanocavities. *Nature Phot.*, **2**, P. 741–747 (2008); K. Hennessy, A. Badolato, M. Winger, et al. Quantum nature of a strongly coupled single quantum dotcavity system. *Nature*, **445**, P. 896–899 (2007).

[22] Q. J. Wanga, C. Yan, N. Yu, et al. Whispering-gallery mode resonators for highly unidirectional laser action. *PNAS*, **107**, P. 22407–22412 (2010).

[23] F. A. Zwanenburg, A. S. Dzurak, A. Morello, et al. Silicon quantum electronics. *Rev. Mod. Phys.*, **85**, P. 961–1019 (2012).

[24] A. Szameit, Th. Pertsch, S. Nolte, A. Tünnermann, and F. Lederer. Long-range interaction in waveguide lattices. *Phys. Rev. A*, **77**, P. 043804 (2008).

[25] N. Cody Jones, R. Van Meter, A. G. Fowler, et al. Layered Architecture for Quantum Computing. *Phys. Rev. X*, **2**, P. 031007 (2012).

[26] C.-H. Su, A. D. Greentree, and L. C. L. Hollenberg. Towards a picosecond transform-limited nitrogen-vacancy based single photon source. *Opt. Express*, **16**, P. 6240–6250 (2008); S. Castelletto, J. P. Harrison, L. Marseglia, et al. Diamond-based structures to collect and guide light. *New J. of Phys.*, **13**, P. 025020 (2011).

[27] A. Dantan, J. Cvilinski, M. Pinard and Ph. Grangier. Dynamics of a pulsed continuous-variable quantum memory. *Phys. Rev. A*, **73**, P. 032338 (2006).

[28] A. Trombettoni, A. Smerzi, and P. Sodano. Observable signature of the Berezinskii-Kosterlitz-Thouless transition in a planar lattice of Bose-Einstein condensates. *New J. of Phys.*, **7**, P. 57 (2005).

NANOSYSTEMS: PHYSICS, CHEMISTRY, MATHEMATICS, 2014, 5 (2), P. 249–257

PLASMON POLARITONS EXCITATION AT RAPIDLY GENERATED PLASMA INTERFACE

A. V. Vozianova

ITMO University, Kronverkskiy 49, 197101, St. Petersburg, Russia

vozianova@gmail.com

PACS 51.50.+v, 42.25.Bs, 41.20.Jb

In this paper we studied the possibility of the appearance of surface plasmon polaritons at the plasma/dielectric interface with rapidly generated plasma in the right half- space, when the field is generated by a plane source, was studied. The source was located parallel to the interface, and at an angle to it. It was shown that the frequency-converted wave outgoing from plasma boundary corresponds to the plasmon polariton in the case when the initial field is generated by the plane source located at the angle α to the plasma boundary for the following condition $\varepsilon_1 \sin^2(\alpha) - \varepsilon - \frac{{w_e}^2}{w^2} > 0$.

Keywords: plasmon polariton, integral equations, plasma, electromagnetic field, non-stationary phenomena, Riemann's surface.

1. Introduction

Recent advances in nano-fabrication enable one to carry numerous nano-photonic experiments including subwavelength metal structures fabrication. In turn,this flurry of activity has, reawakened interest in theoretical research of surface plasmon polaritons, despite the fact that the fundamental properties of surface plasmon polaritons have been known for nearly five decades [1, 2]. By definition, surface plasmons are the quanta of surface-charge-density oscillations, but the same terminology is commonly used for collective oscillations in the electron density at the surface of metal. The surface charge oscillations are naturally coupled to electromagnetic waves, which explains their designation as polaritons [3]. Plasmon polaritons are used in near-field microscopy, optical imaging systems with nanometer resolution, hybrid photonic-plasmonic devices and metamaterials with negative refractive index, environment sensing, surface plasmon sensors for the analysis of biological bonds, etc. Surface plasmon polaritons are electromagnetic waves propagating at the interface between two different media. Surface plasmons have been utilized almost exclusively at optical frequencies because it needs the lossless negative permittivity medium to excite them, which is typical for metal at these frequencies. The negative permittivity of metals is provided by plasma which has a large electron density. Conversely, plasma is a medium which can easily change its own parameters, among which is its electron density, and the plasma can simply be generated in the initial dielectric medium [2]. Therefore, it is of intense interest to investigate the interaction of electromagnetic waves with the non-stationary plasma surface whose density varies over time and its permittivity becomes negative. The initial time of the non-stationary beginning becomes an important factor. The introduction of this initial time moment allows to distinguish the "switching on" of field and the beginning of non-stationarity.

The radiation of the plane source in a homogeneous stationary medium is well known, but in the case of an inhomogeneous layered medium, it is more complicated. If the medium is non-stationary, the radiation of the plane source takes on a less trivial form.

In papers [4,5], the novel mechanism of frequency upshifting of p-polarized electromagnetic wave, which is obliquely incident one on a thin plasma layer with slowly growing electron density, was presented. In this paper the transformation of external field radiation of the plane source from rapidly generated plasma was considered.

2. The radiation of the plane source (initial field is parallel to the plasma boundary)

We consider the medium with dielectric permittivity ε, where the electromagnetic field is radiated by a plane source $\mathbf{j} = \mathbf{q}\delta(x-a)e^{i\omega t}$, where $\mathbf{j}$ is a current describing extrinsic source, $\mathbf{q}$ is the vector directed along a source. The plane source is parallel to the plane YOZ, see Fig. 1

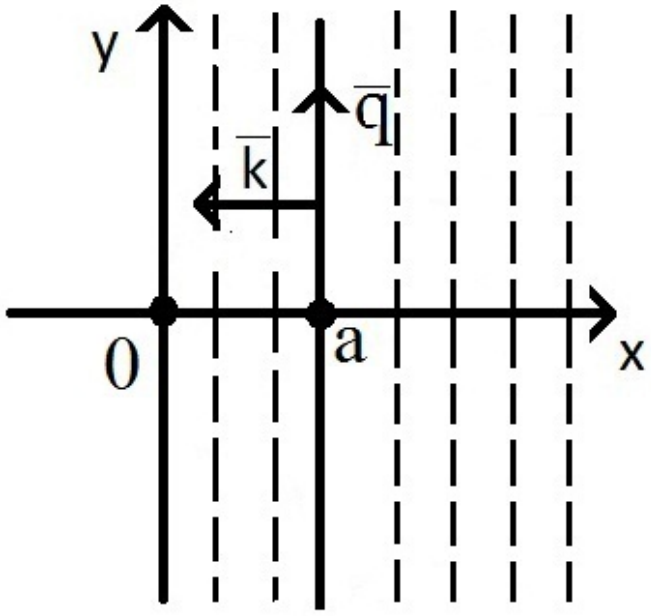

Fig. 1. The plane source is parallel to the plasma boundary and it is located at a distance a from the interface in plasma half-space, where $\mathbf{q}$ is the vector directed along a source, $\mathbf{k}$ is the wave vector. The rapidly generated plasma in the right half-space is designed the vertical dashed lines.

At zero moment of time the half-space $x > 0$ is ionized and the plasma appears in this half-space. The plasma permittivity is given by the known expression $\overline{\varepsilon}(\omega_e, \omega) = \varepsilon_1 - \frac{{\omega_e}^2}{\omega^2}$, where ε_1 describes the dispersionless part of the new medium in the half-space $x > 0$ after the zero moment, ω_e is the plasma frequency [3].The initial field of source radiation is a plane wave propagating perpendicularly to the plane of the source. By using the Green's function G [6] let's find the initial field of the source, which is given by $\mathbf{j} = \mathbf{q}\delta(x-a)e^{i\omega t}$:

$$\mathbf{E_0} = G \cdot \frac{\partial \mathbf{j}}{\partial t} = -\frac{\partial G}{\partial t} \cdot \mathbf{j} = -\frac{v}{4\pi}\hat{D}\mathbf{q}\int_{-\infty}^{\infty} dt' \int_{-\infty}^{\infty} d\mathbf{r}' \frac{\theta(t - t' - \frac{|\mathbf{r}-\mathbf{r}'|}{v})}{|\ \mathbf{r} - \mathbf{r}'\ |}\delta(x'-a)e^{i\omega t'} =$$

$$= -\frac{v}{2\pi}\hat{D}\mathbf{q}e^{i\omega t - i\frac{\omega}{v}|x-a|}\left((\mathbf{e_1}, \mathbf{q})\,\mathbf{e_1} - \mathbf{q}\right) = \frac{v}{2\pi}\mathbf{q}e^{i\omega t - i\frac{\omega}{v}|x-a|}, \quad (1)$$

where differential operator $\hat{D} = \left(\bigtriangledown \bigtriangledown - \frac{1}{v^2} \frac{\partial^2}{\partial t^2} \right)$, and vectors $\mathbf{q} = (0, q, 0)\, \mathbf{e_1} = (1, 0, 0)$.

Let's consider how the electromagnetic field changes after plasma formation. It is convenient to find the solution to this problem using the integral equations method in time domain [6,7]. It follows that the problem's solution in the half-space $x < 0$ (external field) can be represented by two terms:

$$\mathbf{E} = \mathbf{E_0} + \hat{N} * \mathbf{E_0}. \tag{2}$$

Here, $\mathbf{E_0}$ is the field of source and the second term is given by the operator $\hat{N} * \mathbf{E_0} = \int_0^\infty \left\langle \mathbf{x} \mid \hat{N} \mid \mathbf{x}' \right\rangle \mathbf{E_0}(\mathbf{x}') d\mathbf{x}'$. The symbol (*) designates the convolution,

$$(a * b)(\mathbf{x}) = \int_{-\infty}^{\infty} dt' \int_{\infty} d\mathbf{r}' a(\mathbf{x} - \mathbf{x}') b(\mathbf{x}')$$

and $\mathbf{x} = (t, \mathbf{r})$ is a 4D spatial-time vector. Integration is performed over the whole 4D space $-\infty < t' < \infty$, $-\infty < x', y', z' < \infty$. The term in the convolution is determined by the extrinsic current. The transition to the impulse representation (Fourier-Laplace representation)in a rectangular system of coordinates is performed by virtue of transformation functions:

$$< \mathbf{x} || \mathbf{p} >= \delta_{ij} e^{pt + i\mathbf{kr}},\ < \mathbf{p} || \mathbf{x} >= \delta_{ij} e^{-pt - i\mathbf{kr}},$$

where $\mathbf{p} = (p, \mathbf{k})$, p is a complex variable of the Laplace transformation, $\mathbf{k}$ is a real variable of the 3D Fourier transformation.

The kernel of external resolvent operator $\hat{N}$ (reflection operator) in the coordinate representation has the form:

$$\left\langle \mathbf{x} \mid \hat{N} \mid \mathbf{x}' \right\rangle = \theta(-x) \frac{{v_1}^2 - v^2}{v^2 v_1} \int d\mathbf{p}_\perp \frac{1}{2\varphi_1} \{ v_1 v u_m P + p^2 u_e I_\perp \} e^{p(t-t') + \frac{\varphi}{v} x - \frac{\varphi_1}{v_1} x' + i\mathbf{k}_\perp (\mathbf{r}_\perp - \mathbf{r}'_\perp)} \theta(x'), \tag{3}$$

where the vector $\mathbf{r}_\perp = (y, z)$ is located in the plane $x = 0$, and $v = \frac{c}{\sqrt{\varepsilon\mu}}$, $v_1 = \frac{c}{\sqrt{\varepsilon_1 \mu_1}}$ are wave-phase velocities.

In this formula, block matrices are defined as follows:

$$P = \begin{pmatrix} -{k_\perp}^2 & -i\frac{\varphi}{v}\mathbf{k}_\perp \\ -i\frac{\varphi}{v}{\mathbf{k}_\perp}^* & \hat{k}_\perp \end{pmatrix}, I_\perp = \begin{pmatrix} 0 & 0 & 0 \\ 0 & 1 & 0 \\ 0 & 0 & 1 \end{pmatrix}, {\mathbf{k}_\perp}^* = \begin{pmatrix} k_2 \\ k_3 \end{pmatrix}, \hat{k}_\perp = \begin{pmatrix} {k_2}^2 & k_2 k_3 \\ k_3 k_2 & {k_3}^2 \end{pmatrix},$$

$\mathbf{k}_\perp = \begin{pmatrix} k_2 & k_3 \end{pmatrix}$ and ${k_\perp}^2 = {k_2}^2 + {k_3}^2$. The coefficients

$$u_m = \frac{2v_1\varphi}{v\varphi + v_1\varphi_1}, u_e = \frac{2v_1\varphi}{v\varphi_1 + v_1\varphi}$$

are similar to the Fresnel's formulas for parallel and perpendicular polarizations and

$$\varphi = \sqrt{p^2 + v^2 {k_\perp}^2}, \varphi_1 = \sqrt{p^2 + {v_1}^2 {k_\perp}^2}, v_1 = \frac{cp}{\sqrt{\varepsilon_1 p^2 + {\omega_e}^2}}.$$

Here $\mathbf{p}_\perp = (p, \mathbf{k}_\perp)$ - Fourier - Laplace transformation variables. Thus, substituting the expression for the initial field of source (1) and the reflection operator (3) in equation (2), we obtain:

$$\langle \mathbf{x} \mid \mathbf{E} \rangle = \langle \mathbf{x} \mid \mathbf{E_0} \rangle + \left\langle \mathbf{x} \mid \hat{N} \mid \mathbf{x}' \right\rangle * \langle \mathbf{x}' \mid \mathbf{E_0} \rangle = \frac{v}{2\pi} \mathbf{q} e^{i\omega t - i\frac{\omega}{v}|x-a|} +$$
$$+ \frac{v}{2\pi}\theta(-x) \int_0^\infty dt' \int_{-\infty}^\infty d\mathbf{r}' \int d\mathbf{p}_\perp \frac{{v_1}^2 - v^2}{v^2 v_1} \frac{1}{2\varphi_1} \{v_1 v u_m P + p^2 u_e I_\perp\} \mathbf{q} \cdot$$
$$\cdot e^{p(t-t') + \frac{\varphi}{v}x - \frac{\varphi_1}{v_1}x' + i\mathbf{k}_\perp(\mathbf{r}_\perp - \mathbf{r}'_\perp)} \theta(x') e^{i\omega t' - i\frac{\omega}{v}|x'-a|} \quad (4)$$

First, we calculate integrals over the spatial and temporal coordinates, and then over Fourier-Laplace variables. The integration over the variable x' gives the following expression:

$$\int_0^\infty e^{-i\frac{\omega}{v}|x'-a| - \psi_1 x'} dx' = \int_0^a e^{-i\frac{\omega}{v}(a-x') - \psi_1 x'} dx' + \int_a^\infty e^{-i\frac{\omega}{v}(x'-a) - \psi_1 x'} dx' = \frac{e^{-\psi_1 a} - e^{-ika}}{ik - \psi_1} + \frac{e^{-\psi_1 a}}{ik + \psi_1}$$

where $\psi_1 = \frac{\varphi_1}{v_1} = \frac{1}{c}\sqrt{\varepsilon_1 p^2 + {\omega_e}^2 + c^2 {k_\perp}^2})$ for the condition $Re(\psi_1) > 0$. Later, this condition will be taken into account for the calculation of residuals in the integral over the variable p (see the expression (4)).

After integration over the spatial and Fourier transform variables, the second term in (4) takes the following form:

$$\int_{\gamma - i\infty}^{\gamma + i\infty} \frac{e^{p(t+\frac{x}{v})}}{p - i\omega} p \frac{v_1 - v}{v^2} \left(\frac{e^{-\frac{a}{c}\sqrt{\varepsilon_1 p^2 + {\omega_e}^2}} - e^{-ika}}{ik - \frac{1}{c}\sqrt{\varepsilon_1 p^2 + {\omega_e}^2}} + \frac{e^{-\frac{a}{c}\sqrt{\varepsilon_1 p^2 + {\omega_e}^2}}}{ik + \frac{1}{c}\sqrt{\varepsilon_1 p^2 + {\omega_e}^2}} \right) \frac{dp}{2\pi i} =$$
$$= \int_{\gamma - i\infty}^{\gamma + i\infty} \frac{e^{p(t+\frac{x}{v})}}{p - i\omega} \frac{cp}{v^2} \left(\frac{cp}{z(p)} - v \right) \left(\frac{e^{-\frac{a}{c}z(p)} - e^{-ika}}{ikc - z(p)} + \frac{e^{-\frac{a}{c}z(p)}}{ikc + z(p)} \right) \frac{dp}{2\pi i},$$

where $z(p) = \sqrt{\varepsilon_1 p^2 + {\omega_e}^2}$. Note, that the obtained integral will be equal to zero at $t + \frac{x}{v} < 0$, since, in this case, the integration contour can be closed by circle of infinite radius in the right half-plane, where the integrand has no singularities. To calculate the integral in the interval $t + \frac{x}{v} < 0$ the integration contour can be closed only to the left of the line γ: 1) The equation $p - i\omega = 0$, gives a simple pole, $p_1 = i\omega$, which isn't contained in the integration path, as it is located on the section between the branch points. 2) The expressions $ikc - z(p) = 0$, and $ikc + z(p) = 0$ give two poles $p_{2,3} = \pm\frac{i}{\sqrt{\varepsilon_1}}\sqrt{\varepsilon\omega^2 + {\omega_e}^2} = \pm i\omega_2$. There is a removable singularity (a finite limit of the integrand) at the point $p_2 = i\omega_2$, therefore the residual at this point is equal to zero. The selection of root sign in the equations $ikc \pm z(p) = 0$ follows from the condition $Re\psi_1 > 0$.

The integration contour contains all the singularities of the integrand. To obtain the unambiguous integrand, let's choose a Riemann's surface. The integrand is a double-valued function, because $z(p) = \sqrt{\varepsilon_1 p^2 + {\omega_e}^2}$ has two branch points $\pm i\frac{\omega_e}{\sqrt{\varepsilon_1}}$. It is necessary to allocate the branch of $z(p)$, for which the condition $Re\psi_1 = Re\sqrt{z^2 + \varepsilon\omega^2} > 0$ is performed. To uniquely identify $z(p)$, it can be considered the complex plane $p = \xi + i\eta$, as a two-sheeted surface. The surface sheets are joined along the banks of the cuts.

On each sheet, $z(p)$ is uniquely defined as a function of the variable p. To satisfy the condition $Re\sqrt{z^2 + \varepsilon\omega^2} > 0$, it should be glued the sheets of the Riemann's surface along the curve given by the equation $Re\sqrt{z^2 + \varepsilon\omega^2} = 0$. This condition determines the required branch line. We make the cuts in the complex plane p. For this, we write ${\psi_1}^2$ as follows:

$${\psi_1}^2 = \varepsilon_1 p^2 + {\omega_e}^2 + \varepsilon\omega^2 = \varepsilon_1(\xi^2 - \eta^2 + 2i\xi\eta) + {\omega_e}^2 + \varepsilon\omega^2.$$

The correct procedure of the choice of the cut can be made for a dissipative dielectric. To carry out this procedure, we assume that the medium has small losses (μ) $\omega_e = \overline{\omega}_e + i\mu$ and $\overline{\omega}_e \gg \mu$, $\mu \to 0$ corresponds to the limiting case of a lossless medium. Thus we have ${\psi_1}^2 = [\varepsilon_1\xi^2 - \varepsilon_1\eta^2 + {\overline{\omega}_e}^2 - \mu^2 + \varepsilon\omega^2] + 2i\,[\varepsilon_1\xi\eta + \overline{\omega}_e\mu]$. We make cuts for the ψ_1 in the complex plane p, so that the condition $Re\psi_1 > 0$ is fulfilled on one of the sheets of the Riemann's surface, and $Re\psi_1 < 0$ on the second sheet.

To satisfy these two conditions, it should be glued the sheets of the Riemann's surface along the curve given by the equation $Re\psi_1 = 0$. This equation determines the required branch line. We then plot the real and imaginary parts ${\psi_1}^2$ which depend on ξ and η, as shown in Fig. 2.

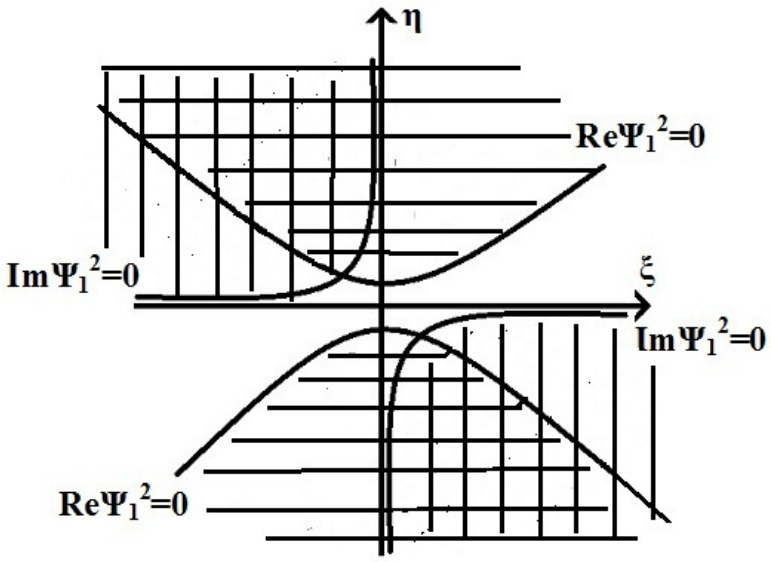

Fig. 2. The regions of the complex plane p ($Imp = \xi$, $Rep = \eta$) are bounded by the curves ${Re\psi_1}^2 = 0$ and ${Im\psi_1}^2 = 0$, for which the real and imaginary parts of ψ_1^2 maintain their signs: ${Re\psi_1}^2 < 0$ in the horizontal shading region, ${Im\psi_1}^2 < 0$ in the vertical shading region.

Then, we divide the plane p into regions by curves on which either ${Re\psi_1}^2 = \varepsilon_1\xi^2 - \varepsilon_1\eta^2 + {\overline{\omega}_e}^2 - \mu^2 + \varepsilon\omega^2 = 0$, or ${Im\psi_1}^2 = 2(\varepsilon_1\xi\eta + \overline{\omega}_e\mu)$. Thus, we obtained two regions formed by hyperboles intersection:

$$\frac{\varepsilon_1(\xi^2 - \eta^2)}{{\overline{\omega}_e}^2 - \mu^2 + \varepsilon\omega^2} = -1 \; and \; \xi = -\frac{\overline{\omega}_e\mu}{\varepsilon_1\eta},$$

for which the conditions ${Re\psi_1}^2 > 0$, ${Im\psi_1}^2 > 0$. To satisfy the condition ${Re\psi_1}^2 > 0$, it is necessary that the inequality $\mid {Arg\psi_1}^2 \mid < \pi$ is performed on the upper sheet of the Riemann surface. Hence, that it needs to choose a cut along the line defined by the equation ${Arg\psi_1}^2 = \pi$ or equivalent equations $Re\psi_1 < 0$ and ${Im\psi_1}^2 = 0$. As a result, the position of the cuts (shown in Fig. 3 by bold lines) was uniquely determined.

Finally, we obtain the following expression for the modified external field:

$$\langle \mathbf{x} \mid \mathbf{E} \rangle = \frac{v}{2\pi}\mathbf{q}e^{i\omega t - i\frac{\omega}{v}|x-a|} + \frac{v}{2\pi}\theta(-x)\mathbf{q}\frac{\varepsilon}{\varepsilon_1}\frac{\Omega - 1}{\Omega + 1}e^{-i\omega_2\left(t + \frac{x}{v}\right) + ika}\theta\left(t + \frac{x}{v}\right), \qquad (5)$$

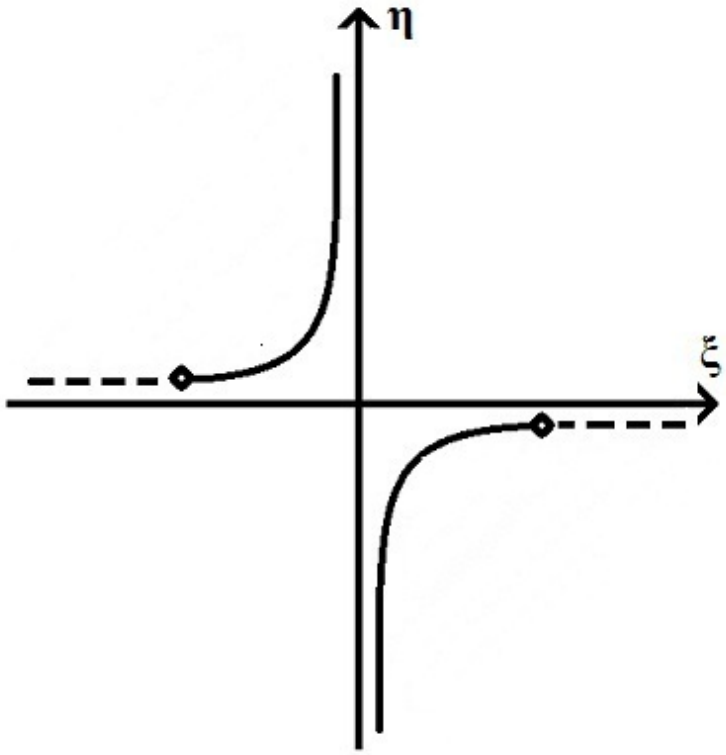

Fig. 3. Cuts in the complex plane p ($Imp = \xi$, $Rep = \eta$), satisfying the condition $Re\psi_1 > 0$ are designated the solid curves.

where $\Omega = \sqrt{\varepsilon + \frac{{\omega_e}^2}{\omega^2}}$. Consequently after the medium parameters jump in the left half-space, the moving boundary $x = -vt$ appears, which moves with the velocity v from the media interface. In the product band, $-vt < x < 0$, the wave propagates with a new frequency, $\omega_2 = \frac{1}{\sqrt{\varepsilon_1}}\sqrt{\varepsilon\omega^2 + {\omega_e}^2}$ and a new wave number, $\frac{\omega_2}{v}$. The external transformed field consists of monochromatic waves with frequencies ω and $\omega_2 = \frac{1}{\sqrt{\varepsilon_1}}\sqrt{\varepsilon\omega^2 + {\omega_e}^2}$. The waves with both frequencies propagate without attenuation in the external half-space.

3. The radiation of the plane source (the initial field is at the angle α to the plasma boundary)

Next, we consider the case when the electromagnetic field is radiated by a plane source $\mathbf{j} = \mathbf{q}\delta(s)e^{i\omega t}$, which is located at an angle α to the YOZ plane boundary, see Fig. 4. Similarly to the above case, at the zero moment of time, the half-space $x > 0$ is ionized and the plasma appears in this half-space. The plasma permittivity is given by the known expression $\overline{\varepsilon}(\omega_e, \omega) = \varepsilon_1 - \frac{{\omega_e}^2}{\omega^2}$, where ε_1 describes the dispersionless part of the new medium in the half-space $x > 0$ after the zero moment, ω_e is the plasma frequency.

Let's consider the transformation of the source field outside the plasma ($x < 0$), after the plasma's appearance. As with the previous case, we find the solution to this problem using the integral equations method in time domain [6, 7]. From this, it follows that the solution in the half-space $x < 0$ (external field) can be represented by formula (2). The problem is to study the field due to the sudden formation of plasma. At first, by using Green's function G [4], we find the initial field of source radiation before the plasma formation in the case when the plane source is located at an angle to the media interface,

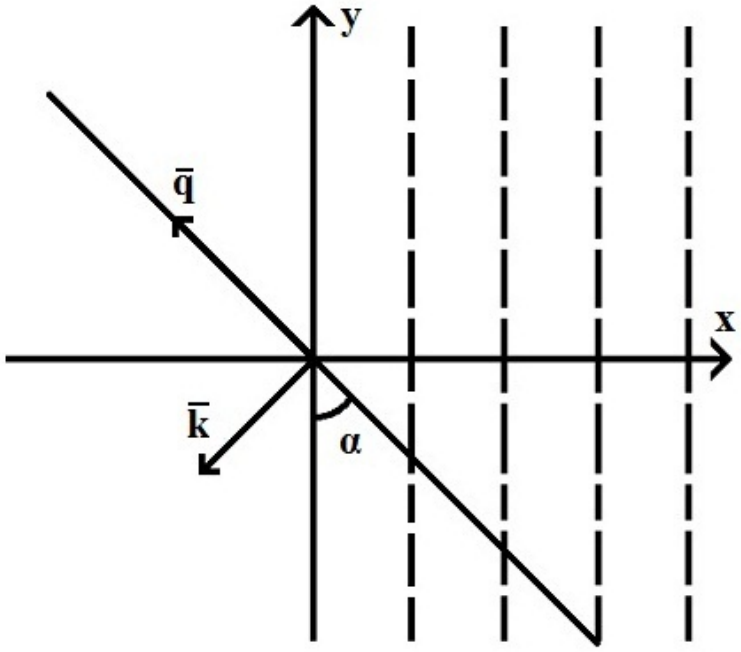

Fig. 4. The plane source is at an angle α to the plasma boundary. The rapidly generated plasma in the right half-space is designed the vertical dashed lines. Here $\mathbf{q}$ is the vector directed along a source, $\mathbf{k}$ is the wave vector.

$$\mathbf{E_0} = G \cdot \frac{\partial \mathbf{j}}{\partial t} = -\frac{\partial G}{\partial t} \cdot \mathbf{j} = -\frac{v^2}{4\pi} \hat{D}\mathbf{q} \int_{-\infty}^{\infty} dt' \int_{-\infty}^{\infty} d\mathbf{r}' \frac{\theta(t - t' - \frac{|\mathbf{r}-\mathbf{r}'|}{v})}{\mid \mathbf{r} - \mathbf{r}' \mid} \delta(s) e^{i\omega t'}. \tag{6}$$

It is more convenient to calculate the radiation of current for the case when the source is located parallel to the interface at the surface $x = 0$, when $a = 0$. That is, setting $\delta(s) = \delta(x)$, it is simple to make the rotation of the coordinate system by a corresponding angle. Then, according to this formula (1), the initial field will have the form:

$$\mathbf{E_0} = \frac{v}{2} \mathbf{q} e^{i\omega t - i\frac{\omega}{v}|x|}, \tag{7}$$

where $\mathbf{q} = (0, q_2, 0)$. Let's make rotation of the coordinate system by the angle α. The coordinate transformation with angle rotation has the following form:

$$x = x' \cos\alpha + y' \sin\alpha,\ y = -x' \sin\alpha + y' \cos\alpha.$$

Substituting the initial field, we obtain:

$$\mathbf{E_0} = \frac{v}{2} \mathbf{q} e^{i\omega t - i\frac{\omega}{v}|x' \cos\alpha + y' \sin\alpha|}, \tag{8}$$

where $\mathbf{q} = (q_2 \sin\alpha, q_2 \cos\alpha, 0)$.
Thus, it can immediately set the initial field of a plane wave which propagates at an angle to the plasma plane. Thereby, substituting the expression for the initial field of source (8) and the reflection operator (3) in (2), we obtain:

$$\langle \mathbf{x} \mid \mathbf{E} \rangle = \langle \mathbf{x} \mid \mathbf{E_0} \rangle + \left\langle \mathbf{x} \mid \hat{N} \mid \mathbf{x}' \right\rangle * \langle \mathbf{x}' \mid \mathbf{E_0} \rangle = \frac{v}{2}\mathbf{q}e^{i\omega t - i\frac{\omega}{v}|x\cos\alpha + y\sin\alpha|} + \\ + \frac{v}{2}\theta(-x)\int_0^\infty dt' \int_{-\infty}^{\infty} d\mathbf{r}' \int d\mathbf{p}_\perp \frac{1}{2\varphi_1}\frac{{v_1}^2 - v^2}{v^2 v_1}\{v_1 v u_m P + \\ + p^2 u_e I_\perp\} e^{p(t-t') + \frac{\varphi}{v}x - \frac{\varphi_1}{v_1}x' + i\mathbf{k}_\perp(\mathbf{r}_\perp - \mathbf{r}'_\perp)}\theta(x')e^{i\omega t' - i\frac{\omega}{v}|x'\cos\alpha + y'\sin\alpha|} \quad (9)$$

The integration over the spatial variables and Fourier transform variable is similar to the previous case for the condition $Re\sqrt{\varepsilon_1 p^2 + {\omega_e}^2 + c^2{k_2}^2} > 0$. Then, the second term in (9) takes the following form:

$$\int_{-\infty}^{\infty}\frac{dk_2}{2\pi}\int_{\gamma-i\infty}^{\gamma+i\infty}\frac{dp}{2\pi i}\left((\varepsilon-\varepsilon_1)p^2 - {\omega_e}^2\right)\frac{c^2\varphi}{\psi}\mathbf{F}(p,k_2)\frac{2i\omega\sin\alpha e^{p(t+\frac{\phi}{v}x + ik_2 y)}}{(p-i\omega)(\psi - ick_2\cot\alpha)\left({k_2}^2 - \frac{\omega^2}{v^2}\sin^2\alpha\right)} \quad (10)$$

The function $\mathbf{F}(p,k_2) = \left(\frac{\mathbf{A_1}}{\varphi(\varepsilon_1 p^2 + {\omega_e}^2) + \sqrt{\varepsilon}p^2\psi} + \frac{\mathbf{A_2}}{c(v\psi + c\varphi)}\right)$ has no singular points on the integration variables.

Here, vectors $\mathbf{A_1} = \begin{pmatrix} k_2 q_2\left(k_2\sin(\alpha) - i\frac{\cos\alpha}{c}\psi\right) \\ k_2 q_2\left(i\frac{\sin\alpha}{v} + k_2\cos\alpha\right) \\ 0 \end{pmatrix}$, $\mathbf{A_2} = \begin{pmatrix} 0 \\ q_2\cos\alpha \\ 0 \end{pmatrix}$, and

$$\varphi = \sqrt{p^2 + v^2{k_2}^2},\ \psi = \sqrt{\epsilon_1 p^2 + {\omega_e}^2 + c^2{k_2}^2}.$$

Let's consider the peculiarities of the integrand in (10) over the variable p. The integrand has two simple poles at the points $p_1 = i\omega$, $p_2 = \frac{i}{\sqrt{\varepsilon_1}}\sqrt{{\omega_e}^2 + \frac{c^2{k_2}^2}{\sin^2\alpha}}$. After calculation of the integral over the variable p in the expression (6) we obtain:

$$\int_{\infty}^{\infty}\frac{dk_2}{2\pi}\mathbf{F}(p_1,k_2)e^{i\omega t + x\sqrt{{k_2}^2 - k^2}}\frac{e^{ik_2 y}}{{k_2}^2 - k^2\sin^2\alpha} + \\ + \int_{\infty}^{\infty}\frac{dk_2}{2\pi}\mathbf{F}(p_2,k_2)e^{\frac{it}{\sqrt{\varepsilon_1}}\sqrt{{\omega_e}^2 + \frac{v^2{k_2}^2\varepsilon}{\sin^2\alpha}} + \frac{x}{v\sqrt{\epsilon_1}}\sqrt{-{\omega_e}^2 + v^2{k_2}^2\left(\varepsilon_1 - \frac{\varepsilon}{\sin^2\alpha}\right)}}\frac{e^{ik_2 y}}{{k_2}^2 - k^2\sin^2\alpha} \quad (11)$$

Finally, we obtain the following expression for the modified external field:

$$\langle \mathbf{x} \mid \mathbf{E} \rangle = \frac{v}{2}\mathbf{q}e^{i\omega t - i\frac{\omega}{v}|x'\cos\alpha + y'\sin\alpha|} + \\ + \frac{v}{2}\theta(-x)\hat{\mathbf{F}}(p_1, -k\sin\alpha)e^{i\left(\omega t - ikx\sqrt{\sin^2\alpha - 1} - ky\sin\alpha\right)}\theta\left(t + \frac{x}{v}\right) + \\ + \frac{v}{2}\theta(-x)\hat{\mathbf{F}}(p_2, -k\sin\alpha)e^{i\left(\omega_1 t - i\frac{kx}{\sqrt{\varepsilon_1}}M(\alpha) - k\,y\,\sin\alpha\right)}\theta\left(t + \frac{x}{v}\right), \quad (12)$$

where frequency $\omega_1 = \frac{\omega}{\sqrt{\varepsilon_1}}\sqrt{\varepsilon + \frac{{\omega_e}^2}{\omega^2}}$ and $M(\alpha) = \sqrt{\varepsilon_1\sin^2\alpha - \varepsilon - \frac{{w_e}^2}{w^2}}$.

Plasmon polaritons can occur only if the projection of the wave vector on the propagation direction of the plasmon polaritons is real and the normal component of the

wave vector is purely imaginary in both media [3]. In the second term (12), the projection of the wave vector on the propagation direction (x axis) is always imaginary, but in the third term this projection of the wave vector (then $x < 0$) can be real if $M^2(\alpha) = \varepsilon_1 \sin^2 \alpha - \varepsilon - \frac{w_e{}^2}{w^2} > 0$. From this, one can make the conclusion that the transformed wave frequency can decay with distance from the plasma boundary when $M^2(\alpha) = \varepsilon_1 \sin^2 \alpha - \varepsilon - \frac{w_e{}^2}{w^2} > 0$ and $\sin \alpha > 0$.

When the value of $M^2(\alpha)$ is positive, it is possible for the plasmon polariton to appear. One can see that the surface plasmon polaritons appearance is impossible for some media for any angle, and it's possible for the second ones at the certain angle α, and for the third ones for any value of the angle.

4. Conclusions

In this paper, the transformation of plane source radiation after medium ionization was studied by using Volterra's integral equations method. The plane source was considered at an angle to the interface with a sharp ionization of the medium, i.e. when the problem becomes non-stationary. It was shown that the wave with transformed frequency outgoing from plasma is similar to the plasmon polariton in the case when the initial field is generated by the plane source located at the angle α to the plasma boundary for the following condition $\varepsilon_1 \sin^2 \alpha - \varepsilon - \frac{w_e{}^2}{w^2} > 0$. The dependence of the wave vector projection on the source angle for various media was discussed and analyzed.

Acknowledgements

This work was financially supported by Government of Russian Federation, Grant 074-U01.

References

[1] Mansuripur M., Zakharian A. R., Moloney J. V. Surface Plasmon Polaritons on Metallic Surface. *OPN.*, **18**(4), P. 44–49 (2007).

[2] Raether H. *Surface plasmons on smooth and rough surfaces and on gratigs*. Berlin, Springer (2013), 136 p.

[3] Novotny L., Hecht B. *Principles of nanooptics*. Cambridge, Cambridge University Press (2012), 578 p.

[4] Bakunov M. I., Gildenburg V. B., Nshida Y., Yugami N. Frequency self-upshifting of microwave radiation via resonantexcitation of plasma oscillations in a thin layer of ma time-varying plasma. *Physics of plasmas*, **8**(6), P. 2987–2991 (2001).

[5] Bakunov M. I., Bystrov A. M., Gildenburg V. B. Frequency self-upshifting of intence microwave radiation producing ionization in a thin gaseous layer. *Physics of plasmas*, **9**(6), P. 2803–2811 (2002).

[6] Nerukh A. G., Scherbatko I. V., Marciniak M. *Electromagnetics of Modulated Media with Applications to Photonics*. Warsaw, National Institute of Telecommunications Publishing House (2001), 267 p.

[7] Nerukh A. G., Khizhnyak N. A. *Modern problems in nonstationary macroscopic electrodynamics* (in Russian). Kharkov, "Test-Radio" Publishing House, Kharkov (1991), 257 p.

NANOSYSTEMS: PHYSICS, CHEMISTRY, MATHEMATICS, 2014, 5 (2), P. 258–293

THERMODYNAMIC INSTABILITY OF COMPOUND AND FORMATION OF NANOSIZED PARTICLES NEARBY THE CRITICAL POINT OF PHASE GENERATING MEDIA

A. N. Kovalenko, N. V Kalinin

Ioffe Physical Technical Institute of RAS, Saint Petersburg, Russia

ras-kan@mail.ru

PACS 64.60.Fr, 64.60.Ht, 65.20.+w

An analysis is presented for the possibility of metal dispersion, driven by the development of thermodynamic instabilities of its physical state in the vicinity of the critical point in an electrical explosion of conductors (EEC). A new geometrical configuration of conductors, arranged in a thin-walled cylindrical shell on a rigid dielectric cylinder with axially guided, internal return current is proposed. This constrains the part played by instabilities of non-thermodynamic origin and provides the required power density distributed uniformly in the conductor. For metals of the aluminum and copper type, the rates of heating have been estimated, which ensure homogeneous vaporization as the key factor governing the mechanism of liquid metal dispersion during the development of thermodynamic instabilities in the material. Directions in which magnetohydrodynamic (MHD) modeling of high-power electrical discharge in EEC should be pursued in the development of optimal regimes for energy injection into the conductor are outlined. Processes governing condensation of explosion products in an aqueous environment in the case of the particles being electrically charged and involved in chemical interaction with supercritical fluids have been analyzed. The method of synthesis proposed will eventually permit the production of oxide nanoparticles which differ from nanoparticles of the same oxides synthesized in electrical discharge in air and other oxygen-containing gas media, as well as in hydrothermal synthesis employed in its classical methodological implementation.

Keywords: thermodynamic instability, critical state, phase explosion, metal dispersion, nanoparticles, oxides, electrical explosion of conductors, supercritical fluid.

Contents

1. Introduction

Nanoparticles can form by condensation or deposition from a matrix medium in close to thermodynamically equilibrium conditions, or by dispersion from consolidated material in nonequilibrium thermodynamic processes driven by the application of powerful external energy fluxes. The latter method increases substantially the energy contained in the nanoparticles, which can account for their unique catalytic, sorption and other properties, as well as for the observed threshold phenomena. Of particular interest for the field of dispersion are extremely fast (close to non-equilibrium) thermodynamic processes involved in high rate phase transitions of a material through the sequence of "solid—liquid—gaseous" aggregate states, including transitions through the critical point. It is the only extremum in the equilibrium curves of the phase diagram, which belong simultaneously to the liquid and vapor. Approaching it is accompanied by substantial growth of density fluctuations in microvolumes of the material compared with the regions where metastable states exist, adjoining the curves describing equilibrium of two phases. For strong enough energy influxes, density fluctuations can become self-organized to the extent where material can lose its thermodynamic stability, being replaced by assembly of dissipative microstructures. They can serve as pre-nuclei for the subsequent formation of dispersed particles during the disruption of the starting consolidated materials, and transfer a part of the energy to the material of the environmental medium. This predetermines the possibility, in principle, of producing particles of an extremely small size, down to a few nanometers, to be compared with the results obtained by application of other well-known mechanisms of dispersion, e.g., mechanical or thermal action, for example, impact crushing of a solid, its melting and breakup of the liquid into drops, vaporization and subsequent deposition from the vapor phase.

Because the size and number of particles depend on the rates of influx and dissipation of energy in the material under dispersion and its environment, methods providing high power of the incoming energy fluxes become particularly important. They should be adequate to the conditions required and the mechanisms involved in development of thermodynamic instability in the material in question, as well as to its characteristic dissipation channels and of the material of the environment. Under laboratory conditions, such means for energy input into a material can be provided by high-power pulsed lasers, charged particle beams and heavy-current electrical discharges. Heavy current electrical discharges offer certain advantages in their potential to generate the desired energy density of particle beams in volumes larger than those obtainable with lasers and corpuscular beams. Electric discharges providing a high density for the discharge current, $J > 10^6$ A/cm^2, in a material with metallic electrical conductivity in the initial state have acquired the name "electric explosion". A number of researchers, including the authors of the present paper, believe the

electric explosion of conductors to rank among the most energy-efficient methods for the preparation of nanosized powders of metals and of their chemical compounds.

Although electrical explosions have been known for more than 200 years [1,2], systematic studies of them have been undertaken already for about fifty years at various research centers [3-54]. Despite this study, a number of points still remain to be clarified. First, this bears on the conditions and mechanisms driving the instabilities of material, which culminate in destruction of the conductor and formation of nanoparticles, allowing for the interrelation among the processes that are at work both in the metal proper and in its environment [34,45,46,52,55,56].

The present work offers an analysis of these points, drawing from the available literature data, as well as from our original research.

2. Conditions and the characteristic pattern of development of instabilities of material in an electric explosion of conductors

In the case of the comparatively slow Joule heating of a metal by electric current, the most significant factors involved in destruction of a wire conductor in the process of variation of its physical state are the forces of surface tension and waist and convective MHD instabilities [4-7,9,15,17,18,20,21,30,32,33,41]. One more possible factor is development of the barocapillary instability [57], which arises in the intense vaporization of material from the surface of the molten metal and turbulization of vapor jets, destroying this surface. Such an instability can be amplified by the positive feedback coupling of the vapor recoil reaction with the depth of piercing of the molten metal surface. Each of these processes has its characteristic time scale. Indeed, the time of action of capillary forces is on the order of $t_k = (\rho_{liq} r^3/\sigma)^{0.5}$, $t_c = \mu_0 r^2/\rho_e$, and the time taken up by development of magnetodynamic instabilities of the neck type $-t_m = (2\pi\rho_{liq} r^2/H_0^2)^{0.5}$ [9,15,33,58,59]. Here, ρ_{liq} – is the density of the metal in its liquid state, r is the conductor radius, σ is the surface tension coefficient, μ_0 is the magnetic constant, ρ_e is the electrical resistivity of the metal, $H_0 = I/r$, and I is the current through the conductor. When a metal is subjected to heating by current for a time longer than the characteristic relaxation time of a material required to reach the equilibrium thermodynamic state (estimates [60-62] yield for it $1-10$ ns far from the critical point), the processes involved in the development of the above instabilities may be considered as being in thermodynamic equilibrium. The effect of each of them becomes manifest when their characteristic metal heating time scales become equal. It can be estimated in terms of the specific current action integral $t = h/I^2$, where $h = \int_0^t I^2 dt$ – is the integral value of the current action required to heat the metal within the range over which the corresponding process extends. The relative part played by each of these instabilities can vary depending on the particular effect of the environment (rarefied gas or a dense liquid) in which the electric explosion of the conductor takes place. The actual size of the particles formed may depend on the uniformity of the heating (current density), level of the energy input, radius of the wire, its initial microstructure, characteristics of the environment (density, chemical activity, electric strength). On the whole, however, the characteristic size of the "drops" formed during the development of such instabilities turns out to be on the order of the diameter of the wire to be exploded (a few hundred to thousands of nanometers) [5,31–33,50,63,64].

Particles of substantially smaller dimensions (down to a few nanometers) can be prepared by noticeably increasing the power input into the conductor. Under the conditions providing fast enough Joule heating in a time shorter than the characteristic time required for relaxation to the equilibrium thermodynamic state, the part played by the

above instabilities becomes of secondary importance, with the mechanism of dispersion stemming from violation of thermodynamic stability of the state of material becoming dominant [35,38,44,49,55,56,65,66]. In the course of intense heating, the temperature of the molten metal can rise above the boiling point at a given pressure above its surface, culminating in a transition of the system into the region of metastable biphasic state, with a fast approach to the line of the highest possible overheating (spinodal) with increasing heating rate (Fig. 1).

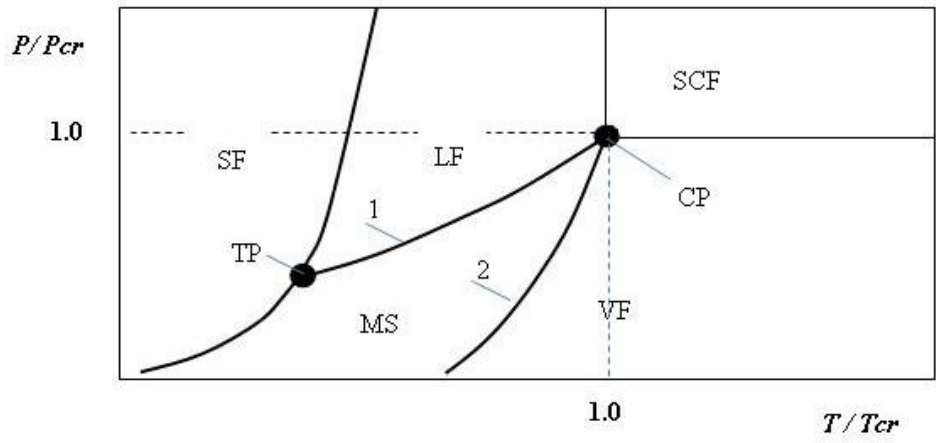

FIG. 1. Typical diagram of the phase state of a material: 1 - binodal (liquid-vapor phase equilibrium curve, or saturation line), 2 - spinodal (curve of maximum possible liquid phase overheating). Notes: SF - Solid Phase; LF - Liquid Phase; VF - Vapor (Gas) Phase; MS - Metastable Sate; SCF - Supercritical Fluid; TP - Triple Point; CP - Critical Point

This brings about reduction of the time the system spends in this state, uncertainty in the thermodynamic parameters and, as a consequence, tendency to spontaneous relaxation to the equilibrium boundary (bimodal) of the metastable region through "explosive" boiling-up of the metal paralleled by a sharp growth in homogeneous vapor bubble formation. The mechanisms governing such a relaxation depend on the properties of the material and conditions of its heating, of which the most important is the specific power of energy input into the material and the pressure (density) of the environmental medium. For instance, for water and organic liquids the critical size of a vapor nucleus whose probability of further growth is higher than that of collapse, just as the magnitude of the Gibbs free energy needed for its formation, in overheating turns out to be lower than those on the bimodal under conditions of thermodynamic equilibrium. Indeed, with overheating increased by only 1 K, the average time taken by a critical nucleus to form may drop by three to four orders of magnitude, with the rate of growth of a vapor bubble of above critical size exhibiting fast rise [35,38,50]. Intense nucleation involving the formation of multiple vapor bubbles in a heavily overheated liquid close to the spinodal initiates "explosive" boiling-up ("phase explosion"), with eventual breakup into a mixture of vapor and droplets [35,38,56].

The possibility of using phase explosion of a liquid metal for preparation of metal powders has been a subject of intense discussion in literature, but without a comprehensive analysis of the dependence of the particle size obtained for particular energy input conditions and the properties of the environmental medium. Significantly, Joule heating of a metal conductor by current gives rise to a number of specific effects, complicating the mechanism of explosive boiling. This comes from the need to consider the effect exerted by the electric and magnetic fields on the work of critical vapor nucleus formation and the frequency (rate)

of homogeneous formation of vapor bubble nuclei. Another specific feature of Joule heating of conductors was found to be the nonuniformity of the pressure field inside the metal initiated by the appearance of the magnetic component, a factor which complicates markedly the overall calculation of the process [33,48,56].

3. A possible scenario of development of a phase explosion in a liquid metal and of formation of nanosized particles of a new phase

As previously mentioned, in the case of comparatively slow Joule heating with a not too close approach to the critical temperature of the metal, $T < (0.8-0.9)T_c$, and in the case of a low-density, chemically-inert environmental medium (rarefied gas), the electric explosion of a conductor may acquire the pattern of explosive decomposition of a molten and boiling-up metal, as a result of development of the above-mentioned instabilities of non-thermodynamic origin. The characteristic size of the "droplets" formed in such an explosion turns out to be $10^2 - 10^3$ nm, depending on the working conditions, i.e. on the order of the diameter of the wire to be exploded.

To reduce the size of dispersed particles, one has to constrain the part played by the non-thermodynamic mechanisms involved in destruction of the metal in the course of varying the physical state of the exploding conductor, so as to ensure its transition to the region of the heaviest possible nonequilibrium metastable state with the maximum possible overheating and fast approach to the critical point through "explosive" boiling-up initiating homogenous vapor formation. This is favored by the magnetic field generated in the liquid metal by the current flowing through it. Its action increases the work and the time passing in waiting for the appearance of a vapor nucleus, which initiates the process of homogeneous vapor formation. After this, the size of the critical nucleus for the liquid (molten) metal will be larger, for the same overheating, than that for water and organic liquids. As a result, spontaneous nucleus formation of vapor bubbles in liquid metals is not reached even under intense overheatings, so that metals can be heated very close to the spinodal and, hence, to the critical temperature, before phase explosion occurs. Besides, a liquid metal may contain centers of heterogeneous boiling-up, which raise significantly the specific metal heating power needed to reach the limiting metastable state defined by the spinodal. It should be stressed, that as a result of the stabilizing action of electric current on the thermodynamic state of a liquid metal, spontaneous relaxation of metastable states may start for most metals only at temperatures $T \geqslant (0.8 - 0.9)T_c$, where T_c is the critical temperature of the metal.

It is the possibility of overheating a liquid metal close to the critical temperature at an adequately high energy input into the conductor that the proposed scenario of new phase formation rests. In these conditions, in the vicinity of the critical point fluctuations of the parameters of state of the material, primarily of the density and entropy, grow substantially, just as the radius of their interaction (correlation), by switching from the exponential law of decrease far from the critical point to the inverse proportionality law close to it [67]. The relation between the probability of system parameter fluctuations and the magnitude of the fluctuations themselves can be defined by the Einstein relation $W \sim \exp[-(\Delta T \Delta S + \Delta\mu\Delta N)/2T]$, which is essentially an outgrowth of the Boltzmann principle relating the probability of an arbitrary state of a system to its total entropy S_Π in the form $W \sim \exp(\Delta S_\Pi)$. Increase of density gradients (density fluctuations) in small volumes of an overheated liquid culminates in the loss of thermodynamic stability of the material and nucleation of vapor bubbles by fluctuations. The material takes on an opalescent, finely dispersed, light-scattering structure, which may be considered as a "gas of liquid drops" [68-70]. The characteristic size of these "drops" (correlation radius) increases, and the magnitude of

the density gradients needed for fluctuation-based nucleation decreases as one approaches the critical point. Estimates based on various models of the critical state [50] suggest that for metals, the size of these drops can vary from a few to several tens of nanometers. At temperatures $T \approx (0.8 - 0.9)T_c$, defining the boundary at which the critical point still can be reached, the size of the liquid drops is on the order of $10 - 30$ nm. Realization of the corresponding conditions rests on the possibility of providing a high enough specific heating power combined with limiting metal expansion. Estimates of the heating power Q_V required to reach this goal yield $Q_V \geqslant 1$ TW/cm^3. Such power densities can provide electric current $J > 10^8$ A/cm^2 flowing through a wire with diameter $d = 0.1$ mm. These estimates were made under the assumption that metal expansion is limited by the local sound velocity and occurs along the bimodal, with the interpolation equation of the Van-der-Waals type used as the equation of state [33]. Additional possibilities for attaining optimum conditions of nanosized dispersion are considered below.

4. Specific features in modeling of local characteristics of phase-forming processes and media

The rich variety of the complex physical and physico-chemical processes involved in an electric explosion of metal conductors in a chemically active water medium accounts for the surprisingly large number of local characteristics required for evaluation of the conditions optimal for dispersion of a metal, a situation stemming from the development of thermodynamic instabilities showing up in its physical state in the vicinity of the critical point. This program is of considerable scientific and practical significance for the field of present-day nanotechnologies, including various aspects of development of adequate physical models, primarily in description of the variations in the state of material within a broad range of parameters, from the triple point to formation of supercritical fluids. The specific choice of the equations of state and of the dependence of transfer coefficients for dissipative processes on density and temperature contribute in more than one respect to the calculated characteristics of heating and subsequent explosion of an electric conductor.

4.1. Statistical modeling of critical phenomena in the close environment of the critical point. Scaling invariance

For more than 350 years, studies aimed at establishing the interrelation among the parameters of state of material, thousands of other publications on this subject have appeared, with many of them having gained recognition [71]. These studies were initiated by R. Boyle (1662) in experiments with gases. Kanjr (1822), M. Faraday (1823) and T. Endres (1869) extended them to the region of phase transitions, "liquid–vapor" critical point and supercritical fluids. Van der Waals (1873) provided theoretical generalization to the available experimental data with the use of an extended phenomenological model of an ideal gas by Clapeyron (1834), in which molecular attraction and repulsion at close distances were included in a simple form. Further systematization was provided by the physical theory of L. D. Landau (1964) in terms of the mean field approximation approach, which described supercritical phase transitions of the system as well [72]. No convenient equation for a physically adequate description of the state of matter over a sizable range of parameters, including phase transitions and the critical point, has, however, been derived, either in the context of the classical mean-field approach or with inclusion of fluctuation-induced deviations through introduction of small corrections into the expansion of free energy $F(T, V)$ in powers of $\nu = (V - V_c)/V_c$ and $\tau = \tau = (|\mathrm{T} - \mathrm{T_c}|)/\mathrm{T_c}$ relative to the critical point [73].

The idea of "scaling invariance (scaling)" involving the characterization of thermodynamic potentials through generalized homogeneous functions of nonintegral (fractional) order with respect to their fields was found to be universal enough for solution of this problem. It was advanced in the 1960's, almost simultaneously, by Bakengem, Widm adanff Patashansky [74-79] for explanation of the experimentally revealed anomalous growth of large-scale fluctuations, as well as of the singular pattern of behavior followed by a number of thermodynamic functions close to the critical point. This idea was subsequently extended to cover description of attendant kinetic phenomena. Among them are the increase of the time of thermal relaxation, slowing down of the mutual diffusion of substances close to the critical points of the solutions, variation of the pattern of Brownian motion, decrease of the coefficients of thermal diffusivity close to the critical point of a pure liquid, the anomalously high absorption of ultrasonic vibrations, critical opalescence and others [68-70]. Significantly, kinetic phenomena occurring close to the critical point are assigned to the existence of a characteristic frequency, expressed in terms of the equilibrium radius of interaction of large-scale fluctuations (correlation radius).

The similarity of the critical phenomena observed in objects of different nature suggests the possibility of unified description of the interrelation of certain physical quantities (order parameters) in the vicinity of the critical point with a simple power function, for instance, reduced temperature $\tau = (T - T_c)/T_c$, or some other reduced parameters of similar type, $P_j(\tau) = B_j \tau^{-\delta j}$, where B_j is a numerical coefficient, and δ_j is the critical index of the quantity P_j. In particular, the asymptotic behavior of the susceptibility $\partial\rho/\partial P$, density $\Delta\rho = \rho - \rho_c$, correlation radius r_c (a quantity approaching in its sense the average size of a fluctuation), specific entropy S, heat capacity C_V, C_P and other parameters in pure liquids, concentration y and chemical potential μ in solutions are expressed with unified temperature dependences:

$$\partial\rho/\partial P, \partial x/\partial\mu \sim \tau^{-\gamma}; \quad C_V, C_P \sim \tau^{-\alpha}; \quad (\rho - \rho_c), (S - S_c), (x - x_c) \sim \tau^{-\beta}; \quad r_c \sim \tau^{-\nu}.$$

Numerical values of the critical indices α, β, γ, ν can be obtained only from experiment or from microscopic theory. The values of these indices, derived from experiment, or from analytical and numerical solutions for lattice-type models (Ising, Heisenberg, Berlin-Katz etc.) turn out to be invariant (equal or very close in magnitude) for phase transitions of different physical nature and are defined only by the dimension d of the space under consideration and the corresponding type of symmetry (order parameter) [68,80,81]. This versatility can be assigned to the cooperative nature of the critical phenomena, which stems from the properties of the totality of particles rather than from individual properties of each particle. The spatial scale of their interaction exceeds by far the average separation between particles. The size of density fluctuations grows as one approaches the critical point, up to hundreds and even thousands of Angstroms, to become comparable to light wavelength, and their amplitude reaching, by order of magnitude, the average values of the density proper. This accounts for the opalescent, finely dispersed structure of material observed in the critical region, which, as already mentioned, is usually referred to as "a gas of liquid droplets".

The free Helmholtz energy can in this case be presented as consisting of components of the regular part and a non-analytical uniform function of its arguments. In such a system, it contains a term proportional to the number N of the "gas droplets" formed $F = F_0 + kT_cN = F_0 + 3kT_cV/4\pi r_c^3$, where F_0 is the regular part of free energy F, which does not depend on the closeness to the critical point; V is the volume of the material, and $4\pi r_c^3$ is the volume of droplet in three-dimensional space. Invoking the power-law dependence of the correlation radius r_c on temperature in the form $r_c \sim \tau^{-\nu}$, one can readily obtain an expression for

the singular part of heat capacity at constant volume $C_V \sim (\partial^2 F/\partial T^2)_V \sim \tau^{3\nu-2} \sim \tau^{-\alpha}$. Now this expression yields a relation connecting the critical indices of the heat capacity and correlation radius in three-dimensional space, $3\nu = 2 - \alpha$. One can then employ the standard similarity relations to establish the relation connecting the two remaining indices $\alpha + 2\beta + \gamma = 2$, $\alpha + \beta(1 + \delta) = 2$, $d\nu = 2 - \alpha$; we see that in the general case, the number of independent critical indices is always two. The numerical values of these indices, derived theoretically by L. Onsager and C. Wilson [82–86] for the plane and three-dimensional Ising lattice and supported by numerous measurements [68], are $\alpha = 0.11$, $\beta = 0.325$, and $\gamma = 2 - \alpha - 2\beta = 1.24$, respectively.

Idealized model concepts of the scaling theory suggest that far from the critical point fluctuations are statistically independent, so that random variations of state at a given point of the sample do not affect other parts of the system. Significantly, at the critical point, the radius of correlation (of fluctuation interaction) becomes theoretically infinitely large, enveloping all of the material [68,79,87–90]. In real systems, however, their susceptibility to external perturbations of various physical origins (gravitational and electric fields, surface forces and shear stresses, nonideal nature of samples and presence of boundaries etc.) also grows $\sim \tau^{\gamma}$, as one approaches the critical point, so that even small perturbations $\Delta E \ll kT$ will be able to distort the pattern of a phase transition by $3 - 4$ orders of magnitude [68]. This not only significantly complicates measurements in an experimental study, but can, at an infinite growth of susceptibility of the system to external influence, culminate in noticeable suppression of critical fluctuations by an external factor. This may result in restoration in the system of the mean-field "classical" behavior with the corresponding set of critical indices close to the critical point, with the area in the immediate vicinity of it becoming again a region of the Van der Waals type. An analysis of this possibility is offered in Ref. [91]. It is shown that in the general case, the pattern of universal behavior for systems near the critical point may include both a transition from the "mean-field" classical behavior to that of the Ising type, whose position is defined by the Ginzburg criterion [92], and the appearance in its nearest environment of a reverse transition from the renormgroup to "mean-field" classical behavior. At the same time, as follows from the data presented by the same author, the transition in the reverse direction expected to occur far from the critical point in pure liquids is not observed experimentally [93]. Now, our own experimental data provided a basis for an analysis of the universal relations connecting critical indices and amplitudes. Consideration is also given to the "pseudospinodal hypothesis" concerning the possible existence of a "pseudospinodal", i.e., of a line, all points of which would possess the properties of a critical line, i.e., a line, on which the isothermal and adiabatic compressibilities, isochoric and isobaric heat capacities diverged simultaneously. It is shown that this possibility is provided only at one and the only "critical" point, which lies simultaneously at the bimodal, spinodal and critical isotherm.

The transcritical state of matter can be employed as an initial approximation in describing its variations far from the critical point by introducing proper corrections to the asymptotic laws. In particular, in this way it becomes possible to describe the state of dense gases and liquids within a fairly large range of parameters, where, in contrast to solids and rarefied gases, straightforward calculation of thermodynamic quantities is impossible because of the uncertainties involved in particle interaction [68]. At the same time, despite numerous attempts undertaken in derivation of a scaling equation of state in physical variables which could be used to calculate the singular component of interest, these attempts have not thus far met with success. This possibility appeared with the use of a transition proposed by Josephson and Scoffield to a parametric form of equation in polar coordinates without direct

expression through physical variables [94,95]. This transition is graphically interpreted in Fig. 2 [68].

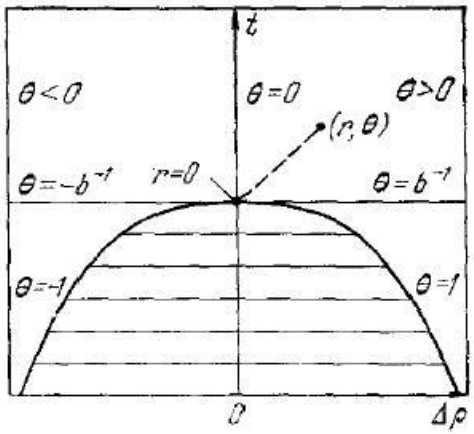

FIG. 2. Parametric presentation of the Sterling equation of state close to the critical point in polar coordinates

Its application turned out, however, to be inconvenient in approximation of experimental data and fairly difficult in the calculation of standard tables and matching with other equations of state, including those of the virial form, which adequately describe the behavior of various characteristics of material far from the critical point. Development of methods which could be employed in derivation of a unified scaling equation of state which would be free of the above shortcomings is still under way. Indeed, a nonparametric equation of state in the "density–temperature" physical variables has recently been obtained [96]:

$$F(\rho,T) = F_0(T) + RT_c f(\omega,t)\,|\Delta\rho|^{\delta+1}\,a_1(x) + RT\ln\rho + RT\omega\sum_{i=1}^{n_3}\sum_{j=0}^{j_3(i)} C_{ij}\tau_1^j(\Delta\rho)^i.$$

This equation satisfies the power laws of critical phenomena. It covers a broad range of parameters, including phase equilibrium lines (from the triple to the critical point), and metastable and single-phase regions, dense gas and liquids down to the solidification line in that number. Here, $\omega = \rho/\rho_c$ is the reduced density, δ is the critical index of the curve of the critical isotherm, $f(\omega,t) = \exp(-a\Delta\rho^2/\sqrt[5]{\omega})/T$ is the transition (crossover) function for a qualitatively correct description of the virial coefficients, $a(x)$ is a scaling function of the Helmholtz free energy in the form $a(x) = A_1(x+x_1)^{2-\alpha} + A_2(x+x_2)^{2-\alpha} + B_1(x+x_3)^{\gamma} + C$, whose parameters are calculated through the critical indices and the value of the scaling variable $x = \tau/|\Delta\rho|^{1/\beta}$ at the saturation line. As a measure of separation from the critical point, we can use here the isothermal compressibility $K_T = \rho^{-1}(\partial\rho/\partial p)_T$, assuming that it behaves similarly at the critical and non-critical isochores. The assumptions made here fit the phenomenological model of A. A. Migdal on the analyticity of the isoclinic line $H(m) = m + \varphi_3 m^3 + \varphi_5 m^5 + \ldots$, where $H = \Delta\mu[P_c V_c^2(\partial\rho/\partial\mu)]^{(\beta+\nu)/\nu}$, and $m = \Delta\rho[P_c V_c(\partial\rho/\partial\mu)]^{\beta/\nu}$ [97], as well as the hypothesis of J. Benedek on the functions $K_T(\rho,T)|_{\rho=\rho c} \sim K_T(\rho,T)|_{\rho\neq\rho c} \sim \tau^{-\gamma}$ following analogous behavior [98]. A comparison of the calculation results with data accumulated from a number of well-studied materials of technological significance, including cryogenic gases and liquids, as well as refrigerants of a variety of molecular structures (refrigerant R23, argon, perfluorpropane), suggests [96] that the scaling equation of state developed reproduces with a high accuracy the thermodynamic properties throughout the range of parameters specified above.

Because this approach has not yet enjoyed application in development of similar scaling equations of state for metals, the variations of their physical state in the course of a phase explosion are described by invoking semiempirical equations and models of transport coefficient calculations of various kinds. In the calculations presented below, we made use of wide range semi-empirical equations of state permitting description of the state of material in the condensed, gas, plasma and two-phase region of the phase diagram.

4.2. Phenomenological modeling of critical phenomena and thermodynamic stability of one- and two-phase systems in the mean-field approximation

If the linear dimensions of phases are large enough, one can neglect the curvature of their interface. In this case, thermodynamic equilibrium sets in when their temperatures, pressures and chemical potentials are equal [67,69]:

$$T' = T'' = T; \quad P' = P'' = P; \quad \mu'(T,P) = \mu''(T,P)$$

These equations define the interfaces for the regions of single-phase liquid and equilibrium two-phase (liquid–vapor) states of matter–the binodal.

For the Van der Waals type state equations, this system can be used to derive Maxwell's "equal areas" condition, which in the subcritical region of the diagram of state ($T < T_c$) is combined with the equation of state $P = P(T,\ \rho)$ to produce a system of equations for finding the equilibrium pressure $P_b(T)$ and densities of liquid $\rho_b'(T)$ and vapor $\rho_b''(T)$ at the binodal. Thermodynamic stability with respect to continuous variations of the parameters of state is defined here by the condition that the second variation of the internal energy of a thermodynamic system ε be a positive quantity. For this purpose it is necessary and sufficient that the following inequalities be met [67,99]:

$$D = \left(\frac{\partial^2\varepsilon}{\partial s^2}\right)\left(\frac{\partial^2\varepsilon}{\partial v^2}\right) - \left(\frac{\partial^2\varepsilon}{\partial s \partial v}\right) > 0,$$

$$\frac{\partial^2\varepsilon}{\partial s^2} = \left(\frac{\partial T}{\partial s}\right)_v = \frac{T}{C_p} > 0,$$

$$\frac{\partial^2\varepsilon}{\partial v^2} = -\left(\frac{\partial P}{\partial s}\right)_s > 0$$

Here, C_P is the specific heat at constant pressure, and s and v are the specific entropy and specific volume, respectively. These expressions can be readily employed to derive other useful relations for isodynamic derivatives as well:

$$\left(\frac{\partial P}{\partial v}\right)_T = -\frac{1}{\beta_T v} = D\left(\frac{\partial T}{\partial s}\right)^{-1},$$

where β_T is the coefficient of isothermal compressibility.

To sum up, for stable states:

$$\left(\frac{\partial T}{\partial s}\right)_p > 0; \quad \left(\frac{\partial P}{\partial v}\right)_T = -\left(\beta_T v\right)^{-1}.$$

The inequality $D < 0$ defines the unstable state region for the homogeneous phase, in which any perturbations grow until it transfers to the equilibrium two-phase state. The equation $D = 0$ identifies the boundary of the phase state parameters stable with respect to their continuous variations, i.e., spinodal. For instance, for the Van der Waals model the equation

for the spinodal in dimensionless variables reduced to the parameters of the critical point reads as:

$$4\,\theta\,\varphi^3 - 3\,\varphi^2 - 6\,\varphi - 1 = 0\,,$$

where $\theta = T/T_c$, $\pi = P/P_c$, $\varphi = \upsilon/\upsilon_c$ are dimensionless variables. Estimates can be conveniently obtained with the equation for spinodal derived in terms of the "hole" theory of liquids [100]:

$$\pi \cong 10\,\theta - 9$$

The coefficients of thermodynamic stability for the liquid phase at the spinodal pass through zero values:

$$\left(\frac{\partial P}{\partial \nu}\right)_T = 0, \quad \left(\frac{\partial \mu'}{\partial n}\right)_{(\nu,T)} = 0, \quad \left(\frac{\partial T}{\partial s}\right)_P = 0,$$

while the thermodynamic fluctuations related to them through the expressions:

$$\left(\frac{\partial P}{\partial v}\right)_T = -\frac{k\,T}{\langle \nu^2 \rangle}; \quad \left(\frac{\partial T}{\partial s}\right)_p = \frac{k\,T^3}{\langle \Delta h^2 \rangle},$$

grow sharply, a factor which may cause dispersion of the liquid.

In the supercritical region ($T > T_c$, $P > P_c$), the transition of material from the condensed to gaseous state takes place under continuous variation of its density within the temperature interval which corresponds to the region of thermodynamic hypostability of the state of material to development of fluctuations of its thermodynamic characteristics. The boundary of existence of a condensed phase in the supercritical region of the diagram of state (quasispinodal is the curve of supercritical liquid–vapor transitions) is defined by the points of extrema in the course of the thermodynamic stability coefficients of the condensed state [35,38,44,49,65,66]:

$$\left(\frac{\partial P}{\partial v}\right)_T < 0; \quad \left(\frac{\partial^2 P}{\partial v^2}\right)_T = 0; \quad \left(\frac{\partial \mu}{\partial n}\right)_{v,T} > 0; \quad \left(\frac{\partial^2 \mu}{\partial n^2}\right)_{v,T} = 0,$$

and is actually a continuation of the binodal into spinodals beyond the critical point. All branches of the binodal, spinodals and quasispinodal converge to the critical point. The coefficients of volumetric expansion and isothermal compressibility at the quasispinodal points pass through the final maxima. This opens the possibility of deriving the equation of quasispinodal from experimental data on the coefficients of volumetric expansion or isothermal compressibility in the supercritical region.

The spinodal–quasispinodal equation was calculated from available experimental data for mercury, whose physical properties were studied in considerable detail. These calculations resulted in the following equation:

$$\pi \cong 11.1\,\theta - 10.1$$

This equation draws upon the law of corresponding states and can apparently be extended to other metals as well. Thus, if one knows equations of state $P = P\,(T, \rho)$ and $\varepsilon = \varepsilon\,(T, \rho)$ or has experimental data on the physical characteristics of the material, it becomes possible to establish the boundary of thermodynamic stability of a material with the use of the above relation.

To disperse a material by subjecting it to thermodynamic instabilities, the heating conditions employed should provide the attainment of extreme metastable states, which in the subcritical region of the diagram of states, are defined by the spinodal, and in the supercritical region, by the quasispinodal. We analyze below the main factors which plague solution of this problem. In the conditions characteristic of "fast" EEW, when instabilities of

other than thermodynamic nature play a limited part, these factors are surface vaporization and heterogeneous boiling.

4.3. Vaporization and dispersion of metal under high-power pulsed heating with a high-density current

Formation of a vapor nucleus in a liquid being limited by inertia and nonequilibrium processes, vaporization starts on the free surface of the liquid. Because the vapor forming in the process allows stronger compression that the liquid, the local velocity of displacement of the interphase cannot exceed the sound velocity at the corresponding point of the binodal. The time taken by a rarefaction wave to propagate to the center of the volume occupied by the liquid and back may be considered as a characteristic "sonic" time scale.

4.3.1. Vaporization wave in metals. If the heating conditions of a liquid are such that the latent heat of evaporation enters the liquid in a time longer than the "sonic" time, the system is in the regime of quasi-steady state evaporation from the surface. In this regime, the temperature at the interphase can be assumed to be determined by external pressure and to remain constant. In the case when the latent heat of evaporation is injected into the liquid during the "sonic" time, and the number of centers of heterogeneous boiling ready to operate is not large enough, the process dominating the mechanism of vaporization will be evaporation from the surface, whose temperature will grow in the course of liquid overheating.

We are interested in more powerful regimes of liquid heating, in which the latent heat of vaporization is injected into the liquid phase in a time much shorter than the "sonic" time. In this case, the internal, not yet expanded regions of the liquid, will suffer overheating substantially above the temperature determined by the binodal at the corresponding local level of pressure. In these regions, conditions favoring the generation of homogeneous volume vaporization will become achievable. In the vicinity of vapor bubble formation, the liquid becomes strongly locally overheated, which initiates a still more intense growth of evaporation. This process may also become compounded by the formation of local electric arcs at the bubbles.

The "sonic" time can be estimated not from the real surface evaporation rate but rather from its maximum value, which is equal to the local sound velocity in the two-phase region at the binodal points [11-13,20,101]. Recalling that at the binodal the pressure $P_b(T)$ and density $\rho_b(T)$ of the liquid phase depend only on temperature, we obtain:

$$v_s = \sqrt{\left(\frac{\partial P}{\partial \rho}\right)_s} \cong \sqrt{\frac{T}{C_v\,\rho_b(T)}} \cdot \frac{dP_b}{dT}$$

In interpretation of the EEW experiments, this velocity was termed the velocity of "evaporation wave" in metals [11-13,20]. The dependences of the evaporation wave velocity calculated from this relation fit well enough the experimental results obtained in the initial region, but the discrepancy between the calculations and experiments was found to grow with increasing temperature. This does not come as a surprise, because the conditions in an overheated metal may become favorable for the onset of volume evaporation, a process developing with increasing overheating.

4.3.2. Volume boiling-up of a metal heated by a high-density current. Volume boiling-up of a liquid metal can be both heterogenic, i.e. develop on already available vaporization centers (structural inhomogeneities, charged particles and so on) and homogeneous, a process in which a water droplet nucleus is borne by thermodynamic density fluctuations.

In the regimes considered by us here, the necessary condition making possible spontaneous boiling-up of a liquid metal is metastability of its state, which can be reached by overheating the liquid above the temperature of its quasistationary boiling in the given ambient conditions. The appearance in the liquid of a "critical" vapor nucleus capable of growing as a center of volume vaporization is accompanied by overcoming a peculiar energy barrier. It can be correlated with the work spent in formation of this vapor nucleus in a given thermodynamic state of the liquid W_{cr}. This work accounts for the probability of spontaneous formation of a vapor nucleus in an overheated liquid and, eventually, for the frequency of homogeneous vaporization, i.e., the number of critical vapor nuclei per unit volume and per unit time [35,38,44,49,65,66]:

$$\frac{dN_{cr}}{dt} = B\left(T,P\right)\cdot\exp\left(-\frac{W_{cr}}{kT}\right)\cdot\exp\left(-\frac{\tau_p}{t}\right)$$

where τ_p is the relaxation time in establishment of steady-state regime of nucleus formation following instantaneous overheating of the liquid (estimates yield $\tau_p \leqslant 10$ns;) $B\left(T,P\right) \cong 10^{23}\mathrm{cm}^{-3}s^{-1}$ is a weakly temperature- and pressure-dependent function.

The work expended in formation of a viable vapor nucleus of volume υ_B of a metastable liquid is [35,38,44,48,49,56,65,66]:

$$W_{cr} = \alpha s + (P' - P'')v'' + W_B$$

where α is the surface tension coefficient; s is the surface area of the forming vapor nucleus; $P'P''$ are the pressures in the liquid and the vapor nucleus, and W_B is the work against the electromagnetic forces, with the dominant contribution to it coming from the work spent on the increase in the inductance of the system associated with formation in the liquid metal of a vapor void [48,56]:

$$W_B \cong \frac{\mu_0}{8\pi}\iint\left[J(r)J(r') - J_0(r)J_0(r')\right]\frac{dv'dv}{|r-r'|},$$

where J_0, J are the currents flowing through the conductor before and after formation of the vapor nucleus. The volume of the work spent in formation of the vapor void depends on its shape. This accounts for the possibility of generating critical nuclei of various shapes. The dimensions of the critical nucleus of a fixed shape correlates with the maximum value of $W_{cr,}$while the actual shape of the nucleus is derived from the condition of minimum W_{cr}.

Close to the binodal, the work expended in formation of a critical vapor nucleus of a critical shape in an overheated liquid can be estimated from the relation [20,32]:

$$W_{cr} \cong \frac{16}{3}\pi\frac{a^3(v'')^2}{\Lambda_{vap}\varepsilon_T^2} + \frac{\pi^3}{4}\mu_0\frac{a^3(v')^3}{\Lambda_{vap}^3\varepsilon_T^3}J_0^2\xi(l_B^2 + R_0^2)\ln\left(\frac{\varepsilon_T\Lambda_{vap}R_0}{2av''}\right)$$

Here, $a = 2\alpha/(P'' - P')$ is the nucleus radius; R_0 is the characteristic size of the conductor cross section; $l_B \cong 2\sqrt{\tau/\left(\mu_0\,\sigma\right)}$ is the distance the magnetic field has passed by diffusion during the time τ the nucleus took to form (estimates yield $\tau \approx 0.1{-}1\ ns$); $\varepsilon_T = \left(T - T_b\right)/T_b$ is the relative overheating of the liquid metal; $\Lambda_{vap}\left(T\right), T_b$ are the latent heat of evaporation and temperature at the binodal, and coefficient $\xi = 2(\sigma' - \sigma'')/(2\sigma' + \sigma'')$, where σ', σ'' are the values of electric conductivity of the liquid metal and of the vapor Significantly, as a rule, $R_0 \gg l_B \gg a$.

Thus, Joule heating of a metal by electric current is characterized by an increase in the work expended in the formation of a critical vapor nucleus and of the time one spends in waiting for its appearance, compared with the case of other than Joule heating of liquid metal, for instance, with laser or beam energy injection. For small overheatings, $\varepsilon_T \to 0$,

homogeneous creation of a viable nucleus is met with difficulties, $W_{cr} \to \infty$ Increasing the overheating brings about a sharp lowering of the activation barrier of W_{cr} and, hence, increase of the probability of homogeneous nucleus formation and of development of homogeneous boiling-up of the liquid metal. The lowest value of W_{cr} corresponds to the highest possible overheating of the condensed phase $\varepsilon_T = \varepsilon_T^{cr}$, which for the given outer conditions is determined by the temperature related to the spinodal, where the thermodynamic stability coefficients pass through zero values.

Estimates of the metal overheating needed for the onset of homogenous vaporization, $(dN/dt)_{cr} > 1\text{cm}^{-3}\text{s}^{-1}$, suggest that the frequency of spontaneous vapor generation grows strongly within a comparatively narrow temperature interval. For the first homogenous nucleus to appear, after which their number grows in an avalanche, the metal should be overheated close to the highest possible level, which corresponds to a very small environment of the critical point.

Reaching conditions favorable to homogeneous boiling-up of the liquid phase can be hindered by heterogeneous boiling developing on the already viable centers of vaporization, which starts at temperatures only slightly exceeding the temperature of quasi-stationary boiling. But if the specific power of heating of the liquid phase is high enough, it can be overheated if it contains artificial viable centers of boiling. This can be realized if we provide a specific energy input into the liquid which would exceed considerably the energy expended for heterogeneous boiling on the already available centers. This heating regime received the name "impact" regime. Its operating conditions are formulated by the relation [35,38]:

$$K = \frac{Q_v}{\Lambda_{vap}\varphi^{\frac{1}{k}}}\left(\frac{3}{4\pi}\frac{1}{\Omega_0}\frac{\rho'}{\rho''}\right)^{\frac{1}{3k}} \cdot \varepsilon_T^{\frac{1}{3k-1}} \gg 1.$$

Here, Q_v is the specific power of the "impact" energy input, Ω_0 is the given concentration of heterogeneous boiling centers, and ρ', ρ'' are the densities of the liquid and vapor, respectively. The growth of the heterogeneous nucleus is approximated by a power-law form $r\,(t) \cong \varphi\,(t)\,t^k$, $\langle\varphi\rangle = \frac{1}{\tau^k}\int\limits_0^\tau \varphi\,(t)\,kt^{k-1}dt$, where $\Delta\tau$ is the time taken by a heterogeneous vapor nucleus to grow, and $<\varphi>$ is the value of function $\varphi(t)$ averaged over the temperature interval $T_b \leqslant T \leqslant T_{cr}$. The condition of "impact" heating can be presented in a more compact way with the relation:

$$\frac{\tau''}{\Delta\tau}\varepsilon_T^{\frac{1}{3k}} \gg 1,$$

where $\Delta\tau = \frac{\Lambda_{vap}\varepsilon_T}{Q_v}$, $\tau'' = \frac{1}{\varphi^{\frac{1}{k}}}\left(\frac{3}{4\pi}\frac{1}{\Omega_0}\frac{\rho'}{\rho''}\right)^{\frac{1}{3k}}$ is the time needed for boiling out of all of the liquid present on the heterogeneous centers. The law by which the nucleus radius grows in this case can be adequately approximated in terms of the thermal approach, in which the penetration of the liquid evaporation surface inside a nucleus is determined by the heat input:

$$r(t) \cong 2\sqrt{\frac{3}{\pi}}\frac{b'}{\Lambda_{vap}\rho''}(T - T_b)\sqrt{t},$$

where $b' = \sqrt{\rho'\lambda'C'}$, and λ' and C' are the heat conductivity and heat capacity of the liquid, respectively.

The above mechanism of metal boiling-up is realized at pressures $P < P_{cr}$ and within a specific range of metal heating power variation. The lower boundary of this range is defined by the criterion of homogeneous boiling-up, and its higher boundary, by the condition of steady-state homogeneous formation of vapor nuclei, $\tau_m > \tau_c \gg \tau_p$. Here τ_m is the maximum

time during which heterogeneous boiling can be neglected, τ_c is the time in which ultimate overheating is reached at a given specific heating power, and τ_p is the time during which steady-state homogeneous formation of vapor nuclei in overheating liquid sets in.

4.3.3. Attainable overheating and heterogeneous boiling of liquid metals. The metallic state of a material is determined by the existence of free electrons; for normal metals there are not less than one of them per atom. At high enough temperatures ($T \geqslant 0.5$ eV, the concentration of charged particles close to the binodal becomes so high that they can become centers of heterogeneous volume vapor generation. Such a mechanism of vapor formation in metals with a low critical temperature ($T_{cr} \sim 1$ eV, e.g. aluminum, copper etc.) can become realized in isentropic conditions [102]. Under certain conditions specified below, heterogeneous vapor formation on charged particles can proceed in a high-power pulsed heating of a liquid metal as well.

The level of overheating of a liquid metal above which charged particles become centers of volume heterogeneous vapor formation can be estimated from the relation [102]

$$\varepsilon_T^c \cong \frac{3}{2\sqrt{2}} \frac{\alpha\,\omega}{\Lambda_{vap} k_B \zeta},$$

where α is surface tension, and the coefficient $\zeta = e^2/\sqrt[3]{16\pi\alpha}$. By substituting ε_T^c into the condition governing the onset of "impact" heating, we come to an estimate of the minimum rate of heating of a liquid metal $\dot{T}$, at which heterogeneous boiling of liquid metal on charged particles cannot already resist development of homogeneous volume evaporation initiated by fluctuations:

$$\dot{T} \gg \left(\frac{3}{4\pi} \frac{1}{\varphi\Omega_0}\right)^{-\frac{1}{3k}} \frac{\varepsilon_T^c}{T_b}.$$

Here, Ω_0 is the concentration of centers of heterogeneous boiling, which in the case under consideration coincides with that of charged particles.

The presence of charged particles close to the binodal shortens the time during which metastable states of the liquid metal persist up to their breakup into equilibrium two-phase states. Under the present conditions, it is primarily governed by the time a vapor nucleus takes to grow to equilibrium size, for which numerical estimates yield ~ 1 ns, with the time of metastable state decay $\sim 0.1 - 1$ ns. Significantly, the time the liquid metal spends in metastable states before the first vapor nucleus born in fluctuations appears extends to approximately $\tau \geqslant 1 - 10$ ns.

If the characteristic times of volume evaporation are shorter than the "sonic" expansion time of a liquid metal, the above analysis suggests the following pattern for volume vapor formation in liquid metals. At heating rates $\dot{T} \leqslant 10^{10}$ K/s, liquid metal overheats insignificantly in the heterogeneous boiling initiated by charged particles. Therefore the conditions needed for the onset of homogeneous boiling-up are not met. To disperse a liquid metal in the conditions supporting homogeneous formation of vapor nuclei, the heating rate should be $\dot{T} \geqslant 10^{10}$ K/s.

5. EEC modeling based on similarity criteria

It is assumed that the EEW regimes most appropriate for the preparation of metal nanopowders are those providing current pause and maximum energy injected into the conductor by its beginning. Such regimes were defined in terms of the theory of dimensionalities and similarity (Kotov Yu.A., Azarkevich E.I., Sedoy V.S., Krivitskij E.V. et al.) [20,32,58,103]. The region of the initial conditions in which EEC develops in the regime

with a current pause was identified by generalization of the available experimental data. One employed for this purpose the similarity criteria derived from an analysis of the dimensionalities of the physical parameters of the phenomenon and phenomenological ideas bearing on its mechanism. For wires of diameter d, the similarity criteria modeling EEC in the stages preceding firing of the discharge have the form:

$$\Pi_1 = \frac{R_0}{Z_0}, \quad \Pi_2 = \frac{C_0\, U_0^2}{d^4 \varepsilon_0 \sigma_0 Z_0}, \quad \Pi_3 = \frac{v_0 \sqrt{L_0 C_0}}{d},$$

where ε_0 and σ_0 are the characteristic values of internal energy and electric conductivity of the metal, v_0 is the velocity of the rarefaction wave in the metal, and Z_0 is the wave resistance of the discharge circuit. In analysis of experiments performed with conductors prepared from the same metal, its characteristics ε_0, σ_0 and v_0 may be dropped, to transfer instead to the generalized variables:

$$\lambda = l\left(nd^2\sqrt{\frac{L_0}{C_0}}\right), \quad \varepsilon = \frac{C_0 U_0^2}{n^2 d^4 \sqrt{L_0/C_0}}, \quad \nu = \frac{\sqrt{L_0 C_0}}{d}.$$

These variables were employed in a quantitative description of the region of initial conditions in the electric explosion of copper wires in the regime with current pause. In particular, for the critical wire length we obtain:

$$\lambda_{cr} \approx A\left(10^{-6}\varepsilon\ \nu\right)^b,$$

where λ_{cr} is expressed in $(\mathrm{mm}^{-1}.\mathrm{Ohm})^{-1}$, ε – in $\mathrm{J/(Ohm.mm^4)}$; $\boldsymbol{v}$ – in mkc/mm; $A = (1,35 \pm 0,03)\cdot 10^3$; $b = 0,358 \pm 0,014$. For wires of critical length, the overvoltage coefficient can be found from the relation:

$$\frac{U_{max}}{U_0} \cong 0.45\left(10^{-6}\nu\right)^{-0.2} \exp\left[-0.011\left(10^{-6}\varepsilon\right)\nu\right].$$

Applying a similar approach to the problem of generalization of experimental results, it was demonstrated that EEW regimes developing in conditions without the current pause can be modeled with the use of the above similarity criteria Π_1, Π_2 and the criterion:

$$\Pi_4 = \frac{A_0 l^3}{U_0^2 \sqrt{L_0 C_0}}.$$

Here, A_0 is a constant characterizing the properties of the medium in which an EEW is conducted; for an underwater EEC, for instance, $A_0 \approx 10^4$ $\mathrm{Vcm^{-2}}$. The magnitude of overvoltage can be derived with the use of an approximate expression

$$\frac{U_{max}}{U_0} \cong 20\ \sqrt[4]{\Pi_2}\sqrt[3]{\Pi_4}.$$

While the criteria relations are certainly useful in practice, they are applicable only in the ranges of variation of the working conditions for which they were derived. In view of the area of applicability of any criterion relations being limited, one has to support activities in the field of engineering EEC research based on the theory of the related dominant processes.

6. MHD modeling of physical processes involved in an electric explosion in a metallic conductor

Complex numerical investigation of the main physical characteristics of dispersion draws from the modified model of magnetic radiation hydrodynamics applicable within a broad range of states (condensed, liquid, gaseous, plasma) [46, 104-162]. It encompasses the critical point and the metastable region, as well as transport coefficients for various kinds

of processes involved in electric- and thermal conduction. In contrast to the conventional MHD model, this model takes into account the radiation component of energy exchange and describes magnetic field diffusion into a conductor, Joule heating, heat transport by electron and radiative heat conductivity, expansion and compression of the medium, including formation of shock waves. A possibility is provided for using various equations of state and of interpolation models for computation of transport coefficients. In a one-dimensional single-temperature approximation and in the case of cylindrical symmetry, this computational model is described by the following system of equations expressed in mass Lagrangian coordinates [33]:

$$\frac{dr}{dt} = u; \quad \frac{du}{dt} = -r\frac{\partial P}{\partial s} + F;$$

$$\frac{d}{dt}\left(\frac{1}{\rho}\right) = \frac{\partial}{\partial s}(ru);$$

$$\frac{d\varepsilon}{dt} = -P\frac{\partial}{\partial s}(ru) + Q_J - \frac{\partial W}{\partial s};$$

$$W = -\chi\rho r\frac{\partial T}{\partial s};$$

$$\frac{d}{dt}\left(\frac{B}{\rho r}\right) = \frac{\partial E}{\partial s}; \quad J = \frac{\rho}{\mu_0}\frac{\partial}{\partial s}(rB);$$

$$F = -JB; \quad J = \sigma E; \quad Q_J = \frac{\sigma E^2}{\rho}$$

Here, r is the radius (Eulerian spatial variable), s is the Lagrangean mass variable, u is the mass velocity, t is the time, ρ and T are the density and temperature of the material, E is the axial component of electric field strength, B is the azimuthal of magnetic field, J is the axial component of current density, Q_j is the specific power of Joulean heating, F is the Lorentz force; $P = P(T, \rho)$, $\varepsilon = \varepsilon(T, \rho)$ are the pressure and specific internal energy of the material, and $\sigma = \sigma(T, \rho)$; $\chi = \chi(T, \rho)$ are the electric conductance and heat conductivity of the material. One considers here two regions separated by a moving boundary $r(t)$. These are the regions occupied by the material of exploded conductor and by the medium in which the explosion takes place, accordingly.

The system of MHD equations is supplemented by the equations of the electric contour, which describe the variation of the current and voltage in components of the discharge circuit, with due account of their capacity, inductance and active resistance, as well as of the characteristics of the source and environmental medium:

$$\frac{d}{dt}[(L_0 + L_1)J] + U_1 + R_0 J = U_c, \quad \frac{dU_c}{dt} = -\frac{J}{C_0}.$$

Here, L_0 and R_0 are the intrinsic inductance and active resistance of the circuit, C_0 and U_0 are the capacity and charging voltage across the capacitor battery, L_V is the inductance of the conductor–return current lead, and U_1 is the voltage at the exploding conductor. To take into account the magnetic field in the environment, a variable inductance is included into the circuit substituting the circuit with the conductor. These equations are solved for the initial conditions $J(t = 0) = 0$, $U_c(t = 0) = U_0$, combined with the system of MHD equations.

Electric conductivities in single-phase regions are calculated with wide-range interpolation models [133-143, 149-162]. Significantly, these models describe in whatever approximation one chooses, the variation of the electric conductivity for a continuous variation of the density of material, from solid-state values to the levels characteristic of gases and the

plasma. Thermal conductivity in single-phase regions was reduced from the Wiedemann–Franz law. In the region of two-phase states, determination of effective transport coefficients rests on the well-known model of the heterogeneous medium, which takes into account its phase composition and structure (mutual phase arrangement) [163]. The extensive characteristics of the material (specific volume, internal energy, enthalpy) in a two phase region are related to the corresponding characteristics of individual phases through the expressions:

$$\rho = g\rho_1 + (1-g)\,\rho_2; \quad \varepsilon = g\varepsilon_1 + (1-g)\,\varepsilon_2.$$

Here, g is the concentration of the first phase in the mixture, ρ_i, ε_i are the density and specific internal energy of phases at the coexistence boundary (binodal), which depend on one thermodynamic variable only, the temperature.

Numerical modeling (simulation) permits one, in particular, select a priori needed EEC regime by properly matching the initial working conditions (physical properties and dimensions of the conductor to be exploded, density of the environmental medium etc.), with the pulsed system of accumulation and transport of energy into the conductor. Its specific power and magnitude, combined with the homogeneity of distribution over the conductor cross section, are dominant factors in reaching the required physico-chemical properties of nanopowders as products of electrical explosion-based dispersion of a metal. Geometrical characteristics of the conductors to be exploded also markedly influence the possibility of developing instabilities, just as unfavorable effects of a dense environmental medium. In this regard, various conditions involved in electric explosion of conductors in the form of wires, plane plates and thin-walled cylindrical shells were modeled in rarefied gas and liquid water medium, with the temperature and density of the material being varied within a broad range of temperature and density of the material (from the condensed to plasma states), depending on the specific density of injected energy.

Calculations revealed that the part played by MHD "waist"-type instabilities in an electric explosion of a foil is insignificant. As for the uniformity of energy injection, however, it is impaired because of the nonuniform distribution of current density over the width of the foil as a result of edge effects. Edge effects can be eliminated by enclosing a plane foil into an envelope. It is these considerations that account for our having chosen the exploding conductor in the form of a thin-walled metallic shell encompassing a rigid dielectric cylinder, with the return current conductor in the form of a massive metallic rod extended along the cylinder axis (Fig. 3).

Such a configuration of the load has one more asset—indeed, it makes possible reducing to a minimum the inductance of the "load—return current" element of the electric circuit, an essential point in reaching high discharge current rise rates. In this case the load may be placed into a chamber, a reactor of an arbitrary shape and size. Preliminary estimates showed that a pulsed source of energy intended for experimental studies should generate current pulses with a leading edge < 10 ns and amplitude of up to 100 kA. For this purpose, one can use a high-voltage pulse generator, with pulse leading edges on the order of 1 ns and amplitudes of up to 200 kV, which was developed at the Ioffe FTI for an "Extreme-M" experimental facility. The basic diagram of the heavy-current electric discharge circuit developed for this facility, complete with the equivalent electric circuit and the corresponding diagram, which was employed in numerical studies of Z discharges, is displayed in Fig. 4. In the present work, the sharpening capacitance was not included, with the shortening switch S and circuit breaker with a steeply growing resistance $R_f(t)$ employed in physical and numerical electric circuit switching experiments.

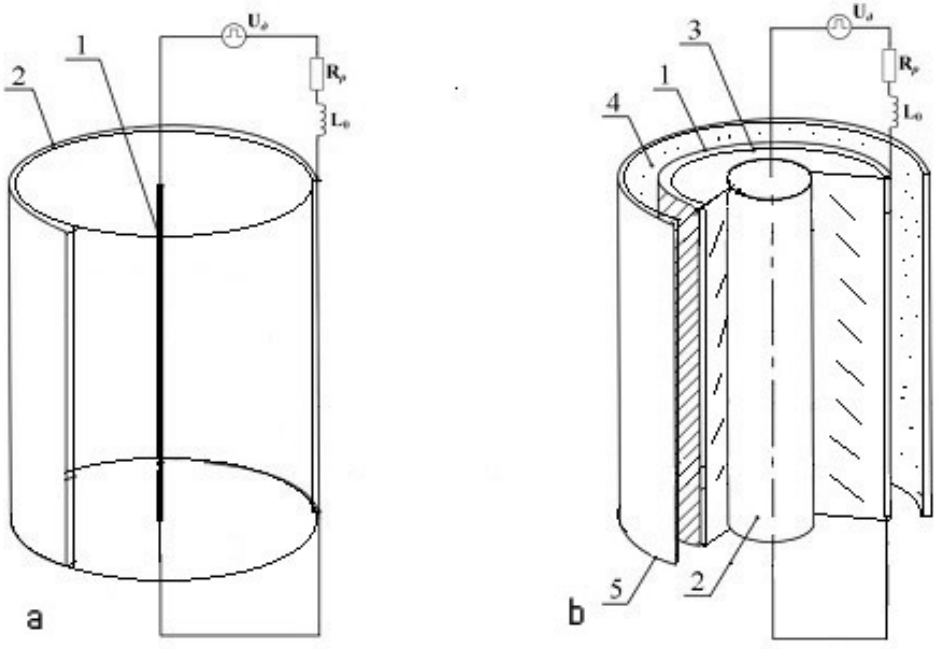

FIG. 3. Diagram of a typical arrangement of exploding conductor in the discharge chamber (a) and a version of its replacement with a thin-walled cylindrical shell mounted on a rigid dielectric cylinder, with a return current conductor – a massive metallic rod fixed on the cylinder axis (b). Notes: a: 1 - exploding conductor; 2 - return current conductor. b: 1 - exploding thin-walled metallic cylindrical shell; 2 - return current conductor; 3 - rigid dielectric cylinder; 4 - water medium; 5 - wall discharge chamber

MHD calculations of a thin-walled metallic shell suggest the possibility of building up the required EEW regime in a water medium, which would provide uniform energy injection into the metal and a current "pause".

Indeed, Fig. 5 demonstrates the behavior with time of the discharge current, voltage and energy injected into the conductor. We readily see that energy is injected into the material predominantly in the stage of the "explosion as such". Significantly, the main condition of matching of the conductor with the power supply is fulfilled, namely, the energy of the magnetic field stored in inductive elements of the electric circuit should be approximately equal to that of metal sublimation.

The data displayed in Fig. 6 show that conductor heating in the initial stage (stage of the conductor "waiting" for the explosion) preceding the stage of the explosion proper is uniform. The nonuniformity of Joule heating of the metal caused by the diffusion of electromagnetic field is seen to level off rapidly, with the distributions of current density and Joule heating over the shell cross section becoming practically uniform in the time which is shorter than the time the conductor is "waiting" for the beginning of the explosion proper, i.e., for the beginning of the discharge current fall-off [33].

Besides calculation of the transition process in the circuit, distribution of the electrostatic field in the apparatus in the vicinity of the load was studied. The distribution of the field in the regions where current and voltage are supplied to the load is shown in Fig. 7. The data obtained in the calculations were employed to determine the probability of breakdowns in the separating diaphragm when current is supplied to the operating inductive load.

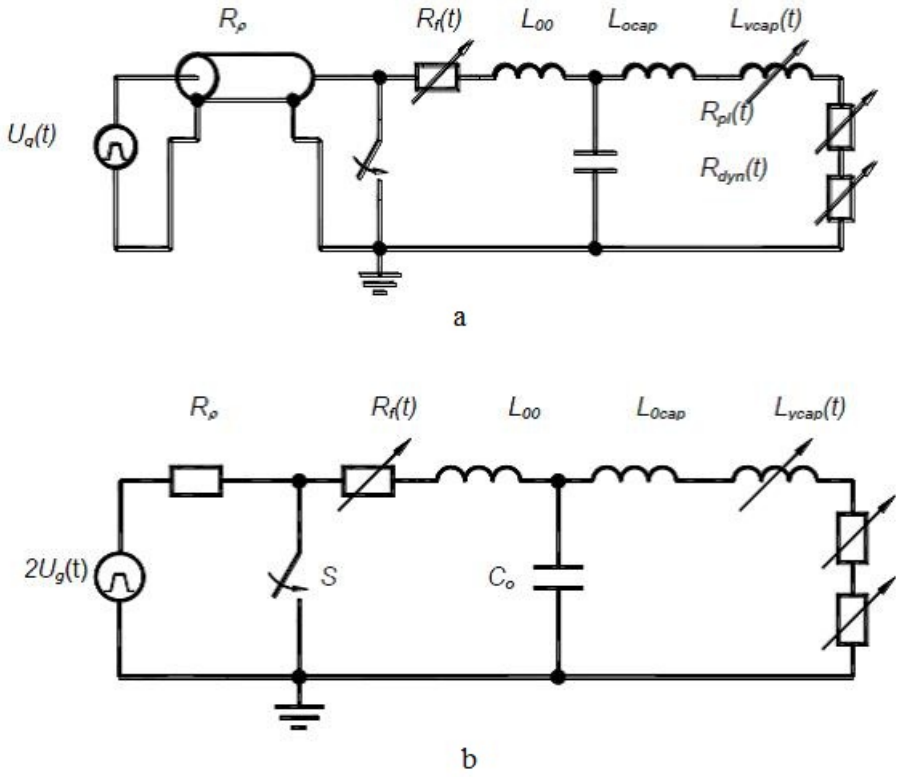

FIG. 4. Equivalent electric circuit (a) and the corresponding diagram (b) of the heavy-current electric discharge circuit which was employed in numerical studies of Z-discharges in the Extreme-M equipment

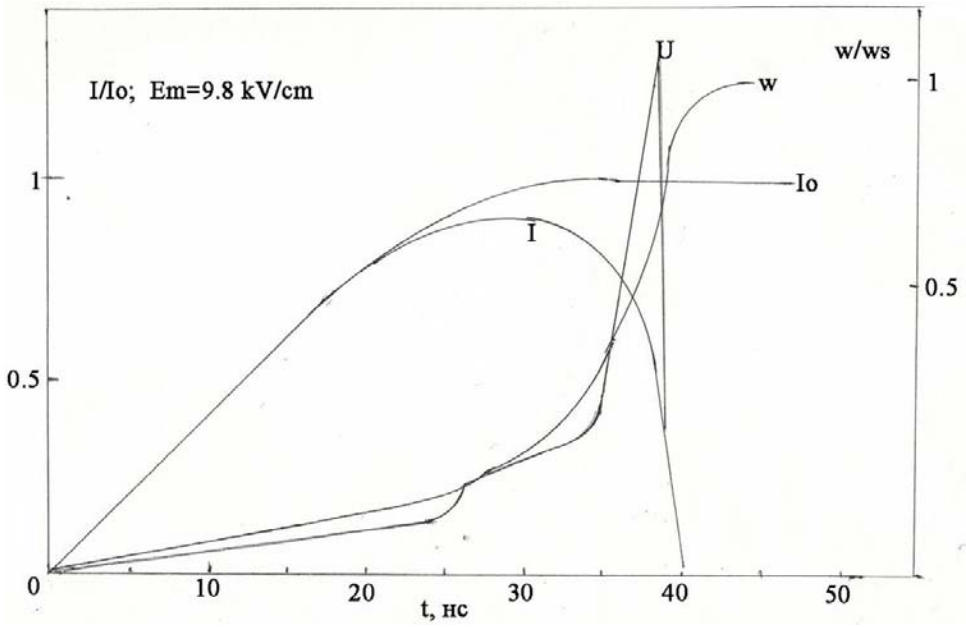

FIG. 5. Variation of discharge current, voltage and energy injected into the conductor of a thin-walled metallic shell during EEW in a water medium. Here I0 is the short circuit current, Em, Ws are the maximum values of voltage and energy

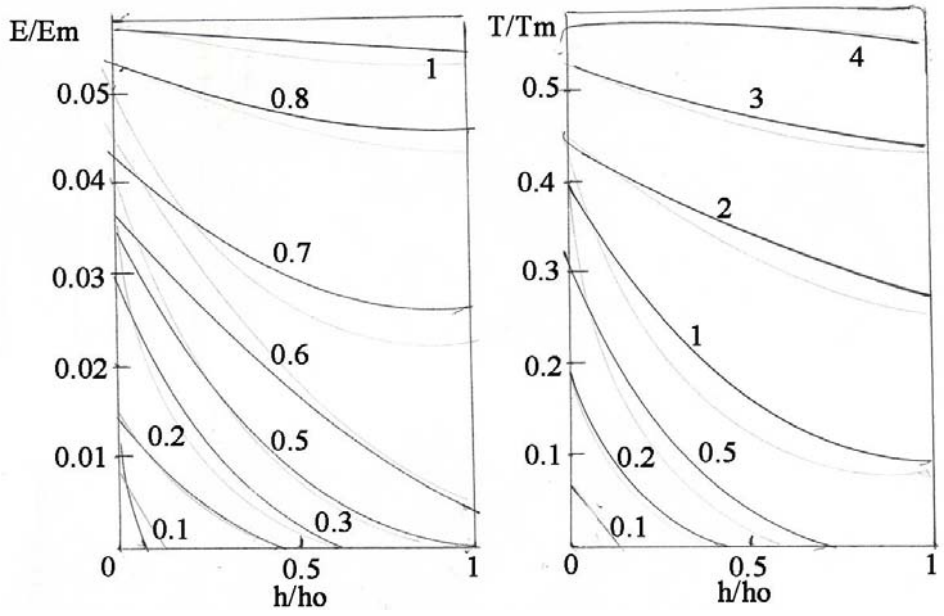

FIG. 6. Variation of the distributions of the relative electric field strength and of the temperature over the shell cross section in the course of Joule heating in the initial stage (conductor before explosion) preceding the stage of the explosion proper at different moments of time (ns)

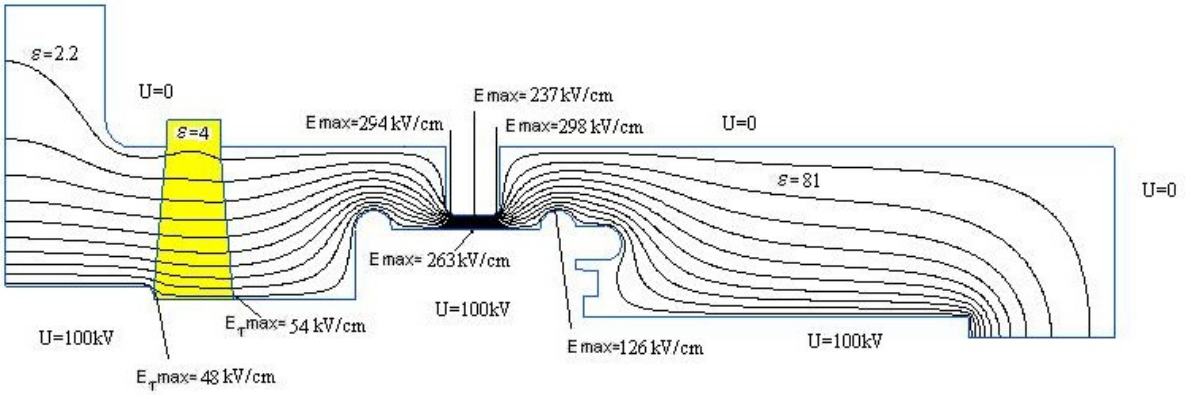

FIG. 7. Distribution of electrostatic field in the region of voltage supply to the load

Incidentally, approach to the critical point in metals is accompanied by a sharp drop of electrical conductivity resulting from free electron scattering from small-scale density fluctuations. For metals, however, whose critical temperature is comparable (in energy units) to the thermal ionization potential ($\sim$ 1 eV and higher) and which near the critical point can be actually a metallic plasma, electrical conductivity grows again with heating. Because ionization is one of the most energy-intensive processes (for aluminum, for instance, the melting heat is 10.8 kJ/mole, sublimation heat—327 kJ/mole, and the first ionization potential is already 577.6 kJ/mole [164]), under pulsed energy supply conditions, equilibrium among different energy dissipation channels does not set in. As a result, material can coexist simultaneously in different energy states. Also possible is repeated electric discharge, and, besides density, temperature, pressure and entropy fluctuations, variations of charge involving a local

violation of electric quasi-neutrality of the plasma can form as well. The ambipolar electric field generated in these conditions should bring about a decrease of density fluctuations, in this way compressing, as it were, the material and raising its critical temperature, and preventing in this way the falloff of electrical conductivity. This could tentatively be assigned to free electrons leaving high-density regions for more rarefied regions of material with density fluctuations, as is the case of gaseous plasma supporting the characteristic phenomenon of double electric layer formation [33].

7. Modeling of the physico-chemical processes involved in condensation of products of an electric explosion of metallic conductors in a water environment

Further development of fluctuations experienced by thermodynamic quantities of a metal as it approaches the critical point by the described scenario, which culminates in a phase explosion and condensation of its products in the environmental medium, may have some aspects essential for the formation of condensing nanosized particles and stemming from the properties both of this medium and of the explosion products proper. The above results of the numerical analysis stress the importance of imposing limits on the rate of metal expansion. It appears reasonable to invoke for this purpose high-power heating not of wires but rather of thin-walled tubular conductors immersed in a dense liquid medium. In contrast to a rarefied gas, a dense, in particular, an aqueous medium can intensify cooling of a melting and boiling-up metal of the conductor, thus inhibiting its expansion in the electric explosion. This medium, however, will experience itself the variations of the thermodynamic state up to development of supercritical fluids generated by fast local heating, shock wave propagation, collapse of cavitation bubbles and other similar phenomena described in considerable detail in the literature [50].

In these conditions, the process of metal vapor condensation reveals its specific features, which are associated not only with efficient cooling but with the presence of electric charge on the particles of explosion products as a result of thermal ionization of the metal close to the critical point, as well as with their interaction with supercritical water. The active $[(H_2O)n(Me)m]$ complexes formed in the process can transform into nuclei of the new phase – the metal oxide Me_mO_n. Formation of oxide nanoparticles in the supercritical fluid thus formed is supposedly governed by a chemical redox reaction accompanied by release of hydrogen $k(Me)+l(H_2O)= g(Me_mO_n)+l(H_2)$, where $k = gm$, $l = gn$. Such a reactor, with a proper choice of the metal to be exploded (Al, Ti, Zr etc.), can provide a highly productive synthesis of oxide nanoparticles. Incidentally, the method of synthesis described above is potentially capable of producing oxide nanoparticles differing from those of the same oxides but prepared by electrical explosion of metals in air or other oxygen-containing gas media, as was proposed in Refs. [43,65,159,165,166], or by hydrothermal synthesis in its classical methodological approach [167]. The oxide nanopowders formed in the above conditions can reveal, due to the reducing medium and the high-energy conditions characteristic of local-hydrothermal synthesis, in particular, a still higher level of catalytic, sorptive and other functional characteristics than, for instance, those obtained by the traditional hydrothermal method of their synthesis [168-172].

Evaluation of the necessary nucleus formation energy (the free Gibbs energy) and of the critical size of the nuclei corresponding to its maximum (Fig. 8), requires, in the conditions considered here, taking into account the contribution not only of the surface tension and of the difference between the "particle-environmental medium" chemical potentials but of the difference between their electric potentials as well.

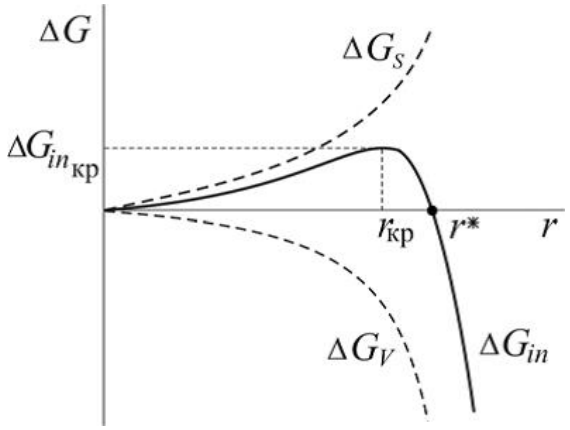

FIG. 8. Dependence of the Gibbs energy and of its components involved in formation of a nucleus on its radius

Spontaneous growth of a nucleus is known to be possible only under further decrease of the Gibbs free energy (Fig. 9). In the particular case of formation of a spherical nanoparticle and of absence in the system of spatial constraints described in Refs. [173,174], the Gibbs free energy can be conceived as a sum of its volume and surface components $\Delta G = -(4/3)\pi R^3 \Delta\mu/V_a + 4\pi R^2\sigma(R)$. Here, $\Delta\mu > 0$ is the difference between the chemical (electrochemical) potentials of a nanoparticle and of the phase-forming medium, $V = (4/3)\pi R^3$ is the volume of the nucleus of a spherical nanoparticle, V_a is the molar volume of the material of the phase-forming medium, and $\sigma = \sigma(R)$ is surface tension. The critical size of the nucleus Rkp is found from the condition of maximum free energy $d(\Delta G)/dR = 0$. It is $Rkp = 2\sigma(\infty)V_a/\Delta\mu$ if one disregards the dependence of surface tension on particle size, and $Rkp = l_0[1 - 2\delta/l_0 + (2\delta/l_0 + 1)^{1/2}]$ – with its inclusion for small particle radii with the relation $\sigma(R) \approx \sigma(\infty)/(1 + 2\delta/R)$ where $l_0 = \sigma(\infty)V_a/\Delta\mu$, and δ is the "Tolman length" [175]. The critical Gibbs energy at the point of the maximum, derived for the case of formation of homogeneous condensation nuclei on the surface of the nuclei appearing spontaneously as a result of fluctuations of the density and concentrations of material in the system, disregarding the dependence of surface tension on particle size, makes up $\Delta Gkp = (4/3)\pi R^2 kp(\sigma - 2/3\sigma)$, or one third of the surface energy of a nucleus. The remaining two thirds are canceled by the chemical component of the excess energy generated in the phase transition. Incidentally, $\Delta\mu = 2\sigma(\infty)V_a/Rkp$.

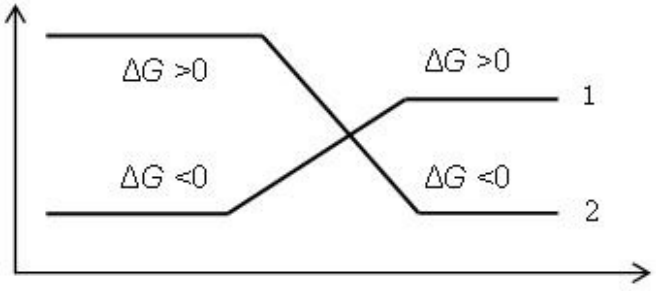

FIG. 9. Variation of the characteristics of thermodynamic processes plotted vs. size of the nanoformations: 1 - spontaneous design process is impossible, 2 - spontaneous design process is possible

The applicability of the general thermodynamic approach to estimation of the homogeneous formation of particles of small size is limited by the condition in which the specific surface energy $\sigma(R) \approx \sigma(\infty)/(1+2\delta/R)$ is higher by far than its RMS fluctuations $\langle\langle\Delta\sigma\rangle^2\rangle = (kT/8\pi R)(\delta\sigma/\partial R)_{P,S} = kT\delta\ \sigma(\infty)/[4\pi R(R+2\delta)^2]$. This condition is met for $R \gg [kT\delta/\sigma(\infty)]^{1/3}$. Estimates suggest that at a low condensation temperature, the critical size of the nucleus can make up $Rkp = (5 \div 10) \cdot 10^{-10}$ m, which is the size of a few atoms. In this case, adding the next atom will change ΔG in a discrete way, which is incompatible with the principle of thermodynamic theory by which surface energy and the Gibbs free energy vary continuously. One has to transfer to the statistical theory of nucleus formation based on the parameters of interatomic interaction among individual atoms, with the specific features of their behavior governing the probabilities of growth and decay of clusters, in which the relative fluctuations of the number of atoms and energy follow the standard law $\sim N^{-1/2}$ [67]. At a high temperature, this condition of thermodynamic approach for nanosized particles is met.

Because in supercritical conditions the main factor responsible for homogeneous aggregation of particles associated with surface tension at the liquid—gas interface is inactive, supercritical water is capable of dissolving substances which are practically insoluble in standard conditions; some oxides also belong here [176-178]. Subsequently, when the solution reaches supersaturation, the solid crystalline phase of oxide nanoparticles of about the same size and with a fairly well developed surface is precipitated. The critical degree of supersaturation $\gamma = c/c_s$ can be evaluated by expressing the difference of the chemical potentials obtained above, $\Delta\mu = 2\sigma(\infty)V_a/Rkp$ of the critical nanoparticle nucleus and of the phase-forming medium, through the concentration c of the material in the supersaturated solution and its equilibrium solubility c_s relative to the crystalline phase. For an ideal solution we obtain $\ln\gamma = \ln(c/c_s) = \Delta\mu/RT = 2\sigma(\infty)V_a/Rkp\ RT$. The parameters of the solid nuclei forming in the liquid phase in a supercooled solution can likewise be derived from the above expression using the relation $\Delta\mu = \Delta H_\Pi - T\Delta S_\Pi = \Delta H_\Pi \Delta T/T_\Pi$ where $\Delta T = T_\Pi - T$s the supercooling, and ΔH_Π is the enthalpy of the process.

In a similar way, one can obtain quantitative estimates for heterogeneous condensation in formation of a new phase on the already available surfaces (walls of the vessel, particles of foreign substances acting as condensation nuclei). As follows from these estimates, the work expended for the formation of solid nuclei in heterogeneous condensation should be smaller than that spent in a homogeneous process by the same factor the volume of the bubble nucleus on the surface of a condensation nucleus is smaller than the volume of the sphere of the same curvature. The processes of adhesion and wetting, active in interaction between the new phase and a foreign surface lower the energy of formation of nuclei, and the stronger are the adhesion and wetting, the smaller is the degree of supersaturation that will initiate condensation. The appearance of a charge in a metastable system will likewise reduce the Gibbs energy of formation for nuclei. Therefore, nuclei carrying a charge form at lower degrees of supersaturation, primarily because surface tension decreases with increasing electric potential of the surface (as follows from Lippmann's relation, $d\sigma/d\phi = -q_s$, the effect being the stronger, the larger is the charge of the unit surface q_s).

The above estimates relate to a single nucleus only and disregard the entropy component of the energy involved in formation of a mass of nuclei. For low interface tensions, the entropy component can cancel out the surface energy and initiate spontaneous dispersion. Evaluation of the conditions governing formation of nuclei from materials residing in non-autonomous state in media with spatial limitations, in particular, those resulting from the presence of nanoparticles of another phase distributed in these media, becomes complicated

significantly, by requiring inclusion of the structure, composition and properties of the latter. In the case of classically-shaped nuclei (cube, sphere, cylinder), one succeeds in deriving analytical expressions relating their geometrical characteristics to the size of the nucleus of the new phase [173,174].

By the theory of M. Volmer and Ya. I. Frenkel [100,179], the kinetics of condensation-based formation of a new phase are determined by the rates both of generation of condensation centers $I = A_1 \exp[-\Delta G_1/(RT)]$, and of the supply of the material to the new condensation centers $U = A_2 \exp[-E_\eta/(RT)]$. The first of them is proportional to the probability of generation of condensation centers in accordance with the Gibbs energy ΔG_1, and the second, proportional to the probability of their "survival", in accordance with the activation energy E_η of the transition of material from the original phase to the surface of the nucleus. The total rate is a product of these probabilities, and it can pass through an extremum, depending on the relative values of the energies ΔG_1, E_η, temperature T and coefficients of proportionality A_1, A_2.

Besides the kinetic characteristics, one can readily use in evaluation of the degree of thermodynamic non-equilibrium of the process involved and conditions of self-organization of dissipative structures, entropy-based indices characterizing internal instability of the conversion of energy, which should be assigned to the increasing part played by the entailed thermodynamic fluxes and forces. It was shown [180,181] that in two-phase media, fluctuations of their characteristics become energetically preferable to steady-state regimes, by supporting lower energy dissipation (gain of entropy) with the coefficient of thermodynamic nonstationarity $\varepsilon = \bar{S}_{nstat}/S_{stat} < 1$. Here, S_{stat} is the gain of entropy in a system with steady-state thermodynamic fluxes and forces, and S_{nstat} is its average value in nonstationary regimes with fluctuations of fluxes and forces.

8. Modeling of integral characteristics of the phase-forming media

In all cases of outwardly random formation of such two-phase macroscopically strongly-inhomogeneous media, they reveal elements of deterministic behavior (deterministic chaos [182] and fractal self-similarity [183]). They are actually consequences of nonlinear interaction among components of a dissipative system and become most prominent near a specific value of phase concentration called the percolation threshold [184].

One of such characteristic effects in the field of consideration is the sharp drop in the electric conductivity of metals caused by electrons scattering from small-scale density fluctuations as they approach the critical point. At the same time, in metals whose critical temperature is comparable to its first ionization potential and which close to the critical point represent, as it were, a metallic plasma, the electric conductivity again increases. In these conditions, electrodual phases, scattered chaotically in a randomly nonuniform medium, assemble into a cluster of a conduction chain (or of its antipode—an insulation chain). One can pass along it through the whole system, retaining or losing its electric conductivity, respectively, as shown in this particular case. Although these effects are governed only by the chain reaching the opposite boundaries of the system (percolation medium), the cluster itself will contain other chains as well, which adjoin this conducting "skeleton" while not maintaining the percolation of the system as a whole. Modeling of such phenomena in a randomly inhomogeneous system was analyzed, in particular, in Ref. [185].

8.1. Effective conductance of electro-dual media

If the characteristic dimension of averaging exceeds by far that of the inhomogeneity, some integral characteristics of the system, for instance, the effective electrical conductivity

σ_e, which relates volume-averaged fields $\langle E\rangle$ and currents $\langle j\rangle$ in the expression $\langle j\rangle = \sigma_e\langle E\rangle$, in the vicinity of the percolation threshold turn out not to depend on the specific geometry of phase arrangement in the system. Above the percolation threshold, the effective conductivity of the system will be determined only by the phase conductivities σ_1 and σ_2, concentration p of phase 1 and concentration $(1-p)$ of phase 2 in the form $\sigma_e = [\sigma_1\sigma_2/p(1-p)]^{1/2}$ [185], and below the percolation threshold the conductivity will be zero.

In the lattice model of the "percolation medium" [184,186,187] the phase conductances are identified as whole (conducting the electric current) or blocked (non-conducting) connections among the lattice sites, and phase concentrations, as the probabilities of the corresponding bonds being whole or blocked. The percolation threshold in the bond problem corresponds to the probability of connection of whole bonds into a cluster chain, which for the first time brings the conductivity of a system as a whole to a non-zero value, and the percolation threshold in a site problem, to the probability of blocking of all connections leaving a site and resulting in zero conductivity of the system. As follows from calculations, although the percolation threshold for the problem of connections for any lattice does not exceed that for the problem of sites for the same lattice, the thresholds themselves depend significantly on the type of the problem considered [184,188]. To that end, it turns out that the number of bonds per site, just as the average fraction of the volume occupied by unblocked sites around each lattice site, does not depend on the lattice proper. It is determined by the dimension of problem only, leaving 2 for two-dimensional lattices and 1.5 for the three-dimensional ones in the first case, as well as 0.45 for two-dimensional lattices and 0.15 for three-dimensional ones in the second case [184]. Another feature common for problems of all types is also the way in which these thresholds are approached by such parameters as the fraction of the lattice sites belonging to the cluster formed, the geometric size of the cluster (correlation radius) and the effective electrical conductivity of the system expressed in the form of power functions of a given phase concentration: $P_j(x) = B_j(x - x_c)^{\beta j}$ for $x > x_c$ and $P_j(x) = 0$ for $x < x_c$, where B_j is a numerical coefficient, and β_j is the critical index of the quantity P_j. Moreover, it turns out that the values of all critical indices are universal for all percolation problems; they do not depend on the specific choice of the model of the medium, and are determined by the dimension of space only. Indeed, for two-dimensional problems the universal critical index of correlation length is $\nu = 1.33$, while for three-dimensional ones $\nu = 0.8 - 0.9$, the index of electrical conductance for three-dimensional problems $t = 2\nu$, for two-dimensional ones $t = \upsilon$, and the mass ratio index for two-dimensional problems $\beta = 0.14$, while for three-dimensional ones – $\beta = 0.4$ [184].

8.2. Fractal characteristics of media with scaling invariance

This can be used as a basis for the determination of the fractal dimension of the conduction chain cluster formed. It is a specific characteristic of the self-organizing scaling symmetry (hierarchical self-similarity) in all space scales in which a system is considered, from the size of a few lattice cells to the characteristic size of fluctuations (correlation radius) encompassing the whole metastable region as one approaches the critical point (percolation threshold). Based upon the determination of fractal dimension as a power exponent D of non-Euclidian expression $\Phi \sim m^D$ relating the rate of variation of the number Φ of elements in the fractal and the variation of the scale m of their consideration [189], one can find the relation connecting the fractal dimension of a percolation cluster with the critical indices in the form $D = d - \beta/\nu$ The numerical values of the fractal dimension of the "percolation medium" is $D \approx 1.895$ for two-dimensional, and $D \approx 2.556$ for three-dimensional problems [188]. This is smaller than the topological (Euclidean) dimension of nested space and can be

identified with versions intermediate between the dimensions of a line and an area, as well as between an area and a volume, so that the percolation skeleton reminds a lace cloth or a sponge in the first and second cases, respectively.

The above figures were taken from one of particular versions of numerical evaluation applied to such multifractal media. The Renji dimension serves as a general expression of their dimensions, used in the description of real dissipative objects [190] $D_{Rq} = \lim\limits_{\varepsilon\to 0}\lim\limits_{\tau\to 0}\lim\limits_{m\to\infty}\left[\frac{1}{1-q}\frac{\ln I_{Rq}(q,\varepsilon)}{\ln(1/\varepsilon)}\right]$. Here, $I_{Rq}(q,\varepsilon) = [\sum\limits_{i=1}^{M(\varepsilon)} p_i^q(\varepsilon)]$ is the generalized Renji entropy of order q; $M(\varepsilon)$ is the minimum number of "measuring" cubes with an edge ε required to cover the fractal in n-dimensional phase coordinate nesting space; p_i are the probabilities of contact of the i-th cube by the phase trajectory; and m is the number of points employed in calculation of the dimension. This relation yields, as particular cases for different q, the well-known relations for entropy of Kolmogorov-Sinay and of fractal dimension of Kolmogorov-Hausdorff ($q = 0$), entropy of Shannon and for the corresponding information dimension ($q = 1$), correlation entropy and correlation dimension ($q = 2$) [191]. The Renji dimension being a monotonically decreasing function of q, mapping of the fractal in the latter case for $q = 2$ requires the smallest dimension n of the nesting space, and it is this dimension that is used in evaluation of the fractal dimension of a percolation cluster as the most appropriate one for calculations.

Significantly, this fractal self-similarity for percolation clusters is met in the statistical meaning only. It reflects elements of deterministic behavior (deterministic chaos) in an externally chaotic formation of similar macroscopically inhomogeneous media as a product of nonlinear interaction of components of a strongly inhomogeneous dissipative thermodynamic system.

9. Conclusion

Dispersion of a metal driven by the development of thermodynamic instabilities of its physical state in the vicinity of the critical point is of a pure and applied research interest in the field of present-day nanotechnologies. This review offers an analysis of the possibility of employing the approach outlined here in obtaining oxide nanoparticles up to a few nanometers in size by electrical explosion of metallic conductors (EEC) in a chemically active dense aqueous medium.

Various physical models were invoked to show that this would require constraining the part played by non-thermodynamic mechanisms in destruction of a metal in the course of varying the physical state of the conductor being exploded, so as to mediate its transition close to the limit of the nonequilibrium metastable state with the maximum possible overheating and fast approach to the critical point through "explosive" boiling-up combined with generation of homogeneous vaporization.

Estimates suggest that the rate of Joule heating by electric current required for this purpose with a metal of the aluminum and copper type, performed with due account of counteracting factors, should be not less than $\dot{T} \geqslant 10^{11}$ K/s. This requirement is met for power densities generated in the material by injected energy in excess of $> 10^{10}$ W/cm^3 and supercritical temperatures ($T \geqslant T_{cr}$) reached in times $\tau < 100$ ns. Among the natural factors which plague reaching the highest possible metastable states of the melting metal and the onset of homogeneous vaporization are the evaporation wave propagating inside the overheating metal and formation of plasma in the vicinity of the critical point, which drives heterogeneous boiling on charged particles. To limit the part played by non-thermodynamic

instabilities driven by surface tension forces, magnetohydrodynamic (MHD) instabilities of the waist and convective types, current skinning and development of barocapillary instability, it is proposed to employ a geometric configuration of electric explosion of conductors new for the problem considered here. It is the explosion of a thin-walled cylindrical shell positioned on a rigid dielectric cylinder, with the return current conductor stretched axially inside the shell. Significantly, the reactor being of a fairly arbitrary shape and size, the load can be placed into a water chamber.

Experimental studies prepared in accordance with the corresponding calculations require development of a pulsed source of energy which would provide a high rate of growth for the discharge current and a high power of electric discharge through the shell, $Q_V \geqslant 1$ TW/cm^3, by generating current pulses with the leading edge less than < 10 ns and amplitude of up to 100 kA. Present-day technology of accumulation and switching of energy offers adequate possibilities for injection of the required specific powers into a material.

Of a particular significance for realization of optimum regimes of energy input into a conductor is matching its physical properties and size with the characteristics of the energy source used. To solve this problem, one can conveniently use MHD calculations of EEC, which demonstrate the possibility of development of the desired EEC regime of a thin-walled metallic shell in a water medium, which would provide uniform power input into the metal and a current "pause". These calculations involve equations of state, which take into account single-phase and equilibrium two-phase states of the material in mean-field approximation bounded by binodal branches. The fairly few attempts undertaken in investigation of EEC-based metastable states by MHD modeling and application of statistical approaches of the theory of macroscopic invariance to description of critical phenomena in the vicinity of the critical point of metals are still far from completion. At the same time, one succeeds in estimating within this framework some integral characteristics of such systems, of the type of their effective electrical conductivity and fractality. They show up as elements of deterministic behavior (deterministic chaos and fractal self-similarity) in all cases of outwardly chaotic formation of such two-phase, macroscopically strongly nonuniform media as a result of nonlinear interaction of components of a dissipative system.

The conclusive stage of nanoparticle formation in an electric explosion of metallic conductors in a water medium encompasses flying apart and condensation of its products. These processes are complicated by the presence on particles of an electric charge produced in thermal ionization of the metal near the critical point, as well as by their chemical interaction with the supercritical fluids forming as a result of fast local heating, shock wave propagation, collapse of cavitation bubbles and other similar phenomena. Because the main reason of homogeneous aggregation of particles, which is surface tension at the liquid—gas interface, is not realized in supercritical conditions, supercritical water is capable of dissolving substances practically insoluble under normal conditions, including some oxides. After the solution had reached subsequently supersaturation, a solid crystalline phase of oxide nanoparticles of about the same size and a fairly developed surface precipitates.

The method of synthesis considered here is potentially capable of producing oxide nanoparticles differing from nanoparticles of the same oxides but synthesized in electric explosion of metals in air or other oxygen-containing gaseous media, as well as in hydrothermal synthesis in its classical methodological form. The oxide nanopowders, formed in EEC of metals in water, can possess, in particular, due to the reducing medium employed and high-energy conditions mediating the locally hydrothermal synthesis in the supercritical fluid nanoreactor, a still higher level of catalytic, sorption and other functional characteristics.

Acknowledgments

The authors would like to thank Prof. V.V. Gusarov for useful discussions.

This work was financially supported by the Russian Foundation for Basic Research, project 12-08-01071-a.

References

[1] Nairne E. Electrical experiments by Mr. Edward Nairne. *Phil. Transact. of Royal Soc.*, London, **64**, P. 79–89 (1774).
[2] Faraday M. Division by the leyden deflagration. *Proc. Royal Inst.*, **8**, P. 356 (1857).
[3] Richardson W.H. Bibliography Exploding-Wire Phenomena. Report No SCR-53. Sandia Corporation, Albuquerque, New Mexico (1958).
[4] Exploding Wires. Plenum Press, N.Y., Vol. 1 (1959).
[5] Exploding Wires. Plenum Press, N.Y., Vol. 2 (1964).
[6] Chace W.G. Exploding Wires. *Phys. Today.* **17**(8), P. 19 (1964).
[7] Exploding Wires. Plenum Press, N.Y., Vol. 3 (1965).
[8] Chace W.G. and Watson E.M. Bibliography of the Electrically Exploded Conductor Phenomenon. Supplement No.1. APCRL – 65 - 384. Commerce Department, Springfield, Virginia (1965).
[9] Abramova K.B., Valickij V.P., VandakurovYu.P. and etc. Magnetohydrodynamic instability at the electric blast. Doklady Akademii Nauk (Proceedings of the USSR Academy of Sciences), **167**(4), P. 778–781 (1966), (in Russian).
[10] Exploding Wires. Plenum Press, N.Y., Vol. 4 (1968).
[11] Bennett F.D. *High-temperature exploding wires. Progress in high-temperature physics and chemistry.* Pergamon Press, N.Y., Vol. 2, P. 1–63 (1968).
[12] Bennett F.D., Kahl G.D. *Vaporization waves in metals.* Exploding Wires, P. 1–25 (1964).
[13] Bennett F.D., Burden H.S., Shear D.D. Expansion of superheated metals. *J. Appl. Phys.*, **45**(8), P. 3429–3438 (1974).
[14] Martynyuk M.M. Role of evaporation and boiling of liquid metal in the process Explorer electric explosion. *Zhurnal Tekhnicheskoi Fiziki* (Technical Physics), **44**(6), P. 1262–1270 (1974), (in Russian).
[15] Abramova K.B., Zlatin N.A., Peregud B.P. Magnetohydrodynamic instability of liquid and solid conductors. Destruction of conductors by an electric current. *Zhurnal Eksperimental'noi i Teoreticheskoi Fiziki* (Journal of Experimental and Theoretical Physics), **69**(6), P. 2007–2022 (1975), (in Russian).
[16] Pavlov A.P. *Boil metals, heated electric shock. Thermal fluid analysis.* Sverdlovsk, Ufa branch of USSR cademy of science, P. 20–24 (1975), (in Russian).
[17] Iskoldskij A.M., Pinus V.K., EpelbaumYa.G. Presented the electric explosion of conductors. Sustainability of the phase transformation. IAE, Novosibirsk, (1976). Preprint No. 32, IAE Sibirian branch of USSR academy of science (in Russian).
[18] Iskoldskij A.M., Pinus V.K., Epelbaum Ya.G. Presented the electric explosion of conductors. Thermal instability of boundaries of the phase. Novosibirsk, IAE, 1976. Preprint No. 41, IAE Sibirian branch of USSR academy of science (in Russian).
[19] Martynyuk M.M. Fuze destruction of metal powerful stream of electromagnetic radiation. *Technical Physics*, **46**(4), P. 741–745 (1976), (in Russian).
[20] Burtsev V.A., Kalinin N.V., Litunovskij V.N. Electric explosion of conductors. Review of OK-17. EFAI, Leningrad (1977), 120 p. (in Russian).
[21] Iskoldskij A.M., Pinus V.K., Epelbaum Ya.G. Presented the electric explosion of conductors. Magnetohydrodynamic and thermal instability. IAE, Novosibirsk, 1977. Preprint No. 47, IAE Sibirian branch of USSR academy of science (in Russian).
[22] Martynyuk M.M. Phase blast metastable liquid. *Fizika Goreniya i Vzryza* (Combustion, Explosion, and Shock Waves), **2**, P. 213–229 (1977), (in Russian).
[23] Burtsev V.A., Dubyanskiy V.A., Egorov N.P. et al. Study of electric explosion cylindrical foils. I. electrical explosion foils. *Zhurnal Tekhnicheskoi Fiziki* (Technical Physics), **48**(7), P. 1419–1427 (1978), (in Russian).
[24] Lebedev S.V. About the electric explosion mechanism of metal. *Teplofizika Vysokikh Temperatur* (High Temperature), **18**(6), P. 273–279 (1980), (in Russian).

[25] Burtsev V.A., Bezdol′nyj A.M., DubyanskiyV.A..etc. Study of electric explosion cylindrical foils. III. Current divergent level. *Zhurnal Tekhnicheskoi Fiziki* (Technical Physics), **50**(6), P. 1216–1226 (1980), (in Russian).

[26] Kalinin N.V. Kinetics of vaporization at the electric explosion of conductors. NIIEFA; Leningrad, 1981, 13 p. Preprint of NIIEFA, P-K-0518, Efremov Research Institute for electrical-physical equipment (in Russian).

[27] Lebedev S.V. The disappearance of metal conductivity at electrical explosion and development of macroscopic inhomogeneities along the exploding wire. *Teplofizika Vysokikh Temperatur* (High Temperature), **19**(6), P. 301–308 (1981), (in Russian).

[28] Dorovskij V.P., Iskol′dskij A.M., Romensky, E.I. Dynamics of Pulsed electric current and the metal heating conductors/explosion. *Prikladnaya Mekhanika i Tekhnicheskaya Fizika* (Journal of Applied Mechanics and Technical Physics), **4**(140), P. 10–25 (1983), (in Russian).

[29] Stolovich N.N. *Elektro-explosion energy converters*. Nauka i Tekhnika, Minsk (1983), (in Russian).

[30] Ivanenkov G.V., Samokhin A.I. Nanosecond burst of procrastination in the vacuum diode mosad is an accelerator. FIAN, Moscow (1984). /Preprint FIAN No. 80 (in Russian).

[31] Lebedev S.V., Savvatimskii A.I. Metals during rapid heating by dense current. *Sov. Phys. Usp.*, **27**, P. 749–771 (1984).

[32] Krivickij E.V. *Dynamics the electric explosion in liquid*. Naukova Dumka, Kyiv (1986), (in Russian).

[33] Burtsev V.A., Kalinin N.V., Lucinschi A.V. *Electric explosion of conductors and its application of electrophysical installations*. Energoatomizdat, Moscow (1990), 288 p. (in Russian).

[34] Sedoy V.S., Valevich V.V., Gerasimova N.N. Synthesis of highly dispersed powders method of electric explosion in Gaza with a pressure. *Fizika I Khimia Obrabotki Materialov* (Physics and Chemistry of Materials Treatment), **4**, P. 92–95 (1999), (in Russian).

[35] Vorobjev V.S., Eronin A.A., Malyshenka S.P. Phase blast conductor. *High Temperature*, **39**(1), P. 97–103 (2001).

[36] Tkachenko S.I., Hiŝenko K. V., Vorobjev V.S., etc. Metastable state of liquid metal electrical blast. *High Temperature*, **39**(5), P. 674–687 (2001).

[37] Oreshkin V.V., Sedoj V.S., Chemezova L.I. Electric explosion delay for nano-sized powders. *Prikladnaya Fizika* (Applied Physics), **3**, P. 94–102 (2001), (in Russian).

[38] Volkov A.A., Grebnev E.V., Dydykin P.S., etc. Electrical explosion of a wire by microsecond pulses in a longitudinal magnetic field. *Technical Physics*, **47**(5), P. 628–633 (2002).

[39] Pavlov P.A. *Dinamic speaker effervescence strongly overheated liquids*. Ekaterinburg, Ural branch of the USSR Academy of Sciences (1988), (in Russian).

[40] Ilyin A.P. Development electroexplosive technologies in production of ceramic Nanopowders high voltage in Research Institute of Tomsk Polytechnic University. *Izvestiya TPU* (Bulletin of the Tomsk Polytechnic University), **306**(1), P. 133–139 (2003), (in Russian).

[41] Ivanenkov G.V., Pikuz S.A., Shelkovenko T.A. et al. Review on modeling of processes of electric explosion of thin metal wires. Part 1. The basic processes of electric explosion of conductors in a vacuum. FIAN, Moscow (2004), 26 p. Preprint FIAN No 9 (in Russian).

[42] Ivanenkov G.V., Pikuz S.A., Shelkovenko T.A. et al. Review on modeling of processes of electric explosion of thin metal wires. Part 2. The physical properties of substances with high energy density in places through the metal wires. FIAN, Moscow (2004), 30 p. Preprint FIAN No 10 (in Russian).

[43] Kuskova N.I., Baklar′ V.Yu., Khainatskii S.A. Obtaining Ultrafine Metal Powders under Electric Explosion of Conductors in Liquid: Part III. The Optimum Mode for Explosion of Conductors in Gases; Comparison with Explosion in Liquid. *Surface Engineering and Applied Electrochemistry*, **45**(5), P. 382–386 (2009).

[44] Adamian Yu.E., Reznichenko P.V., Shneerson G.A. High-energy radiation generated during electric explosion of a conductor in a longitudinal magnetic field. *Technical Physics Letters*, **32**(4), P. 317–319 (2006).

[45] Kortkhondjia V.P. On the wire burst in water. *Technical Physics*, **51**(12), P. 1636–1638 (2006).

[46] Rousskikh A.G., Oreshkin V.I., Labetsky A.Yu., Chaikovsky S.A., Shishlov A.V. Electrical explosion of conductors in the high-pressure zone of a convergent shock wave. *Technical Physics*, **52**(5), P. 571–576 (2007).

[47] Kotov Yu.A., Ivanov V.V. Powder nanotechnology to create functional materials and devices for electrochemical energy. *Vestnik Rossiiskoi Akademii Nauk* (Herald of the Russian Academy of Sciences), **78**(9), P. 777–787 (2008), (in Russian).

[48] Belko V.O., Emelyanov O.A Nanosecond electric explosion of thin aluminum films. *Technical Physics Letters*, **35**(9), P. 861–864 (2009).
[49] Grigoriev A.N., Pavlenko A.V. Pressure at the electric explosion metal foils. *Technical Physics Letters*, **35**(9), P. 865–868 (2009).
[50] Bulgakov A.V., BulgakovaN.M., Burakov I.M., etc. *Synthesis of nanoscale materials under the influence of powerful streams of energy on substance*. Institute of Thermophysics, Siberian branch of Russian Academy of science, Novosibirsk (2009), 462 p. (in Russian).
[51] Hajnackij S.A. Conditions for realization of an optimum regime of the electric explosion of conductors in liquid media. *Technical Physics Letters*, **35**(4), P. 299–301 (2009).
[52] Volkov N.B., Meyer A.E., Sedoj V.S. etc. Mechanisms of metallic nanoparticle generation during an electric explosion of conductors. *Technical Physics*, **55**(4), P. 509–513 (2010).
[53] Doney R.L., Vunni G.B., Niederhaus J.H. Experiments and Simulations of Exploding Aluminum Wires: Validation of ALEGRA-MHD. ARL-NR-5299. SAND (2010), 6028 p.
[54] Rashmita Das, Basanta Kumar Das, Rohit Shukla et al. Analysis of electrical explosion of wire systems for the production of nanopowder. *Sadhana*, **37**(5), P. 629–635 (2012).
[55] Vorobiev V.S., Malyshenka S.P., TkachenkoS.i., Fortov V.E. Than initiated blast conductor? *Pis'ma v Zh. Eksp. Teor. Fiz.* (JETP Letters) **75**(8), P. 445–449 (2002), (in Russian).
[56] Pikuz S.A., Tkachenko S.I., Barishpol'tsev D.V., Ivanenkov G.V., Mingaleev A.R., Romanova V.M., Ter-Oganes'yan A.E., Shelkovenko T.A. Interpreting experimental data on the electric explosion of thin wires in air. *Technical Physics Letters*, **33**(8), P. 651–654 (2007).
[57] Lev M.L., Mirzabekov A.M., OstrovskyYu.N., Peregoud B.P. Explorer, Evaporation exceeds MHD instabilities. *Pis′ma v Zhurnal Tekhnicheskoi Fiziki* (Technical Physics Letters), **4**(14), P. 840–846 (1983), (in Russian).
[58] Sedoj V.S. *Direct receiving of nano-sized powders by electric explosion. Synthesis of nanoscale materials under the influence of powerful streams of energy on substance. Institute of Thermophysics* (chapter 4, 15), Siberian branch of Russian Academy of science, Novosibirsk (2009), 462 p. (in Russian).
[59] Lev M.L., Peregoud B.P. Development Time upholstering MHD instability of liquid conductors under its own power. *Zhurnal Tekhnicheskoi Fiziki* (Technical Physics), **47**(10), P. 2116–2121 (1977), (in Russian).
[60] Skripov V.P. *Metastable liquid*. Nauka, Moscow (1972), (in Russian).
[61] Skripov V.P., Skripov A.V. Spinodal decomposition (phase transitions via unstable states). *Sov. Phys. Usp.*, **22**(6), P. 389–410 (1979).
[62] Skripov V.P., Faysullin M.Z. Phase transitions Crystal-liquid-vapor and thermodynamic similarity. PHYSMATHLIT, Moscow (2003), 160 p. (in Russian).
[63] Rukhadze A.A. The electric explosion of conductors. Mir, Moscow, 1965, 360 p. (in Russian).
[64] Kotov Yu.A., Bagazeev A.V., Beketov I.V. etc. Properties of nickel oxide nanopowders prepared by electrical explosion of a wire. *Technical Physics*, **50**(10), P. 1279–1283 (2005).
[65] Khishchenko K.V., Tkachenko S.I., Levashov P.R. The melting wave in a metal fast heated by a high-power current pulse. *Technical Physics Letters*, **32**(2), P. 126–128 (2006).
[66] Pavlenko A.V., Grigoriev A.N., Afanasyev V.V. etc. Pressure waves generated by a nanosecond electric explosion of a tungsten wire in water. *Technical Physics Letters*, **34**(2), P. 129–132 (2008).
[67] Rumer Yu.B., Rivkin M.Sh. *Thermodynamics, statistical physics and kinetics*. Nauka, Moscow (1977), 552 p. (in Russian).
[68] Anisimov M.A. Investigations of critical phenomena in liquids. *Sov. Phys. Usp.*, **18**, P 722–744 (1974).
[69] *The physical encyclopedic dictionary*. Ed. A.M. Prokhorov Soviet encyclopedia, Moscow (1988), (in Russian).
[70] *Physical encyclopedia*, Vol. 5. Ed. A.M. Prokhorov. The great Russian encyclopedia, Moscow (1998), (in Russian).
[71] Stanley M. Walas. Phase Equilibria in Chemical Engineering. University of Kansasand The C.W. Nofsinger Company Butterworth Publishers Boston. London. Sydney, Wellington. Durban. Toronto (1985), 304 p.
[72] Landau L.D., Lifshitz M.E. Satistical physics. Nauka, Moscow (1964). (in Russian)
[73] Braut P. *Phase transitions*. Mir, Moscow (1967), (in Russian).
[74] Critical Phenomena Proceeding of conference on phenomena in the neighborhood of critical points. Washington, NBS Misc. Publ. 273 (1966) P. 1–242.

[75] adanff L.. Scaling, universality and operator algebras. In: Phase Transitions and Critical Phenomena, C. Domb, M.S. Green (eds.), Vol. 5a, Academic Press, New York (1976), P 1–34.
[76] Widm . Equation of state in neighborhood of the critical point. *J. Chem. Phys.*, **43**(11), P. 255–262 (1965).
[77] Kadanoff L.P. Scaling Laws for Ising Models Near Tc. *Physics*, **2**, P. 263–272 (1966).
[78] Patashinskii A.Z., Pokrovskii V.L. Behavior of ordered systems near the transition point. *Journal of Experimental and Theoretical Physics*, **23**(2), P. 292–297 (1966).
[79] Patashinskij A.Z., Pokrovskii V.L. *The theory of phase transitions*. Nauka, Moscow (1982), 381 p. (in Russian).
[80] Liu A.J., Fisher M.E. The three-dimensional Ising model revisited numerically, *Physica A*, **156**, P. 35–76 (1989).
[81] Guida R., Zinn-Justin. J. Critical exponents of the N-vector model. *J. Phys. A.: Math. Gen.* **31**, P. 8103–8121 (1998).
[82] Onsager L. Crystal Statistics. I. A two-dimensional model with an order-disorder transition. *Phys. Rev.* **65**(3,4), P. 117–149 (1944).
[83] Kaufman B., Onsager L. Crystal Statistics. III. Short-Range Order in a Binary Ising Lattice. *Phys. Rev.* **76**(8), P. 1244–1252 (1949).
[84] Wilson K.G. Renormalization Group and Critical Phenomena. I. Renormalization Group and the Kadanoff Scaling Picture. *Phys. Rev. B*, **4**(9), P. 3174–3183 (1971).
[85] Wilson K.G., Fisher M.E. Critical Exponents in 3.99 Dimensions. *Phys. Rev. Lett.*, **28**(4), P. 240–243 (1972).
[86] Wilson , Kogut J. The renormalization group and the ε-expansion. *Physics Reports*, **12**(2), P. 75–199 (1974).
[87] Anisimov, M.A. Critical phenomena in liquids and liquid crystal. Nauka, oscow (1987), (in Russian).
[88] Fisher M. *The nature of the critical state*. Moscow (1986), (in Russian).
[89] Ma Shang-keng. *The modern theory of critical phenomena*. Moscow (1986), 582 p.
[90] Ivanov D.Y. Critical phenomena in clean liquids. *Vestnik SibSUTI* **3**, P. 94–104 (2009), (in Russian).
[91] Ivanov D.Y. *Critical behavior of nonideal systems*. PHYSMATHLIT, Moscow (2003), 248 p. (in Russian).
[92] Ginzburg V.L. Several comments on the phase transitions of the second kind and microscopic theory of ferroelectric. *Fizika Tverdogo Tela* (Physics of the Solid State), **2**(9), P. 2031–2043 (1960), (in Russian).
[93] Ivanov D. Yu. Critical phenomena in clean liquids. *Vestnik SibSUTI* **3**, P. 94-104 (2009), (in Russian).
[94] Jsephsn B.D. Equation of state near the critical point. *J. Phys. C: Solid State Phys*, **2**(7), P. 1113–1116 (1969).
[95] Schofield P. Parametric representation of the equation of state near the critical point. *Phys. Rev. Lett.*, **22**(12), P. 606–609 (1969).
[96] Kudryavtseva A.V., Rykov A.V., Rykov S.V. Single nonanalityc equation of perfluoropropane state satisfiing a major theory of critical phenomena. *Vestnik of International Academy of Refrigeration*, **3**, P. 22–26 (2013), (in Russian).
[97] Migdal A.A. Equation of State of near critical point. *Zhurnal Eksperimental'noĭ i Teoreticheskoi Fiziki* (Journal of Experimental and Theoretical Physics), **62**(4), P. 1559–1573 (1972), (in Russian).
[98] Benedek G.B. *Optical mixing spectroscopy, with applications to problem in physics, chemistry, biology and engineering*. Polarisation, matiereetrayonnement. Presses Universitaires de France, Paris (1969), p. 49.
[99] Prigogine I., Kondepudi D. *Modern Thermodynamics*. / Ed. Odile Jacgb. John Wiley & Sons: Chichester, New York, Weinheim, Brisbane, Toronto, Singapore (1999).
[100] Frankel Ya.I. *Kinetic theory of liquids*. Nauka, Leningrad (1975), 562 p. (in Russian).
[101] Bennett F. *Wave of evaporation in metals. Physics of high energy densities*. Mir, Moscow (1974), (in Russian).
[102] Oreshkin V. I., Baksht R. B., Labetsky A. Yu., Rousskikh A. G., Shishlov A. V., Levashov P. R., Khishchenko K. V., Glazyrin I. V. Study of metal conductivity near the critical point using a microwire electrical explosion in water. *Technical Physics*, **49**(7), P. 843–848 (2004).
[103] KotovYu.A., Jaworski N.A. Study particles formed at the electric explosion of conductors. *Fizika I Khimia Obrabotki Materialov* (Physics and Chemistry of Materials Treatment), **4**, P. 24–28 (1978), (in Russian).

[104] Andreev S.V., Orlov S.N., *Samokhin A.N. Modeling of explosive boiling under Pulse-Laser heating. Effect of laser radiation on the absorbing medium.* Nauka, Moscow (2004), P. 127–148. (IOFAN, 60) (in Russian).

[105] Rosenthal S.E., Desjarlais M.P., Spielman R.B. et al. MHD Modeling of Conductors at Ultrahigh Current Density. *IEEE Trans. Plasma Sci.*, **28**(5), P. 1427–1433 (2000).

[106] Oreshkin V.I., Barengol′c S.A., Tchaikovsky S.A. Numerical calculation of the current specific action integral at the electrical explosion of wires. *Technical Physics*, **52**(5), P. 642–650 (2007).

[107] Sarry M.F. Thermodynamic theory of the equation of state of materials. *Technical Physics*, **43**(10), P. 1137–1144 (1998).

[108] Oreshkin V.I. Overheat instabilities in the electric explosion of wires. *Technical Physics Letters*, **35**(1), P. 36–39 (2009).

[109] Baksht R.B., Tkachenko S.I, Romanov V.M. etc. Stratification dynamics and the development of electrothermal instability at the wire explosion. *Technical Physics*, **58**(8), P. 1129–1137 (2013).

[110] Borisevich A. E., CherkasS.l. Effect of the conductor radius on the electric explosion dynamics: Magnetohydrodynamic simulation. *Technical Physics*, **57**(10), P. 1380–1386 (2012).

[111] Altshuler L.V., Kormer S.B., Bakanova A.A., Trunin R.F. The equation of state of aluminium, copper and lead to high pressure. *Zhurnal Eksperimental'noi i Teoreticheskoi Fiziki* (Journal of Experimental and Theoretical Physics). **38**(3), P. 791–798 (1960), (in Russian).

[112] Kormer S.B., Urlin V.D., Popova L.T. Interpolation equation of State and its application to the description of the experimental data on shock compression of metals. *Fizika Tverdogo Tela* (Physics of the Solid State), **3**, P. 2131 (1961), (in Russian).

[113] Altshuler L.V., Bakanova A.A., Trunin R.F. Drums isentropic and zero isotherm under high pressures. *Zhurnal Eksperimental'noi i Teoreticheskoi Fiziki* (Journal of experimental and theoretical physics), **42**(1), P. 91–104 (1962), (in Russian).

[114] Kormer S.B., Funtikov A.I., Urlin V.D., Komel'kov A.N. Dynamic compression of porous metals and equations of state with variable heat capacity at high temperatures. *Zhurnal Eksperimental'noi i Teoreticheskoi Fiziki* (Journal of Experimental and Theoretical Physics), **42**(3), P. 686–702 (1962), (in Russian).

[115] Kalitkin N.N., Kuzmina L.V. Curves cold compression at high pressures. *Fizika Tverdogo Tela* (Physics of the Solid State), **12**, P. 2314 (1971), (in Russian).

[116] Boissiere C., Fiorese G. Equation d′etat des metauxprenant en compte les changementsd′etat entre 300 et 200000 K pour toute compression appliation au cas du cuivre et de l'alluminium. *Rev. Phys. Appl.*, **12**(5), P. 857–872 (1977).

[117] Altshuler L.V., Bushman A.V., Fortov V.E., Sharipdzhanov I.I. An semi empirical equation of metals state in the wider area of phase diagram. In: Chislennye metody mehaniki sploshnoy sredy (Numerical methods for continuum mechanics), **7**(1), P. 5 (1976), (in Russian).

[118] Altshuler L.V., Bushman A.V., Zhernokletov M.V., Zubarev V.N., Leont′ev A.A., Fortov V.E. Izoentropy and equation of state of metals under high energy densities. *Zhurnal Eksperimental'noi i Teoreticheskoi Fiziki* (Journal of Experimental and Theoretical Physics), **78**(2), P. 741–760 (1980), (in Russian).

[119] Bushman A.V., Gryaznov V.K., Canelle G.I., et al. The dynamics of condensed matter in intense pulsed exposures. Thermodynamic properties of materials at high temperatures and pressures. (Preprint/Department of the Institute of Chemical Physics of the USSR). OIHF, Chernogolovka (1983), 48 p. (in Russian).

[120] Bushman A.V., Lomonosov I.V., Fortov V.E. Model full-range State equations of substances with high energy densities. (Preprint No. 6-287 / Institute of high temperatures of the USSR) IVTAN, Moscow (1989), 44 p. (in Russian).

[121] Altshuler L.V., Brusnikin S.E., Kuzmenkov E.A. Isotherms and functions Grûnajzena 25 metals. *Prikladnaya Mekhanika i Tekhnicheskaya Fizika* (Journal of Applied Mechanics and Technical Physics), **1**(161), P. 134–146 (1987), (in Russian).

[122] Altshuler L.V., Brusnikin S.E. Simulation of high-energy processes and wide-ranging State equation of metals. *Voprosy atomnoy nauki i tekhniki.* Seriya: matematicheskoe modelirovanie fizicheskih processov (Problems of atomic science and technology. Series: mathematic modelling of fisical processes), **1**, P. 3–42 (1992), (in Russian).

[123] Altshuler L.V., Brusnikin S.E. About determination of gruneisen parameter for strong unideal plasm. *Teplofizika Vysokikh Temperatur* (High Temperature), **27**(1), P. 42 (1989), (in Russian).

[124] Atzeni S., Caruzo A., and Pais V.A. Model equation-of-state for any material in condition relevant to ICF and to stellar interiors. *Laser and Particle Beams*, **4**(3-4), P. 393–402 (1986).

[125] Kolgatin S.N., Khachatur′yants A.V. Interpolation equation of state list of metals. *Teplofizika Vysokikh Temperatur* (High Temperature), **20**(3), P. 477–451 (1982), (in Russian).

[126] Basco M.M. Equation of state of metals in the approximation of the average ion. *Teplofizika Vysokikh Temperatur* (High Temperature), **23**(3), P. 483–491 (1985), (in Russian).

[127] Gathers G.R. Thermophysical properties of liquid copper and aluminum. *Intern. J. Thermophysics*, **4**(3), P. 209–226 (1983).

[128] Sapozhnikov A.T., Pershina A.V. Semi empirical equation of State of metals in a wide range of densities and temperatures. *Voprosy atomnoy nauki i tekhniki.* Seriya: Metodiki i programmy chislennogo resheniya zadach matematicheskoy fiziki (Problems of atomic science and technology. Series: methods and applications of numerical solution of problems of mathematical physics), **4**(6), P. 47–56 (1979), (in Russian).

[129] Karpov V.A., Fadeev A.P., Shpatakovskaja G.V. Calculation equations of state in laser fusion targets. (Preprint No. 147 / Keldysh Institute of applied mathematics Academy of sciences of USSR) IPM, Moscow (1982), 28 p. (in Russian).

[130] Belarusian A.V. Model equations of State, taking into account evaporation, ion and fusion. *Voprosy atomnoy nauki i tekhniki.* Seriya Termoyaderniy sintez (Problems of atomic science and technology. Series: thermonuclear fusion), **1**, P. 12-19 (1992), (in Russian).

[131] Medvedev A.B. *Modification model of van der Waals equation for dense states. Shock waves and extreme States.* Nauka, Moscow (2000), 341 p. (in Russian).

[132] Bespalov I.M., PolishchukA.Ya. Method of calculating the degree of ionization, thermal and electrical conductivity of Plasmas in a wide range of densities and temperatures. *Pis′ma v Zhurnal Tekhnicheskoi Fiziki* (Technical Physics Letters), **15**(2), P. 4–8 (1989), (in Russian).

[133] Bespalov I.M., Polishchuk A.Ya. Method of calculating transport coefficients of Plasmas in a wide range of parameters. (Preprint No. 1-257, USSR ACADEMY of SCIENCES, Institute of high temperatures). IVTAN, Moscow, 36 p. (in Russian).

[134] Mott N.F., Jones H. The theory of the properties of metals and alloys. New York (1958), 326 p.

[135] Zyryanov P.S. To the theory of electrical conductivity of metals. *Zhurnal Éksperimental'noĭ i Teoreticheskoi Fiziki* (Journal of Experimental and Theoretical Physics), **29**(3), P. 333–338 (1955), (in Russian).

[136] Keldysh L.V. Ionization in the Field of a Strong Electromagnetic Wave. *Soviet Physics JETP*, **20**, P. 1307–1314 (1965).

[137] Yermakov V.V., Kalitkin N.N. Electronic transport in dense plasma. *Fizika Plazmy* (Plasma Physics Reports), **5**(3), P. 650–658 (1979), (in Russian).

[138] Volkov N.B. Plasma conductivity model of metal. *Zhurnal Tekhnicheskoi Fiziki* (Technical Physics), **49**(9), P. 2000–2002 (1979), (in Russian)

[139] Burtsev V.A., Kalinin N.V. On electric conduction in the stage of proper explosion of conductors. Proceeding of 15th International Conference on High-Power Particle BEAMS St Petersburg, Russia, 2004 July 18-23, Efremov Scientific Research Institute of Electrophysical Apparatus, 830-833.

[140] Burtsev V.A., Kalinin N.V. On electrical conductivity at the stage of the actual explosion of conductors. In: Physics of Extreme States of Matter. Chernogolovka city, 2005, 156-158 (in Russian).

[141] Lee Y.T., More R.M. Electron conductivity model for dense plasmas. *Phys. Fluids*, **27**(5), P. 1273–1286 (1984).

[142] Likal′ter A.A. Conductivity degenerate gas quasi-atomic. *Teplofizika Vysokikh Temperatur* (High Temperature), **25**(3), P. 424–429 (1987), (in Russian).

[143] Likal′ter A.A. Gaseous metals. *Sov. Phys. Usp.*, **35**(7), P. 591–605 (1992).

[144] Rolader G.E., Batteh J.H., Desai P.V. Comparison of partition function calculation for metal plasmas. *J. Appl. Phys.*, **64**(3), P. 1101–1107 (1988).

[145] Vorobiev V.S., Rachel A.D. Numerical study of some modes of electric explosion of conductors. *Teplofizika Vysokikh Temperatur* (High Temperature), **28**(1), P. 18–23 (1990), (in Russian).

[146] Vorobiev V.S. Study of equilibrium liquid-vapor using interpolation equations of state. *Teplofizika Vysokikh Temperatur* (High Temperature), **33**(4), P. 557–564 (1995), (in Russian).

[147] Vorob′ev V.S., Malyshenko S.P. Phase equilibrium in a current-carrying liquid conductor in Z-pinch geometry. *Journal of Experimental and Theoretical Physics.* **84**(6), P. 1098–1105 (1997).

[148] Vorobiev V.S. On model description crystalline or liquid state. *Teplofizika Vysokikh Temperatur* (High Temperature), **34**(3), P. 397–406 (1996), (in Russian).

[149] Tkachenko S.I. Simulation of an early stage of a conductor's electrical explosion. *Technical Physics*, **45**(7), P. 950–952 (2000).

[150] Rinker G.A. Systematic calculation of plasma transport coefficients for the Periodic Table. *Phys. Rev. A*, **37A**(4), P. 1284–1297 (1988).

[151] Bobrov V.B., Allahyarov E.A. To the calculation of the electrical conductivity of fully ionized plasma with arbitrary electron degradation. II. Liquid metal plasma. *Teplofizika Vysokikh Temperatur* (High Temperature), **31**(3), P. 352–356 (1993), (in Russian).

[152] Perrot F., Dharma-Wardama M.W. Equation of state and transport properties of multispecies plasma: Application to multiply ionized Al plasma. *Phys. Rev. E*, **52**, P. 5352 (1995).

[153] Silverstrelli P.L. No evidence of a metal–insulator transition in a dense aluminum: a fist principle study. *Phys. Rev. B*, **60(II)**, P. 16382 (1999).

[154] Redmer R., Kuhbolt S. Transport coefficients for dense metal plasma. *Phys. Rev. E.* **62**, P. 7191 (2000).

[155] Apfelbaum E.M., Ivanov M.F. Calculation of transport coefficients with allowance for the chemical composition of a low-temperature high-density metal plasma. *Plasma Physics Reports*, **27**(1), P. 76–81 (2001).

[156] Apfelbaum E.M. Calculation of the electrical conductivity of liquid aluminium, copper and molybdenum. *High Temperature*, **41**(4), P. 466–471 (2003).

[157] Fortov V.E., Leontjev A.A., Dremin A.N. Parameter estimation of the critical point. *Teplofizika Vysokikh Temperatur* (High Temperature), **13**(5), P. 1072–1080 (1975), (in Russian).

[158] Fortov V.E., Leontiev A.A. Kinetics of evaporation and condensation on metal expansion by uniform entropy conditions. *Teplofizika Vysokikh Temperatur* (High Temperature), **14**(4), P. 711–717 (1976), (in Russian).

[159] Romanov G.S., Smetannikov A.S. Numerical simulation of layer pulsed discharge. *Pis′ma v Zhurnal Tekhnicheskoi Fiziki* (Technical Physics Letters), **51**(4), P. 678–685 (1981), (in Russian).

[160] Bushman A.V., Romanov G.S., Smetannikov A.S. Theoretical Modelling of the initial layer of pulse discharge in the light of the State equation of Explorer. *Teplofizika Vysokikh Temperatur* (High Temperature), **22**(5), P. 849–856 (1984), (in Russian).

[161] Romanov G.S., Smetannikov A.S. Numerical simulation of pulsed discharge with the layer of energy transfer radiation. *Zhurnal Tekhnicheskoi Fiziki* (Technical Physics), **52**(9), P. 1756–1761 (1982), (in Russian).

[162] Romanov G.S., Smetannikov A.S. Modeling of flat high current digits. Calculation of discharge in the MHD approximation. *Teplofizika Vysokikh Temperatur* (High Temperature), **28**(2), P. 209–215 (1990), (in Russian).

[163] Dul′nev G.N., Novikov V.V. Thermal mode of a lamp operating in the pulse. *Journal of Engineering Physics and Thermophysics*, **41**(1), P. 757–762 (1981).

[164] Grigoriev I., E.Z. Mejlihova (editors). *Physical Quantities. Guide.* Energoatomizdat, oscow (1991). 1232 p.(in Russian)

[165] Kotov Y.A., Azarkevich E.I., Medvedev A.I., Murzakaev A.M., Kuznetsov V.L., Samatov O.M., Demina T.M., Timoenkova A.K., Stoltz A.K. Nanopowders of oxides of iron, the electric wire explosion. *Inorganic Materials*, **43**(6), P. 633–637 (2007).

[166] Kotov Yu.A. Electric wire explosion-method of obtaining weal agregated powders. *Rossiiskie Nanotekhnologii* (Nanotechnologies in Russia), **4**(1-2), P. 40–51 (2009), (in Russian).

[167] Pozhidaeva O.V., Korytkova E.N., Drozdova I.A., Gusarov V.V. Phase state and particle size of ultradispersed zirconium dioxide as influenced by conditions of hydrothermal synthesis. *Russian Journal of General Chemistry*, **69**(8), P. 1219–1222 (1999).

[168] Almjasheva O.V., Gusarov V., Danilevich Ya.B., Kovalenko A.N., Ugolkov V.L. Nanocrystals of ZrO_2 as sorption heat accumulators. *Glass Physics and Chemistry*, **33**(6), P. 587–589 (2007).

[169] Almjasheva O.V., Ugolkov V.L, Gusarov V.V. Thermochemical analysis of desorption and adsorption of water on the surface of zirconium dioxide nanoparticles. *Russian Journal of Applied Chemistry*, **81**(4), P. 609–613 (2008).

[170] Almjasheva O.V., Vlasov E.A., Khabenskii V.B., Gusarov V.V. Thermal stability and catalytic properties of the composite amorphous Al_2O_3-nanocrystals ZrO_2. *Russian Journal of Applied Chemistry*, **82**(2), P. 217–221 (2009).

[171] Almjasheva O.V., Antonov U.F., Gusarov V.V., Danilevich Y.B., Didenko A., Kovalenko A.N. Dispersion of powdered coal with an oxide catalysts in water, as the liquid fuel. Proceedings of Photonics and Optoinformatike. SpbSU ITMO, St. Petersburg, 2010, P. 168–186 (in Russian).

[172] Almjasheva O.V., PostnovA.Yu., Maltseva N.V., Vlasov E.A. Thermostable catalysts for oxidation of hydrogen based on ZrO_2–Al_2O_3 nanocomposite. *Nanosystems: Physics, Chemistry, Mathematics*, **3**(6), P. 75–82 (2012), (in Russian).

[173] Almjasheva O.V, Gusarov V.V. Nucleation in media in which nanoparticles of another phase are distributed. *Doklady Physical Chemistry*, **424**(2), P. 43–45 (2009).

[174] Almjasheva O.V., Gusarov V.V. Features of the phase formation in the nanocomposites. *Russian Journal of General Chemistry*, **80**(3), P. 385–390 (2010).

[175] Rekhviashvili S. Sh., Kishtikova E. V. On the size dependence of the surface tension. *Technical Physics*, **56**(1), P. 143–146 (2011).

[176] Galkin A.A., Lunin V.V. Subcritical and supercritical water: a universal medium for chemical reactions. *Rus. Chem. Rev.*, **74**(1), P. 21–35 (2005).

[177] Valyashko V.M. Phase equilibrium with supercritical fluids. *Supercritical Fluids. Theory and practice*, **1**(1), P. 10–25 (2006), (in Russian).

[178] Gorbaty J.E., Bondarenko G.V. Overcritical State water. *Supercritical Fluids. Theory and practice*, **2**(2), P. 5-19 (2007), (in Russian).

[179] Volmer M. *Kinetics of new phase formation.* Nauka, Moscow (1986), 208 p. (in Russian).

[180] Kovalenko A.N. Limit possibilities of process intensification of energy conversion in nonequilibrium thermodynamic systems. Procceding of Two-phase Flow in Power Machines and Apparatus. Leningrad, Nauka (1991) (in Russian).

[181] Kovalenko A.N. Regulation and thermodynamic stability of non-equilibrium processes of energy conversion of speed. *Trudy CKTI*, JSC, **281**(2), (1996),(in Russian).

[182] Schuster H.G. Deterministic Chaos. An Introduction. WILEY-VCH Verlag GmbH & Co. KGaA, Weinheim, 1985.

[183] Feder J. Fractals. Plenum Press, New York (1988).

[184] Shklovskii B.I., Efros A.L. Percolation theory and conductivity of strongly inhomogeneous media. *Sov. Phys. Usp.*, **18**, P. 845–862 (1975).

[185] Dykhne A.M., Snarskii A.A., Zhenirovskii M.I. Stability and chaos in randomly inhomogeneous two-dimensional media and LC circuits. *Phys.Usp.* **47**, P. 821–828 (2004).

[186] Ziman J.M. *Models of Disorder.* Cambridge Univ. Press, Cambridg (1979), 592 p.

[187] Aranson I.S., Gaponov-Grekhov A.V., Rabinovitch M.M., Rogalsky A.V., Sagdeev R.Z. Lattice models in nonlinear dynamics of non-equilibrium environments. (Preprint of IAP AS USSR 163). Gorkij, 1987 (in Russian).

[188] Sokolov I.M. Dimensionalities and other geometric critical exponents in percolation theory. *Sov. Phys. Usp.*, **29**, P. 924–945 (1986).

[189] Mandelbrot B.B. *Fractals: Form, Chance and Dimension.* Freeman, San Francisco (1977), 365 p.

[190] Rényji A. On a new axiomatic theory of probability. *Acta Mathematica Hungaria*, **6**(3-4), P. 285–335 (1955).

[191] Klimontovich Yu.L. Entropy and information of open systems. *Phys. Usp.*, **42**, P. 375–384 (1999).

NANOSYSTEMS: PHYSICS, CHEMISTRY, MATHEMATICS, 2014, 5 (2), P. 294–306

SYNTHESIS OF GRAPHENE NANOPLATELETS FROM PEROXOSULFATE GRAPHITE INTERCALATION COMPOUNDS

A. V. Melezhyk, A. G. Tkachev

Tambov State Technical University, Tambov, Russia

nanocarbon@rambler.ru, nanotam@yandex.ru

PACS 81.07.-b, 81.05.ue

Ultrasonic exfoliation of expanded graphite compound obtained by cold expansion of graphite intercalated with peroxodisulfuric acid was shown to allow the creation of graphene nanoplatelets with thickness of about 5-10 nm. The resulting graphene material contained surface oxide groups. The expanded graphite intercalation compound was exfoliated by ultrasound much easier than thermally expanded graphite. A mechanism for the cleavage of graphite to graphene nanoplatelets is proposed. It includes: (1) formation of ionic graphite compound intercalated with peroxodisulfate anions; (2) decomposition of intercalated peroxodisulfate anions with formation of active free radicals which (3) attach covalently to carbon atoms; (4) cleavage and expansion of the graphite crystal due to the thickening of the peripheral region of graphene layers and release of gaseous oxygen between graphene layers; (5) hydrolysis of the expanded graphite compound; and, finally, (6) ultrasonic breaking of graphene nanoplatelet agglomerates.

Keywords: graphene, graphene nanoplatelets, peroxodisulfuric acid, graphite intercalation compounds, cold expansion.

1. Introduction

Currently graphene and graphene-based nanocomposites attract great attention. Both pure graphene and nanocomposite materials, such as graphene/carbon nanotubes, graphene/polyaniline, graphene/metal oxides and more complex systems, containing different functional groups, structures, and particles are currently being investigated. By definition, graphene is a monolayer of carbon atoms. However, sometimes "graphene" is used as a general term including few-layered and multi-layered graphene materials. Graphene nanoplatelets are one of the graphene materials produced by a number of carbon nanomaterial manufacturers, for example, xGnP by XG Sciences (http://xgsciences.com/). This is multi-layered graphene in the form of flakes or plates with thickness of 1–20 nm and size in plane of 1–50 microns (various grades available). Among the most promising applications of xGnP XG Sciences claims are for electrode materials for supercapacitors, anode materials for lithium batteries, conductive ink, heat-conductive films and coatings, additives for light composite materials, films and coatings shielding electromagnetic radiation, substrates for chemical and biochemical sensors, packing materials with improved barrier properties, additives which increase the strength of concrete, additives for composites with metal matrix. Furthermore, as follows from published data, the addition of graphene nanoplatelets into polymer composite materials, besides increasing electrical and heat conductivity, also increases strength, resistance to cracking, fire, wear and reduces the friction coefficient. Using graphene is highly efficient as an additive to liquid, consistent and solid lubricants. For example, the introduction of graphene nanoplatelets to polytetrafluoroethylene reduces friction wear by more

than three orders of magnitude [1]. There are several reviews on graphene materials, their methods of preparation and applications in various fields [2-5].

It should be noted that although the terms "nanoplatelets", "size in plane", "diameter in plane" are often used, in fact, these particles usually are not flat but deformed flakes of irregular shapes, often aggregated.

Theoretically, graphene monolayers provide the highest performance in a variety of applications. However, graphene monolayers are very expensive and it is difficult to work with them because of their tendency to agglomerate in dry form and in suspensions. Currently, graphene monolayers were obtained as deposits on different supports or as dilute dispersions stabilized with surfactants in solvents. The use of such dilute graphene monolayer dispersions as additives into composite materials is problematic because of need to remove surfactant, which is strongly adsorbed on the surface of graphene. Multilayered graphene, in the form of graphene nanoplatelets, provides better effect-to-cost ratio than graphene monolayers in most applications, with the exception of nanoelectronics. In many applications, such as polymeric composite materials, graphene nanoplatelets and carbon nanotubes give similar results.

An analogy with single-walled and multiwalled carbon nanotubes (CNTs) can be used. Although by a number of parameters single-walled CNTs are most efficient, currently they are too expensive, and using multi-walled CNTs provides better effect-to-cost ratio. For some applications, graphene nanoplatelets can be more effective than multiwalled CNTs, due to higher electric and heat conductivity and low coefficient of friction.

For mass application of graphene-based materials, one of the key issues is the development of an effective, inexpensive and scalable process for their production. Various methods for obtaining graphene materials were reviewed in [2-5]. The first group of methods is based on the cleavage of crystalline graphite, expanded graphite or graphite intercalation compounds by ultrasonic treatment of the graphite materials suspended in organic solvents or in water in presence of surfactants. Thin flakes, consisting of single or multiple layers of graphene, were thus obtained by these methods.

In the second group of methods, crystalline graphite or thermally expanded graphite is oxidized to graphite oxide, which spontaneously exfoliates to monolayers when dispersed in water. Then graphite oxide is reduced to graphene in presence of substances, preventing the collapse of graphene layers back into the graphite structure. Such substances may be surfactants, nanoparticles of various compounds or water-soluble polymers.

Ultrasonic exfoliation of various forms of graphite usually gives graphene nanoplatelets with a wide distribution of thicknesses, containing some amount of graphene monolayers. Concentration of the graphene nanoplatelets in dispersions obtained by these methods is very small, on the order of 0.01–0.1 g/l. Furthermore, the content of surfactant in the dispersions obtained is usually much higher than the content of graphene materials itself. For these reasons, the mass production of graphene materials by these methods is rather expensive, which is reflected in high cost of various forms of graphene materials, including graphene nanoplatelets offered by manufacturers of carbon nanomaterials.

Methods of obtaining graphene via graphite oxide, principally, are most flexible for the synthesis of various graphene-based nanostructures and other nanosized components [5]. However, the known methods of graphite oxide syntheses, for example by oxidation of crystalline graphite with potassium chlorate in nitric acid or potassium permanganate in sulfuric acid, are very expensive, take long time and become dangerous (risk of explosion) when performed at larger scales. So the cost of graphite oxide is also high.

In [6-8], graphite material was described called as "microflaky graphite". In modern terminology, this material was graphene nanoplatelets. In these studies, the key step was intercalation of graphite with solution of peroxide compounds (peroxomonosulfuric acid, peroxodisulfuric acid, ammonium persulfate) in sulfuric acid. Under certain conditions, the graphite intercalation compounds were formed containing intercalated anions of peroxosulphuric acids (peroxomonosulphuric or peroxodisulfuric). These compounds are unstable at room temperature and decompose, forming molecular oxygen between graphene layers, swelling the crystal, so a phenomenon similar to the thermal expansion of graphite was observed, but at room temperature. The extent of such "cold" expansion, defined by the apparent volume, is close to thermal expansion which occurs at high-temperature treatment (thermal shock) of graphite intercalated compounds in the common technology of the thermally expanded graphite production. In worm-like particles of both expanded graphite compounds and thermally expanded graphite, the graphite crystal is already split into nanoplatelets and all that remains is to break their aggregates and remove intercalated species if needed.

The purpose of this paper is to explore the possibility of obtaining graphene materials from expanded graphite formed by cold expansion of graphite intercalated with peroxosulfate compounds and determine the parameters of materials obtained depending on the preparation conditions.

2. Experimental

2.1. Starting materials

The following starting materials were used in this study.

Natural graphite GSM-1, 99.9% purity (supplied by "Resource-C" Ltd., Russian Federation).

Ammonium persulfate (APS), "Pure for analysis" grade.

Thermally expanded graphite with bulk density of 4 kg/m^3, produced by UniChimTek-Graflex Ltd. (Russian Federation).

Surfactant "NF" (Russian standard GOST 6848-79) produced by "Pigment" Ltd. (Russian Federation), comprises oligomeric product of polycondensation of naphtalenesulfonic acid with formaldehyde, sodium salt.

100% sulfuric acid was prepared by addition of pre-calculated amount of 65% oleum to 95% sulfuric acid.

Ultrasonic treatment was performed with IL-10-2.0 installation (electrical power up to 2 kW). Optical density was measured with KFK-3 spectrophotometer.

2.2. Synthesis procedure

Synthesis of expanded graphite compound was performed as described previously [6-8]. Graphite was treated with a solution of APS in sulfuric acid (6.67 g APS per 1 g graphite). In a few minutes, the blue intercalation compound of graphite formed, which, according to [8], was graphite peroxodisulfate of the composition $C_{22.5}\ HS_2O_8^-\ 2.5H_2SO_4$. This compound gradually decomposed at room temperature with expansion of the crystals due to the evolution of gaseous oxygen between graphene layers. The rate of expansion depended on temperature. For example, at 40° C, 2 hours was sufficient for complete expansion. Very bulky mass formed consisting of yellow-brown worm-like particles. This process was called "cold expansion of graphite" [8]. The apparent volume of expanded graphite compound at the above specified ratio of reactants was 300 cm^3/g of starting graphite. The resulting

expanded graphite compound was treated with water and washed on filter to neutral pH. Upon hydrolysis, the color of the expanded material changed from yellow-brown to gray. This material, containing 0.9% of dry substance, was used in following experiments in wet form without drying. Mass content of sulfur in the dry substance was 0.7%. Worm-like particles of this product were very similar to thermally expanded graphite and represented aggregates of interconnected graphene nanoplatelets, forming a very bulky porous structure. Drying resulted in dramatic decrease of the apparent volume and bonding of graphene nanoplatelets, probably due to capillary forces.

2.3. Samples properties and methods of testing

The crude material, obtained as described above, consisted of worm-like particles. Under ultrasonic treatment of an aqueous suspension, these particles were dispersed to graphene nanoplatelets. The degree of dispersion was evaluated by optical density (D) of treated dispersions. Thinner graphene particles, in general, produced larger D values. Aggregation tended to decrease D values. To determine the optical density, 0.250 g surfactant NF, 200 cm^3 water and a weighed portion of wet graphene material were placed in a 250 cm^3 beaker, so that the mass concentration of solids in the resulting mixture was from 0.02–0.035 g/dm^3, an optical density range convenient for measurement. The mixture was sonicated under cooling in a water bath and periodically, samples were taken for optical density measurement. The absorbance was measured in a 1 cm optical length cuvette at wavelength of 500 nm. Determination was carried out for no more than 2 minutes after ultrasound was off, because optical density slowly dropped over time, probably due to reversible particle aggregation. The resulting dispersions exhibited the characteristic pearlescence due to orientation of nanoplatelets in stream of liquid under stirring. Lambert-Beer law was observed in these systems. This allowed the calculation of the light absorbance coefficient (K):

$K=D/(CL)$, where

K – Light absorbance coefficient, $dm^3/g.cm$;

D – Optical density (corrected by subtraction of slight absorbance of surfactant NF at 500 nm), dimensionless;

C – Concentration of graphene material, g/dm^3;

L – Optical length of cuvette, cm.

The K value relatively weakly dropped with increasing wavelength in the visible region of spectrum (reduced by 15% from 500 to 800 nm).

Electronic images of samples were obtained using a dual-beam scanning electron microscopic complex Neon 40, Carl Zeiss.

3. Results and discussion

3.1. Preparation of graphene nanoplatelets via graphite intercalation compounds

At first glance, intercalation of foreign particles between the layers of graphite could weaken the bond between them and allow easier exfoliation. This might work with covalent attachment of fluorine atoms to the graphene skeleton. However, almost all known intercalants, capable of penetrating between the graphite layers are strong electron donors or acceptors and form charge transfer or ionic structures with graphene layers in which the bonding between graphene layers is reinforced due to electrostatic forces.

However, many graphite intercalation compounds are able to undergo secondary thermal or chemical transformations that result in a profound restructuring of the crystal structure, accompanied with exfoliation of crystalline intercalated compounds to graphene nanoplatelets and even graphene monolayers. The most common example is the thermal expansion of graphite intercalation compounds (mostly graphite sulfate or nitrate), which leads to the formation of expanded graphite. Thermally expanded graphite may be dispersed by sonication to graphene nanoplatelets in alcohol solution. However, graphene nanoplatelets obtained in this way were relatively thick, on the order of 50 nm [2].

Highly exfoliated thermally expanded graphite (HETEG) was obtained, which can be split into much finer nanoplatelets. HETEG was obtained by thermal decomposition of the graphite compound C_2F*nClF_3 at 573–723 K. As a result, molecular chlorine and chlorofluoro-carbons were generated as by-products. The HETEG easily dispersed in organic solvents or in aqueous solutions of sodium dodecylbenzenesulfonate, and formed one-, two-, and few-layered graphene [2, 9]. However, this method has a serious disadvantage – very toxic and dangerous reagents and by-products, so it is hardly acceptable for the mass production of graphene.

In [10], expanded graphite with a structure resembling the thermally expanded graphite was obtained by treatment of graphite intercalation compound KC_8 with water or ethanol. Processing alcoholic suspension of the product obtained by microwave radiation resulted in graphene nanoplatelets with thickness of about 10 nm.

3.2. Preparation of graphene nanoplatelets via expanded graphite peroxosulfate compound

Fig. 1 shows the dependence of light absorption coefficients for ultrasonic treatment time for different forms of expanded graphite in aqueous suspensions containing surfactant NF (1.25 g/dm^3) as stabilizer. Four types of expanded graphite or expanded graphite compounds were examined in these experiments:
1) thermally expanded graphite (TEG);
2) expanded compound of graphite obtained by cold expansion (at 40° C) of graphite intercalated with ammonium persulfate solution in concentrated (95%) sulfuric acid;
3) expanded compound of graphite obtained by cold expansion (at 40° C) of graphite intercalated with ammonium persulfate solution in 100% sulfuric acid;
4) expanded compound of graphite obtained by cold expansion (at 40° C) of graphite intercalated with ammonium persulfate solution in 100% sulfuric acid containing 1% of free SO_3.

As it follows from Fig. 1, thermally expanded graphite showed the least ultrasonic exfoliation in our experiments.

As can be seen from Fig. 1, the expanded graphite compounds obtained by cold expansion of graphite intercalated with APS in sulfuric acid was dispersed ultrasonically significantly better than thermally expanded graphite. Moreover, the dispersal strongly depends on content of water in the sulfuric acid used as a solvent. The presence of 5% water in sulfuric acid significantly retards dispersing ability. Considering the data obtained earlier [6-8, 11], we can assume the following mechanism for the processes occurring in this system. The first step is formation of blue graphite intercalation compound containing intercalated anions of peroxodisulfuric acid. Its composition was determined to be $C_{22.5}HS_2O_8^-$*$2.5H_2SO_4$ [11]. This compound gradually decomposed at room temperature with the evolution of oxygen gas (with admixture of ozone) and formed worm-like particles of expanded graphite compound with apparent volume up to 300 cm^3/g of starting graphite. A similar graphite intercalation compound formed (at low temperature) with peroxomonosulfuric acid, but it

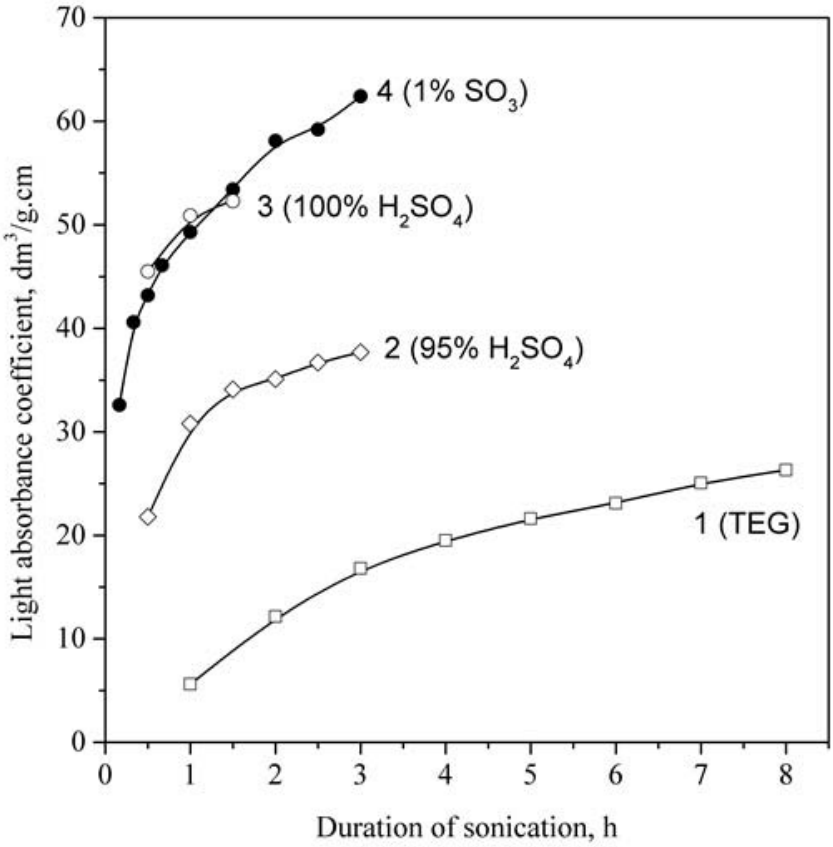

FIG. 1. Dependence of light absorbance coefficient on time of ultrasonic treatment for different forms of expanded graphite in aqueous suspensions containing surfactant NF (1.25 g/dm^3) as a stabilizer

was less stable and its decomposition, accompanying with "cold" expansion, proceeded even at 0° C. Visually, the process of cold expansion of graphite peroxosulfate compounds is very similar to the thermal expansion of intercalated graphite, however, occurs at temperature close to room temperature.

This process consists of complex chemical and structural transformations. Presumably, the cold expansion process begins with the decomposition of intercalated and dissolved peroxosulfate compounds, which give rise to highly reactive species:

$$H_2S_2O_8 \rightarrow 2HSO_4^{\cdot} \tag{1}$$

$$H_2SO_5 \rightarrow HSO_4^{\cdot} + OH^{\cdot} \tag{2}$$

$$HS_2O_8^{-} \rightarrow HSO_4^{-} + SO_4 \tag{3}$$

$$SO_4 \rightarrow SO_3 + O \tag{4}$$

$$S_2O_8^{2-} \rightarrow 2SO_4^{-\cdot} \tag{5}$$

These active species react with graphene layers, forming covalent bonds with carbon. The color of the resultant expanded graphite compound is yellow to yellow-brown. XRD data for the expanded substances show a broad halo with no sharp peaks characteristic for crystalline graphite compounds [11]. Increasing the apparent volume and conversion of the crystalline flake graphite particles into worm-like ones is due to the evolution of oxygen gas between the graphene layers. This gas was produced simultaneously in peroxide compounds decomposition and the oxidation of the graphene skeleton.

We can assume that in the yellow expanded graphite compound, the flat aromatic system of graphene layers is broken by the covalent attachment of -OSO_3H groups to carbon atoms, similarly to graphite fluoride and graphite oxide. In [11], based on the measurements of the volume of oxygen gas evolved in the process of "cold" expansion, the degree of oxidation of carbon skeleton was determined for the expanded graphite compounds obtained in the graphite-$H_2S_2O_8$-H_2SO_4 ternary system.

It was found that one group -OSO_3H (attached covalently or as an anion) corresponds to x=7 carbon atoms, wherein, the x value decreases with excess $H_2S_2O_8$ in the starting system. It should be noted that for ionic compounds of graphite particles with electron accepting species characteristic value of x usually is in the range of 22 to 24, while for graphite fluorides x value usually is 1 to 6. However, in graphite monofluoride CF the C-F bond is purely covalent, carbon layers are non-planar, non-aromatic and do not conduct electric current. In lower graphite fluorides (C_2F, C_4F, C_6F), the fluorine bond with carbon skeleton becomes more ionic, and carbon layers become more planar and gain conductivity. Possibly, by degree of oxidation of carbon skeleton the products of "cold" expansion of graphite intercalated with peroxosulfates can be compared with lower graphite fluorides.

As can be seen from Fig. 1, the expanded graphite compound obtained by using anhydrous sulfuric acid, dispersed under ultrasonic treatment was significantly better than that obtained using 95% sulfuric acid. This can be attributed to the difference in acidity. It is known that auto-dissociation of concentrated sulfuric acid occurs according to the scheme:

$$H_2SO_4 + H_2O \leftrightarrow HSO_4^- + H_3O^+ \tag{6}$$

Thus, acidity of concentrated sulfuric acid corresponds to ion H_3O^+. Auto-dissociation of anhydrous sulfuric acid proceeds in another way:

$$2H_2SO_4 \leftrightarrow HSO_4^- + H_3SO_4^+, \quad [H_3SO_4^+] \cdot [SO_4^-] = 2 \cdot 10^{-4} \tag{7}$$

$$2H_2SO_4 \leftrightarrow HS_2O_7^- + H_3O^+, \quad [H_3O^+] \cdot [HS_2O_{7^-}] = 4 \cdot 10^{-5} \tag{8}$$

Molecular-ion composition of anhydrous sulfuric acid can be described by the following data [12]:

H_2SO_4 — 99.5%
HSO_4^- — 0.18%
$H_3SO_4^+$ — 0.14%
H_3O^+ — 0.09%
$HS_2O_7^-$ — 0.05%
$H_2S_2O_7$ — 0.04%

Even a small admixture of water (tenths %) inhibits reactions (7) and (8), and dissociation scheme (6) becomes dominant [12].

Thus, in anhydrous sulfuric acid, the $H_3SO_4^+$ cation dominates among ions, causing acidity, and it is a much stronger acid than H_3O^+. In a solution of ammonium persulfate in anhydrous sulfuric acid, peroxodisulfuric acid is formed:

$$(NH_4)_2S_2O_8 + 2H_2SO_4 \leftrightarrow 2NH_4HSO_4 + H_2S_2O_8 \tag{9}$$

In an anhydrous sulfuric acid medium it can be protonated:

$$H_2S_2O_8 + H_3SO_4^+ \leftrightarrow H_3S_2O_8^+ + H_2SO_4 \tag{10}$$

Obviously, the protonated form of peroxodisulfuric acid is a much stronger oxidant than peroxodisulfuric acid, and this results in higher oxidation state of graphite in the compounds formed. It is also obvious that the presence of ammonium salts somewhat reduces the acidity of the system because HSO_4^- anions are basic in the medium of sulfuric acid and

form a buffer system with acidic cations. For this reason, using peroxodisulfuric acid without ammonium salts (obtained by mixing sulfuric acid with concentrated hydrogen peroxide and oleum as described in [7]) would be more efficient for oxidative intercalation of graphite. However, the preparation and use of this system is dangerous because of great evolution of heat when mixing the components.

Hydrolysis of the cold-expanded graphite compounds formed in the systems studied resulted in transition of yellow or yellow-brown color to gray, and this was accompanied by some evolution of oxygen gas (with admixture of ozone). One can suppose that addition of water not only leads to hydrolytic cleavage of sulfate groups attached to carbon or removing hydrosulfate anions from interlayer space, but also causes redox disproportionation according to the scheme proposed in [13]. Namely, the central area of the carbon layers is reduced to graphene structure and peripheral area is oxidized to graphite oxide structure.

According to [14], samples of "microflaky graphite" contained 6% of the graphite oxide phase on the surface of graphite microflakes (nanoplatelets in modern terminology). It is due to the presence of these hydrophilic graphite oxide groups that the hydrolyzed material is well dispersed in water by ultrasonication (however, aggregation takes place in the absence of a surfactant). When dried, the relatively strong bonding of graphene nanoplatelets occurs with formation of elastic films [7]. This feature of graphene nanoplatelets, obtained via peroxosulfate graphite intercalation compounds, favors application of this material in composites with polar polymers (epoxy, phenol-formaldehyde, etc.).

The value of the light absorbance coefficient (Fig. 1) depends on the thickness of the graphene nanoplatelets and their aggregation in an aqueous dispersion. The smaller the average thickness of graphene nanoplatelets and the less they are aggregated, the greater should be the value of K. Unfortunately, due to overlap of these two factors, it is not possible to evaluate each of them separately by the value of K. However, in the presence of a sufficiently effective surfactant, such as dispersant NF, sonication of graphene material suspensions resulted in completely transparent dispersions, while ultrasonic treatment without the addition of a surfactant led to transformation of the initial worm-like particles (which can be regarded as strong agglomerates of nanoplatelets chemically bonded at their edges) into the large loose flakes (weak agglomerates of nanoplatelets connected by adsorption forces). Thus, we can assume that in the presence of an effective surfactant, agglomeration is minimal and change in the K value is mainly due to splitting of the initial worm-like particles and changing the average thickness of graphene nanoplates depending on the preparation conditions and dispersion. Furthermore, observing of the Lambert-Beer law indicates that agglomeration is minimal in the systems studied. It is interesting to compare our data (Fig. 1) with similar data in literature. In [15], the ultrasonic cleavage of graphite crystal in an aqueous solution of sodium dodecylbenzene sulfonate (graphite starting concentration of 0.1 g/dm^3, DDBS 0.5 g/dm^3) was investigated. The light absorbance coefficient of the sonicated substance at 660 nm (after separation of the coarse fraction by centrifugation) was found to be 1390 ml/mg.m, which is equivalent to 13.9 dm^3/g.cm. The number of monolayers in graphene nanoplatelets so obtained, as estimated by transmission electron microscopy, was in the range of 1–15, with maximum at the distribution of about 5 monolayers.

In [16], the optical properties of aqueous dispersions of chemically derived graphene monolayers were studied. It was found that optical density vs. concentration plots in this system deviate from Lambert-Beer law. From the data given in this work, the effective light absorbance coefficient can be estimated (very approximately because of deviation from Lambert-Beer law) to be 33 dm^3/g.cm at 400 nm and 25 dm^3/g.cm at 600 nm. It was shown in [16] that at concentrations of graphene over 10 mg/dm^3 aggregation of graphene

nanoplatelets was observed, but at lower concentrations spontaneous curling of graphene layers into scrolls occurred. Thus, the optical properties of aqueous dispersions of chemically derived graphene were dependent on aggregation and scrolling of graphene nanoplatelets.

It is difficult to compare our data with the above-cited, because it is obvious that aggregation strongly depends on the nature of surfactant and surface groups on graphene nanoplatelets. Relatively large values of K observed in the present work probably are due both factors — presence of hydrophilic surface groups and efficient surfactant used.

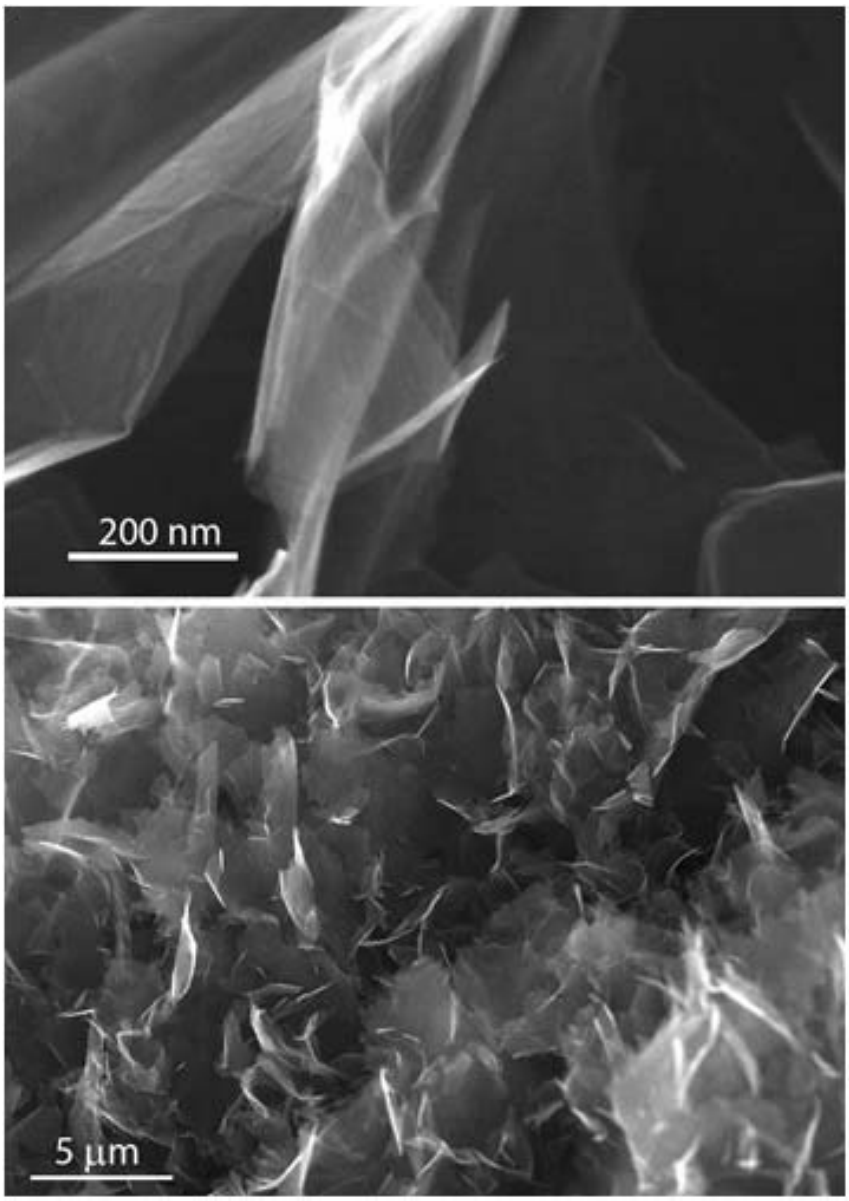

Fig. 2. SEM images of graphene material obtained by sonication of expanded graphite compound in aqueous suspension without addition of surfactants

Fig. 2 shows SEM images of the graphene material obtained upon ultrasonic treatment of cold-expanded graphite compound (after hydrolysis) in aqueous suspension without the addition of surfactants. These images are very similar to the analogous materials described in numerous literary sources and avenues of firms producing graphene materials. The thickness of nanoplatelets can be estimated very roughly from nanoplatelets butt-ends

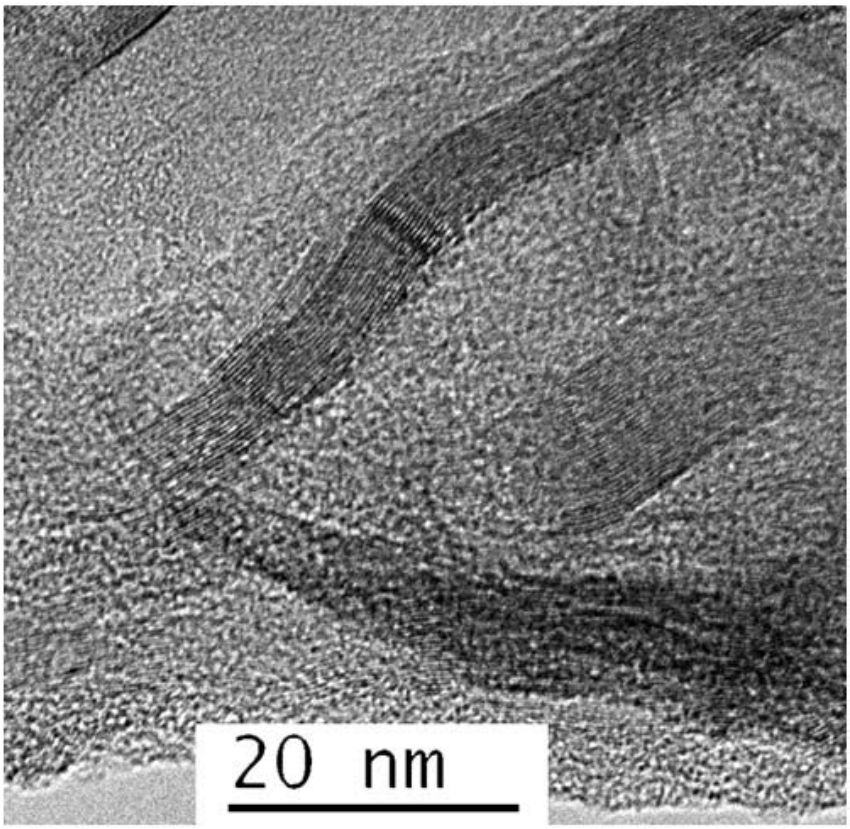

FIG. 3. TEM images of graphene material obtained by sonication of expanded graphite compound in aqueous suspension without addition of surfactants

as the order of not more than 5–10 nm. More accurate estimation from SEM images is not possible because of limited resolution of the scanning electron microscope.

In Fig. 3 there are images of the material in transmission electron microscope. In places where nanoplatelets fragments were directed along electron beam, images were observed allowing estimation of the number of graphene layers. As is seen from Fig. 3, the platelets are of different thickness. Two platelets in the field of view contain nearly 15 and 25 carbon layers correspondingly. Attempts to determine average thickness of nanoplatelets via surface area of dry samples were unsuccessful because drying resulted in strong glueing of nanoplatelets. The surface area of graphene nanoplatelet samples obtained by sonication of expanded graphite compound in aqueous suspension (without surfactant) was determined by adsorption of Methylene Blue in acidic aqueous solution according to Russian standard GOST 13144-79 (Graphite. Methods of determination specific surface area) to be 120 m^2/g. If compared to the theoretical surface area of graphene monolayer, 2630 m^2/g, this corresponds to 22 layers as the average-by-weight number of graphene layers in the material obtained, and average thickness of 7.4 nm. Probably, more prolonged sonication or addition of surfactants could decrease the average thickness of nanoplatelets in the material obtained.

In aqueous dispersions without added surfactant, despite the presence of hydrophilic graphite oxide groups, particles of the investigated graphene materials form large aggregates in the form of fuzzy flocks with visual size up to several millimeters. Apparently, these aggregates are weak. Obviously, ultrasonic treatment of much diluted aqueous dispersion of expanded graphite compound (after hydrolysis) in presence of a surfactant could provide most efficient separation of graphene nanoplatelets and retard aggregation. However, such

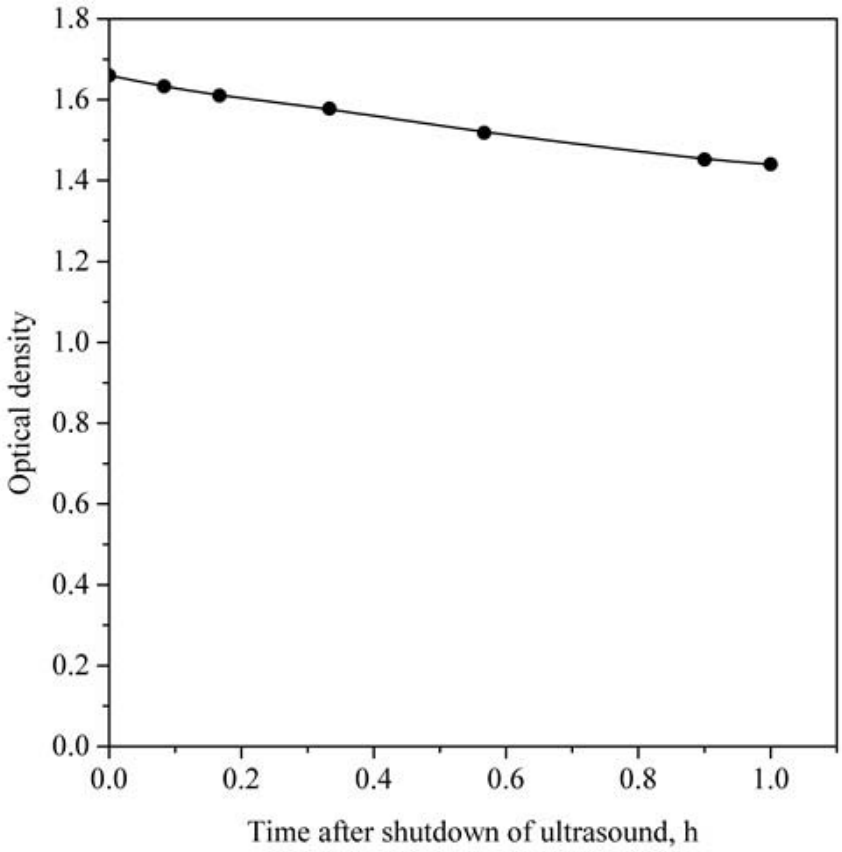

FIG. 4. Dependence of optical density of graphene nanoplatelets dispersion in aqueous solution of 1.25 g/dm^3 surfactant NF on time after switching off ultrasonic apparatus

a method is too expensive for mass production. Besides, surfactants commonly used for stabilization of graphene (monolayer and multilayered) dispersions in water, are strongly adsorbed on graphene surface and it is very difficult to remove them by washing. This creates a problem if the graphene material is intended for application in polymeric composite materials. Sonication of the aqueous dispersions of the expanded graphite compound in water without adding a surfactant gives aggregated material, consisting of weak agglomerates, without problems caused by the presence of surfactant. This material can be easily produced large scale and can be introduced into organic formulations by exchange of water for organic solvent. So, sonication without surfactant is a compromise between suitability of preparation and quality of the graphene nanoplatelets obtained, if we accept thickness of nanoplatelets and degree of aggregation as criteria of quality.

When storing aqueous dispersions of graphene nanoplatelets, obtained by sonication of dilute suspensions of graphene material (0.02-0.035 g/dm^3) in the presence of surfactant NF (1.25 g/dm^3), optical density slowly decreases after shutdown of ultrasound (Fig. 4). This most likely indicates reversible aggregation of nanoplatelets.

With prolonged standing (several days), the initially transparent dispersion of graphene nanoplatelets partially precipitated in form of flocks, but formed again transparent brownish-gray solution at shaking. The solution exhibited characteristic pearl effect due to orientation of nanoplatelets in flow of liquid. It can be assumed that aggregates of nanoplatelets formed

in these conditions are not strong and aggregation is easily reversible upon stirring. It is possible that there would be no aggregation when using a more efficient surfactant.

Thus, the process of cold expansion of peroxosulfate graphite intercalation compounds can be used to obtain graphene nanoplatelets.

4. Conclusions

1. Expanded graphite compounds formed upon cold expansion of the graphite intercalated with peroxosulfate compounds easily exfoliate under sonication to form graphene nanoplatelets.

2. Intercalation of graphite with a solution of ammonium persulfate in anhydrous sulfuric acid gives more fine graphene nanoplatelets compared to intercalation in concentrated (95%) sulfuric acid. Presumably, admixture of water reduces the medium acidity and oxidative efficiency of the intercalation system, and this, in its turn, decreases the degree of carbon skeleton oxidation.

3. Presumably, covalent attachment of hydrosulfate groups to graphene layers occurs during the cold expansion process, resulting in yellow expanded graphite compound.

4. Expanded graphite compounds, obtained by cold expansion, exfoliate to graphene nanoplatelets under sonication significantly easier than thermally expanded graphite.

References

[1] Kandanur S.S., Rafiee M.A., Yavari F., Schrameyer M., Yu Z.-Z., Blanchet T.A., et al. Suppression of wear in graphene polymer composites. *Carbon*, **50**(9), P. 3178–3183 (2012).

[2] Graifer E.D., Makotchenko V.G., Nazarov A.S., Kim S.-G., Fedorov V.E. Graphene: chemical approaches to synthesis and modification. *Uspekhi Khimii* (Advances in chemistry, Russian), **80**(8), P. 784–804 (2011).

[3] Soldano C., Mahmood A., Dujardin E. Production, properties and potential of graphene. *Carbon*, **48**(8), P. 2127–2150 (2010).

[4] Singh V., Joung D., Zhai L., Das S., Khondaker S.I., Seal S. Graphene based materials: Past, present and future. *Progress in Materials Science*, **56**(8), P. 1178–1271 (2011).

[5] Zhu Y., Murali S., Cai W., Li X., Suk J.W., Potts J.R., et al. Graphene and Graphene Oxide: Synthesis, Properties, and Applications. *Advanced Materials*, **22**(35), P. 3906–3924 (2010).

[6] Melezhyk A.V., Makarova L.V., Konoplya M.M., Chuiko A.A. Synthesis and morphology of particles of microflaky graphite. *Khimiya tverdogo topliva* (Chemistry of solid fuel, Russian), **3**, P. 137–143 (1991).

[7] Melezhyk A.V., Rudyi R.B., Makarova L.V., Chuiko A.A. Synthesis and properties of self-bonding microflaky graphite. *Zhurnal Prikladnoi Khimii* (Journal of applied chemistry, Russian), **68**(1), P. 54–57 (1995).

[8] Melezhyk A.V., Chuiko A.A. Cold expansion of graphite – the way to new technologies. *Khimicheskaya tekhnologiya* (Chemical technology, Ukrainian), **2**, P. 3–11 (1992).

[9] Lee J.H., Shin D.W., Makotchenko V.G., Nazarov A.S., Fedorov V.E., Kim Y.H., et.al. One-Step Exfoliation Synthesis of Easily Soluble Graphite and Transparent Conducting Graphene Sheets. *Advanced Materials*, **21**(43), P. 4383–4387 (2009).

[10] Viculis L.M., Mack J.J., Mayer O.M., Hahn H.T., Kaner R.B. Intercalation and exfoliation routes to graphite nanoplatelets. *J. Mater. Chem.*, **15**(9), P. 974–978 (2005).

[11] Melezhyk A.V., Makarova L.V., Chuiko A.A. About the interaction of graphite with peroxodisulfuric acid. *Zhurnal neorganicheskoi khimii* (Journal of Inorganic Chemistry, Russian), **34**(2), P. 352–357 (1989).

[12] Nekrasov B.V. *Fundamentals of general chemistry* (Russian). Vol. 1. Khimiya (Chemistry) Edition, Moscow (1973) 656 p. – P. 337.

[13] Melezhyk A.V., Pyatkovskyi M.L., Yanchenko V.V., Prikhod'ko G.P., Sementsov Yu.I. Graphite intercalation compounds: peculiarities of formation and hydrolysis. *Khimichna promyslovist' Ukrayiny* (Chemical Industry of Ukraine), **6**(71), P. 7–16 (2005).

[14] Melezhyk A.V., Talanov V.S., Makarova L.V., Platonova E.P., Chuiko A.A. About the nature of surface groups of microflaky graphite. *Khimiya tverdogo topliva* (Chemistry of solid fuel, Russian), **5**, P. 13–16 (1991).

[15] Lotya M., Hernandez Y., King P.J., Smith R.J., Nicolosi V., Karlsson L.S., et al. Liquid Phase Production of Graphene by Exfoliation of Graphite in Surfactant/Water Solutions. *J. Amer. Chem. Soc.* **131**(10), P. 3611–3620 (2009).

[16] Zhang X.-F., Liu S., Shao X. Fluorescence of chemically derived graphene: Effect of self-rolling up and aggregation. *Journal of Luminescence*, **136**, P. 32–37 (2013).

NANOSYSTEMS: PHYSICS, CHEMISTRY, MATHEMATICS, 2014, 5 (2), P. 307–314

EFFECT OF THE MILD METHOD OF FORMATION V_xO_y/InP STRUCTURES USING V_2O_5 GEL ON THE PROCESS OF THEIR OXIDATION AND COMPOSITION OF NANOSIZED OXIDE FILMS

I. Ya. Mittova, E. V. Tomina, B. V. Sladkopevtcev

Voronezh State University, Voronezh, Russia

inorg@chem.vsu.ru

PACS 81.05.Ea, 81.16.Be, 81.65.Mq

A V_xO_y/InP structure was formed by the deposition of a V_2O_5 gel aerosol on an InP surface, followed by thermal annealing. This approach avoids chemostimulator interactions with the substrate prior to thermal oxidation, which is characteristic of 'hard' methods of chemostimulator deposition. The oxidation process of such structures occurs in the transit mechanism with a slight increase growth rate of films by 20–40 % in comparison with the oxidation of InP. The transit action of chemostimulator has been associated with the chemical bonding of V_2O_5 into $InVO_4$ (XRD), which predominates over mutual transformations of vanadium oxide, which forms in different oxidation states.

Keywords: indium phosphide, chemical stimulated oxidation, V_2O_5 gel.

1. Introduction

Advantages of the $A^{III}B^{V}$ semiconductor materials compared with silicon is largely shown by the low dielectric properties of thin films grown on surfaces by thermal oxidation. This is due to a lack of quality and technologically compatible dielectric, which in silicon electronics is silicon dioxide. Based on InP, it is possible to create heterostructures for high-frequency field transistors, long-wavelength lasers, multi-layered structures (ITO)/InP for use in solar cells [1–4], etc. One approach is the formation of insulating films on a semiconductor surface (as in the case of silicon), which can serve methods based on various kinds of oxidation processes for $A^{III}B^{V}$ semiconductors. There are various methods for indium phosphide oxidation, such as thermal, chemical, electrochemical, anodic and plasmic [5–10].

Released unoxidized indium promotes the growth of metallization layers on the indium phosphide surface, dramatically affecting their electrical properties and making them unsuitable for use as insulators or semiconductors in semiconductor electronics (due to ohmic conduction). Furthermore, the evaporation of the volatile component (phosphorus) degrades the surface and does not provide regular film growth with satisfactory dielectric characteristics.

In order to increase the efficiency of thermal oxidation of $A^{III}B^{V}$ semiconductors, substance-chemostimulators are used. At present, there are a large number of papers related to the study of chemical stimulating processes for indium phosphide oxidation [11]. The nature of these processes is the introduction into the system of substances, which, depending on the conditions, change the mechanism of the process, accelerate growth of films on semiconductor surface, modify composition and improve its characteristics, primarily electrical. Oxides, sulfides, chlorides, oxochloride and some other compounds may act as chemostimulators.

V_2O_5 is the most interesting of the d-metal oxides, which are efficient chemostimulators for the thermal oxidation of $A^{III}B^{V}$-semiconductors [12]. This oxide is capable of providing

a stimulating effect on the oxidation process of a semiconductor on both transit and catalytic mechanisms [13, 14].

The composition of films formed by chemostimulating the thermal oxidation InP and hence the properties of the synthesized structures and the quality of the interface are determined by the physico-chemical nature and method of chemostimulator introduction - through the gas phase or directly on the surface of the semiconductor. In the latter case, two groups of methods are used - hard (magnetron sputtering, electric explosion) and soft (sol-gel processes, low temperature MOCVD, etc.).

The widely used magnetron sputtering of chemostimulators is a high-energy method, which intensively acts on the substrate surface, stimulating interaction between the chemostimulator and the components of the semiconductor prior to thermal oxidation. So the question of finding less harsh methods for modifying the semiconductor's surface by vanadium oxide, which occurs at low temperature, is relevant. The ability of V_2O_5 to form sols and gels can be used in a V_2O_5 gel aerosol deposited on indium phosphide, is one such mild method. This does not significantly affect the surface of the semiconductor substrate prior to its oxidation.

The purpose of this research is to establish the features for an oxidation process of V_xO_y/InP structures, formed by mild methods, in comparison with the hard magnetron sputtering of V_2O_5, as well as determining the composition and morphology of the formed oxide films.

2. Experimental

The synthesis of vanadium oxide gel was carried out by the sol-gel method using the procedure proposed in [15]. A dispersed V_2O_5 gel was deposited via aerosol phase on the surface of InP FIE-1A [100], which was treated prior to the thermal oxidation with a H_2SO_4 (reagent grade, Russian State Standard GOST 4204-77, 92.80 %) : H_2O_2 (analytical grade, Russian State Standard GOST 177-88, 56 %): H_2O = 2 : 1 : 1 etchant for 10 minutes and then rinsed repeatedly with doubly-distilled water.

The aerosol, with 4–5 micron droplets, was obtained using a dispersant compressor that allows the use of viscous solutions. Deposition was carried out for 3 minutes on a substrate cooled by a Peltier element.

Annealing of the V_2O_5 gel layer, deposited on the surface of InP, was carried out in a horizontal quartz reactor of resistive heating furnace (MTP-2M-50-500) with a temperature control accuracy of $\pm$ 1 °C (OWEN TPM-10) at various time-temperature conditions. Oxidation of the V_xO_y/InP structures was carried out at 480–580 °C for 60 minutes, while control of the layer thickness growth was carried out every 10 minutes. The thicknesses of the deposited and growing films were determined by laser ellipsometry (LE, LEF-754, $\lambda = 632.8$ nm, absolute accuracy $\pm$ 1 nm).

Surface morphology of the samples was measured by scanning tunneling microscopy (STM) by a complex of nanotechnological equipment 'UMKA'. The data were processed using the microscope's software. The software of microscope and SPIP editor were used for processing the results (construction profiles, 3D-visualization). The phase composition of the formed films was studied by X-ray phase analysis (XRD) by diffractometer ARL X'TRA on copper radiation ($\lambda = 1.5406$ Å). The elemental composition of the oxide films on InP and distribution of the components thickness was investigated by Auger electron spectroscopy (AES, ESP-3 analyzer DESA-100, an accuracy of $\pm$ 10 %) with layer etching by argon ions.

3. Results and discussion

The structure of the $V_2O_5 \cdot nH_2O$ gel, is that the layers are connected by the edges of the VO_5 tetragonal pyramids, in which the space between the water molecules are introduced [16,

17]. Heating first leads to the removal of adsorbed water at about 100 °C followed by removal of part of the polymer chain-associated water, and at temperatures of about 370–400 °C the crystallization of vanadium oxide is completed [18, 19]. Thermal annealing of V_2O_5 gel layer on the surface of indium phosphide is necessary for removal of water from the interlayer space and the crystallization of the amorphous phase. This leads to the formation of polycrystalline films with a sufficiently ordered structure with an average crystallite size of 250–300 nm [15].

According to the results of XRD [15], the deposit on the indium phosphide layer after thermal annealing is composed of the vanadium oxides V_2O_5 and VO_2. Components of a semiconductor substrate have not been detected. The presence of V^{+4} cation is a necessary factor for the process of gelation [18]. The cation ratio of V^{+4} to V^{+5} was determined by the temperature and residence time of the melt [20]. V^{+4} content increases with increasing temperature, so the optimal mode of melting vanadium pentoxide was chosen to increase the content of V^{+5} in the deposited layer. Furthermore, the vanadium pentoxide may be decomposed to vanadium dioxide during thermal annealing. In the limiting case, non-stoichiometric vanadium dioxide, similar in composition to V_6O_{13}, can be formed when $V_2O_5 \cdot nH_2O$ films are heated in vacuo [20, 21]. Since in our work, the deposition on InP gel layers are heat treated aerobically to complete the transition, V_2O_5 vanadium oxides with low oxidation states do not occur.

Thus, the XRD data shows that the formation of chemostimulator layers on the surface of InP by the mild method (using of vanadium oxide (V) gel) interactions between chemostimulator and components of the semiconductor do not occur prior to the process of thermal oxidation. Deposition of the activator by hard electric explosion of wire leads to the oxidation of InP with the formation of indium phosphate prior to thermal oxidation of the substrate [22].

Kinetic curves of oxidation of the structures V_xO_y/InP from 480–580 °C are shown in Fig. 1, while the parameters of the equation $d = k^n t^n$ [11] of the process are displayed in Table 1. The effective activation energy of the process (EAE) is determined from the Arrhenius dependence of the rate constant averaged $\ln k_{av} = f(10^3/RT)$, shown in Fig. 2. For its calculation, they are averaged over n in a single mechanism of the process, and then, we find the value of $\ln k_{av}$. The values of n, ranging from 0.23 to 0.35, are typical for the diffusion-limited processes in the solid phase [11]. In this case, there is a similarity with thermal oxidation processes of V_2O_5/InP structures formed by magnetron sputtering with deposited layers of chemostimulator of varying thickness [23]. However, the value of EAE for the oxidation process of mildly-formed structures (Table 1) in the same order, although somewhat reduced in comparison to the EAE of indium phosphide oxidation (270 kJ/mol [11]). This fact points to the transitory nature of interaction between the deposited activator and the components of the semiconductor in thermal oxidation process. For structures formed by the hard magnetron sputtering method, the EAE value is much lower (30 kJ/mol) as compared with its own oxidation, regardless of the thickness of V_2O_5 layer deposited on InP surface [23]. This result and the lack of influence of the amount of deposited activator (change in amount of V_2O_5 by more than 20 fold) on the rate of oxidation and significant quantities of accelerating the rate of the film growth (from 70 % to 115 %) are proof of the catalytic mechanism of the oxidation [23].

Low values of relative increase of the rate process (20–30 %) were observed for the oxidation of V_2O_5 gel-formed structures in comparison to the direct oxidation of InP (see Fig. 3). Calculation of these values for the deposited layers (by magnetron sputtering, using the V_2O_5 gel) is carried out as follows:

$$b = \frac{\Delta d_{\mathrm{V_2O_5/InP}} - \Delta d_{\mathrm{InP}}}{\Delta d_{\mathrm{InP}}} \cdot 100\ \%.$$

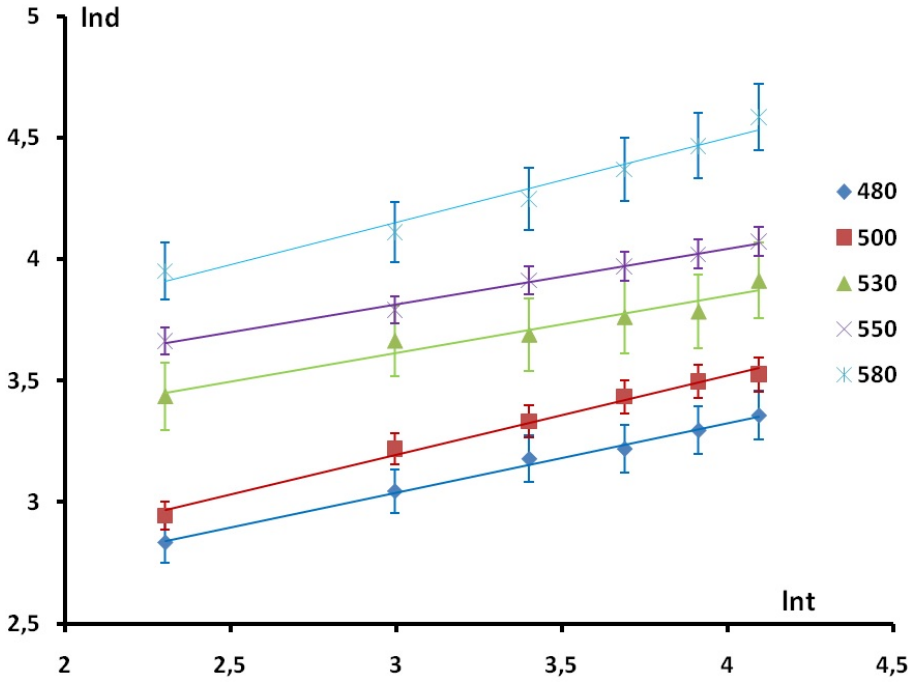

FIG. 1. Isotherms of V_xO_y/InP structures oxidation at 480, 500, 530, 550 and 580 °C under oxygen (in double logarithmic coordinates)

TABLE 1. Kinetic parameters of oxidation of V_xO_y/InP structures, formed using the gel of vanadium oxide (V)

T, °C	**480**	**500**	**530**	**550**	**580**
$\mathbf{lnk_{av}}$	7.65	7.75	10.20	10.95	10.90
$\mathbf{n \pm \Delta n}$, $\mathbf{nm^{1/n}\ min^{-1}}$	0.29 ± 0.006	0.33 ± 0.009	023 ± 0.055	0.23 ± 0.006	0.35 ± 0.031
$\mathbf{n_{av}}$	0.29				
EAE, kJ/mol	**210**				

The maximum rate of the process, when compared with the standard was achieved by 10 minutes of oxidation (Fig. 3, curve 1), when the diffusion restrictions have little effect, and the concentration of the reactants at the inner interface is maximized. During the developed stage, the values of acceleration fall, reaching a plateau, which is typical for chemical stimulated oxidation processes occurring on a transit mechanism. This is due to the absence of chemostimulator consumption and regeneration of the active form of vanadium in the +5 oxidation state during oxidation. With oxidation of magnetron-formed V_2O_5/InP structures (see curve 2 in fig. 3), the value of the acceleration changes little over time, and increases slightly at the maximum time of oxidation. This characteristic of the curve is proof for the regeneration of the chemostimulator V_2O_5 during the oxidation and, accordingly, its catalytic mechanism of action.

After thermal oxidation, the V_xO_y/InP, structures formed by the proposed mild method, in oxide films are present VO_2 and $InVO_4$ (XRD), the latter is a product of the of secondary interaction between V_2O_5 and In_2O_3 (Fig. 4). The $InVO_4$ formation determines the transit mechanism of thermal oxidation due to chemical bonding of vanadium pentoxide, prevailing over the mutual transformations of various forms of vanadium oxide. VO_2, unlike V_2O_5, can

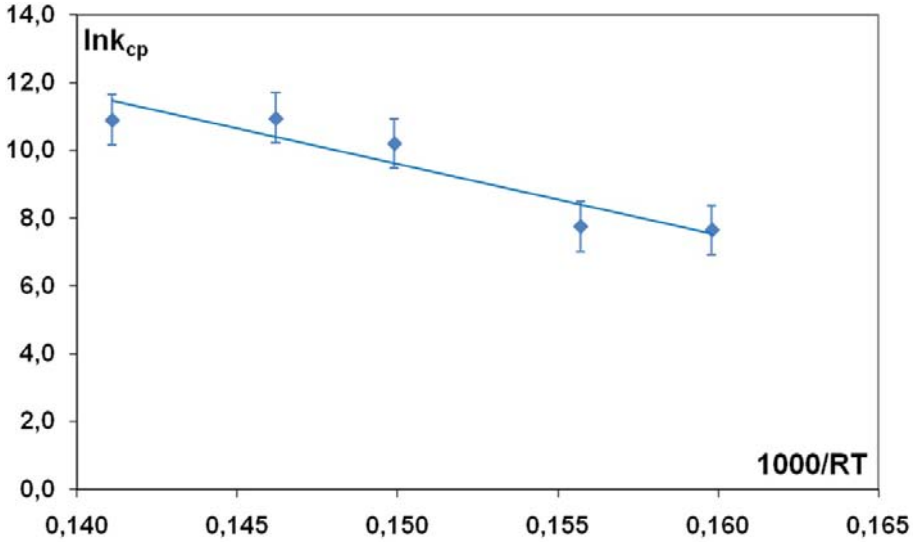

FIG. 2. Arrhenius plot of the average of the rate constant $\ln k_{av} = f(10^3/RT)$

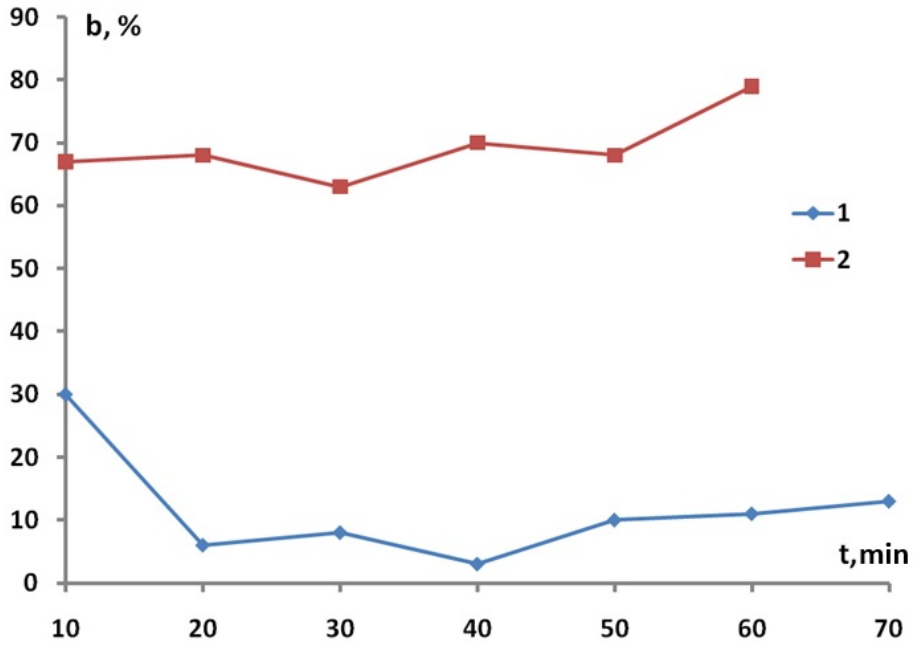

FIG. 3. Dependences of relative acceleration of oxidation process at 500 °C structure V_xO_y/InP formed by using the gel of vanadium pentoxide (1) and formed by magnetron structure V_2O_5/InP (2) compared with oxidation of InP

transmit oxygen only the semiconductor components due to transit interactions with its ability to transit much less pronounced than that of vanadium (V) oxide [23].

The results of Auger electron spectroscopy prove transit mechanism of chemostimulating action of deposited V_2O_5 gel in the oxidation of these structures. For the oxide film synthesized at 500 °C for 60 min (Fig. 5) there is an uneven vertical distribution of vanadium. In the region corresponding to the InP substrate, the vanadium content is about 5–6 at.%, which suggests a noticeable diffusion of the active chemostimulator element into the substrate (see fig. 5, the concentration profile of vanadium). The diffusion of the element-activator through the internal interface of the structure, leading to its partial regeneration, is inherent in the transit mechanism

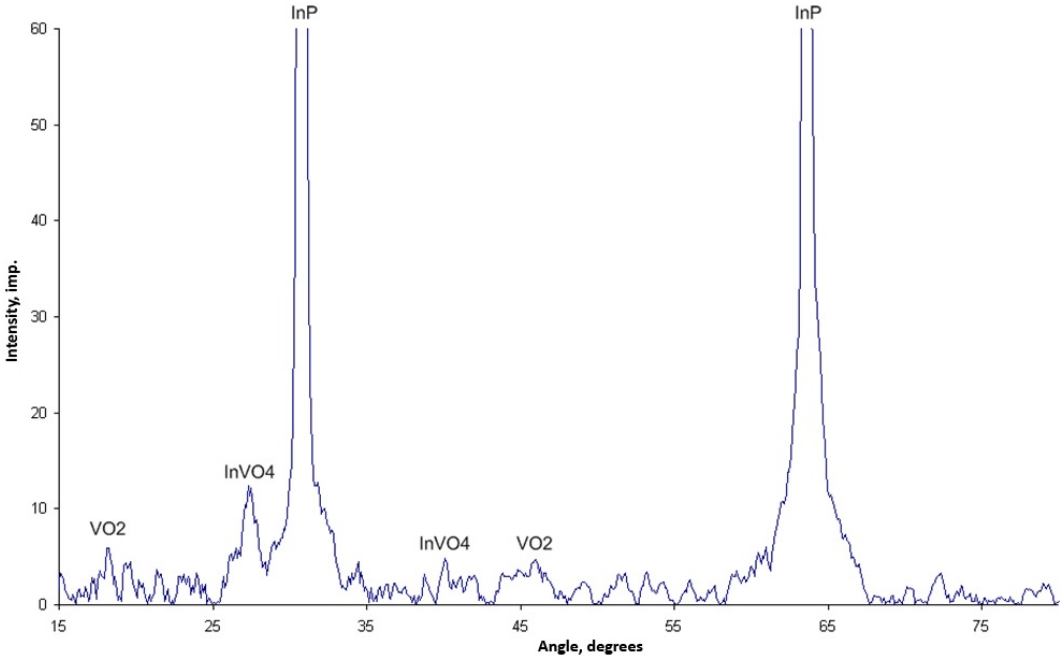

FIG. 4. The XRD pattern of the V_xO_y/InP structure after oxidation at 530 °C during 60 min.

of oxidation and proved by numerous experiments [11]. A characteristic feature of the films is a strong depletion of subsurface region by phosphorus. The curve corresponding to the profile of the distribution of phosphorus, appears closer to the interface 'substrate-film' (see Fig. 5, the profile of phosphorus concentration), which is a result of the evaporation of the volatile component of the semiconductor during the thermal oxidation.

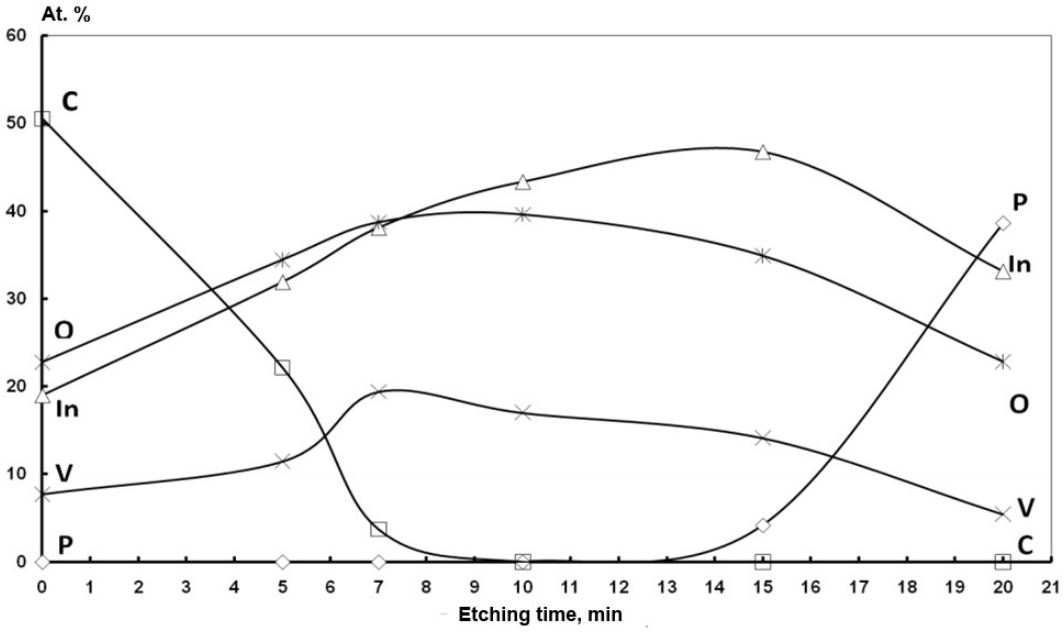

FIG. 5. Concentration profiles of elements (AES) in the sample V_xO_y/InP, synthesized using the vanadium oxide gel (annealing 200 °C, 120 min.) after 60 min. oxidation at 500 °C

Sufficiently smooth films are formed as a result of InP oxidation with deposited V_2O_5 layers, formed with both hard and mild methods (Fig. 6). The size of the structural elements of the films averaged 300–400 nm, depending on the oxidation temperature in the case of modification of InP by mild method, elevation topography $\sim$ 30–40 nm. When applying the magnetron, the size of V_2O_5 structural elements of the oxide films are 30–40 nm, with a relief height of 10–20 nm [24].

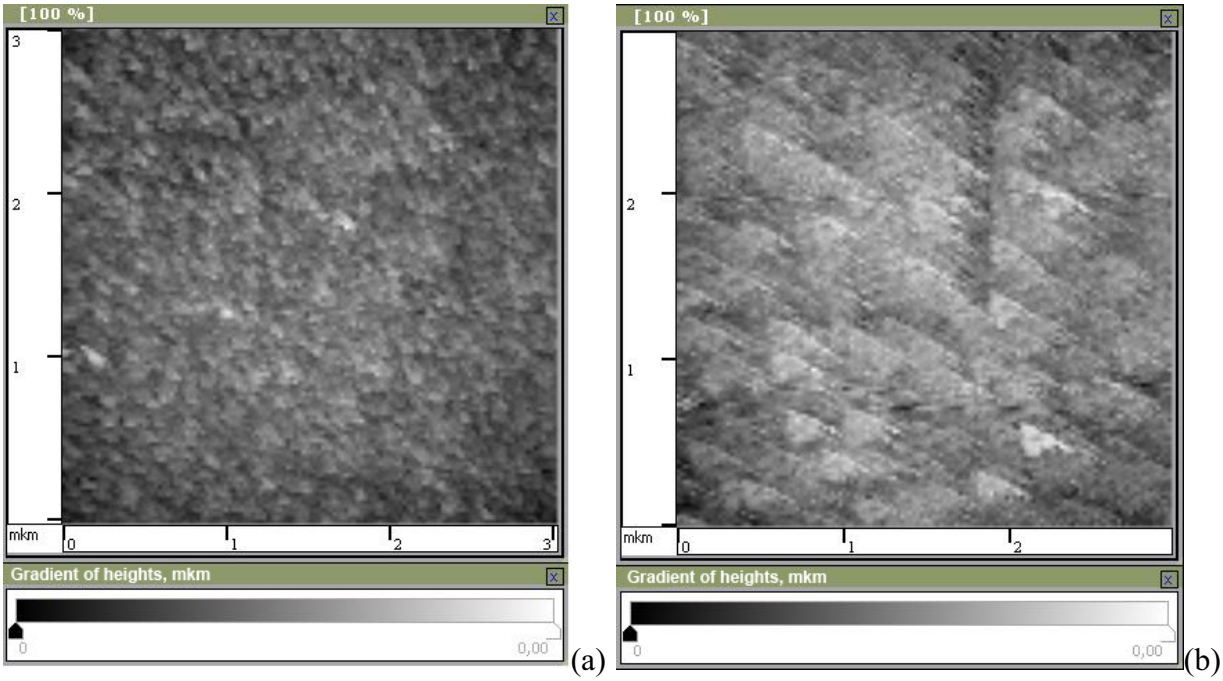

FIG. 6. STM image of surface of V_xO_y/InP structures (mild method) oxidized at 500 °C, (a) and 530 °C, (b). Scan size 3×3 mkm

4. Conclusions

Layers with an average crystallite size of 250–300 nm (STM) were formed on the surface of InP by mild deposition method of vanadium oxide gel via aerosol phase followed by thermal annealing. This method is characterized by the lack of interaction chemostimulator-substrate before thermal oxidation of V_xO_y/InP structures (XRD). Modified of InP by V_2O_5 gel leads to oxidation of semiconductor via a transit mechanism with low acceleration values for the process compared with oxidation of InP (about 20–40 %) in contrast to the oxidation process of V_2O_5/InP structures, formed by magnetron sputtering. The implementation of the activator action on transit mechanism is due to preferential binding of V_2O_5 in $InVO_4$, prevailing over the mutual transformations of various forms of vanadium oxide.

Acknowledements

This work was supported by the Ministry of Education and Science of the Russian Federation in line with government order for Higher Education Institutions in the field of science for 2014-2016 years (project No. 673) and by RFBR grant No. 13-03-00705-a.

References

[1] J. Henry, J. Livingstone. Design, fabrication, and characterization of photonic devices II. *Proc. SPIE*, **4594**, P. 447 (2001).

[2] Nikolaev Yu.A., Rud' Yu.V., Terukov E.I., Rud' V.Yu. Photosensitivity of heterojunctions obtained using thermal oxidation of indium phosphide. *Technical Physics Letters*, **33** (4), P. 313–315 (2007).

[3] Schimper H.-J., Kollonitsch Z., et al. Material studies regarding InP-based high-eficiency solar cells. *Journal of Crystal Growth*, **287** (2), P. 642–646 (2006).

[4] Lee S., Kim H.J., et al. Transferred-substrate InP/InGaAs/InP double heterojunction bipolar transistors with $f_{\max} = 425$ GHz. *Electronics Letters*, **37** (17), P. 1096–1098 (2001).

[5] Wilmsen C.W. Oxide layers on III-V compound semiconductors. *Thin solid films*, **30**, P. 105–117 (1976).

[6] Yamaguchi M., Ando K. Thermal oxidation of InP and properties of oxide films. *J. Appl. Phys.*, **5** (9), P. 5007–5012 (1980).

[7] Berman L.S., Gabaraeva A.D., et al. Temporal drift parameter interface indium phosphide – silicon dioxide. *Technical Physics Letters*, **22** (2), P. 65–69 (1996).

[8] Pulver D., Wilmsen C.W., Niles D., Kee R. Thermal oxides of $In_{0.5}Ga_{0.5}P$ and $In_{0.5}Al_{0.5}P$. *Journal of Vacuum Science & Technology B: Microelectronics and Nanometer Structures*, **19**, P. 207–214 (2001).

[9] Pakes A., Skeldon P., et al. Composition and growth of anodic and thermal oxides on InP and GaAs. *Surface and Interface Analysis*, **34**, P. 481–484 (2002).

[10] Belyakova E.D. Investigation of InP own oxides. *Surface. Physics, chemistry, mechanics*, **7**, P. 88–93 (1992).

[11] Mittova I.Ya., Pshestanchik V.R. The chemistry of processes which create dielectric layers with functional group substituents on semiconductors by impurity thermo-oxidation. *Russian chemical reviews*, **60** (9), P. 967–979 (1991).

[12] Mittova I.Ya., Tomina E.V., et al. Thermal oxidation of InP surfaces modified with NiO + PbO mixtures. *Inorganic Materials*, **41** (4), P. 323–330 (2005).

[13] Mittova I.Ya., Tomina E.V., Lapenko A.A., Khorokhordina A.O. Solid-state reactions during thermal oxidation of vanadium-modified GaAs surfaces. *Inorganic Materials*, **40** (5), P. 441–444 (2004).

[14] Lapenko A.A., Tomina E.V., et al. Dynamics of the surface composition and structure of InP oxidized in the presence of V and V_2O_5. *Inorganic Materials*, **44** (11), P. 1163–1168 (2008).

[15] Sladkopevtsev B.V., Mittova I.Ya., Tomina E.V., Burtseva N.A. Growth of vanadium oxide films on InP under mild conditions and thermal oxidation of the resultant structures. *Inorganic Materials*, **48** (2), P. 161–168 (2012).

[16] Giorgetti M., Berrettoni M., Smyrl W.H. Doped V_2O_5-Based cathode materials: Where does the doping metal go? An -ray absorption Spectroscopy study. *Chemistry of materials*, **19** (24), P. 5991–6000 (2007).

[17] Petkov V., Trikalitis P.N., et al. Structure of V_2O_5nH2O xerogel solved by the atomic pair distribution function technique. *Journal of the American Chemical Society*, **124** (34), P. 10157–10162 (2002).

[18] Semenenko D.A., Kulova T.L., et al. Electrophysical properties of V_2O_5 xerogels with lithium embedding as a function of the synthesis process. *International scientific journal for alternative energy and ecology*, **4** (48), P. 82–86 (2007).

[19] Balakhonov S.V., Ivanov V.K., Barantchikov A.E., Churagulov B.R. Differences in physical and chemical properties of vanadium oxide nanomaterials synthesized by hydrothermal and microwave-hydrothermal methods. *Nanosystems: physics, chemistry, mathematics*, **3** (4), P. 66–74 (2012).

[20] Berezina O.Ya., Velichko A.A., et al. Metal-semiconductor transition in nonstoichiometric vanadium dioxide films. *Inorganic Materials*, **43** (5), P. 505–511 (2007).

[21] Vinichenko D.A., Zlomanov V.P., et al. Synthesis of vanadium dioxide films by a modified sol-gel process. *Inorganic Materials*, **47** (3), P. 279–284 (2011).

[22] Mittova I.Ya., Tomina E.V., Lapenko A.A., Sladkopevtsev B.V. Synthesis and catalytic performance of V_2O_5 nanoislands produced on the surface of InP crystals by electroexplosion. *Inorganic Materials*, **46** (4), P. 383–388 (2010).

[23] Mittova I.Ya., Tomina E.V., Lapenko A.A., Sladkopevtsev B.V. The catalytic action of vanadium and its oxides (V) in the oxidation process of $A^{III}B^{V}$ semiconductors. *Nanosystems: physics, chemistry, mathematics*, **3** (2), P. 116–138 (2012).

[24] Tret'yakov N.N., Mittova I.Ya., et al. Effect of the procedure of chemostimulator application on the surface characteristics of V_xO_y/InP structures in the process of their thermooxidation. *Russian Journal of General Chemistry*, **83** (8), P. 1589–1593 (2013).

NANOSYSTEMS: PHYSICS, CHEMISTRY, MATHEMATICS, 2014, 5 (2), P. 315–319

SYNTHESIS AND IDENTIFICATION WATER-SOLUBLE TRIS-MALONATE OF LIGHT FULLERENE – $C_{60}[=C(COOH)_2]_3$

K. N. Semenov[1], N. A. Charykov[2,3], A. S. Kritchenkov[1], I. A. Cherepkova[2], O. S. Manyakina[2], D. P. Tyurin[2], A. A. Shestopalova[2], V. A. Keskinov[2], K. V. Ivanova[2], N. M. Ivanova[1], D. G. Letenko[4], V. A. Nikitin[5], E. L. Fokina[1], O. V. Rakhimova[3]

[1]St. Petersburg State University, Saint-Petersburg, Russia
[2]St. Petersburg State Technological Institute (Technical University), Saint-Petersburg, Russia
[3]St. Petersburg State Electro-Technical University (LETI), Saint-Petersburg, Russia
[4]St. Petersburg State University Architecture Academy, Saint-Petersburg, Russia
[5]St. Petersburg State Technical University, Saint-Petersburg, Russia

keskinov@mail.ru

PACS 61.48.+c

The water soluble tris-malonate adduct of light fullerene – $C_{60}[=C(COOH)_2]_3$ was produced in laboratory quantities. The product was identified by several analytical methods: elementary H–C–O–N analysis, IR-, Electronic, NMR- Spectroscopy, Mass Spectrometry.

Keywords: tris-malonate of light fullerene, synthesis, elementary analysis, IR-, Electronic, NMR- Spectroscopy, Mass Spectrometry.

1. The synthesis of tris-malonate C_{60}

Diethyl malonate (100 mg) was dissolved in o-xylene (50 ml) under gaseous nitrogen in the presence of a twentyfold molar excess of NaH for 3 hours at 60 °C. After this procedure, the NaH was almost homogeneously suspended in toluene while the diethyl malonate was unaffected. The transformation of the malonate was accompanied by a vigorous gaseous evolution and the quantitative precipitation of the sodium salt of the tris-malonate C_{60} took place after the addition of methanol (1 ml). After centrifugation and removal of the liquid phase, the precipitate was washed with toluene, 2 M H_2SO_4, then water and finally dried under vacuum at 60 °C for 12 hours. Such scheme was described earlier in the original paper [1]. Scheme of the synthesis is represented lower in the Fig. 1. It is worth noting that carboxylic acid formation probably occurs as a result of acidic hydrolysis during the treatment with 2 M H_2SO_4.

2. Identification of tris-malonate C_{60}

2.1. Element C–H–O–N analysis

EuroEA3028-HT Eurovector Element C–H–O–N analyzator was used. The result of the analysis is represented lower in the Table 1.

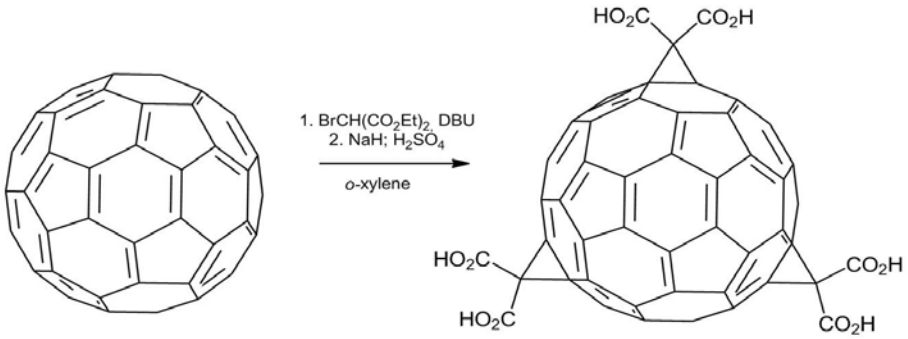

or $C_{60}(=C=(COOH)_2)_3$

FIG. 1. Scheme of the synthesis of tris-malonate C_{60}

TABLE 1. Data of element C–H–O–N analysis

Element	Calculated composition C^{cal} (% mass)	Experimental composition C^{exp} (% mass)	$/C^{exp} - C^{cal}/$ (% mass)
C	80.71	80.73	0.002
H	0.59	0.54	0.005
O	18.70	18.73	0.003

2.2. High resolution mass spectrometry

High resolution Electrospray ionization mass spectrometry (positive mode) was performed using a Shimadzu GCMS-QP2010Ultra ($[C_{60}(=C=(COOH)_2)_3 - H]^+$) . The experimental value for M/z (M, z – ion mass in atomic units and ion charge, correspondingly) in the case $z = 1$ was equal to the calculated value of M/z in the positive charged form, represented above: $M/z = 1026 + 1 = 1027$ atomic units.

3. Nuclear magnetic resonance

A Bruker Avance 400 NMR-spectrometer was used. Experimental NMR-peak data (in ppm) were as follows:
δ_H (300 MHz, D_2O): 11.7 (wide singlet, H – from carboxyl groups –COOH);
δ_C (75.5 MHz, D_2O): 166.57, 166.54, 166.27, 150.04, 148.79, 147.91, 147.85, 147.59, 147.05, 146.86, 146.74, 146.68, 146.47, 146.24, 146.15, 146.12, 145.90, 145.68, 145.53, 145.33, 144.85, 144.54, 144.47, 143.54, 143.28, 143.16, 143.07, 140.40, 140.13, 74.32, 69.16, 62.25.

3.1. Infrared Spectroscopy

A Shimadzu IR Spectrometer IRAffinity-1 was used in the wave-numbers range $\tilde{\nu} = 450 - 4500$ cm^{-1}. Solid tablets of tris-malonate C_{60} in dry KBr were used aas samples. Experimental IR main reflexes data in $\tilde{\nu}$ (cm^{-1}) were the following: 3470, 1811, 1723, 1715, 1431, 1405, 1410, 1222, 1231, 1057, 820, 833, 730, 580, 528, 522. One can see that long-wavelength part of spectrum: $\tilde{\nu} = 522-1715$ cm^{-1}, corresponds to the oscillations of C–C bonds in fullerene C_{60}, compare with the main absorption data in $\tilde{\nu}$ (cm^{-1}) for C_{60}: [1,2]. At the same, time short- wavelength part of spectrum: $\tilde{\nu} = 1700-1725$ cm^{-1}, corresponds to the oscillations

of C=O bonds in malonate-groups in $C_{60}[=C(COOH)_2]_3$, $\tilde{\nu} = 3450 - 3550$ cm^{-1} corresponds to the oscillations of rather free O–H groups. A standard absorption at 1811 cm^{-1} we associated with the oscillation of C–C bonds in external cyclopropanes in tris-malonates (see Fig. 1). Similar results were obtained by us earlier in the course of studying of another moderately soluble derivative of light fullerenes C_{60} and C_{70} – fullerenols – $C_{60}(OH)_n$, $C_{70}(OH)_m$ [2–5].

3.2. Electronic Spectroscopy

An Evolution 201 Thermo Fischer spectrophotometer was used for wavelengths ranging from 190 – 1100 nm (water solutions of tris-malonate of C_{60} against pure water). The spectrum is presented lower in Fig. 2.

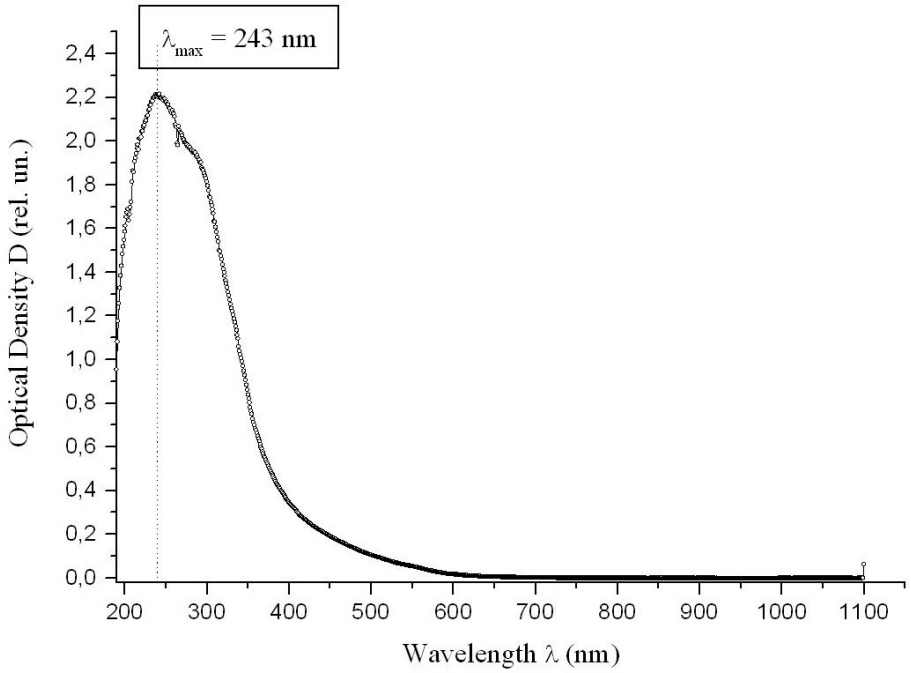

FIG. 2. Electronic spectrum of water solutions of tris-malonate of C_{60} against pure water

One can see that electronic spectrum of tris-malonate of C_{60} in visible and near ultraviolet, near infrared region (250 – 1100 nm) is very simple, it has no light absorption peaks and may be characterized by consequently strengthening of light absorption with the lower wavelengths. In the near infrared region, the spectrum of the tris-malonate C_{60} adduct is practically transparent and has no light absorption. The unique light absorption peak ($\lambda \approx 243$ nm) exists in the spectrum.

The electronic spectrum may be efficiently used for the determination of the concentration via the Beer-Lambert-Bouguer law in near ultraviolet region (for example at $\lambda \approx 330$ nm) (see Fig. 3).

Similar results were obtaines by us earlier during the studying of fullerenols – $C_{60}(OH)_n$, $C_{70}(OH)_m$ [2–5].

3.3. Optical polarizing microscopy

Optical polarizing microscopy was performed with a Leica 4500P instrument. Samples were prepared by crystallization of tris-malonate of C_{60} crystals from water solutions at the isothermal evaporation of water from the solutions with the different concentrations at 25 °C

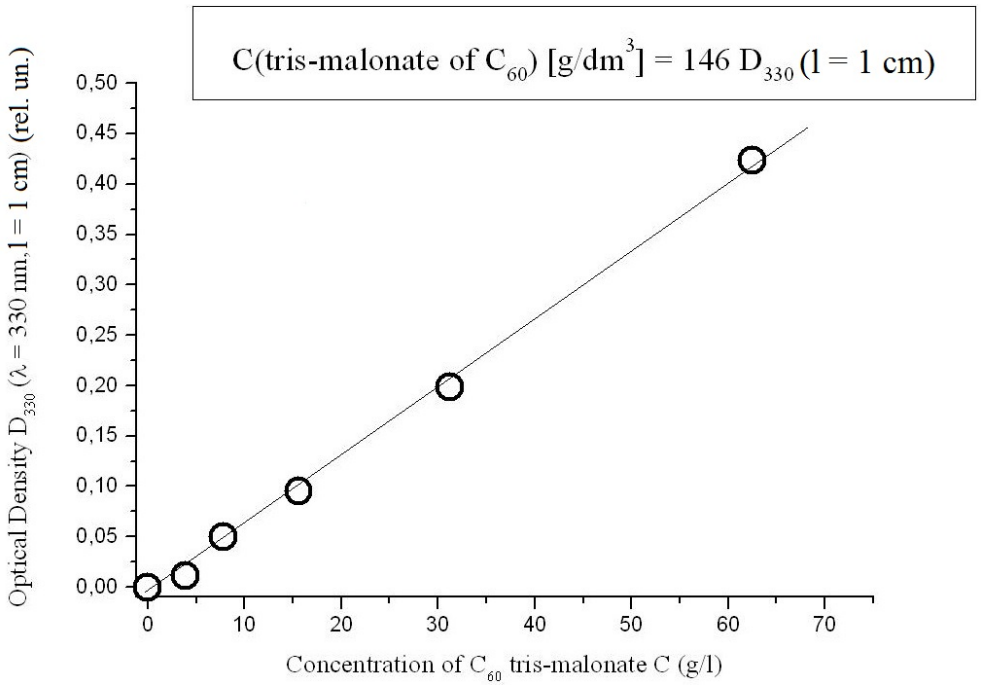

FIG. 3. Buger-Lamber-Ber law at $\lambda = 330$ nm in water solutions of tris-malonate of C_{60}

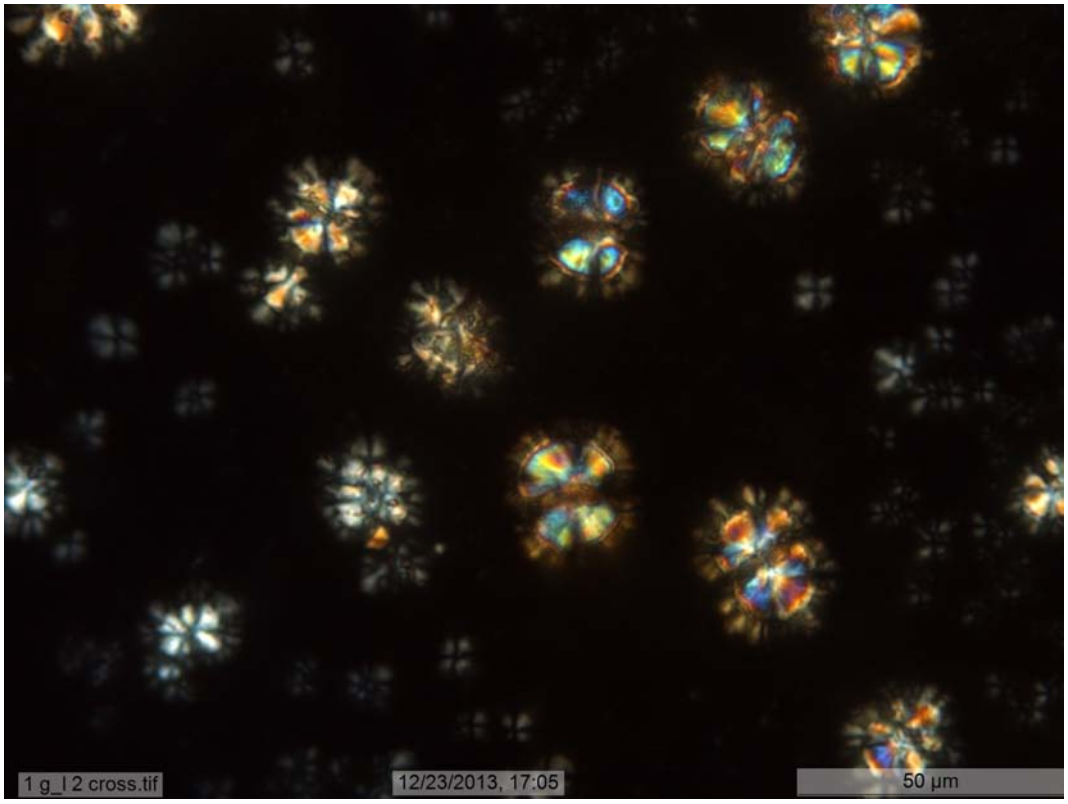

FIG. 4. Optical polarizing microscope photo of the crystals of tris-malonate of C_{60} (scale $\times 500$). Initial (before evaporation) solution had concentration $C = 1$ g of tris-malonate of C_{60} per dm^3

(the drop of the solution was put on the surface of silicate glass). A typical photo is presented in Fig. 4.

Thus, synthesis in gram quantities and identification by the modern methods of physico-chemical analysis of water soluble derivative of light fullerene – $C_{60}[=C(COOH)_2]_3$, was performed.

Acknowledgments

Research was executed with the help of the equipment of the Resource Center 'Geo-Model' of Saint-Petersburg State University.

This work has been accomplished as the part of the Ministry of Education and Science of the Russian Federation research assignment 'Realization of scientific research (fundamental studies, applied research and advanced developments)'. Project code: 2548.

References

[1] Lamparth I., Hirsch A. Water-soluble malonic acid derivatives of C_{60} with a defined three-dimensional structure. *J. Chem. Soc. Chem. Commun.*, P. 1727–1728 (1994).

[2] Semenov K.N., Charykov N.A., Pronskih A.E, Keskinov V.A. Fullerenol-70-d: synthesis, identification, polythermal solubility and density of water solutions. *Nanosystems: Physics, Chemistry, Mathematics*, **3** (6), . 1–10 (2012).

[3] Semenov K.N., Charykov N.A., Keskinov V.A. Synthesis and Identification. Properties of Fullerenol Water Solutions. *J. Chem. Eng. Data*, **56**, P. 230–239 (2011).

[4] Semenov K.N., Charykov N.A. Solubility of Light Fullerenes and Fullerenol in Biocompatible with Human Beings Solvents. Chapter in Handbook: Grapes: Cultivation, Varieties and Nutritional Uses, Nova Sciences Publishers, Inc., Editor R.P. Murphy et al., P. 1–48 (2011).

[5] Semenov K.N., Charykov N.A. Phase Equilibria in the Fullerene-Containing Systems. Handbook on Fullerene: Synthesis, Properties and Applications. Editor R.F.Verner, C.Benvegny, P. 1–91 (2012).

NANO Ф&Х&М

NANOSYSTEMS:

PHYSICS, CHEMISTRY, MATHEMATICS

INFORMATION FOR AUTHORS

The journal publishes research articles and reviews, and also short scientific papers (letters) which are unpublished and have not been accepted for publication in other magazines. Articles should be submitted in English. All articles are reviewed, then if necessary come back to the author to completion.

The journal is indexed in Chemical Abstract Service of the American Chemical Society and in Russian Scientific Citation Index.

Author should submit the following materials:

1. Article file in English, containing article title, the initials and the surname of the authors, Institute (University), postal address, the electronic address, the summary, keywords, MSC or PACS index, article text, the list of references.
2. Files with illustrations, files with tables.
3. The covering letter in English containing the article information (article name, MSC or PACS index, keywords, the summary, the literature) and about all authors (the surname, names, the full name of places of work, the mailing address with the postal code, contact phone number with a city code, the electronic address).
4. The expert judgement on possibility of publication of the article in open press (for authors from Russia).

Authors can submit a paper and the corresponding files to the following addresses: nanojournal.ifmo@gmail.com, popov1955@gmail.com.

Text requirements

Articles should be prepared with using of text editors MS Word or LaTEX (preferable). It is necessary to submit a pdf copy. In the name of files the English alphabet is used. The recommended size of short communications (letters) is 4-6 pages, research articles – 6-15 pages, reviews – 30 pages.

Recommendations for text in MS Word:

Formulas should be written using Math Type. Figures and tables with captions should be inserted in the text. Additionally, authors present separate files for all figures and Word files of tables.

Recommendations for text in LaTex:

Please, use standard LaTex without macros and additional style files. The list of references should be included in the main LaTex file. Single LaTex file of the paper with the corresponding pdf file should be submitted.

References in the article text are given in square brackets. The list of references should be prepared in accordance with the following samples:

[1] N. Surname. *Book Title*. Nauka Publishing House, Saint Petersburg, 281 pp. (2000).
[2] N. Surname, N. Surname. Paper title. *Journal Name*, **1**(5), P. 17-23 (2000).
[3] N. Surname, N. Surname. Lecture title. In: Abstracts/Proceedings of the Conference, Place and Date, P. 17-23 (2000).
[4] N. Surname, N. Surname. Paper title (2010). URL: http://books.ifmo.ru/ntv.
[5] N. Surname, N. Surname. Patent Name. Patent No. 11111, Bul. No. 33, 5 pp. (2010).
[6] N. Surname, N. Surname. Thesis Title. Thesis for full doctor degree in math. and physics, Saint Petersburg, 105 pp. (2000).

Requirements to illustrations

Illustrations should be submitted as separate black-and-white files. Formats of files – jpeg, eps, tiff.

N A N O
Ф&Х&М

NANOSYSTEMS:

PHYSICS, CHEMISTRY, MATHEMATICS

Журнал зарегистрирован
Федеральной службой по надзору в сфере связи, информационных технологий и массовых коммуникаций
(свидетельство ПИ № ФС 77 - 49048 от 22.03.2012 г.)
ISSN 2220-8054

Учредитель: федеральное государственное бюджетное образовательное учреждение высшего профессионального образования
«Санкт-Петербургский национальный исследовательский университет информационных технологий, механики и оптики»

Издатель: федеральное государственное бюджетное образовательное учреждение высшего профессионального образования
«Санкт-Петербургский национальный исследовательский университет информационных технологий, механики и оптики»

Отпечатано в учреждении «Университетские телекоммуникации»
Адрес: 197101, Санкт-Петербург, Кронверкский пр., 49

Подписка на журнал НФХМ
На второе полугодие 2014 года подписка осуществляется через
ОАО Агентство «Роспечать»
Подписной индекс 57385 в каталоге «Издания органов научно-технической информации»